

# **The Quest for High Entropy Alloy Catalysts**

Inaugural dissertation  
of the Faculty of Science,  
University of Bern

presented by

Vladislav Mints

from the Netherlands



Supervisor of the doctoral thesis:

Prof. Dr. Matthias Arenz

Department of Chemistry Biochemistry and Pharmaceutical  
Sciences



# **The Quest for High Entropy Alloy Catalysts**

Inaugural dissertation  
of the Faculty of Science,  
University of Bern

presented by

Vladislav Mints  
from the Netherlands

Supervisor of the doctoral thesis:

Prof. Dr. Matthias Arenz

Department of Chemistry Biochemistry and Pharmaceutical Sciences

Accepted by the Faculty of Science.

Bern, 09-02-2024

The Dean

Prof. Dr. Marco Herwegh

Illustrations by Anna larchuk.

This work has been written with the assistance of ChatGPT.



© 2024. This work is licensed under the Creative Commons Attribution-NonCommercial-NoDerivatives 4.0 International License. <https://creativecommons.org/licenses/by-nc-nd/4.0/>

This license enables reusers to copy and distribute the material in any medium or format in unadapted form only, for noncommercial purposes only, and only so long as attribution is given to the creator.

This license does not apply to reprinted articles in Chapter 2, 3, 4, and their corresponding Supplementary Information.

SOMETIMES WE FORGET THAT DOING SCIENCE IS FUN

Preprint

Paper 1

Mints, V. A.; Pedersen, J. K.; Bagger, A.; Quinson, J.; Anker, A. S.; Jensen, K. M.; Rossmeisl, J.; Arenz, M. Exploring the Composition Space of High-Entropy Alloy Nanoparticles for the Electrocatalytic H<sub>2</sub>/Co Oxidation with Bayesian Optimization. *ACS Catalysis* **2022**, *12* (18), 11263–11271. DOI:10.1021/acscatal.2c02563.

Paper 2

Pedersen, J. K.; Clausen, C. M.; Krysiak, O. A.; Xiao, B.; Batchelor, T. A.; Löffler, T.; Mints, V. A.; Banko, L.; Arenz, M.; Savan, A.; Schuhmann, W.; Ludwig, A.; Rossmeisl, J. Bayesian Optimization of High-entropy Alloy Compositions for Electrocatalytic Oxygen Reduction\*\*. *Angewandte Chemie International Edition* **2021**, *60* (45), 24144–24152. DOI:10.1002/anie.202108116.

Paper 3

Plenge, M. K.; Pedersen, J. K.; Mints, V. A.; Arenz, M.; Rossmeisl, J. Following Paths of Maximum Catalytic Activity in the Composition Space of High-entropy Alloys. *Advanced Energy Materials* **2022**, *13* (2). DOI:10.1002/aenm.202202962.

Paper 4

Tirmidzi, A.; Arenz, M.; Mints, V.A.. Investigating Particle Swarm Optimization in High Entropy Alloy Research as an alternative to Bayesian Optimization. *Manuscript in preparation*.

Paper 5

Mints, V.A.; Pedersen J.K.; Wiberg. G.K.H.; Rossmeisl, J.; Arenz, M. Learning in Higher Dimensions: A Strategy for Alloy Electrocatalyst Discovery. *Manuscript submitted*.

Paper 6

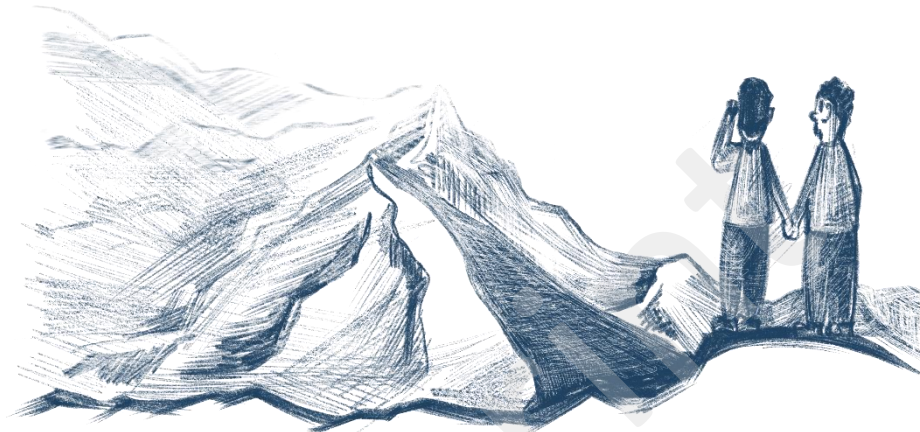
Mints, V.A.; Svane, K.L.; Rossmeisl, J.; Arenz, M. Exploring the high entropy oxide composition space: insights through comparing experimental with theoretical models for the oxygen evolution reaction. *Manuscript submitted*.

# Table of Contents

Chapter 1. Introduction .....	7
Chapter 2. Paper 1 .....	11
Chapter 3. Paper 2 .....	23
Chapter 4. Paper 3 .....	35
Chapter 5. Paper 4 .....	43
Chapter 6. Paper 5 .....	49
Chapter 7. Paper 6 .....	67
Chapter 8. Literature Review .....	87
Epilogue. Outlook .....	101
Acknowledgments .....	111
Supporting Information. Paper 1 .....	113
Supporting Information. Paper 2 .....	125
Supporting Information. Paper 3 .....	147
Supporting Information. Paper 5 .....	183
Supporting Information. Paper 6 .....	219
Bibliography .....	247
Declaration of Consent.....	261



# 1 Every scientific project has a beginning, but not necessarily an end



The idea of high entropy alloys originated in 2004 from the research of two groups. Brian Cantor and co-workers authored a publication in which they studied alloys with up to 20 different elements.<sup>1</sup> They observed that alloys composed of 5-6 elements surprisingly yielded a single FCC phase, instead of multiple phases as allowed by the Gibbs Law. At the same time, Yeh and co-workers published their work in which they investigated multiple equimolar 5-element alloys characterized by their large configurational entropy.<sup>2</sup> According to their work, this large configurational entropy favored elemental mixing producing, a random solid solution over an ordered intermetallic phase. Yeh and co-workers also defined for the first-time high entropy alloys as alloys which are composed of at least 5 elements with each having a concentration range between 5 and 35 at.%. Yeh revisited this definition in 2013 by redefining high entropy alloys as alloys with a configurational entropy larger than  $1.5R$ .<sup>3</sup>

Since their discovery, high entropy alloys have been widely extensively investigated for their material properties. These properties as outlined in Yeh's 2013 paper<sup>3</sup> are often explained by four core-effects unique to high entropy alloys: high entropy effect, sluggish diffusion, lattice distortion and cocktail effect. In the future, these effects will often get invoked to explain the observed performance of High Entropy Alloy catalysts. Therefore, for a critical comprehension of the literature it is necessary to understand the concepts behind these core-effects.

The high entropy effect states that the large configurational entropy of  $1.5R$  can compete with the formation enthalpy of strong intermetallic binary compounds. Consequently, when a high entropy alloy is synthesized at elevated temperature there is a thermodynamic driving force ensures random mixing of the elements. This also provides high entropy alloys with an increased

thermal stability. When the mixture is rapidly cooled, this random mixture is preserved. Consequently, it can be safely assumed that a high entropy alloy is a disordered mixture of elements which exhibits only a single phase. Furthermore, this effect enables the alloying of elements which in low entropy alloy configurations are non-miscible. This opens a pathway to synthesize novel materials containing elements which previously would not come together.

The sluggish diffusion effect is a key property of high entropy alloys that kinetically stabilizes the chaotic structure at low temperatures. It is hypothesized that diffusion kinetics in a metal are dependent on the lattice potential energy.<sup>4</sup> In the case of a high entropy alloy, each lattice site has a different atomic surrounding leading to distinct lattice potential energies. Consequently, this inhomogeneous energy landscape hinders bulk diffusion by trapping elements in low potential regions.

High entropy alloys are also known to display a severe lattice distortion. This distortion increases the hardness and strength of high entropy alloys over conventional alloys. However, it also affects electrical and thermal conductivity. In the context of electrocatalytic applications, it is hypothesized that as the lattice distortion affects the d-band structure of the material it should also influence the catalytic performance.

Lastly, exceptional unexplainable performances of high entropy alloys are often ascribed to the cocktail effect. The cocktail effect is defined as: “a synergistic mixture where the end result is unpredictable and greater than the sum of the parts”.<sup>5</sup> Consequently, the cocktail effect is just an idea that high entropy alloys may possess properties that we cannot explain by studying its components. As this is not a hypothesis which has underlying physical properties it requires no proof. Conversely, attributing observations to the cocktail effect is only postulating them as truth instead of providing a deeper physical explanation.

In 2019, Jan Rossmeisl and co-workers decided to investigate high entropy alloys for catalytic applications. At that time, only 15 publications referenced the terms “high entropy alloy” and “catalysis”, limiting the knowledge about high entropy alloy catalysis. Therefore, essentially all we knew about high entropy alloy catalysts were fruits of philosophical discussions. The four known core-effects served as the foundational concepts for them. The high entropy effect allowed to create materials containing active sites that under other circumstances cannot exist. The sluggish diffusion effect could provide alloys with additional stability and corrosion resistance. The lattice distortion effect might fine tune the electronic structure of the active sites enhancing their activity. Lastly, the cocktail effect stated that a numerous unique and unexpected properties may lie ahead. Combined, studying high entropy alloys became a promising venture.

Jan Rossmeisl’s and co-workers pioneering work<sup>6</sup> in high entropy alloy catalysis proposed a density functional theory (DFT) based model to calculate the activity of high entropy alloy catalysts for the oxygen reduction reaction. This work assumed that a high entropy alloy surface according to the high entropy effect is a random arrangement of atoms. This randomness implies that each atom has a unique environment leading to variation in the binding energy of the catalytic intermediates. Consequently, unlike traditional catalysts described by a single

binding energy, high entropy alloys are described by a distribution of different binding energies. The prevalence of each binding energy adheres to statistical principles. This research highlighted that high entropy alloy catalysts can produce active sites with optimal binding energies demonstrating their feasibility as a research topic.

Their findings laid the foundation for the establishment of the Center for High Entropy Alloy Catalysis, which opened in January 2020. I had the privilege of joining this center in the summer of the same year. Thus, I ventured into uncharted territory, studying it and contributing fresh ideas to the realm of high entropy alloy catalysis research. These ideas and findings will be explored in detail in the subsequent chapters.



# 2 It is time to kick the donkey



At the start of my PhD I had a discussion with my supervisor Matthias Arenz regarding the direction of my PhD project. As a conclusion of this talk, he gave me all the freedom in designing my project. So, I had to come up with a research plan. For high entropy alloy studies, a template for the typical *modus operandi* already existed which is still widely employed. A high entropy alloy catalyst is synthesized and characterized with X-ray diffraction, energy-dispersive X-ray spectroscopy and transmission electron microscopy. Thereafter its electrocatalytic performance is measured against a benchmark catalyst. This template can further be extended to include additional material characterization methods such as X-ray photoelectron spectroscopy, X-ray absorption spectroscopy as well as electrochemical stability measurements. However, even though there exists a template for studying high entropy alloy catalysts, the research field faced a major challenge. Namely, which composition to study in the first place?

The high entropy alloy composition space is vast and complex, presenting a challenging scenario for systematic exploration. According to the analysis of Yeh, it is possible to make 7000 equimolar high entropy alloys out of a selection of 13 elements.<sup>3</sup> Additionally, the tunability of combinations within each alloy expands the possibilities to millions of possible compositions. Finally, the constraint of using only 13 elements can be lifted, which according to the analysis of Cantor allows to design  $10^{80}$  alloys.<sup>7</sup> This number is in the range of the number of atoms in the universe making it impossible to study all alloys and record their data. Furthermore, we cannot expect that all high entropy alloys will show exceptional catalytic performance. Therefore, considering our resource limitations it becomes imperative to rationalize which high entropy

alloys to study and which are better left in the dark. In complete absence of prior knowledge on high entropy alloy catalysis we faced a similar problem as the Buridan's Ass paradox.

The Buridan's Ass paradox, originating in the 14<sup>th</sup> century, presents a thought experiment where a donkey is placed exactly in the center between two completely equal stacks of hay. Due to the absolute equivalence of the choices, the donkey remains immobilized leading to its eventual starvation. The only means of saving the donkey is to perturb the system by pushing him slightly in one of the two directions. Likewise, choosing which high entropy alloy to study is an impossible task in absence of knowledge. Therefore, the most rational decision is to wait for more research or the development of a high entropy alloy theory. However, instead of waiting, I decided to search for strategies on how to choose which high entropy alloy composition is worth investigating in greater detail.

While I was searching for a suitable strategy, I came across the paper of Nugraha and co-workers.<sup>8</sup> The authors optimized the composition of PtPdAu alloy films for methanol oxidation with the means of Bayesian optimization. Bayesian optimization, an algorithm for black box optimization, uses a Gaussian process to propose compositions that may yield a novel optimal performance. Therefore, Bayesian optimization offered a promising strategy to explore and identify which high entropy alloy compositions are worth investigating in greater detail. Recognizing the applicability of this algorithm, I was inspired to adapt and replicate their methodology in my investigation of PtRuPdRhAu for CO oxidation.

This work started by evaluating the CO oxidation performance for 25 randomly selected PtRuPdRhAu compositions. Subsequently, I used these samples to construct a random forest regression, which facilitated the Bayesian optimization algorithm to propose batches of 10 compositions rather than just one. Reflecting on this process, I've come to realize that it might not have been the brightest idea. Bayesian optimization works by creating a Gaussian process model based on the observed data. This model is used to propose a single new observation that should be added to the model. Each added observation updates the gaussian process leading to changes in its mathematical landscape. However, when the Bayesian optimization is used on the surrogate random forest regression the mathematical landscape is not updated between the first point and the last point in the batch. As a result, Bayesian optimization was suggesting compositions that were closely related, diminishing the optimization efficiency. Therefore, in later studies we have also considered other optimization algorithms.

Within the PtRuPdRhAu composition space, Bayesian optimization identified the global optimum of PtRu without requiring any prior assumptions. This optimum, coincided with the already known observation that PtRu is the optimal CO resistant hydrogen oxidation reaction catalyst. In addition, this optimization study produced a dataset of 68 different compositions, which allowed the construction of a simple experimental based machine learning model. Here we realized in collaboration with Jan Rossmeisl's group that this machine learning model can be used to assist the development of a DFT model. Assuming that the machine learned experimental model is representing reality, this comparison allows to identify which DFT model best represent all trends across different gradients. Later, we explored this idea of combining experimental machine learning models with DFT models in greater detail.

To summarize, even though this study was using of a previously published methodology, it had lots of resonance within the Center for High Entropy Alloy Catalysis. We found a treasure chest containing lots of valuable techniques and methods that can be integrated in our experimental studies. Suddenly, machine learning methods which were seen as something distant to our research field got within our grasp. Now, we are actively exploring the newly opened possibilities by employing mathematical methods not only in the field of high entropy alloy catalysis but also in other electrochemical divisions.

# Exploring the Composition Space of High-Entropy Alloy Nanoparticles for the Electrocatalytic H<sub>2</sub>/CO Oxidation with Bayesian Optimization

Vladislav A. Mints, Jack K. Pedersen, Alexander Bagger, Jonathan Quinson, Andy S. Anker, Kirsten M. Ø. Jensen, Jan Rossmeisl, and Matthias Arenz\*



Cite This: *ACS Catal.* 2022, 12, 11263–11271



Read Online

ACCESS |

Metrics & More

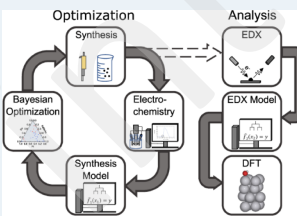
Article Recommendations

Supporting Information

Downloaded via UNIV BERN on January 7, 2024 at 14:41:08 (UTC).  
See https://pubs.acs.org/sharingguidelines for options on how to legitimately share published articles.

**ABSTRACT:** High-entropy alloy (HEA) electrocatalysts offer a vast composition space that awaits exploration to identify interesting materials for energy conversion reactions. While attempts have been made to explore the composition space of HEA thin-film libraries and compare experimental and computational studies, no corresponding approaches exist for HEA nanoparticles. So far, catalytic investigations on HEA nanoparticles are limited to small sets of individual catalysts. Here, we report the experimental exploration of the composition space of carbon-supported Pt–Ru–Pd–Rh–Au nanoparticles for the H<sub>2</sub>/CO oxidation reaction by constructing a dataset using Bayesian optimization as guidance. Applying a surfactant-free synthesis platform, a dataset of 68 samples was investigated. By constructing machine learning models, the relationship between the concentrations of the constituent elements and the catalytic activity was analyzed and compared to density functional theory calculations. The machine learning models confirm findings from previous studies concerning the role of Ru in the H<sub>2</sub>/CO oxidation reaction. This has been achieved starting from a random set of compositions and without any prior assumptions for the reaction mechanism nor any in-depth design of the active site. In addition, by comparing the trends of the computational and experimental studies, it is seen that the “onset potentials” across the compositions can be correlated with the adsorption energy of \*OH. The best correlation between the computational and experimental data is obtained when considering 5% of the most strongly \*OH adsorbing sites.

**KEYWORDS:** high-entropy alloy nanoparticles, H<sub>2</sub>/CO oxidation reaction, electrocatalysis, machine learning



## 1. INTRODUCTION

Achieving a carbon neutral society through fossil fuel-free technologies is one of the main challenges faced by mankind today. Within the scope of this challenge, the proton exchange membrane fuel cell has been developed.<sup>1–3</sup> In this specific fuel cell, electrocatalysts carry out the hydrogen oxidation reaction (HOR) and the oxygen reduction reaction (ORR) to generate electricity. The ORR is a major topic for studies as it requires large overpotentials to take place.<sup>4</sup> On the other hand, the HOR is efficiently catalyzed by Pt with negligible overpotentials.<sup>5</sup> However, Pt is highly susceptible to CO poisoning, that is, the blocking of active sites for the HOR by adsorbed CO, whose traces are present in hydrogen gas from the widely employed water gas shift reaction or potentially from on-board methanol reformers.<sup>6–8</sup> Therefore, it is still an ongoing quest to find HOR catalysts that show resilience toward CO poisoning.<sup>9</sup>

A common strategy to increase the CO tolerance of Pt is to alloy it with Ru.<sup>10</sup> This produces a bifunctional catalyst that can perform both the HOR and the CO oxidation at low

overpotentials.<sup>11</sup> The proposed mechanism for PtRu-mediated catalysis is that Ru facilitates the formation of adsorbed OH species at lower potentials.<sup>12</sup> These adsorbed OH species can oxidize the CO adsorbed on Pt, which leads to the reactivation of the surface. In addition, it has been proposed that an electronic effect of Ru weakens the CO bond on Pt.<sup>13</sup> Studies on alloy catalysts are conventionally limited to bi- and trimetallic alloys. However, recently, HEAs emerged as potential catalyst materials for electrocatalytic energy conversion reactions.<sup>14–18</sup> HEAs contain five or more elements in a randomized order, which produces a surface with multiple different active sites.<sup>19</sup> Further, the diversity of elements with different sizes distorts the crystal lattice which gives HEAs not

Received: May 25, 2022

Revised: August 22, 2022

Published: September 1, 2022

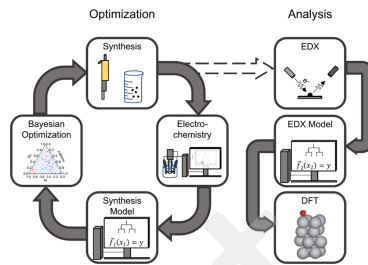


only unique mechanical properties but also a tunable electronic structure.<sup>20</sup> The statistical nature of the HEA surface compositions is also expected to provide unique catalytic properties that have yet to be explored.<sup>21</sup> Furthermore, the comparison of activity trends in the HEA composition space observed in experiment with results from computational investigations enables a unique approach to obtain improved insight into catalytic reactions.

Experimental investigations of HEAs form a major challenge due to the vast composition space. In an HEA containing five elements, there are  $99!/95!4! = 3,764,376$  compositions possible when each elemental concentration is varied between 1 and 96 at. % (atomic percent) in steps of 1 at. %. Neither can this many compositions be investigated experimentally in a timely manner nor can it be expected that the majority of compositions exhibit interesting catalytic properties. Consequently, new strategies to approach the study and discovery of relevant HEAs with dedicated properties are necessary.<sup>22,23</sup> Currently, one approach is focused on constructing a methodology employing density functional theory (DFT) that enables prediction of highly active HEA compositions, which then are evaluated experimentally in the form of thin-film libraries.<sup>24,25</sup> Such investigations can be combined with machine learning tools to guide an efficient exploration of the composition space.<sup>26,27</sup> In addition to the potential discovery of new materials of high activity, the comparison of activity trends in the computational model with trends observed in experiments potentially allows new approaches of understanding catalytic reactions. In contrast to thin-film libraries that allow compositional gradients, studies with HEA nanoparticles are particularly demanding. The compositions are discrete instead of continuous, and not all compositions can necessarily be synthesized. Furthermore, catalysts employed in fuel cells typically need to be supported onto a high surface area carbon, which complicates the synthesis. For this reason, to the best of our knowledge, so far, no studies have been reported for the machine learning-guided exploration of the composition space of carbon-supported HEA nanoparticles for electrocatalytic reactions.

Here, we present an experimental strategy guided by Bayesian optimization to explore the composition space of carbon-supported HEA nanoparticles for electrocatalytic energy conversion reactions. The conceptual design of the study is summarized in Scheme 1. Using a surfactant-free synthesis platform,<sup>28,29</sup> carbon-supported Pt–Ru–Pd–Rh–Au nanoparticles are prepared starting from a random set of compositions and experimentally tested for the electrocatalytic H<sub>2</sub>/CO oxidation reaction. The ratio of the precursor mixtures was used as the input parameter for a Bayesian optimization algorithm, whereas a defined CO oxidation “onset potential” in the presence of H<sub>2</sub> served as the output parameter to describe the H<sub>2</sub>/CO oxidation activity. As the well-defined precursor mixtures did not necessarily result in defined nanoparticle compositions, in the second part, machine learning models were constructed with a new input parameter, namely the compositions of the as-prepared nanoparticles determined by energy-dispersive X-ray spectroscopy (EDX). Finally, the correlations were related to physical phenomena using DFT models. In a predictive model, we compared the trends in the observed “onset potentials” to the weighted sum of normally distributed \*OH adsorption energies giving insight into the required number of active sites for CO oxidation site reaction in the HOR.

**Scheme 1. Schematic Representation of the Optimization Loop and the Analysis Steps**



## 2. EXPERIMENTAL SECTION

**2.1. Catalyst Synthesis.** The solid precursors, H<sub>2</sub>PtCl<sub>6</sub> (Sigma-Aldrich, 99.9%), HAuCl<sub>4</sub> (Alfa Aesar, 99.99%), RuCl<sub>3</sub> (Sigma-Aldrich, ReagentPlus), PdCl<sub>2</sub> (Sigma-Aldrich, ReagentPlus, 99%), and RhCl<sub>3</sub> (Sigma-Aldrich, 99.98%), were dissolved in methanol (Merck, EMSURE) to produce 20 mM precursor solutions. A total of 1 mL of precursor solutions was added in stoichiometric ratios to 5.6 mL of 57 mM NaOH MeOH with 50 wt % (metal to carbon) dispersed high surface area carbon support (Vulcan XC72R). The obtained solution was stirred for 10 min at room temperature and stored overnight in a centrifuge tube. The following day, the suspensions were centrifuged, decanted, and left to dry in air. Catalyst inks were prepared by adding isopropanol and H<sub>2</sub>O (3:1, v/v) to the dry catalyst powder to produce 0.83 mg metal per mL ink. These inks were drop-cast onto a glassy carbon rotating disk electrode (RDE) tip to produce a metal loading of 35  $\mu\text{g cm}^{-2}$ .

**2.2. Electrochemistry.** All experiments were carried out in a three-electrode RDE setup. In between experiments, the electrochemical cell and all glass components were stored in 1 g mL<sup>-1</sup> KMnO<sub>4</sub> acidified with H<sub>2</sub>SO<sub>4</sub>. Before the experiments, this solution was removed and residual MnO<sub>2</sub> was dissolved by adding a dilution of H<sub>2</sub>SO<sub>4</sub> and H<sub>2</sub>O<sub>2</sub>. Following that, the electrochemical cell and components were boiled three times in MilliQ water.

All measurements were carried out with a Nordic Potentiostat EC200. As a reference electrode, a trapped RHE electrode was employed. A platinum wire separated by a glass frit was used as a counter electrode. The electrolyte was 0.1 M H<sub>2</sub>SO<sub>4</sub> (Merck Suprapur). The working electrode consisted of a Radiometer RDE, which has a glassy carbon disk on which the catalyst containing ink was drop cast. This working electrode was put under a controlled potential of 0.05 V versus RHE into the solution. In the first 30 s, CO gas (Air Liquide, Quality 37) was bubbled through the electrolyte, which was followed by 10 cyclic voltammograms (CVs) between 0 and 0.6 V versus RHE at a scan speed of 100 mV s<sup>-1</sup>. Afterward, the electrode was kept for 2 min longer at 0.05 V versus RHE in a CO atmosphere. Next, the solution was degassed for 20 min with H<sub>2</sub> (ALPHAGAZ, 99.999%), and 2 CVs were recorded between 0 and 1.4 V versus RHE at a scan speed of 10 mV s<sup>-1</sup>.

**2.3. EDX and TEM Analysis.** The samples for EDX were prepared by drop-casting several times 10  $\mu\text{L}$  of catalyst ink onto a copper foil to yield a thick catalyst film. The EDX measurements were performed in a GeminiSEM450 (Zeiss), operated with Smart SEM 6.0S, using the EDX Photodetector Ultim Max 65 (Oxford Instruments), operated with AZtec 4.2. The EDX spectra were measured at four different locations with a size of 800  $\mu\text{m}^2$  at a working distance of 8 mm and an accelerating voltage of 25 kV. The transmission electron microscopy (TEM) samples were prepared by drop-casting once the catalyst ink on a copper grid. TEM micrographs and their associated EDX spectra were acquired on a JEOL 2100 TEM operated at 200 kV.

**2.4. Machine Learning.** *2.4.1. Dataset Construction.* The dataset for the different Pt–Ru–Rh–Pd–Au alloy compositions was constructed in a Bayesian manner similar to the research of Nugraha et al.<sup>26</sup> The first 25 data points were selected randomly, but they included the 5 “extreme” compositions that span the domain of interest. These “extreme” HEA compositions consisted of 96% of one element and 1% of each remaining element. The electrochemistry for the CO oxidation was evaluated using the HOR as a probe reaction. Subsequently, only particles that remained active for the HOR after the CO got oxidized were included into machine learning. This resulted in an initial dataset containing a total of 21 points. The input parameter for the machine learning models was the precursor ratios used in the synthesis as this is the most defined parameter. The output parameter was the CO oxidation “onset potential”. This potential was defined at a current increase of 1.5 mA mg<sup>-1</sup> on top of the capacitive current. For every synthesized alloy, three electrochemical experiments were carried out.

This obtained information was used to construct a random forest regression model using the python package scikit learn.<sup>30</sup> The parameters,  $n$  estimators, bootstrap, max depth, max features, min sample leaf, min sample split, and criterion, were tuned using 500 Bayesian optimization cycles which optimized the k-fold cross validation score. All Bayesian optimization loops made use of the GpyOpt library in python.<sup>31</sup> The obtained random forest regression model was further used to find new alloy compositions of interest for investigation. It was optimized using Bayesian optimization, in which the first iteration consisted of the compositions that were used to train the model initially. This way, the Bayesian optimization constructed the prior probability distribution using the same data that were acquired from laboratory experiments. Following, the Bayesian optimization was continued for an additional 50 iterations, in which new compositions were suggested for evaluation. From these 50 compositions, 10 compositions were selected based on their Euclidian distance in space to other suggested or studied compositions and their predicted activity. Subsequently, these 10 samples were synthesized, evaluated, and added to the optimization. The expansion of the dataset was halted after five optimization cycles, as the mean absolute error (MAE) of the leave-one-out cross validation (LOOCV) showed to reach a constant value around 13 mV. This suggested that an exponential amount of data is becoming necessary to improve the models. In addition, the target of finding the best performing alloy was reached in the first cycle. In the end, this resulted in a dataset of 68 unique catalysts. The scripts used in this paper together with the final data set are available on [https://github.com/vamints/Scripts\\_BayesOpt\\_PtRuPdRhAu\\_paper](https://github.com/vamints/Scripts_BayesOpt_PtRuPdRhAu_paper).

After the catalysts were analyzed with EDX, new input parameters were obtained, which corresponded to elemental ratios observed by EDX. These allowed to construct a new random forest model, which used the same hyperparameter tuning script as the synthesis model. All random tree models were explained using the SHAP package.<sup>32</sup>

**2.4.2. Linear Models.** Linear models were constructed using the scikit learn package. Features were expanded to include also polynomial terms up to the second degree. The best lasso regression model was selected by using a custom loop that varied the lambda penalty until the change in lambda was less than 1%. The ternary contour plots were created by using the plotly library.<sup>33</sup> The models were fitted using the entire dataset of 68 experimental points. Following these models were used to predict the values of a grid that spanned the slice of the hyperspace that is shown in the contour plot.

**2.5. DFT Calculations.** DFT calculations were done with the GPAW code<sup>34,35</sup> version 19.8.1 and the revised Perdew–Burke–Ernzerhof (RPBE) exchange–correlation functional.<sup>36</sup> Manipulation of atomic structures was performed with the atomic simulation environment.<sup>37</sup> Four-layered face-centered cubic (fcc) (111) surface slabs measuring 2  $\times$  2 atoms laterally and periodically repeated laterally from orthogonal unit cells were constructed for each of the constituent elements Au, Pd, Pt, Rh, and Ru for \*OH adsorption energy calculations. The surface slabs were constructed with fcc lattice constants that were obtained as the minimum energy lattice parameters for the pure fcc bulk constituents (see Table 1).

**Table 1. Fcc Lattice Constants and \*OH Adsorption Free Energies of the Pure Elements Used**

metal	Au	Pd	Pt	Rh	Ru
DFT fcc lattice constant (Å)	4.2149	3.9814	3.9936	3.8648	3.8285
DFT $\Delta G_{\text{OH}}$ (eV)	1.30	0.80	0.76	0.44	0.04

During structure relaxations, all but the two top layers of the slab were fixed, and the \*OH adsorbate was put at on-top positions with the oxygen atom constrained to move only perpendicular to the surface. The slabs were constructed with a vacuum of 15 Å above and below the structure. The wave functions were expanded in plane waves with an energy cut-off of 500 eV, and sampling of the Brillouin zone was done on a Monkhorst–pack grid of k-points sized  $8 \times 8 \times 1$ . The structures were relaxed so that the maximum force on any atom did not exceed 0.05 eV/Å. For other parameters, the default parameters of GPAW were used.

\*OH adsorption free energies were calculated relative to the \*OH adsorption energy on Pt(111) which has been shown to adsorb \*OH about 0.1 eV stronger<sup>38</sup> than the maximum of the ORR activity volcano at 0.86 eV relative to  $\text{H}_2\text{O(l)}$  and  $\text{H}_2\text{g}$ ,<sup>39</sup> that is, setting the free energy of \*OH adsorption on Pt(111) to about 0.76 eV.

$$\Delta G_{\text{OH}} = (E_{\text{*OH}} - E_{\text{*}}) - (E_{\text{*OH}}^{\text{Pt}(111)} - E_{\text{*}}^{\text{Pt}(111)}) + 0.76 \text{ eV}$$

Here,  $\Delta G_{\text{OH}}$  is the free energy of \*OH adsorption, and  $E_{\text{*OH}}$  and  $E_{\text{*}}$  are the DFT calculated energies of the surface slab with and without \*OH adsorbed, respectively. The adsorption energies used in this work are given in Table 1.

### 3. RESULTS AND DISCUSSION

To explore the composition space of HEA nanoparticles, we developed a simple and straightforward approach that was adopted from our surfactant-free colloidal synthesis method using alkaline mono-alcohols optimized for mono- and bimetallic nanomaterials.<sup>28,29,40,41</sup> Here, we take advantage of the room-temperature reduction of  $\text{HAuCl}_4$  in alkaline methanol<sup>42</sup> to initiate the particle formation and the reduction of the multicomponent precursor in solutions and in the presence of a high surface area carbon support. Alkaline methanol serves as the reducing agent,<sup>43</sup> whereas the presence of the carbon support limits the formation of macroscopic Au particles. Nevertheless, relatively large Au nanoparticles were formed ( $<20$  nm) when only a single Au precursor was used, while the presence of multiple precursors comprising elements like Pt, Ir, Ru, Rh, and Pd led to a very fast reaction at room temperature, as demonstrated in Figure S1, and the formation of small, supported nanoparticles. Using a combination of TEM and EDX analysis, it is shown that the formed nanoparticles are ca. 3 nm in diameter and incorporate all the precursor metals, for example, Pt, Ru, Pd, Rh, and Au (see Figures 1 and S2). The particle size is only slightly larger than

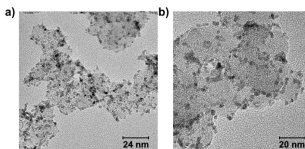


**Figure 1.** (a,b) TEM micrographs of the sample  $\text{Pt}_{1.2}\text{Ru}_{3.8}\text{Pd}_3\text{Rh}_{4.1}\text{Au}_{1.2}$ .

monometallic Pt or Ir nanoparticles obtained in alkaline methanol by heating<sup>28,43,44</sup> and is ideal for achieving a high active surface area. On the other hand, the small particle size inhibits the verification of a single phase with random elemental composition by X-ray diffraction (XRD) or high-resolution scanning transmission electron microscopy (STEM) with EDX.

To explore and optimize the composition of the Pt–Ru–Pd–Rh–Au nanoparticles for the electrocatalytic  $\text{H}_2/\text{CO}$  oxidation reaction, 25 samples were selected as starting point for the Bayesian optimization,<sup>26,27</sup> whereof 20 were selected randomly and 5 were selected close corner points of the composition space. To obtain a well-defined output parameter as a measure for the  $\text{H}_2/\text{CO}$  oxidation activity in the optimization process, a CO oxidation “onset potential” was defined. For this, first, a saturated CO monolayer was deposited on the nanoparticles, which was subsequently electrochemically oxidized by a potential scan in an  $\text{H}_2$ -rich environment using RDE configuration. The HOR thereby amplified the potential at which the CO monolayer was oxidized by a rapid increase in current for the catalysts that are active for the HOR. The CO “onset potential” was then defined as the potential where an increase of 1.5 mA  $\text{mg}_{\text{RuPdRh}}^{-1}$  on top of the capacitive current was measured (see Figures S3 and S4).

Feeding the experimental results of the initial samples to the Bayesian optimization process which was performed in conjunction with a random forest regression model, 10 new

compositions were suggested, which were experimentally investigated and added to the dataset. This addition of 10 new samples concludes a single optimization cycle. In total, five optimization cycles were carried out, whose results are summarized in Figure 2. It can be observed that after the

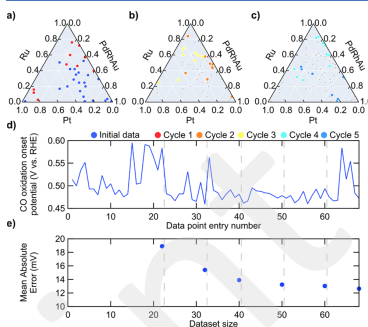


**Figure 2.** (a–c) Representation of the precursor mixtures that were used to synthesize the particles in each Bayesian optimization cycle. (d) Experimentally determined CO oxidation onset potential for each data point in the investigated order. The dashed lines indicate the regions of each Bayesian optimization cycle. (e) Change in the MAE, obtained from the LOOCV method of the synthesis random forest regression model with each Bayesian optimization cycle.

second optimization cycle, the computational methods start to select samples with a large Ru content. Figure 2d shows the average CO oxidation onset potentials for the investigated samples. It can be seen that the most active catalyst composition, with a precursor ratio of  $\text{Pt}_{1.2}\text{Ru}_{4.0}\text{Pd}_3\text{Rh}_{3.4}\text{Au}_{1.2}$ , was found within the first optimization cycle at the 32nd entry. The actual composition of this alloy, determined by EDX, was  $\text{Pt}_{1.2}\text{Ru}_{3.8}\text{Pd}_3\text{Rh}_{4.1}\text{Au}_{1.2}$ . In the subsequent 2nd, 3rd, and 4th cycles, the onset potentials mainly stay around 0.47 V versus RHE. Furthermore, in the 3rd–5th cycle, the Bayesian optimization suggests on average large Ru contents. Thus, it can be implied that Ru is playing a major role in the CO oxidation reaction. In the 5th cycle, several low performing compositions were selected for investigation, to explore further poorly represented regions. This exploration produced samples with low CO tolerance, in line with the prediction, and suggests that the optimization has already found the most active composition in the first cycle. Finally, the evolution of the synthesis random forest regression models can be studied in Figure 2e represented by the MAE, which was calculated with LOOCV. The MAE shows an exponential decrease with increasing dataset size, the final synthesis model having a MAE of 13 mV.

While the precursor ratios serve as an excellent input parameter for the Bayesian optimization procedure, they might poorly reflect the true catalyst compositions. Thus, the obtained correlations between the precursor ratios and the CO oxidation onset might not be as informative as required to understand in more depth the composition–activity relationship of the investigated catalysts. Therefore, all sampled

catalysts were investigated with EDX to determine their actual composition. The results were used to construct two intrinsically different machine learning models, here referred to as EDX models.

The first model was an EDX random forest regression, which is highly flexible in its nature as it has no bias on the expected correlations. An interpretation of the model was achieved using SHApely Additive exPlanation (SHAP), the results of which are shown in Figure 3a. The SHAP value

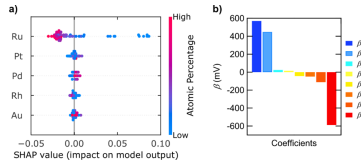


**Figure 3.** (a) SHAP analysis of the EDX random forest regression model. (b) Coefficients of the EDX lasso regression model.

represents the perturbation of the CO oxidation “onset potential” by the element from the average onset potential. Hence, negative SHAP values are associated with a decrease in overpotential for CO oxidation. It turns out that of the investigated elements, Ru has the largest impact on CO oxidation. In low quantities, Ru exhibits a very large positive SHAP value, and at large quantities, a negative SHAP value. This is congruent with the already reported activity of Ru toward CO oxidation being much higher compared to the other investigated metals.<sup>46</sup> The next elements that shown an improvement in CO oxidation in large quantities are Pt and Rh. These two metals have also been shown to oxidize the CO monolayer at higher potentials compared to Ru, however, at lower potentials than Pd.<sup>47</sup> In contrast to Ru, Pt, and Rh, large quantities of Pd showed an increase in the CO oxidation onset potential, relative to the average, as shown in Figure 3a. Au, in comparison to other elements, did not show a large impact on H<sub>2</sub>/CO oxidation. This could be explained by a different mechanism for the formation of the CO monolayer on Au. While CO forms a stable chemisorbed monolayer on Pt, Pd, Rh, and Ru, this is not the case for Au in a CO deficient environment.<sup>48</sup> In addition, Au is inactive for the HOR.<sup>49</sup>

The second model is a more rigid linear model, which was limited to the first- and second-degree polynomial terms to avoid overfitting with higher degree terms. The obtained coefficients were corrected to account for the statistical probability of finding a specific elemental arrangement at the surface. This model is outlined in eq 1 and can be used for a discussion of the active surface sites for the H<sub>2</sub>/CO oxidation reaction. In equation 1,  $E(X)$  is the CO oxidation onset potential,  $f$  is the fraction of an element  $m$  in %,  $\beta$  is the fitted coefficient,  $P(X = m)$  is the probability of finding an element at the surface, and  $P(X = m_i m_j)$  is the probability of finding two neighboring elements. Nevertheless, this model has a total of 21 predictors, which would severely overfit the small dataset of 68 points by using the ordinary least squares regression. Therefore, to reduce the amount of predictors, the model was fitted using the lasso regression.<sup>50</sup>

$$E(f_{\text{Pt}}, f_{\text{Ru}}, f_{\text{Pd}}, f_{\text{Rh}}, f_{\text{Au}}) = \beta_0 + \sum \beta_{m_i} P(X = m_i) + \sum_{i>j} \beta_{m_i m_j} P(X = m_i m_j)$$

$$P(X = m_j) = 0.5f_{m_j}$$

$$P(X = m_i m_j) = \begin{cases} f_{m_i} f_{m_j} & \text{if } i > j \\ 0.5f_{m_i} f_{m_j} & \text{if } i = j \end{cases}$$
(1)

The terms of the lasso regression with their coefficients can be observed in Figure 3b. Similar to the random forest model, the lasso regression shows that the term  $P(X = \text{Ru})$  has the largest associated negative coefficient. Therefore, Ru has the biggest impact on reducing the onset potential. In addition, linear models show that  $P(X = \text{RuRu})$  has a large associated positive coefficient. This suggests that there is an optimum amount of Ru in an alloy; that is, too much Ru limits the activity for H<sub>2</sub>/CO oxidation. The next term that improves the H<sub>2</sub>/CO oxidation is  $P(X = \text{PtPt})$ , which is also in agreement with the random forest model. When the linear model is used to predict the performance for a Pt–Ru alloy, an optimum is found around the Ru<sub>0.5</sub>Pt<sub>0.5</sub> composition. This composition overlaps with previous studies that observed a similar maximum for this binary alloy.<sup>51,52</sup> Finally, the lasso regression includes the terms  $P(X = \text{Rh})$ ,  $P(X = \text{Au})$ ,  $P(X = \text{RuRh})$ , and  $P(X = \text{PdPd})$  in the fit. However, their coefficients are too small to draw a solid conclusion upon.

The analysis of the SHAP values calculated on the EDX model concluded that among the investigated five elements, Ru, Pt, and Rh lower the CO oxidation “onset potential” the most. This allows visualization of the activity of this hypothetical Ru–Pt–Rh ternary alloy. In Figure 4a,b, the

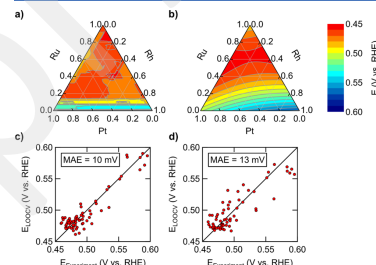


**Figure 4.** (a,b) Slice of the hyperspace spanned by Ru, Pt, and Rh and (c,d) prediction of the LOOCV vs the experimental value of the models: (a,c) EDX random forest regression and (b,d) EDX lasso regression.

CO oxidation onset potential of the Ru–Pt–Rh alloys is predicted using the EDX random forest regression and EDX lasso regression, respectively. Both models show that there is not a single most active alloy, but different composition regions contain alloys that exhibit similar high H<sub>2</sub>/CO oxidation activities. The shapes of these regions differ between the two EDX models due to their intrinsic flexibility. The lasso regression assumes a quadratic relationship, which produces straight and smooth boundaries for the maximum domain. In comparison, the random forest regression has no prior bias, which produces domains with an irregular boundary. However,

both models show relative broad composition regions of high activity, facilitating the fast identification of active catalysts in the Bayesian optimization.

Finally, the performance of the two EDX models was compared using the MAE of the LOOCV. This evaluation is shown in Figure 4c–d. The EDX random forest regression model outperforms the lasso regression slightly with an MAE of 10 mV. This is highly correlated with the high flexibility of the model. On the other hand, the lasso regression has an MAE of 13 mV. It should be noted that the investigated compositions were selected using an optimization algorithm, which focused mainly on samples in the high-performance region. As observed, this region consists mostly of alloys with large concentrations of Ru. Therefore, the models in this study can predict the activity of catalysts that fall into the Pt–Ru–Pd–Rh–Au space with large Ru quantities. However, the error increases for alloys with little to no Ru content.

To gain further physical understanding of the modelled composition–activity relationships, DFT simulations were conducted. The task of finding the limiting step of the reaction enabling HOR is formidable given that the surface structures of the nanoparticle catalysts are not well defined. Additionally, many possible adsorption sites on the HEA nanoparticle surface contribute to an inherent complexity in the variation of active sites. This further hinders a successful and timely discovery of the responsible chemical step. Instead, we pursued a predictive model which could explain the trend in the observed onset potentials through electronic structure insights. The model considers the weighted sum of normally distributed  ${}^*\text{OH}$  adsorption energies with means given by the pure metal constituents of the HEA and with standard deviations set to 0.13 eV as observed previously for  ${}^*\text{OH}$  adsorption energy distributions on a comparable HEA.<sup>19</sup> The molar fractions of each element in the compositions found with EDX of each HEA constituted the weights of each of the normal distributions in the linear combination given by eq 2. Here,  $P$  is the resulting distribution of  ${}^*\text{OH}$  adsorption energies,  $\Delta G_{\text{OH}}^*$  for a given HEA composition,  $f_m$  is the molar fraction of metal  $m$ ,  $\mu_n$  is the adsorption energy obtained for the pure metal  $m$ , and  $\sigma = 0.13$  eV is the spread in the adsorption energies.

$$\begin{aligned} P(\Delta G_{\text{OH}}^*) &= \sum_m f_m N(\Delta G_{\text{OH}}^*; \mu_m, \sigma) \\ &= \sum_m f_m \frac{1}{\sqrt{2\pi}\sigma} e^{-\frac{1}{2}\left(\frac{\Delta G_{\text{OH}}^* - \mu_m}{\sigma}\right)^2} \end{aligned} \quad (2)$$

Figure 5 shows the overall predictive trend obtained by the computationally inexpensive model. The best fit between the experimentally obtained onset potential and the computational model is obtained using the adsorption energy at the 5 percentile of most strongly adsorbing sites in the modeled  ${}^*\text{OH}$  adsorption energy distributions for each of the sampled HEA compositions (see the trend line in Figure 5). The 5 percentile of most strongly adsorbing sites was chosen since it was found to constitute a minimum in the prediction error compared to other possible percentiles (see Figure S13).

A somewhat linear relationship can be observed with a capability of predicting onset potentials with an MAE of 11 mV, comparable to the machine learning models. This observed trend indicates that the oxidation of water at the catalyst surface and subsequent formation of oxygen adsorbed

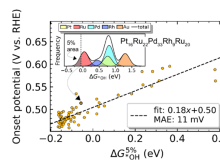


**Figure 5.** Correlation of experimental onset potentials with the  ${}^*\text{OH}$  adsorption energy at the 5 percentile of most strongly bound sites of the  ${}^*\text{OH}$  adsorption energy distribution for the EDX-analyzed compositions. The inset shows an example of the modeled  ${}^*\text{OH}$  adsorption energy distribution for an HEA sample. The 5 percentile  ${}^*\text{OH}$  adsorption energy is found as the energy at which 5% of the area of the distribution is to the left.

intermediates are involved in the potential-limiting step. Although the  ${}^*\text{OH}$  adsorption energy seems to be a good descriptor for the overall trend of the onset potential across a large span of  ${}^*\text{OH}$  adsorption energies, there is a substantial variance for the sampled Ru-rich compositions with strong  ${}^*\text{OH}$  adsorption at around  $-0.1$  eV that is not explained by the simple model and calls for more in-depth investigations. In other words, this simple model is not able to predict the details of highly performing catalysts. In contrast to the experimental results, the simple model predicts pure Ru as the most active catalyst. It is expected that a more advanced model needs to take into account the CO adsorption energy as well. Nevertheless, comparing the trends from experimental investigations and computational studies over a large composition space of supported multi-element nanoparticles indicates that a relatively small number of surface sites with high  ${}^*\text{OH}$  adsorption energy is sufficient to determine the catalytic activity of the nanoparticle catalysts.

#### 4. CONCLUSIONS

In this research, the composition space of Pt–Ru–Pd–Rh–Au nanoparticles was optimized for the  $\text{H}_2/\text{CO}$  oxidation reaction using Bayesian optimization. Starting from a synthesis with a random set of precursor compositions and experimentally testing the electrocatalytic  $\text{H}_2/\text{CO}$  oxidation activity, a guided search among the vast number of different compositions is achieved. The most active alloy was found within the first optimization cycle, after 32 experiments. Subsequent cycles provided mostly alloys within the high-performance region, with only several exploration points in the low performance region. The results are obtained without an in-depth characterization of the samples that would have been very time consuming and difficult due to the very small particle size. Thus, it remains unresolved if all catalysts with high performance can be considered HEAs.

In a step further, the obtained dataset was used to scrutinize the composition–activity relationship of the  $\text{H}_2/\text{CO}$  oxidation reaction. This was achieved by constructing a random forest regression and a lasso regression. In good agreement with previous studies, both models point out that Ru is the key element in the CO oxidation reaction. The models show that Ru should be present in the nanoparticle neither at too low nor at too high concentrations. Using the lasso regression to predict the performance for a bimetallic Pt–Ru alloy, a similar optimum in composition is found to what has been reported to

be the best performing Pt–Ru catalyst. These results strongly indicate that the presented strategy of using a simple, surfactant-free synthesis as well as an optimization process with minimal characterization of the nanoparticle catalyst that relies mainly on well-defined synthesis variables and introduces a measure for the catalytic performance is an effective strategy to explore the vast composition space of HEA nanoparticle catalysts. This becomes, in particular, important when including further metals to the composition space.

Last but not least, comparing the experimental results of the trend in onset potential with DFT calculations, the relationships were shown to correlate with the  $^{\bullet}\text{OH}$  adsorption energy. These are lowest for Ru. Therefore, within this composition space, sufficient amounts of Ru are obligatory for a high-performing CO oxidation catalyst. The best fit between DFT calculations and experimental results is obtained when considering for each of the sampled HEA compositions the adsorption energy at the S percentile of most strongly adsorbing sites in the modeled  $^{\bullet}\text{OH}$  adsorption energy distributions. This indicates that a relative low number of strongly adsorbing  $^{\bullet}\text{OH}$  sites are sufficient for a rough prediction of the performance of a  $\text{H}_2/\text{CO}$  oxidation catalyst. In conclusion, the presented study outlines an efficient and feasible approach for the exploration of multidimensional composition spaces of carbon-supported, multi-component nanoparticles combining experimental and computational means.

## ■ ASSOCIATED CONTENT

### ● Supporting Information

The Supporting Information is available free of charge at <https://pubs.acs.org/doi/10.1021/acscatal.2c02563>.

Synthesis procedure, TEM of particles, Data processing procedure, CV of particles, and MEA of DFT models at different at. % percentiles ([PDF](#))

## ■ AUTHOR INFORMATION

### Corresponding Author

**Matthias Arenz** — Department of Chemistry, Biochemistry and Pharmaceutical Sciences, University of Bern, Bern 3012, Switzerland; [@orcid.org](https://orcid.org/0000-0001-9765-4315); Email: matthias.arenz@unibe.ch

### Authors

**Vladislav A. Mints** — Department of Chemistry, Biochemistry and Pharmaceutical Sciences, University of Bern, Bern 3012, Switzerland; [@orcid.org](https://orcid.org/0000-0002-0540-2717)

**Jack K. Pedersen** — Department of Chemistry, University of Copenhagen, Copenhagen Ø 2100, Denmark; [@orcid.org](https://orcid.org/0000-0002-5601-5450)

**Alexander Bagger** — Department of Chemistry, University of Copenhagen, Copenhagen Ø 2100, Denmark; [@orcid.org](https://orcid.org/0000-0002-6394-029X)

**Jonathan Quinson** — Department of Chemistry, University of Copenhagen, Copenhagen Ø 2100, Denmark; Present Address: Department of Biological and Chemical Engineering, Hangovej 2 8200 Aarhus N, Denmark; [@orcid.org](https://orcid.org/0000-0002-9374-9330)

**Andy S. Anker** — Department of Chemistry, University of Copenhagen, Copenhagen Ø 2100, Denmark; [@orcid.org](https://orcid.org/0000-0002-7403-6642)

**Kirsten M. O. Jensen** — Department of Chemistry, University of Copenhagen, Copenhagen Ø 2100, Denmark; [@orcid.org](https://orcid.org/0000-0003-0291-217X)

**Jan Rossmeisl** — Department of Chemistry, University of Copenhagen, Copenhagen Ø 2100, Denmark; [@orcid.org](https://orcid.org/0000-0001-7749-6567)

Complete contact information is available at: <https://pubs.acs.org/10.1021/acscatal.2c02563>

### Notes

The authors declare no competing financial interest.

## ■ ACKNOWLEDGMENTS

This work was supported by the Swiss National Science Foundation (SNSF) via the project no 200021 184742 and the Danish National Research Foundation Center for High Entropy Alloys Catalysis (CHEAC) DNRF149. J.P. and K.M.O.J. acknowledge support from the Danish Ministry of Higher Education and Science [Structure of Materials in Real Time (SMART) grant]. K.M.O.J acknowledges support from the Villum Foundation (VKA00015416). S.B. Simonsen and L. Theil Kuhn, Technical University of Denmark, are thanked for access to TEM.

## ■ REFERENCES

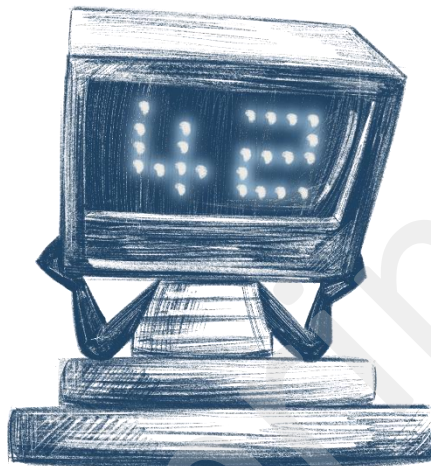
- (1) Andújar, J. M.; Segura, F. Fuel Cells: History and Updating. A Walk along Two Centuries. *Renew. Sustain. Energy Rev.* **2009**, *13*, 2309–2322.
- (2) Rath, R.; Kumar, P.; Mohanty, S.; Nayak, S. K. Recent Advances, Unsolved Deficiencies, and Future Perspectives of Hydrogen Fuel Cells in Transportation and Portable Sectors. *Int. J. Energy Res.* **2019**, *43*, 8931–8955.
- (3) Alaswad, A.; Omran, A.; Sodre, J. R.; Wilberforce, T.; Pignatelli, G.; Dassietti, M.; Baroutaji, A.; Olabi, A. G. Technical and Commercial Challenges of Proton-Exchange Membrane (PEM) Fuel Cells. *Energies* **2020**, *14*, 144.
- (4) Gasteiger, H. A.; Kocha, S. S.; Sompalli, B.; Wagner, F. T. Activity Benchmarks and Requirements for Pt, Pt-Alloy, and Non-Pt Oxygen Reduction Catalysts for PEMFCs. *Appl. Catal., B* **2005**, *56*, 9–35.
- (5) Gasteiger, H. A.; Panels, J. E.; Yan, S. G. Dependence of PEM Fuel Cell Performance on Catalyst Loading. *J. Power Sources* **2004**, *127*, 162–171.
- (6) Jackson, C.; Raymakers, L. F. J. M.; Mulder, M. J. J.; Kucernak, A. R. J. Poison Mitigation Strategies for the Use of Impure Hydrogen in Electrochemical Hydrogen Pumps and Fuel Cells. *J. Power Sources* **2020**, *472*, 228476.
- (7) Zheng, T.; Zhou, W.; Li, X.; You, H.; Yang, Y.; Yu, W.; Zhang, C.; Chu, X.; San Hui, K.; Ding, W. Structural Design of Self-Thermal Methanol Steam Reforming Microreactor with Porous Combustion Reaction Support for Hydrogen Production. *Int. J. Hydrogen Energy* **2020**, *45*, 31745–31759.
- (9) Uchida, H.; Izumi, K.; Watanabe, M. Temperature Dependence of CO-Tolerant Hydrogen Oxidation Reaction Activity at Pt, Pt-Co, and Pt-Ru Electrodes. *J. Phys. Chem. B* **2006**, *110*, 21924–21930.
- (10) Koper, M. T. M. Electrocatalysis on Bimetallic and Alloy Surfaces. *Surf. Sci.* **2004**, *548*, 1–3.
- (11) Freitas, K. S.; Lopes, P. P.; Ticinelli, E. A. Electrocatalysis of the Hydrogen Oxidation in the Presence of CO on RhO<sub>2</sub>/C-Supported Pt Nanoparticles. *Electrochim. Acta* **2010**, *56*, 418–426.
- (12) Watanabe, M.; Furuchi, Y.; Motoo, S. Electrocatalysis by AD-Atoms. Part XIII. Preparation of Ad-Electrodes with Tin Ad-Atoms

- for Methanol, Formaldehyde and Formic Acid Fuel Cells. *J. Electroanal. Chem.* **1985**, *191*, 367–375.
- (13) Bautier de Mongeot, F.; Scherer, M.; Gleich, B.; Kopatzki, E.; Behm, R. CO Adsorption and Oxidation on Bimetallic Pt/Ru(0001) Surfaces—a Combined STM and TPD/TPR Study. *Surf. Sci.* **1998**, *411*, 249–262.
- (14) Yeh, J. W.; Chen, S. K.; Lin, S. J.; Gan, J. Y.; Chin, T. S.; Shun, T. T.; Tsau, C. H.; Chang, S. Y. Nanostructured High-Entropy Alloys with Multiple Principal Elements: Novel Alloy Design Concepts and Outcomes. *Adv. Eng. Mater.* **2004**, *6*, 399–303.
- (15) Zou, Y.; Ma, H.; Spolenak, R. Ultrastrong Ductile and Stable High-Entropy Alloys at Small Scales. *Nat. Commun.* **2015**, *6*, 7748.
- (16) Ye, Y. F.; Wang, Q.; Lu, J.; Liu, C. T.; Yang, Y. High-Entropy Alloy: Challenges and Prospects. *Mater. Today* **2016**, *19*, 349–362.
- (17) Wu, D.; Kusada, K.; Yamamoto, T.; Toriyama, T.; Matsumura, S.; Kawaguchi, S.; Kubota, Y.; Kitagawa, H. Platinum-Group-Metal High-Entropy-Alloy Nanoparticles. *J. Am. Chem. Soc.* **2020**, *142*, 13833–13838.
- (18) Nellaipappan, S.; Katiyar, N. K.; Kumar, R.; Parui, A.; Malviya, K. D.; Pradeep, K. G.; Singh, A. K.; Sharma, S.; Tiwary, C. S.; Biswas, K. High-Entropy Alloys as Catalysts for the CO<sub>2</sub> and CO Reduction Reactions: Experimental Realization. *ACS Catal.* **2020**, *10*, 3658–3663.
- (19) Batchelor, T. A. A.; Pedersen, J. K.; Winther, S. H.; Castelli, I. E.; Jacobsen, K. W.; Rossmeisl, J. High-Entropy Alloys as a Discovery Platform for Electrocatalysis. *Joule* **2019**, *3*, 834–845.
- (20) Xin, Y.; Li, S.; Qian, Y.; Zhu, W.; Yuan, H.; Jiang, P.; Guo, R.; Wang, L. High-Entropy Alloys as a Platform for Catalysis: Progress, Challenges, and Opportunities. *ACS Catal.* **2020**, *10*, 11280–11306.
- (21) Löflöer, T.; Savan, A.; Garzón-Manjón, A.; Meischien, M.; Scheu, C.; Ludwig, A.; Schuhmann, W. Toward a Paradigm Shift in Electrocatalysis Using Complex Solid Solution Nanoparticles. *ACS Energy Lett.* **2019**, *4*, 1206–1214.
- (22) Yao, Y.; Liu, Z.; Xie, P.; Huang, Z.; Li, T.; Morris, D.; Finrock, Z.; Zhou, J.; Jiao, M.; Gao, J.; Mao, Y.; Miao, J.; Zhang, P.; Shahbazian-Yassar, P.; Wang, R.; Wang, C.; Hu, G.; Hu, L. Computationally Aided, Entropy-Driven Synthesis of Highly Efficient and Durable Multi-Elemental Alloy Catalysts. *Sci. Adv.* **2020**, *6*, No. eaaz0510.
- (23) Ludwig, A. Discovery of New Materials Using Combinatorial Synthesis and High-Throughput Characterization of Thin-Film Materials Libraries Combined with Computational Methods. *npj Comput. Mater.* **2019**, *5*, 1–7.
- (24) Batchelor, T. A. A.; Löflöer, T.; Xiao, B.; Krysiak, O. A.; Strotkötter, V.; Pedersen, J. K.; Clausen, C. M.; Savan, A.; Li, Y.; Schuhmann, W.; Rossmeisl, J.; Ludwig, A. Complex-Solid-Solution Electrocatalyst Discovery by Computational Prediction and High-Throughput Experimentation. *Angew. Chem., Int. Ed.* **2021**, *60*, 6932–6937.
- (25) Pedersen, J. K.; Batchelor, T. A. A.; Bagger, A.; Rossmeisl, J. High-Entropy Alloys as Catalysts for the CO<sub>2</sub> and CO Reduction Reactions. *ACS Catal.* **2020**, *10*, 2169–2176.
- (26) Nugraha, A. S.; Lambard, G.; Na, J.; Hossain, M. S. A.; Asahi, T.; Chaikittisilp, W.; Yamauchi, Y. Mesoporous Trimetallic Pt/Pd/Al Alloy Films toward Enhanced Electrocatalytic Activity in Methanol Oxidation: Unexpected Chemical Compositions Discovered by Bayesian Optimization. *J. Mater. Chem. A* **2020**, *8*, 15352.
- (27) Pedersen, J. K.; Clausen, C. M.; Krysiak, O. A.; Xiao, B.; Batchelor, T. A. A.; Löflöer, T.; Mints, V. A.; Banko, L.; Arenz, M.; Savan, A.; Schuhmann, W.; Ludwig, A.; Rossmeisl, J. Bayesian Optimization of High-Entropy Alloy Compositions for Electrocatalytic Oxygen Reduction\*\*. *Angew. Chem., Int. Ed.* **2021**, *60*, 24144–24152.
- (28) Quinson, J.; Neumann, S.; Wannmacher, T.; Kacenauskaitė, L.; Inaba, M.; Bucher, J.; Bizzotto, F.; Simonsen, S. B.; Theil Kuhn, L.; Bujak, D.; Zana, A.; Arenz, M.; Kunz, S. Colloids for Catalysts: A Concept for the Preparation of Superior Catalysts of Industrial Relevance. *Angew. Chem., Int. Ed.* **2018**, *57*, 12338–12341.
- (29) Quinson, J.; Kacenauskaitė, L.; Bucher, J.; Simonsen, S. B. S. B.; Theil Kuhn, L.; Oezaslan, M.; Kunz, S.; Arenz, M. Controlled Synthesis of Surfactant-Free Water-Dispersible Colloidal Platinum Nanoparticles by the Co4Cat Process. *ChemSusChem* **2019**, *12*, 1229. (30) Pedregosa, F.; Varoquaux, G.; Gramfort, A.; Michel, V.; Thirion, B.; Grisel, O.; Blondel, M.; Prettenhofer, P.; Weiss, R.; Dubourg, V.; Vanderplas, J.; Passos, A.; Cournapeau, D.; Brucher, M.; Perrot, M.; Duchesnay, E. Scikit-Learn: Machine Learning in [Python]. *J. Mach. Learn. Res.* **2011**, *12*, 2825–2830.
- (31) The GPYOpt authors. GPYOpt: A Bayesian Optimization Framework in Python, 2016.
- (32) Lundberg, S. M.; Lee, S. I. A Unified Approach to Interpreting Model Predictions. *Adv. Neural Inf. Process. Syst.* **2017**, *2017*, 4766–4776.
- (33) Plotly Technologies Inc. *Collaborative Data Science*; Plotly Technologies Inc.: Montreal, QC, 2015.
- (34) Mortensen, J. J.; Hansen, L. B.; Jacobsen, K. W. Real-Space Grid Implementation of the Projector Augmented Wave Method. *Phys. Rev. B: Condens. Matter Mater. Phys.* **2005**, *71*, 35109.
- (35) Enkovaara, J.; Rostgaard, C.; Mortensen, J. J.; Chen, J.; Dulak, M.; Ferrighi, L.; Gavnholt, J.; Glinsvad, C.; Haikola, V.; Hansen, H. A.; Kristoffersen, H.; Kuusma, M.; Larsen, A. H.; Lehtovaara, L.; Ljungberg, M.; Lopez-Acevedo, O.; Moses, P. G.; Ojanen, J.; Olsen, T.; Petzold, V.; Romero, N. A.; Stausholm-Møller, J.; Strange, M.; Tritsaris, G. A.; Vanin, M.; Walter, M.; Hammer, B.; Häkinnen, H.; Madsen, G. K. H.; Nieminen, R. M.; Norskov, J. K.; Puska, M.; Rantala, T. T.; Schiøtz, J.; Thygesen, K. S.; Jacobsen, K. W. Electronic Structure Calculations with (GPAW): A Real-Space Implementation of the Projector-Augmented-Wave Method. *J. Phys. Condens. Matter* **2010**, *22*, 252302.
- (36) Hammer, B.; Hansen, L. B.; Nørskov, J. K. Improved Adsorption Energies within Density-Functional Theory Using Revised Perdew-Burke-Ernzerhof Functionals. *Phys. Rev. B: Condens. Matter Mater. Phys.* **1999**, *59*, 7413–7421.
- (37) Hjorth Larsen, A. H.; Jørgen Mortensen, J. J.; Blomqvist, J.; Castelli, I. E.; Christensen, R.; Dulak, M.; Friis, J.; Groves, M. N.; Hammer, B.; Hargas, C.; Hermes, E. D.; Jennings, P. C.; Bjær Jensen, P. B.; Kermode, J.; Kitchin, J. R.; Leonhard Kolsbjerg, E. L.; Kubal, J.; Kaasbjer, K.; Lysgaard, S.; Bergmann Marsson, J. B.; Maxson, T.; Olsen, T.; Pastewka, L.; Petersen, A.; Rostgaard, C.; Schiøtz, J.; Schütt, O.; Strange, M.; Thygesen, K. S.; Vegge, T.; Vilhelmsen, L.; Walter, M.; Zeng, Z.; Jacobsen, K. W. The Atomic Simulation Environment (textdash) a Python Library for Working with Atoms. *J. Phys. Condens. Matter* **2017**, *29*, 273002.
- (38) Stephens, I. E. L.; Bondarenko, A. S.; Gronberg, U.; Rossmeisl, J.; Chorkendorff, I. Understanding the Electrocatalysis of Oxygen Reduction on Platinum and Its Alloys. *Energy Environ. Sci.* **2012**, *5*, 6744.
- (39) Pedersen, J. K.; Batchelor, T. A. A.; Yan, D.; Skjestad, L. E. J.; Rossmeisl, J. Surface Electrocatalysis on High-Entropy Alloys. *Curr. Opin. Electrochem.* **2021**, *26*, 100651.
- (40) Quinson, J.; Simonsen, S. B.; Kuhn, L. T.; Kunz, S.; Arenz, M. Size Effect Studies in Catalysis: A Simple Surfactant-Free Synthesis of Sub 2 nm Pd Nanocatalysts Supported on Carbon. *RSC Adv.* **2018**, *8*, 33794.
- (41) Quinson, J. Colloidal Surfactant-Free Synthesis of Precious Metal Nanoparticles for Electrocatalysis. *Curr. Opin. Electrochem.* **2022**, *34*, 100977.
- (42) Quinn, M.; Mills, G. Surface-Mediated Formation of Gold Particles in Basic Methanol. *J. Phys. Chem.* **1994**, *98*, 9840–9844.
- (43) Bizzotto, F.; Quinson, J.; Schröder, J.; Zana, A.; Arenz, M. Surfactant-Free Colloidal Strategies for Highly Dispersed and Active Supported IrO<sub>2</sub> Catalysts: Synthesis and Performance Evaluation for the Oxygen Evolution Reaction. *J. Catal.* **2021**, *401*, 54.
- (44) Bizzotto, F.; Quinson, J.; Zana, A.; Kirkensgaard, J. J. K.; Dworzak, A.; Oezaslan, M.; Arenz, M. Ir Nanoparticles with Ultrahigh Dispersion as Oxygen Evolution Reaction (OER) Catalysts: Synthesis and Activity Benchmarking. *Catal. Sci. Technol.* **2019**, *9*, 6345–6356.

- (45) Lundberg, S. M.; Erion, G.; Chen, H.; DeGrave, A.; Prutkin, J. M.; Nair, B.; Katz, R.; Himmelfarb, J.; Bansal, N.; Lee, S.-I. From Local Explanations to Global Understanding with Explainable AI for Trees. *Nat. Mach. Intell.* **2020**, *2*, S6.
- (46) Papandrew, A. B.; Atkinson III, R. W.; Unocic, R. R.; Zawodzinski, T. A. Ruthenium as a CO-Tolerant Hydrogen Oxidation Catalyst for Solid Acid Fuel Cells. *J. Mater. Chem. A* **2015**, *3*, 3984–3987.
- (47) Lai, S. C. S.; Lebedeva, N. P.; Housmans, T. H. M.; Koper, M. T. M. Mechanisms of Carbon Monoxide and Methanol Oxidation at Single-Crystal Electrodes. *Top. Catal.* **2007**, *46*, 320–333.
- (48) Rodriguez, P.; Koper, M. T. M. Electrocatalysis on Gold. *Phys. Chem. Chem. Phys.* **2014**, *16*, 13583–13594.
- (49) Goyal, A.; Marcandalli, G.; Mints, V. A.; Koper, M. T. M. Competition between CO2Reduction and Hydrogen Evolution on a Gold Electrode under Well-Defined Mass Transport Conditions. *J. Am. Chem. Soc.* **2020**, *142*, 4154–4161.
- (50) James, G.; Witten, D.; Hastie, T.; Tibshirani, R. *Linear Model Selection and Regularization*; Springer Texts in Statistics; Springer New York: New York, NY, 2021.
- (51) Lin, W. F.; Zei, M. S.; Eiswirth, M.; Ertl, G.; Iwasita, T.; Vielstich, W. Electrocatalytic Activity of Ru-Modified Pt(111) Electrodes toward CO Oxidation. *J. Phys. Chem. B* **1999**, *103*, 6968–6977.
- (52) Gasteiger, H. A.; Markovic, N.; Ross, P. N.; Cairns, E. J. CO Electrooxidation on Well-Characterized Pt-Ru Alloys. *J. Phys. Chem.* **1994**, *98*, 617–625.

# 3

## O Deep Thought computer, what is the meaning of Bayesian optimization, high entropy alloys, and everything?



I introduced the idea of using Bayesian optimization to find the most active high entropy alloy catalysts to the Center of High Entropy Catalysis. This positively received concept quickly led to a second project, carried out by Jack Pedersen. In this follow up project Bayesian optimization was benchmarked on a DFT high entropy alloy activity model. As the DFT activity model spans the entire composition space, the global and local optima can be identified using a grid search. Consequently, knowing which compositions Bayesian optimization needs to find, we can evaluate the number of iterations required to find these compositions. Furthermore, with the sampled dataset it is possible to construct learning curves that show the number of experiments required to develop an adequately predictive machine learning.

This work, investigated two DFT models of  $\text{AuIrPdPtRu}$  and  $\text{IrPdPtRhRu}$  for the oxygen reduction reaction. The  $\text{IrPdPtRhRu}$  composition space is mathematically relatively simple as it only has two optima with similar activities. Bayesian optimization required on average only 20 iterations to find each of these optima. On the other hand, the  $\text{AuIrPdPtRu}$  space has 4 local optima with a strong global optimum. The local optima can potentially trap the optimization algorithm slowing it down. Consequently, Bayesian optimization required a slightly higher average of 50 iteration to successfully find the global optimum of this composition space.

Bayesian optimization relies on the Gaussian process regression to approximate the composition activity space. The Gaussian process assumes an infinite set of possible function, with certain function being more probable than others. Specifically, when there are known

observations, all functions must pass through these points. Prediction of new points involves utilizing a covariance matrix constructed using a kernel function. The kernel that we currently employ for our high entropy alloy studies is the radial basis function kernel (Eq. 3.1). In this kernel, the length scale  $l$  is the tuning parameter that describes the correlation strength of two observations ( $x_1$  and  $x_2$ ) based on their Euclidean distance.

$$k(x_1, x_2) = e^{-\frac{\|x_1 - x_2\|^2}{2l^2}} \quad (3.1)$$

This work showed that around 50 experiments, the gaussian process converges to a fitted value 30 at. % for  $l$ . The fact that the length scale converged indicates that adding observations to the model after is not accompanied with large changes in the mathematical landscape. Therefore, it can be inferred that the model reached an adequate level of prediction accuracy. In addition, this large length scale indicates that within the high entropy alloy compositions space observations exert a considerable influence on predicting unknown compositions over a considerable Euclidean distance. Hence, the activity-composition space can be characterized as mathematically smooth requiring as little as 50 experiments to construct an adequate machine learning model.

As a summary, this work highlights the effectiveness of Bayesian optimization for high entropy alloy systems. This established it presently as the main optimization algorithm for high entropy alloy composition-activity optimization. In addition, this work demonstrated that a relatively small data set is necessary to construct an adequate model for a high entropy alloy system, showcasing the feasibility of machine learning with manual acquired date even in the absence of high-through put stations. These findings encouraged me to investigate the 8-element AuIrOsPdPtReRhRu alloy system for the oxygen reduction reaction and oxygen evolution reaction, which will be covered in Chapter 5 and Chapter 6, respectively. Prior to delving into these chapters, I would like to discuss two other optimization algorithms that the Center for High Entropy Alloy catalysis explored during my PhD project.



## Bayesian Optimization of High-Entropy Alloy Compositions for Electrocatalytic Oxygen Reduction\*\*

Jack K. Pedersen, Christian M. Clausen, Olga A. Krysiak, Bin Xiao, Thomas A. A. Batchelor, Tobias Löffler, Vladislav A. Mints, Lars Banko, Matthias Arenz, Alan Savan, Wolfgang Schuhmann, Alfred Ludwig, and Jan Rossmeisl\*

**Abstract:** Active, selective and stable catalysts are imperative for sustainable energy conversion, and engineering materials with such properties are highly desired. High-entropy alloys (HEAs) offer a vast compositional space for tuning such properties. Too vast, however, to traverse without the proper tools. Here, we report the use of Bayesian optimization on a model based on density functional theory (DFT) to predict the most active compositions for the electrochemical oxygen reduction reaction (ORR) with the least possible number of sampled compositions for the two HEAs Ag–Ir–Pd–Pt–Ru and Ir–Pd–Pt–Rh–Ru. The discovered optima are then scrutinized with DFT and subjected to experimental validation where optimal catalytic activities are verified for Ag–Pd, Ir–Pt, and Pd–Ru binary alloys. This study offers insight into the number of experiments needed for optimizing the vast compositional space of multimetallic alloys which has been determined to be on the order of 50 for ORR on these HEAs.

### Introduction

High-entropy alloys (HEAs; in the form of single-phase compositionally complex solid solutions) offer a vast composition space for optimization of catalytic properties.<sup>[1–5]</sup> The many multi-element atomic surface sites found on such complex surfaces contribute to a near-continuum of the reaction intermediate adsorption energies that are descriptive of catalytic activity. Tailoring the HEA composition can improve the distribution of these adsorption energies to yield

better catalysts.<sup>[6]</sup> This is advantageous since new catalysts are especially needed to facilitate chemical reactions for sustainable energy conversion in order to meet the increasing global energy demand and to combat climate change.<sup>[6]</sup> One example of a key reaction in the hydrogen cycle is the oxygen reduction reaction (ORR), where current catalysts are still far from ideal and cannot meet the demands for commercially viable industrial implementation on a global scale. Thus, further innovations are highly sought after, to get to that ultimate goal.<sup>[7,8]</sup>

Combinatorial exploration of vast alloy composition spaces has been actively used as a tool in experimental catalyst discovery for a variety of reactions and constituent elements,<sup>[9–16]</sup> and efficient sampling of catalyst materials has also progressed.<sup>[17]</sup> However, as the number of constituent elements increases, the number of possible compositions grows combinatorially large and individual point testing cannot be accomplished within realistic time scales (see Supporting Information (SI), Figure S2). This calls for the need to sample the composition space more efficiently, such as by guiding the search with the aid of a surrogate function. Bayesian optimization of a Gaussian process (GP) is a feasible choice for intelligent sampling problems<sup>[18]</sup> and Bayesian optimization has also been employed to optimize the catalytic activity for methanol oxidation of a ternary alloy.<sup>[19]</sup> However, knowing beforehand how many experiments would be needed in such a compositional search is crucial for determining if such a search is tractable in the first place.

\*<sup>[1]</sup> J. K. Pedersen, C. M. Clausen, Dr. T. A. A. Batchelor, Prof. M. Arenz, Prof. J. Rossmeisl  
 Center for High Entropy Alloy Catalysis (CHEAC)  
 Department of Chemistry, University of Copenhagen  
 Universitetsparken 5, 2100 Copenhagen Ø (Denmark)  
 E-mail: janrossmei@chem.ku.dk

Dr. O. A. Krysiak, Dr. T. Löffler, Prof. W. Schuhmann  
 Center for Electrochemical Sciences (CES)  
 Faculty of Chemistry and Biochemistry  
 Ruhr University Bochum  
 Universitätsstrasse 150, 44780 Bochum (Germany)  
 Dr. B. Xiao, Dr. T. Löffler, L. Banko, A. Savan, Prof. A. Ludwig  
 Chair for Materials Discovery and Interfaces  
 Institute for Materials, Faculty of Mechanical Engineering, Ruhr  
 University Bochum  
 Universitätsstrasse 150, 44780 Bochum (Germany)  
 Dr. T. Löffler, Prof. A. Ludwig  
 ZGH, Ruhr University Bochum  
 Universitätsstrasse 150, 44780 Bochum (Germany)

V. A. Mints, Prof. M. Arenz  
 Center for High Entropy Alloy Catalysis (CHEAC)  
 Department of Chemistry, Biochemistry and Pharmaceutical Sciences  
 University of Bern  
 Freiestrasse 3, 3012 Bern (Switzerland)

[\*\*] A previous version of this manuscript has been deposited on a preprint server (<https://arxiv.org/abs/2106.08212>).

[#] Supporting information and the ORCID identification number(s) for the author(s) of this article can be found under:  
<https://doi.org/10.1002/anie.202108116>.

© 2021 The Authors. Angewandte Chemie International Edition published by Wiley-VCH GmbH. This is an open access article under the terms of the Creative Commons Attribution Non-Commercial NoDerivs License, which permits use and distribution in any medium, provided the original work is properly cited, the use is non-commercial and no modifications or adaptations are made.

Modeling the catalytic activity of highly diverse and complex surfaces is still in its infancy with only a few studies conducted<sup>[1,3,4,20,21]</sup> and modeling of other aspects relevant for catalysis, such as surface stability under reaction conditions, is also being investigated.<sup>[22,23]</sup> We propose a way to estimate the number of experiments needed using a model that has been found to correctly predict experimental trends for electrocatalytic ORR across hundreds of different alloy compositions within the Ag–Ir–Pd–Pt–Ru system.<sup>[4]</sup> Because of that, we expect the model to reproduce the complexity of an equivalent experimental search, and therefore be likely suitable as a proxy for substituting most of the necessary experiments by simulations. By sampling alloy compositions from the model, the number of experiments needed for future composition optimizations can thus be estimated.

Using the Ag–Ir–Pd–Pt–Ru and Ir–Pd–Pt–Rh–Ru HEAs as exemplary systems for a composition optimization, we use the kinetic model combined with Bayesian optimization to suggest alloy compositions for which high catalytic activities for the ORR are predicted. Doing this affords sampling of as few compositions as possible and yields the estimate of the minimum number of experiments needed to discover activity optima. The predicted optima subsequently undergo experimental validation. Moreover, by sampling the whole space of alloy compositions with the model in, for example, 5 atomic percent (at.%) intervals, it is possible to assure with reasonable certainty that all local and global optimal compositions have indeed been identified by the Bayesian optimization.

## Results and Discussion

We apply our previously published model<sup>[4]</sup> for predicting current densities at 0.82 V vs. the reversible hydrogen electrode (RHE) on the face-centered cubic (fcc) (111) surfaces of the disordered quinary alloy systems of Ir–Pd–Pt–Rh–Ru and Ag–Ir–Pd–Pt–Ru. This kinetic model is based on the \*OH and O\* adsorption energies and their success at describing the catalytic activity for the ORR through the associative mechanism.<sup>[24,25]</sup> The dissociative mechanism, where O<sub>2</sub> dissociates on the catalyst surface, will not contribute to the current density when the potential exceeds 0.8 V vs. RHE.<sup>[26]</sup> For construction of the model, thousands of \*OH and O\* adsorption energies were calculated with DFT in order to enable \*OH and O\* adsorption energy predictions on any surface site of the alloy at any composition (for details see SI). Due to the linear scaling between \*OH and \*OOH adsorption energies, focusing on the \*OH and O\* intermediates is sufficient to predict the catalytic activity.<sup>[27]</sup> The model effectively maps an alloy composition to a relative measure of a current density at a given potential using Equations (1)–(3). By doing so it takes as input net adsorption energies of on-top \*OH and hollow site O\* obtained by considering an intersite neighbor blocking effect that ensures that no neighboring on-top and hollow sites can adsorb intermediates at the same time (for details see SI).

$$j = \frac{1}{N} \sum_i^{N_{\text{ab}}} j_i \quad (1)$$

$$\frac{1}{j_i} = \frac{1}{j_D} + \frac{1}{j_{k,i}} \quad (2)$$

$$j_{k,i} = -\exp\left(-\frac{|\Delta G_i - \Delta G_{\text{opt}}| - 0.86eV + eU}{k_B T}\right) \quad (3)$$

Here  $j$  is the per site current density (in arbitrary units only used for comparing catalytic activity between compositions),  $N$  is the number of surface atoms in the simulated surface,  $N_{\text{ab}}$  is the number of sites at which adsorption has happened (after considering the intersite neighbor blocking),  $j_i$  is the current at surface site  $i$  modeled using the Koutecký–Levich equation,  $j_D$  is the diffusion-limited current (set to  $-1$ ) ensuring that the current at each site only increases sigmoidally at high overpotentials,  $j_{k,i}$  is the kinetically limiting current for site  $i$  modeled using an Arrhenius-like expression assuming a Sabatier volcano relationship with the adsorption energies,  $\Delta G_i$  is the \*OH or O\* adsorption free energy,  $\Delta G_{\text{opt}}$  is the optimal \*OH or O\* adsorption free energy (set to 0.1 eV<sup>[24]</sup> and 0.2 eV<sup>[25]</sup> larger than for Pt(111) for \*OH and O\* respectively as suggested by theory and experiment),  $e$  is the elementary charge,  $U_{\text{RHE}}$  is the applied potential vs. RHE,  $k_B$  is the Boltzmann constant, and  $T$  is the absolute temperature (set to 300 K).

The posterior mean of a GP was used to construct a surrogate function mapping alloy composition to current density. For estimating the uncertainty at any composition, the posterior variance of the GP was used. The GP prior mean was set to zero everywhere, and the squared exponential kernel in Equation (4) was used as the covariance function. This prior mean and kernel are convenient standard choices that have applicability for many problems and therefore form a natural starting point for an unbiased analysis (see SI for details).

$$k(\mathbf{x}_i, \mathbf{x}_j) = C^2 \exp\left(-\frac{(\mathbf{x}_i - \mathbf{x}_j)^T (\mathbf{x}_i - \mathbf{x}_j)}{2l^2}\right) \quad (4)$$

In Equation (4),  $\mathbf{x}_i$  and  $\mathbf{x}_j$  are molar fraction vectors, specified as the molar concentrations of each of the constituent elements in the alloy. For example, the alloy Ag<sub>20</sub>Ir<sub>30</sub>Pd<sub>40</sub>Pt<sub>10</sub> corresponds to the molar fraction vector  $\mathbf{x} = (0.2, 0.3, 0.1, 0.4, 0.0)^T$ .  $C$  and  $l$  are the constant value and length scale hyperparameters, respectively, of the kernel, which were optimized with every update of the sampled data. The superscript  $T$  denotes taking the transpose of the vector.

Figure 1 shows the workflow of the Bayesian optimization algorithm. Two random compositions were initially chosen to initiate the surrogate function. The *expected improvement* acquisition function was then used to suggest the next composition to investigate. The expected improvement takes into consideration the current densities predicted by the surrogate function as well as the readily obtained uncertainties of the predictions.<sup>[28]</sup> It is a standard choice and a widely used acquisition function,<sup>[29]</sup> making it a natural starting point

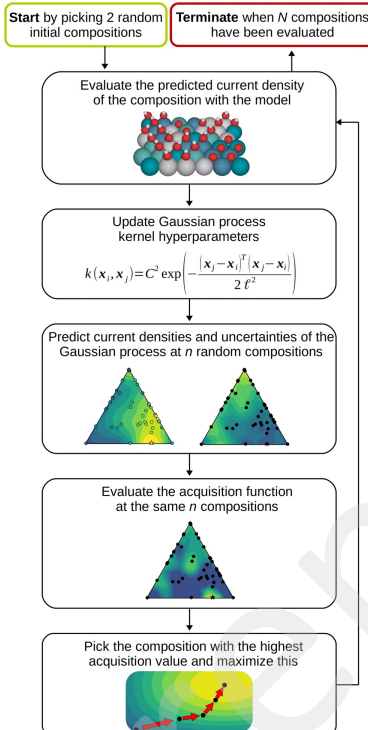


**Figure 1.** Workflow of the Bayesian optimization algorithm. The algorithm was terminated after  $N = 150$  samples to ensure enough evaluations for gauging the deviation in the number of samples needed for discovery of the optimal compositions. For evaluation of the acquisition function  $n = 1000$  random compositions were sampled.

for the current study (see the SI for details on the implementation). The kinetic model was then used to compute the catalytic activity of the selected composition via Equations (1)–(3), and the GP posterior was updated with this new sample using Bayesian inference as implemented in scikit-learn.<sup>[30]</sup> By repeating this process we let the updated acquisition function choose the next composition of interest, and allowing the optimization to run for 150 iterations was enough to discover the most active locally optimal compositions in most cases.

The quinary alloy composition space is equivalent to the set of all points in a 4-simplex (the 4-dimensional version of a regular tetrahedron), so plotting the resulting surrogate functions directly is hindered by the dimensionality of the plot. Instead, the local optima obtained from the resulting surrogate functions for each of the quinary alloys are listed in Table 1 in order of descending catalytic activity with the most active catalyst at the top. For illustration, a projection of the surrogate function for the Ag-Ir-Pd-Pt-Ru HEA at various stages of the optimization is given in Figure 2a. Figure 2b shows the modeled current densities that are sampled during a run of the optimization with some noticeable minima (i.e. compositions with high absolute values of modeled current densities) shown explicitly as well as the emergence of the local minima of the surrogate function. Figure 2c,d shows the evolution of the constant value and length scale kernel hyperparameters in Equation (4) as more compositions are sampled. Important to notice is the length scale of the kernel which, although not directly transferable to the compositions, does give an indication of the frequency with which the current density is expected to change with composition. To be specific, the found length scale of about 0.4 is rather large compared to the molar fractions with values between 0 and 1, indicating that the current density is expected to vary with rather low frequencies. This is also indicated by the contours of the surrogate function in Figure 2a which is seen to vary slowly with changes in the molar fractions. This also means that only a few local optima are expected for this hypersurface which will likely decrease the number of samples needed for their discovery.

Indeed, the most active discovered optimal compositions in Table 1 form three groups of alloys, namely the binaries  $\text{Ag}_{18}\text{Pd}_{82}$ ,  $\text{Ir}_{50}\text{Pt}_{50}$ , and the ternary  $\text{Ir}_{50}\text{Pd}_{50}\text{Ru}_{50}$ , with the latter two compositions discovered independently from both the Ag-Ir-Pd-Pt-Ru and the Ir-Pd-Pt-Rh-Ru quinary alloy models, supporting the robustness of the presented methodology.

For proof of concept and to verify that all local optima had indeed been discovered by the Bayesian optimization, we simulated all compositions in 5 at. % for both HEA systems, corresponding to 10626 simulations for each. This is a much more demanding task compared to Bayesian optimization. Without a high degree of automation it is also an impractical objective for an actual experimental realization, not to mention the cost associated with the precursor materials and the automated instrumentation.

The discovered locally optimal compositions using this 5 at. % grid search of the quinary composition space are shown in Table 2. It indeed appears that the most important compositions for catalysis were found by the Bayesian optimization. Most noticeably, the locally optimal compositions  $\text{Ag}_{50}\text{Pd}_{50}$  and  $\text{Ir}_{50}\text{Pt}_{50}$  with high absolute values of predicted current densities are confirmed. Simplifying the list of optimum compositions by grouping similar compositions makes it possible to match the other optima found by Bayesian optimization in Table 1 with corresponding counterparts in the 5 at. % grid search analysis in Table 2. For example, the closely related  $\text{Ir}_{50}\text{Pd}_{50}\text{Ru}_{50}$  optimum for the Ag-Ir-Pd-Pt-Ru HEA and the  $\text{Ir}_{12}\text{Pd}_{50}\text{Rh}_{18}\text{Ru}_{20}$  optimum for the

**Table 1:** Locally optimal compositions and the number of compositions needed to identify them for the two quinary HEAs.

HEA	Local optimum <sup>[a]</sup>	Predicted current density (arb. units) <sup>[b]</sup>	Identification success rate [%] <sup>[c]</sup>	Number of samples for identification of local optimum <sup>[b,d]</sup>
Ag-Ir-Pd-Pt-Ru	Ag <sub>13</sub> Pd <sub>82</sub>	-0.203(2)	100	50(21)
	Ir <sub>5</sub> Pd <sub>95</sub> Ru <sub>27</sub>	-0.160(2)	100	28(28)
	Ir <sub>45</sub> Pt <sub>52</sub>	-0.147(2)	100	25(10)
	Ag <sub>78</sub> Ru <sub>22</sub>	-0.063(3)	69	93(27)
	Ir <sub>6</sub> Ru <sub>94</sub>	-0.003(0)	2	73(20)
	Ir <sub>50</sub> Ru <sub>50</sub>	-0.002(1)	14	110(27)
	Ru	-0.001(1)	14	48(33)
	Ir <sub>45</sub> Pt <sub>55</sub>	-0.165(2)	100	23(8)
	Ir <sub>15</sub> Pd <sub>85</sub> Ru <sub>28</sub>	-0.164(1)	100	19(10)
	Rh	-0.001(2)	27	48(42)

[a] Determined as the local optima of the resulting surrogate function after sampling of 150 compositions for 64 random realizations of the two initial compositions (one such realization is shown in Figure 2). The spread in these compositions is on the order of 1 at. %. [b] Given as the mean followed by the sample standard deviation on the last digit(s) in parentheses. [c] Determined as the proportion of the resulting surrogate functions after sampling of 150 compositions for 64 random initializations that identify the optimum as a local maximum. [d] Determined as the number of samples needed for those of 64 surrogate functions with random initializations that successfully identified the optimum. The optimum has been considered identified when the molar fraction is within a 10 at. % difference of the optimum, for example, Ag<sub>13</sub>Pd<sub>82</sub>, would be regarded as a successful discovery of the Ag<sub>13</sub>Pd<sub>82</sub> optimum.

Ir-Pd-Pt-Rh-Ru HEA with a modeled current density of about -0.16 (arb. units) in Table 1 correspond to the Ag<sub>13</sub>Ir<sub>5</sub>Pd<sub>95</sub>Pt<sub>52</sub>Ru<sub>27</sub> and Ir<sub>10</sub>Pd<sub>50</sub>Pt<sub>50</sub>Rh<sub>50</sub>Ru<sub>50</sub> groups of compositions with similar current density highlighted in boldface in Table 2. In fact, the optima found with Bayesian optimization may constructively be thought of as the locally optimal compositions that the 5 at. % grid search would converge to if the step resolution was increased. We note that the trace amounts of other elements in the group of Pd-Ru-rich optima appear not to be very influential on the modeled current density, because the quinary composition space forms a rather flat plateau around Pd<sub>85</sub>Ru<sub>15</sub> as shown in Figure S4. We therefore simplify our analysis of

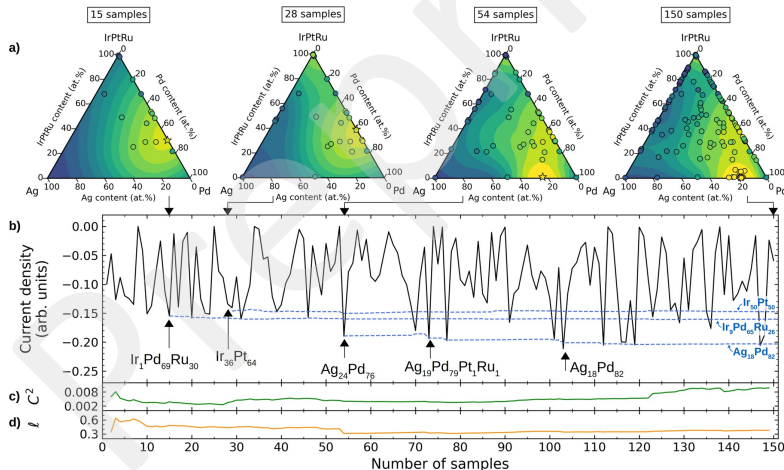


**Figure 2.** Example of a Bayesian ORR composition optimization for the quinary Ag-Ir-Pd-Pt-Ru system. a) Pseudo-ternary plots (with Ir, Pt, and Ru collected into a single concentration) of the surrogate function after sampling of 15, 28, 54, and 150 compositions. Yellow colors signify regions with high absolute values of modeled current density, and blue colors signify regions with correspondingly low values. Previously sampled compositions are shown as black circles, and the best composition found so far is marked with a star. When projecting current densities from the quinary to the pseudo-ternary composition space, more compositions will inevitably occupy the same points in the diagram. In the shown plots the maximal absolute value of the current density for overlapping compositions has therefore been depicted. b) Current densities sampled during the Bayesian optimization (black solid line) and the emergence of the three most active locally optimal compositions (blue dashed lines). c,d) Variation of the GP squared exponential kernels' [Eq. (4)] constant term (c) and length scale (d) hyper-parameters.

**Table 2:** Locally optimal compositions found using a 5 at.% grid search over the two quininary composition spaces.

HEA	Local optimum <sup>[a]</sup>	Modeled current density (arb. units)
Ag-Ir-Pd-Pt-Ru	Ag <sub>30</sub> Pd <sub>40</sub>	-0.21
	Ag <sub>40</sub> Pd <sub>30</sub> Pt <sub>10</sub> Ru <sub>10</sub>	-0.16
	Ag <sub>40</sub> Pd <sub>30</sub> Pt <sub>10</sub> Ru <sub>20</sub>	-0.16
	Ir <sub>50</sub> Pd <sub>20</sub> Ru <sub>30</sub>	-0.16
	Pd <sub>50</sub> Pt <sub>20</sub> Ru <sub>30</sub>	-0.16
	Pd <sub>50</sub> Pt <sub>20</sub> Ru <sub>25</sub>	-0.15
	Ir <sub>55</sub> Pt <sub>45</sub>	-0.15
	Ir <sub>45</sub> Pt <sub>55</sub>	-0.15
	Ag <sub>40</sub> Ir <sub>10</sub> Pd <sub>20</sub> Pt <sub>55</sub>	-0.09
	Ag <sub>50</sub> Ru <sub>10</sub>	-0.06
Ir-Pd-Pt-Rh-Ru	Ir <sub>10</sub> Pd <sub>20</sub> Rh <sub>20</sub> Ru <sub>30</sub>	-0.17
	Ir <sub>50</sub> Pt <sub>50</sub>	-0.17
	Ir <sub>40</sub> Pt <sub>60</sub>	-0.17
	Ir <sub>15</sub> Pd <sub>30</sub> Pt <sub>55</sub> Ru <sub>10</sub>	-0.16
	Ir <sub>15</sub> Pd <sub>30</sub> Pt <sub>55</sub> Ru <sub>10</sub>	-0.08
	Pt <sub>55</sub> Rh <sub>35</sub>	-0.07

[a] Defined as compositions for which a  $\pm 5$  at. % change in any molar fraction would result in a less active catalyst. Compositions in **boldface** refer to the group of Ir<sub>10</sub>Pd<sub>30</sub>Pt<sub>20</sub>Ru<sub>30</sub> compositions with similar predicted current densities.

this optimum in the following, and treat it as a binary Pd–Ru alloy.

Similarly, the less optimal Ag<sub>78</sub>Ru<sub>22</sub>, can be assigned a counterpart (Ag<sub>60</sub>Ru<sub>40</sub>) in Table 2. However, it also appears that local optima with relatively low absolute current densities are not matched as well between the Bayesian optimization and the grid search. For instance, the similar compositions Ag<sub>5</sub>Ir<sub>10</sub>Pd<sub>30</sub>Pt<sub>55</sub> (from Ag-Ir-Pd-Pt-Ru) and Ir<sub>15</sub>Pd<sub>30</sub>Pt<sub>55</sub>Ru<sub>10</sub> (from Ir-Pd-Pt-Rh-Ru) from the grid search in Table 2 do not have counterparts from the Bayesian optimization in Table 1. The reason for this is either that these compositions are not actually local optima and therefore not identified as such by the Bayesian optimization, or that they are weak local optima but were not sampled by the acquisition function due to small predicted absolute current densities. In either case this highlights the advantage of efficient sampling, where compositions that are not expected to be active are left untested.

We note that the Bayesian optimization algorithm in the current study could have been implemented in a number of other ways. For instance, the constraint that the molar fractions add to unity could be accounted for using constrained GPs.<sup>[31]</sup> In the current study this constraint was only included in the sense that evaluations only were done for valid molar fractions. This, however, appears to have been sufficient, which is evident from the fact that the 5 at. % grid search gave identical optima to the Bayesian optimization. Moreover, for a practical experimental composition optimization, a proper termination criterion is needed to know when to stop the search with confidence that the global optimum has been found. This criterion could for instance be based on the value of the acquisition function.<sup>[29]</sup>

Since the model uses calculated adsorption energies of the quininary alloys, it is essentially extrapolating to the edges of the composition space when predicting the current density of the

discovered near-binary optimal compositions. This is because only the most central composition space is likely to be sampled when generating random configurations of five elements for the simulated surfaces. To confirm the current density optima and the model's predictive ability for the binary alloys, DFT adsorption energies computed solely on the Ag-Pd, Ir-Pt and Pd-Ru binary alloys were used as input for the model.

Additionally, several regression algorithms were tested with two schemes for choosing the features of the simulated adsorption sites in order to predict the adsorption energies accurately on the binary alloys (see Tables S6, S7 and Figure S6). This confirmed that a combination of a per-unique-site based linear regression model and the most influential neighboring atoms<sup>[32,33]</sup> maintains a low model complexity while still providing high adsorption energy prediction accuracy. However, for the binary alloys it was possible to achieve exceptionally low prediction error by using a non-linear regression algorithm (a gradient-boosted decision tree) and an extensive description of the adsorption site motif. This is true even though the simulated  $2 \times 2$  atom-sized surfaces limit the variations of the nearest neighbors due to the periodic boundary conditions (see SI for details).

Plotting the predicted current density of the binary alloy gradient-boosted model against the same results from the linear model trained on the quininary alloys, it is seen for the Ag-Pd system in Figure 3 that at high Pd content both models predict an activity maximum around Ag<sub>40</sub>Pd<sub>60</sub>. This activity stems almost exclusively from O<sup>2-</sup> bound in fcc hollow sites composed of two Pd atoms and one Ag atom with some contribution from three-fold Pd sites as shown in Figure 3b,c. However, due to the discrepancy of the models' prediction of OH bound at on-top Pd sites (Figure 3d,e), the binary-trained model retains high catalytic activity for a wider span of compositions compared to the quininary-trained model which drops below the activity of Pt(111) at around 45 at. % Ag content as shown in Figure 3a. We would thus still expect appreciable catalytic activity for Ag-Pd at the equimolar composition using the binary alloy model.

Ir-Pt and Pt-Ru were similarly scanned as shown in Figure 4 and more detailed in Figures S7 and S8 and display overall good agreement with the quininary alloy model. Both models predict optimum compositions around Ir<sub>40</sub>Pt<sub>60</sub> and Pd<sub>60</sub>Ru<sub>40</sub>, and equivalent trends in the predicted current densities for the entire composition spans are observed.

The high catalytic activity of the Ag-Pd, Ir-Pt, and Pd-Ru alloys is not surprising since alloying the active elements Pd and Pt is a general way to enhance the activity for ORR.<sup>[34]</sup> Moreover, these alloys have indeed been tested experimentally with optimal compositions determined for the respective reaction conditions to be around Ag<sub>10</sub>Pd<sub>90</sub>,<sup>[35]</sup> Ir<sub>15</sub>Pt<sub>85</sub>,<sup>[36]</sup> and Pd<sub>60</sub>Ru<sub>40</sub>.<sup>[37]</sup>

To validate and compare the proposed catalytic trends of the discovered binary compositions, thin-film composition spreads of the predicted Ag-Pd, Ir-Pt, and Pd-Ru binary alloys were synthesized and then analyzed by the use of a scanning droplet cell (SDC) in 0.1 M HClO<sub>4</sub>. This high-throughput electrochemical technique allows localized characterization of selected compositions along the compositional

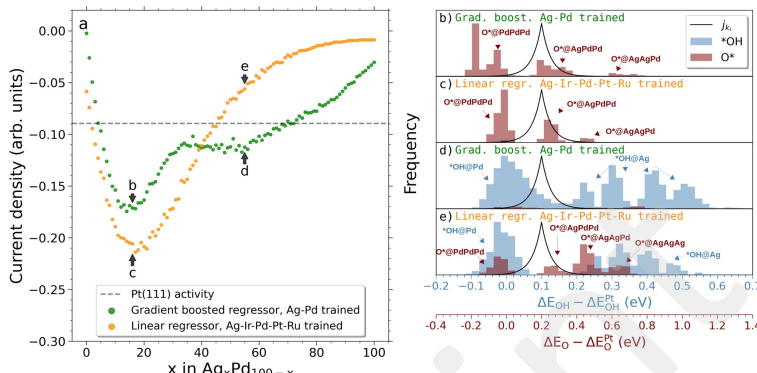


**Figure 3.** a) Simulated current densities of the Ag-Pd system in a composition range from pure Pd to pure Ag with 1 at.% increments. A linear regression model trained on DFT-calculated samples of the Ag-Ir-Pd-Pt-Ru alloy is used alongside a gradient-boosted model trained on DFT-calculated samples of Ag-Pd to predict the adsorption energies of the simulated surface. These predictions serve as input for Equations (1)–(3) which yield the resulting current densities. b–e)  $\text{O}^{\bullet}\text{@H}$  and  $\text{O}^{\bullet}$  net adsorption energy distributions (after intersite blocking) for selected compositions corresponding to the annotations in (a). A scaled visualization of the modeled current density in Equation (3) is shown (black solid line).

gradient. Precise positioning above the investigated sample is enabled by assembling the SDC head with robotic arms and a force sensor. An electrochemical cell is formed by pressing the Teflon tip to the surface of the sample, defining the surface of the working electrode in every measurement area (MA).

We used an automated setup to exclude any human error and provide the same measuring conditions for each measurement. Together with the high reliability and accuracy of the data this allows credible comparison of the activity between different MAs and samples. Figure 4 shows measured current density values vs. the composition of the Ag-Pd, Pd-Ru, and Ir-Pt systems. All linear sweep voltammograms (LSVs) are available in Figure S9. We note that catalytic trends on the quinary alloys obtained with the same experimental setup have been reported previously.<sup>[4]</sup> Therefore the scope of the current study is on the verification of the discovered optimal compositions. For the Pd-Ru composition spread we observed a broad minimum in ORR current densities for compositions ranging from ca.  $\text{Pd}_{48}\text{Ru}_{32}$  to  $\text{Pd}_{32}\text{Ru}_{68}$ , covering the predicted optimal composition of  $\text{Pd}_{48}\text{Ru}_{32}$ . In the case of the Ag-Pd composition spread, only the lower Ag content compositions could be measured without visible corrosion (see Figure S9a). Here, a current density optimum was found at the composition  $\text{Ag}_{12}\text{Pd}_{88}$ , corresponding very well to the predicted optimum of  $\text{Ag}_{13}\text{Pd}_{86}$ .

In contrast, the Ir-Pt composition spread shows a clear increase of the activity toward ORR with decreasing content of Ir, that is, here we do not observe an agreement with the

predicted optimal composition. In order to examine if the plateau at low Ir content observed in Figure 4c is the expected optimum, a sample covering higher Pt contents was prepared and tested as shown in Figure 4d.

To ensure the enhanced activity can indeed be fully assigned to the composition effect and the impact of changes in surface roughness can be ruled out, atomic force microscopy (AFM) measurements of surface roughness at different spots of the binary thin-film composition spreads were made. For all of the considered samples the changes in surface roughness between different areas of the sample are negligible. Correlation of measured current densities with composition of the samples and their surface roughness are presented in Figure S10.

In order to determine the crystal structure and fully understand the measured correlation between current densities and binary compositions, X-ray diffraction (XRD) was conducted. The crystal structures of as-deposited Ag-Pd, Pd-Ru, and Ir-Pt thin films for various compositions were determined from XRD diffractograms shown in Figure S11. Five XRD peaks were observed in all three binary systems, which are characteristic for Bragg reflections from fcc structures. The diffraction patterns exhibit the highest intensity reflection along the (111) plane and four weak reflections along the (200), (220), (311), and (222) planes. For Ag-Pd and Pd-Ru, the diffraction peaks continuously shift to lower  $2\theta$  values with increasing Ag or Pd amount. The lattice parameters for these two systems are determined from Bragg's law, and the calculated results show that the variation of lattice parameters with chemical composition agrees well

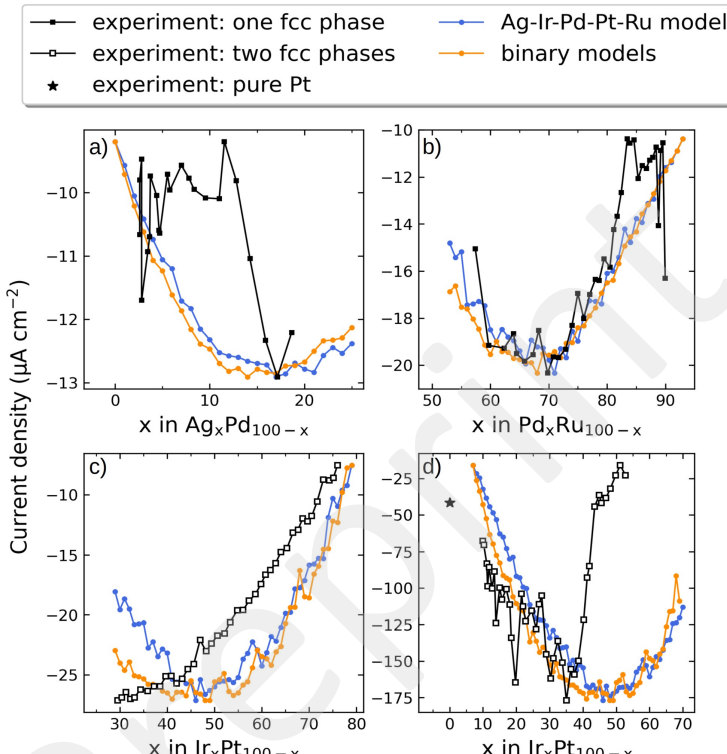


**Figure 4.** Comparison of simulated and experimental catalytic activities (black curves) for a) Ag-Pd, b) Pd-Ru, and c,d) Ir-Pt (for different composition ranges in (c) and (d)) at 800 mV vs. RHE. The simulated current densities were normalized to the experimental current densities by ensuring that the minimum and maximum current densities match up. For Pd-Ru in (b) three outliers that gave rise to very high current densities were left out (see Figure S9b).

with a linear dependence based on Vegard's law. This reveals that as-deposited Ag-Pd and Pd-Ru binary systems with different compositions form continuous solid solutions with an fcc structure. In the case of the Ir-Pt system, the (111) peak splits into two peaks. This is due to the coexistence of two phases and implies that Ir and Pt are not completely mixed, which is consistent with the large miscibility gap of the Ir-Pt phase diagram.

### Conclusion

To summarize, we have combined a kinetic model with Bayesian optimization to predict compositions of highest current density for ORR starting from the quinary HEAs Ag-Ir-Pd-Pt-Ru and Ir-Pd-Pt-Rh-Ru. The most important locally optimal compositions come out at around  $\text{Ag}_{15}\text{Pd}_{45}$ ,  $\text{Ir}_{40}\text{Pt}_{50}$ , and  $\text{Ir}_{10}\text{Pd}_{60}\text{Ru}_{30}$ . The model, trained on DFT-calculated  ${}^{\circ}\text{OH}$  and  ${}^{\circ}\text{O}$  adsorption energies on Ag-Ir-Pd-Pt-Ru and Ir-Pd-Pt-Rh-Ru HEAs, was successful in extrapolating catalytic

activity trends to the discovered optimal binary alloys Ag–Pd, Ir–Pt, and Pd–Ru as confirmed by training new models with new data specific for these. The model was also shown to reasonably reproduce the catalytic activity trend from synthesized thin-film composition spreads of the Ag–Pd, Ir–Pt, and Pd–Ru systems for which optimal compositions of around  $\text{Ag}_{30}\text{Pd}_{60}$ ,  $\text{Ir}_{30}\text{Pt}_{60}$ , and  $\text{Pd}_{30}\text{Ru}_{35}$  were determined. A direct comparison between the model and the experiment, however, should be done with caution since many reaction condition parameters are not accounted for in the model. While suggesting optimal alloy catalysts, the model is at the same time able to estimate the number of experiments needed for the discovery of optimal compositions in the vast compositional space of quinary alloy systems. With the Bayesian optimization of the kinetic model employed herein, the number of experiments comes out at about 50 for discovery of the most important optima for the two investigated quinary HEAs. This number gives hope that composition optimizations of vast multi-metallic composition spaces are indeed experimentally realizable in the laboratory.

### Acknowledgements

J.P., C.C., V.M., T.B., M.A., and J.R. acknowledge support from the Danish National Research Foundation Center for High-Entropy Alloy Catalysis (CHEAC) DNRF-149. J.P. acknowledges support from the Danish Ministry of Higher Education and Science (Structure of Materials in Real Time (SMART) grant). T.B. acknowledges support from VILLUM FONDEN (research grant 9455). W.S. acknowledges funding from Deutsche Forschungsgemeinschaft (DFG) under Germany's Excellence Strategy (EXC 2033-390677874—RESOLV) and from the European Research Council (ERC) under the European Union's Horizon 2020 research and innovation programme (grant agreement CasCat [833408]). A.L. and B.X. acknowledge funding from DFG project LU1175/26-1. ZGH at RUB is acknowledged for use of its experimental facilities.

### Conflict of Interest

The authors declare no conflict of interest.

### Data Availability

All data and commented code necessary to reproduce the presented results have been made freely available at <https://nano.ku.dk/english/research/theoretical-electrocatalysis/katlab/bayesian-optimization-of-hea/>.

**Keywords:** Bayesian optimization · complex solid solutions · density functional calculations · electrochemistry · high-entropy alloys

- [1] T. A. A. Batchelor, J. K. Pedersen, S. H. Winther, I. E. Castelli, K. W. Jacobsen, J. Rossmeisl, *Joule* **2019**, *3*, 834.
- [2] T. Löffler, A. Savan, H. Meyer, M. Meischin, V. Strotkötter, A. Ludwig, W. Schuhmann, *Angew. Chem. Int. Ed.* **2020**, *59*, 5844; *Angew. Chem.* **2020**, *132*, 5893.
- [3] J. K. Pedersen, T. A. A. Batchelor, A. Bagger, J. Rossmeisl, *ACS Catal.* **2020**, *10*, 2169.
- [4] T. A. A. Batchelor, T. Löffler, B. Xiao, O. A. Krysiak, V. Strotkötter, J. K. Pedersen, C. M. Clausen, A. Savan, Y. Li, W. Schuhmann, et al., *Angew. Chem. Int. Ed.* **2021**, *60*, 6932; *Angew. Chem.* **2021**, *133*, 7008.
- [5] Y.-C. Qin, F.-Q. Wang, X.-M. Wang, M.-W. Wang, W.-L. Zhang, W.-K. An, X.-P. Wang, Y.-L. Ren, X. Zheng, D.-C. Lv, et al., *Rare Met.* **2021**, *40*, 2354.
- [6] A. P. O'Mullan, M. Escudero-Escrivano, I. E. L. Stephens, K. Krischer, *ChemPhysChem* **2019**, *20*, 2900.
- [7] A. Kulikarni, S. Siahrostami, A. Patel, J. K. Nørskov, *Chem. Rev.* **2018**, *118*, 2302.
- [8] M. Shao, Q. Chang, J.-P. Dodelet, R. Chenitz, *Chem. Rev.* **2016**, *116*, 3594.
- [9] E. J. Klunder, J. L. Hedrick, K. A. Brown, R. Rao, B. Meckes, J. S. Du, L. M. Moreau, B. Maruyama, C. A. Mirkin, *Proc. Natl. Acad. Sci. USA* **2019**, *116*, 40.
- [10] Y. Yao, Z. Huang, T. Li, H. Wang, Y. Liu, H. S. Stein, Y. Mao, J. Gao, M. Jiao, Q. Dong, et al., *Proc. Natl. Acad. Sci. USA* **2020**, *117*, 6316.
- [11] E. Reddington, A. Sapienza, B. Gurau, R. Viswanathan, S. Sarangapani, E. S. Smotkin, T. E. Mallouk, *Science* **1998**, *280*, 1735.
- [12] M. Prochaska, J. Jin, D. Rochefort, L. Zhuang, F. J. DiSalvo, H. D. Abruna, R. B. van Dover, *Rev. Sci. Instrum.* **2006**, *77*, 054014.
- [13] S. Kumari, J. R. C. Junqueira, W. Schuhmann, A. Ludwig, *ACS Comb. Sci.* **2020**, *22*, 844.
- [14] O. A. Krysiak, S. Schumacher, A. Savan, W. Schuhmann, A. Ludwig, C. Andronescu, *Nano Res.* **2021**, <https://doi.org/10.1007/s12274-021-3637-z>.
- [15] A. Ludwig, *npj Comput. Mater.* **2019**, *5*, 70.
- [16] R. Gutkowski, C. Khare, F. Conzuelo, Y. U. Kayran, A. Ludwig, W. Schuhmann, *Energy Environ. Sci.* **2017**, *10*, 1213.
- [17] M. Zhong, K. Tran, Y. Min, C. Wang, Z. Wang, C. T. Dinh, P. De Luna, Z. Yu, A. S. Rasouli, P. Brodersen, et al., *Nature* **2020**, *581*, 178.
- [18] J. A. G. Torres, P. C. Jennings, M. H. Hansen, J. R. Boes, T. Bligaard, *Phys. Rev. Lett.* **2019**, *122*, 156001.
- [19] A. S. Nugraha, G. Lambard, J. Na, M. S. A. Hossain, T. Asahi, W. Chaikittilisop, Y. Yamauchi, *Mater. Chem. A* **2020**, *8*, 13532.
- [20] Z. Lu, Z. W. Chen, C. V. Singh, *Mater* **2020**, *3*, 1318.
- [21] W. A. Saidi, W. Shadid, G. Veser, *J. Phys. Chem. Lett.* **2021**, *12*, 5185.
- [22] A. Ferrari, F. Körmann, *Appl. Surf. Sci.* **2020**, *533*, 147471.
- [23] A. Ferrari, B. Dutta, K. Gubav, Y. Ikeda, P. Srinivasan, B. Grabowski, F. Körmann, *J. Appl. Phys.* **2020**, *128*, 150901.
- [24] I. E. L. Stephens, A. S. Bondarenko, U. Grönberg, J. Rossmeisl, I. Chorkendorff, *Energy Environ. Sci.* **2012**, *30*, 6744.
- [25] J. Greeley, I. E. L. Stephens, A. S. Bondarenko, T. P. Johansson, H. A. Hansen, T. F. Jaramillo, J. Rossmeisl, I. Chorkendorff, J. K. Nørskov, *Nat. Chem.* **2009**, *1*, 552.
- [26] J. K. Nørskov, J. Rossmeisl, A. Logadottir, L. Lindqvist, J. R. Kitchin, T. Bligaard, H. Jonsson, *J. Phys. Chem. B* **2004**, *108*, 17886.
- [27] J. K. Pedersen, T. A. A. Batchelor, D. Yan, L. E. J. Skjegstad, J. Rossmeisl, *Curr. Opin. Electrochem.* **2021**, *26*, 100651.
- [28] D. R. Jones, M. Schonlau, W. J. Welch, *J. Global Optim.* **1998**, *13*, 455.

- [29] V. Nguyen, S. Gupta, S. Rana, C. Li, S. Venkatesh, *Regret for Expected Improvement over the Best-Observed Value and Stopping Condition*, Proceedings of the Ninth Asian Conference on Machine Learning (November, 2017) 77, 279.
- [30] F. Pedregosa, G. Varoquaux, A. Gramfort, V. Michel, B. Thirion, O. Grisel, M. Blondel, P. Prettenhofer, R. Weiss, V. Dubourg, et al., *J. Mach. Learn. Res.* **2011**, *12*, 2825.
- [31] C. Jidling, N. Wahlström, A. Wills, T. B. Schön, *Linearly constrained Gaussian processes*, 31st Conference on Neural Information Processing Systems (December, 2017).
- [32] C. M. Clausen, T. A. A. Batchelor, J. K. Pedersen, J. Rossmeisl, *Adv. Sci.* **2021**, *8*, 2003357.
- [33] S. Agnoli, G. Barcaro, A. Barolo, A. Fortunelli, M. Sambi, F. Sedona, M. Di Marino, T. Skala, G. Granozzi, *J. Phys. Chem. C* **2011**, *115*, 14264.
- [34] A. U. Nilekar, Y. Xu, J. Zhang, M. B. Vukmirovic, K. Sasaki, R. R. Adzic, M. Mavrikakis, *Top. Catal.* **2007**, *46*, 276.
- [35] J. A. Z. Zeledón, M. B. Stevens, G. T. K. K. Gunasooriya, A. Gallo, A. T. Landers, M. E. Kreider, C. Hahn, J. K. Nørskov, T. F. Jaramillo, *Nat. Commun.* **2021**, *12*, 620.
- [36] T. Ioroi, K. Yasuda, *J. Electrochem. Soc.* **2005**, *152*, A1917.
- [37] J. Tian, W. Wu, Z. Wen, Z. Tang, Y. Wu, R. Burns, B. Tischnell, Z. Liu, S. Chen, *Catalysts* **2018**, *8*, 329.

Manuscript received: June 18, 2021

Revised manuscript received: August 24, 2021

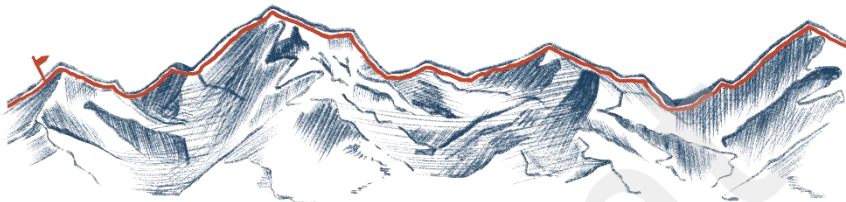
Accepted manuscript online: September 10, 2021

Version of record online: October 5, 2021



# 4

## A hike through Swiss mountains



Bayesian optimization has paved the pathway for a substantial reduction in the number of experiments required to study high entropy alloy composition spaces. However, even when using Bayesian optimization, the number of experiments needed to study all possible high entropy alloy spaces remains tremendous. To illustrate, if we are to make all possible 5 element compositions out of a selection of 20 different elements, 15 504 combinations can be made. If each requires 50 experiments, a total of 775 200 experiments is required to study all these composition spaces for a single reaction. Even with a high-throughput set-up that can perform 1 000 experiments per week, this would require multiple years.

To reduce the number of spaces that are worth to study, we conceived the idea of searching for ridges in the activity-composition space. Similar to the mountain landscape of Switzerland, the summits of the mountains can be seen as different optima in the activity-composition space. If you start at an optimum and follow the path with the gradient of least descent, you should end up at the next summit. Therefore, by knowing the location of one optimum, the next optimum can be found by travelling these ridges. This way, this method also strings the different composition spaces together. This leads to the hypothesis, that by walking along the ridges we would need less experiments to identify all optima than when studying the entire composition spaces.

In practice, detecting these ridges turned out to be easier said than done. Evaluating the gradient in all directions at each step is experimentally a very costly process. Therefore, instead of calculating the gradient at each step, Mads Plenge who at the time was a Bachelor student of Jack Pedersen and Jan Rossmeisl, investigated the nudged elastic band algorithm. Even though the nudged elastic band significantly reduced the number of evaluations, it is still an iterative process that requires many evaluations to find the ridge.

Mads work showed that the nudged elastic band algorithm can successfully find the ridges in a three-element composition space. However, the number of evaluations required to find the

ridge reaches comparable numbers as performing a grid search. Moreover, in higher dimensions, the nudged elastic band algorithm did not prove to be reliable in ridge detection. Ultimately, this work introduces a new perspective on thinking about the high entropy alloy composition space. It also calls for further improvement in the ridge detection algorithm.

## RESEARCH ARTICLE



# Following Paths of Maximum Catalytic Activity in the Composition Space of High-Entropy Alloys

Mads K. Plenge, Jack K. Pedersen, Vladislav A. Mints, Matthias Arenz, and Jan Rossmeisl\*

The search for better and cheaper electrocatalysts is vital in the global transition to renewable energy resources. High-entropy alloys (HEAs) provide a near-infinite number of different alloys with approximately continuous properties such as catalytic activity. In this work, the catalytic activity for the electrochemical oxygen reduction reaction as a function of molar composition of Ag-Ir-Pd-Pt-Ru HEA is treated as a landscape wherein it is shown that the maxima are connected through ridges. By following the ridges, it is possible to navigate between the maxima using a modified nudged elastic band (NEB) model integrated in a machine learning NEB algorithm. These results provide a new understanding of the composition space being similar to an evolutionary landscape. This provides a possible new search and design strategy for new catalysts in which the composition of known catalysts can be optimized by following ridges rather than exploring the whole alloy composition space.

## 1. Introduction

The globe faces a grand challenge with increasing energy demand and global warming accelerated by greenhouse gases. An important part of transitioning to renewable energy sources is efficient energy conversion and storage.<sup>[1-3]</sup> Converting energy from renewable energy into chemical fuels, which, e.g., is possible via water splitting, will play an important part in the transition from fossil fuels.<sup>[4]</sup> A way to extract the energy is by the use of hydrogen fuel cells, where oxygen and hydrogen recombine to form water where the oxygen reduction reaction (ORR) plays a major role.<sup>[4,5]</sup> This reaction must be catalyzed, but today's most used catalyst is platinum which is scarce and expensive,<sup>[1,5-7]</sup> and

there is theoretically room for improvement.<sup>[4]</sup> Finding a cheaper and better catalyst for ORR is therefore vital.<sup>[5,7]</sup>

In this search for better catalysts, high-entropy alloys (HEAs) have shown great promise, because they offer an unbounded number of different alloys within a continuous composition space.<sup>[8,9]</sup> Because each material will give many different adsorption sites, HEAs can serve as a discovery platform for new catalysts,<sup>[10]</sup> with several discoveries recently made using computational models for various catalyzed reactions.<sup>[10-15]</sup> The idea of thinking of the catalytic activity as a continuous function of the HEA composition to be optimized in an experimental context where the number of experiments must be kept as low as possible has developed recently.<sup>[16-19]</sup> It was found with simulations that the function of ORR catalytic activity for the Ag-Ir-Pd-Pt-Ru HEA composition space has a relatively long length scale of around 0.3 with respect to molar composition.<sup>[16]</sup> This means that the correlation between molar compositions is still expected to be significant even when they are spaced 30 atomic percent (at%) apart in composition space. This matches well experimental investigations of thin-film libraries with continuous variations in the compositions of the same five elements, where the observed length scale comes out the same as in the simulations.<sup>[20]</sup>

It is a further investigation of this composition space and its nature that is scrutinized in the current work. We hypothesize that locally optimal catalysts are connected by ridges of suboptimal compositions on the function of catalytic activity. This is analogous to a mountain landscape, where the best catalysts are the mountain tops, and the mountains are connected via ridges. In other words, it is possible that there is a common thread that connects optimal compositions and hence can lead to active catalysts in the composition space. This could be a way to limit where to look in the vast composition space of HEAs. Instead of finding the needle in the haystack, we may only need to find a thread and follow it. Searching for optimal catalysts by following ridges is analogous to mutations in a biological evolutionary fitness landscape, where small gradual mutations following the ridge will lead to an increase in fitness while going too far off the path of the ridge may lead to extinction.<sup>[21]</sup> Thus, the composition space can be treated like an evolutionary landscape where the mutations are slight changes in molar fractions of elements.

In the current work, simulations of the electrochemical ORR are used to model the landscape of the catalytic activity as a function of the composition of the quinary Ag-Ir-Pd-Pt-Ru alloy.

M. K. Plenge, J. K. Pedersen, M. Arenz, J. Rossmeisl  
Center for High Entropy Alloy Catalysis (CHEAC)  
Department of Chemistry  
University of Copenhagen  
Universitetsparken 5, 2100 Copenhagen Ø, Denmark  
E-mail: jan.rossmeisl@chem.ku.dk  
V. A. Mints, M. Arenz  
Department for Chemistry  
Biochemistry and Pharmaceutical Sciences  
University of Bern  
Freiestrasse 3, 3012 Bern, Switzerland

The ORCID identification number(s) for the author(s) of this article can be found under <https://doi.org/10.1002/aenm.202202962>.

© 2022 The Authors. Advanced Energy Materials published by Wiley-VCH GmbH. This is an open access article under the terms of the Creative Commons Attribution License, which permits use, distribution and reproduction in any medium, provided the original work is properly cited.

DOI: [10.1002/aenm.202202962](https://doi.org/10.1002/aenm.202202962)

Being composed of noble metals, this HEA is expected to show superior corrosion resistance and therefore is a candidate that would make for easier comparison with experimental tests. The HEA is, however, at best expected to be meta-stable with surface segregation and surface dissolution being inevitable for prolonged experimental durations. Prediction of the meta-stability of the alloy surfaces has not been carried out in the current study as it is out of the scope of the presented analysis since even transitory surface compositions can be associated with a catalytic activity. However, meta-stability remains an interesting path of investigation for the field of HEA catalysis. Simulation of the catalytic activity is achieved by applying a previously applied<sup>[16]</sup> kinetic model for each individual catalyst surface site, considering a face-centered cubic (fcc) (111) disordered surface of the HEA. Trained on hundreds of density functional theory (DFT) simulations, the model estimates adsorption energies of <sup>18</sup>O and <sup>16</sup>O and outputs a measure of catalytic activity, the current density, based on these. The adsorption energies of <sup>18</sup>O and <sup>16</sup>O have been simulated relative to those of Pt(111) which has been found to bind <sup>18</sup>O and <sup>16</sup>O about 0.1 and 0.2 eV too strongly compared to the optimal adsorption energy through tight collaboration between simulations and experiments.<sup>[22]</sup> In this way the adsorption energies of <sup>18</sup>O and <sup>16</sup>O emerge as the most important descriptors for ORR catalytic activity on comparable alloy surfaces and many interface effects, such as adsorbate solvation can be eliminated in this comparison (see Section S1, Supporting Information). The model has previously been shown to have satisfactory predictive power in experiments on the Ag-Ir-Pd-Pt-Ru composition space,<sup>[20]</sup> with multiple locally optimal compositions detected.<sup>[16]</sup> It is found that maxima of catalytic activity in composition space are indeed connected through ridges in this landscape and a new strategy for searching for catalysts is suggested in which already optimal catalyst in one composition space are optimized even further in another.

## 2. Results and Discussion

### 2.1. Connecting Maxima via Ridges

The concept of connecting points via ridges has been especially useful in the search for minimum energy pathways for chemical reactions where the coordinates are expressed in terms of atomic configurations. One way to obtain the minimum energy pathway is with the nudged elastic band (NEB) algorithm<sup>[23,24]</sup> and its machine learning variants.<sup>[25,26]</sup> In the current work, a revised NEB algorithm was implemented to connect two compositions via ridges on the function for catalytic activity obtained with the kinetic model described above (see Section S2, Supporting Information).

The implemented NEB algorithm works by creating an elastic band which is fastened at two end points, here two compositions. The band itself is defined by a set of points, traditionally called images, corresponding to a molar composition with springs between each image giving rise to the elasticity. The elastic band is nudged orthogonally to the gradients of the catalytic activity function to make it follow the ridges. These ridges thus correspond to the maximum activity pathways.

The activity function which the NEB operates on, and which forms the activity landscape, is modelled using a Gaussian process regressor (GPR) fitted to simulations of the catalytic ORR activity (see Section S3, Supporting Information). The compositions for these simulations were sampled on a uniform grid with a spacing of 5 at% of the Ag-Ir-Pd-Pt-Ru composition space. The GPR activity function has a 2% mean relative prediction error and a coefficient of determination ( $R^2$  value) of 0.996 compared to the results obtained with simulations (see Figure S3, Supporting Information). It has an absolute error of  $\approx 0.001$  (arb. units), which is on the same order of magnitude as the standard deviation of the kinetic model.<sup>[16]</sup> By using the GPR activity function for the NEB algorithm rapid evaluations of the activity are enabled, while at the same time maintaining the same accuracy as if simulations from the model were called in series. The continuity and differentiability possessed by the smooth GPR activity function is reasonable to assume for the real activity function that would be produced in an experimental realization as well as the currently employed kinetic model. The reason is that a smoothly varying activity functions has previously been observed for the current HEA.<sup>[20]</sup>

All pure metals were connected in each of the 10 ternary subspaces of Ag-Ir-Pd-Pt-Ru (see Figure S4, Supporting Information), demonstrating that the NEB algorithm forms a path along a ridge, given there is any, between the chosen end points. If one combines these ternary composition spaces along their edges, it becomes apparent that the ridges connect when going to a different ternary composition space. Figure 1 is a result of this idea. Here, a known active binary catalyst,<sup>[16]</sup> namely Ir<sub>45</sub>Pt<sub>55</sub>, in the data is chosen as a starting point. The third element to describe the initial ternary composition space is picked arbitrarily as Pd and it is chosen as the final point in the NEB algorithm. When the NEB algorithm has converged, it identifies the maximum point on an opposite edge from the initial edge. Then, the element which is no longer in the composition gets substituted with a random new element that was not in the previous composition, thereby changing the composition space. Figure 1 shows the seven first ternary subspaces that the algorithm went through, stitched together. The nonconnected red

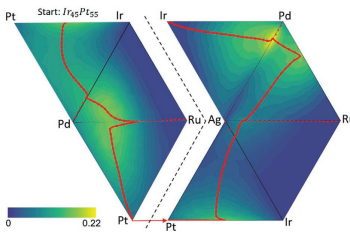


**Figure 1.** Substituting elements through ternary subspaces starting at Ir<sub>45</sub>Pt<sub>55</sub>. The red dots are images, and the solid red line is an interpolated path between the images. The contour plot shows the value of the catalytic activity function in arbitrary units from the regular 5 at% grid of simulations with the kinetic model.

dots are the images going from the maximum edge image to the final image.

The simulation successfully manages to walk along the ridges through compositions to find the global maximum  $\text{Ag}_5\text{Pd}_{45}$ . Along this path it passes through all local maxima within the ternary compositions in the data, which we have found previously.<sup>[16]</sup> From this it thus seems that all maxima are indeed connected through ridges, at least in the ternary composition spaces. It also suggests the substitution of elements at edges as a possible new search strategy for optimizing already active catalysts even further.

Since the maxima are connected by ridges in the ternary composition spaces, it was investigated whether this also holds in higher dimensions. This hypothesis was tested by connecting two pure metals through the entire quinary composition space of Ag–Ir–Pd–Pt–Ru by doing multiple climbing images, which are images accelerated directly along the gradient (see Section S2, Supporting Information). With Ag as the initial image and Ir as the final image, it is seen in Figure 2a that the path does indeed go through several maxima. It actually goes through all four noticeable maxima found previously<sup>[16]</sup> with Bayesian optimization:  $\text{Ag}_{85}\text{Ru}_{15}$ ,  $\text{Ag}_{70}\text{Pd}_{25}$ ,  $\text{Ir}_{20}\text{Pd}_{65}\text{Ru}_{25}$ , and  $\text{Ir}_{49}\text{Pt}_{51}$ .

## 2.2. Following Ridges by Sampling

The NEB algorithm requires many simulations of the catalytic activity of a given composition which is why it is run on the fitted GPR. However, were this to be used in an experimental application, the algorithm must be able to choose compositions by itself and find the same path without sampling the whole space. The machine learning (ML) NEB method attempts to

solve this challenge by sampling the most uncertain image in each iteration until the path converges (see Section S4, Supporting Information). In Figure 3, the converged ML NEB path is compared to the classic NEB path for Ag to Pd in the ternary Ag–Ir–Pd composition space. The found path clearly resembles the classic one with negligible deviation. The ML NEB used only 33 evaluations in this case. In comparison, the 5 at% ternary grid contains 231 samples. All 10 ternary subspaces connecting all metals with comparison to the classic NEB algorithm were equivalently evaluated, showing overall good agreement (see Figure S7, Supporting Information). The average number of samples for each ternary composition space was 50 and a standard deviation of 15 samples. The only way to get better results would be to draw more samples, which could lower the uncertainty. However, it would not ensure a different path found as there is limited exploration as it is constrained to the path. It should also be noted that in some of the cases with discrepancies, the ML NEB algorithm finds a seemingly more satisfactory path compared to the classic NEB algorithm (see, e.g., Ag–Ir–Ru (right column) in Figure S7, Supporting Information). The convergence of the uncertainty of the ML NEB algorithm with the number of samples varies between composition spaces, and in a very few cases the convergence criterion acts as an asymptote (see Figure S8, Supporting Information).

Figure 1 that was made with data from the classic NEB algorithm was recreated using the ML NEB algorithm, and the two show almost identical ridges (see Figure S9, Supporting Information), making this a possible experimental strategy in practice. When starting on the ridge in the ternary composition space, the ML NEB in general converged with less samples than when connecting between pure metals (see Table S1, Supporting Information).

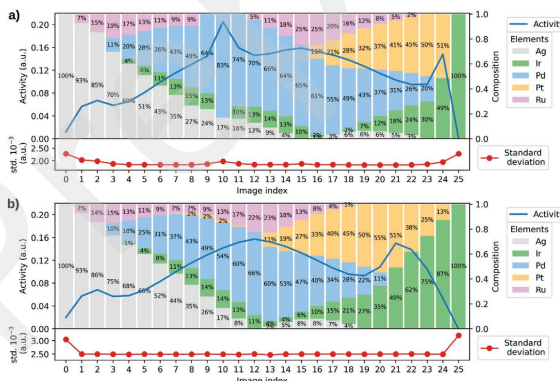


**Figure 2.** Activity height profile of the converged NEB paths between Ag and Ir for the classic NEB algorithm using the GPR model trained on a uniform 5 at% grid a), and for the ML NEB algorithm with convergence after 269 samples b). In the background the molar fractions are displayed and at the bottom is the uncertainty from the GPR prediction at each point.

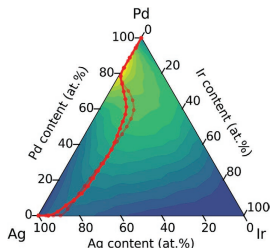


**Figure 3.** ML NEB compared to classic NEB. The converged ML NEB is shown clear while the path found from the classic NEB is faded. Same color scale for the contour plot as in Figure 1.

For the ML NEB algorithm to be more effective as an experimental strategy it should be scalable in dimensions, i.e., with more elements. From Figure 2a, it seems that the NEB algorithm is able to follow ridges between maxima in the quinary space. Moreover, by connecting Ag and Ir, several maxima, including the global maximum  $\text{Ag}_{57}\text{Pd}_{43}$ , were found. When using the ML NEB algorithm, nearly the same path through the composition space is found as for the NEB algorithm as shown in Figure 2b. However, the global maximum  $\text{Ag}_{57}\text{Pd}_{43}$  is bypassed in this case. One possible explanation for this is that the ML NEB algorithm is missing gradient information to point it toward the optimal composition  $\text{Ag}_{57}\text{Pd}_{43}$ .

In general, it seems that for an increasing dimensionality of the composition space, it becomes increasingly more difficult for the GPR, via the ML NEB, to get an accurate prediction of the whole space. The fact that the  $\text{Ag}_{57}\text{Pd}_{43}$  maximum is quite narrow in composition space, see for example Figure 3, supports this idea. To find this specific maximum, there must be samples close to it, which is the case when choosing Ag and Pd as initial and final compositions in quinary composition space as well as Ir and Pd (see Figure S10, Supporting Information). The reason is that the maximum is close to one of the end points of the ML NEB.

Traditionally for the ML NEB algorithm for atomic systems, gradient information is used in the GPR to increase the accuracy of the predicted function.<sup>[25,26]</sup> However, in the current work the surface is not an energy surface, and the gradient information cannot be directly extracted from the simulations of the catalytic activity. Gradient information in the GPR would likely provide faster and more accurate convergence of the paths. The reason for  $\text{Ag}_{57}\text{Pd}_{43}$  being difficult for the ML NEB to find could also in part be due to the shape of the ridge throughout the composition space. It seems like the ridge going toward  $\text{Ag}_{57}\text{Pd}_{43}$  from the ridge path in Figure 2a is not a continuation of the ridge but rather a blind alley, since the molar fraction of the images before and after  $\text{Ag}_{57}\text{Pd}_{43}$  (image index 9 and 11 in Figure 2a) seem to represent the same path, indicating that the found pathway turns back around at  $\text{Ag}_{57}\text{Pd}_{43}$ .

In an attempt to understand the nature of the ridges in composition space and especially in higher dimensions where it

cannot be plotted, a ridge detection algorithm was developed, which can determine if a given point is on a  $d$ -dimensional ridge directly from the trained GPR (see Section S5, Supporting Information). The ridge detection algorithm does confirm that the NEB indeed follows ridges, also in higher dimensions (see Figures S11–S14, Supporting Information). However, the ridge detection algorithm revealed potential problems with the GPR in the composition space. The reason is that ridges would be detected at unexpected locations, where in some cases this could be attributed to the way the GPR has learned the landscape of catalytic activity. This includes forming maxima of catalytic activity outside the simplex that is bounding the composition space (see Figure S15, Supporting Information). This is especially a problem for the shape of the 1D-ridges, i.e., one-dimensional curves that are maximized with respect to all directions that are orthogonal to the direction of the ridge itself, which are the ones of interest in higher dimensional composition spaces. The unphysical maxima that the GPR learns influence the shape of the 1D-ridges, making the combination of the GPR and ridge detection unsuitable to get a reliable trace of the ridge in higher dimensional composition space.

From the results using the NEB algorithm it is indeed possible to follow ridges between maxima on the activity function in composition space. The exact shape and interconnectivity of these ridges in higher dimensions is still not perfectly understood and the GPR shows some limitations because it is bounded by a hyperdimensional simplex in composition space. It is also not entirely conclusive whether all local maxima are connected via ridges in higher dimensions. The fact that the classic NEB algorithm in the quinary composition space seems able to connect most maxima, without the height profile of the activity dropping to zero or near-zero between maxima (see, e.g., Figure 2a), indicates that the maxima are indeed still connected via ridges in higher dimensional space.

To further investigate the nature of this activity landscape and the behavior of the model in general by studying an arbitrary activity function, randomly generated parameters for the kinetic model, corresponding to “artificial elements,” were chosen to model a different activity function (see Section S6, Supporting Information). Even though the activities were much smaller with the generated artificial elements, the activity landscape was still showing ridges and it was possible to navigate between the maxima using the element substitution strategy with ML NEB (see Figure S16, Supporting Information).

### 2.3. Directed Evolution to Follow Ridges

A downside of using a NEB algorithm is that the found path depends on the initial and final composition. To circumvent this and to further explore the analogy of the evolutionary landscape, a possible experimental strategy similar to directed evolution<sup>[27]</sup> (DE) is suggested (see Section S7, Supporting Information). Figure 4 shows the results of a DE simulation through ternary compositions. The DE was started at a composition,  $\text{Ir}_{50}\text{Pt}_{50}$ , with a relatively good activity to show how an already well-performing catalyst can be optimized further. The DE then progressed through several maxima by following the ridge. Interestingly the path seems to get “trapped” around

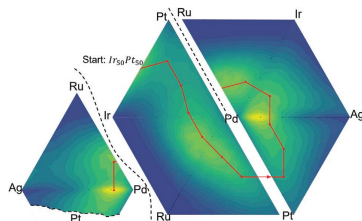


**Figure 4.** Simulation of DE starting at  $\text{Ir}_{50}\text{Pt}_{50}$  in the Ir-Pd-Pt composition space. The path taken through six ternary composition spaces plus the final selected mutation is shown. In this simulation the maximum mutation angle was set to  $90^\circ$ , i.e., the path was allowed to make turns of maximally  $90^\circ$ . This would limit the tendency to go back to an already discovered maximum. The number of mutations made in each step was 13. The activities of the mutations are simulated with the kinetic model. The path is plotted on contour plots based on the 5 at% grid data.

palladium, circling around it along the ridge. Ridges around Pd is also visible in Figure S12 (Supporting Information). The selected points do not sample the exact maxima and are unlikely to do so, because of the relatively big and constant step length of 25 at% that was found to be appropriate for these simulations. To sample the maxima between the sampled points on the path, one could for example use Bayesian optimization in one dimension along the path or just simple intuition to predict where the maximum may lie. In Figure 4, the simulations on ternary composition spaces only are shown to visualize the concept in the activity landscape, but the strategy is scalable in dimensions.

As presented in this work, the evolutionary landscape only has one fitness parameter, namely the catalytic activity. Other fitness parameters to influence the landscape could be stability or simply the cost of the materials. To get an idea of how the scarcity of the constituent elements could influence the fitness landscape, the catalytic activity is plotted against a measure of the scarcity, the inverse of the production rates of the constituent elements normalized to the production rate of Pt, for all compositions on a uniform 5 at% grid of the Ag-Ir-Pd-Pt-Ru HEA composition space. The results are shown in Figure 5. The Pareto optima<sup>[28]</sup> are the points at which improving either the catalytic activity or alleviating the element scarcity necessarily leads to worsening of the other. Because Ag is produced in markedly larger proportions than the remaining elements, most of the Pareto front, i.e., the set of Pareto optima, essentially comes out as Ag-Pd binary alloys in various proportions.

By introducing the scarcity of the constituent elements, the interesting compositions are no longer just the ones with the highest catalytic activity, but also those that are composed of abundant elements. Had the element scarcity been introduced as a fitness parameter in the DE simulation, the path taken would likely have favored the Pareto optimal compositions. Thus, favoring compositions that have high concentrations of Ag.

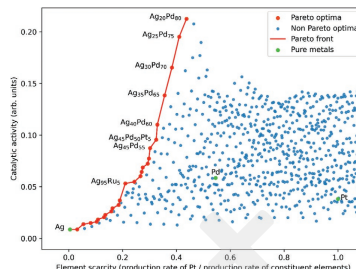


**Figure 5.** Pareto points found from a 5 at% grid of all compositions of Ag-Ir-Pd-Pt-Ru. The Pareto efficient points are shown in red, the Pareto inefficient in blue. The shown plot is an excerpt of a full range plot (see Figure S17, Supporting Information). Production rates of the elements are obtained from ref. [29].

Overall, the results show that the catalytic activity function indeed behaves comparatively to an evolutionary landscape in composition space. By making small “mutations” in the composition, the activity can be continuously altered. By moving along the ridges, the maxima can be reached. This has the implication that when experimentally looking for a new catalyst, it is a feasible strategy to start from what is known to be a well-performing catalyst and then locating the ridges around it. The element substitution in Figures 1 and 4 are both simulations of this idea. To illustrate the differences between the presented classic NEB, the ML NEM, and the DE algorithms if applied in an experimental realization, two optimums,  $\text{Ir}_{50}\text{Pt}_{50}$  and  $\text{Ag}_{50}\text{Pd}_{50}$ , were connected through two ternary composition spaces, Ir-Pd-Pt and Ag-Ir-Pd. The cost of the methods was measured as the number of samples necessary to follow the ridge from one optimum to the other, because both experimentally and computationally with our kinetic model, making and measuring a sample is the time limiting step. The NEB, ML NEB, and DE algorithms were found to need 4717, 112, and 52 samples, respectively (Figure S18 and Table S2, Supporting Information). Thus, while all three algorithms are able to find a connecting ridge between the optima, it shows that the classic NEB approach is not practical when the composition space is not already known.

In terms of finding the global maximum within a larger composition space, Bayesian optimization<sup>[16]</sup> with its nonlocal sampling may turn out to be the fastest strategy compared to the locally constrained ML NEB and DE algorithms. A combination with Bayesian optimization could be an even better strategy. Finding Bayesians optimization could help the Bayesian optimization on to which directions to look and steer it away from uninteresting areas, which likely is the greater part of the vast composition space. The fact that there are ridges within the composition space could be exploited when designing catalyst. If one can design a catalyst so that when it starts decomposing, it will do so along a ridge, it could thereby theoretically lose less catalytic activity over time.

### 3. Conclusion

By modeling the composition space using a GPR and by modifying the NEB algorithm, paths following ridges of catalytic activity in composition space were produced. Using a developed ridge detection algorithm on the GPR predicted activity function, it was shown that the maxima are indeed connected by ridges in ternary and quaternary compositions. Furthermore, an ML NEB algorithm was implemented, and for the ternary compositions the ML NEB was shown to make accurate predictions of the paths of maximum catalytic activity with relatively few calculations compared to the classic NEB algorithm. In higher dimensions the performance of the ML NEB was less robust in finding the maximum activity path that was found with the classical NEB algorithm.

A possible new strategy of following the ridges of catalytic activity to an edge in composition space followed by substitution of one element with another has been suggested and simulated on ternary compositions. This strategy resembles an evolutionary landscape in which substitution of elements correspond to mutations. By introducing more fitness parameters, the fitness landscape can be altered to find the Pareto efficient compositions in terms of the parameters. Thus, not limiting the search for just the most catalytically active compositions. The evolutionary behavior of the composition space may alter how this vast space is conceived and provides new ways of thinking when both searching for and designing new catalysts.

### Supporting Information

Supporting Information is available from the Wiley Online Library or from the author.

### Acknowledgements

This work was supported by the Danish National Research Foundation Center for High Entropy Alloy Catalysis (CHEAC) DNRF-149.

### Conflict of Interest

The authors declare no conflict of interest.

### Data Availability Statement

The data that support the findings of this study are available in the supplementary material of this article.

### Keywords

electrocatalysis, high-entropy alloys, oxygen reduction reaction, ridges

Received: August 30, 2022

Revised: October 28, 2022

Published online: November 24, 2022

- [1] S. Chu, Y. Cui, N. Liu, *Nat. Mater.* **2017**, *16*, 16.
- [2] S. P. S. Badwal, S. S. Giddey, C. Munnings, A. I. Bhatt, A. F. Hollenkamp, *Front. Chem.* **2014**, *2*, 79.
- [3] X. Zhang, X. Cheng, Q. Zhang, *J. Energy Chem.* **2016**, *25*, 967.
- [4] A. Kulkarni, S. Siahrostami, A. Patel, J. K. Norskov, *Chem. Rev.* **2018**, *118*, 2302.
- [5] X. Tian, X. F. Lu, B. Y. Xia, X. W. Lou, *Joule* **2020**, *4*, 45.
- [6] M. Shao, Q. Chang, J.-P. Dodelet, R. Chenitz, *Chem. Rev.* **2016**, *116*, 3594.
- [7] H. A. Gasteiger, N. M. Markovi  , *Science* **2009**, *324*, 48.
- [8] E. P. George, D. Raabe, R. O. Ritchie, *Nat. Rev. Mater.* **2019**, *4*, 515.
- [9] T. L  ffler, A. Ludwig, J. Rossmeisl, W. Schuhmann, *Angew. Chem., Int. Ed.* **2021**, *60*, 26894.
- [10] T. A. A. Batchelor, J. K. Pedersen, S. H. Winther, I. E. Castelli, K. W. Jacobsen, J. Rossmeisl, *Joule* **2019**, *3*, 834.
- [11] J. K. Pedersen, T. A. A. Batchelor, A. Bagger, J. Rossmeisl, *ACS Catal.* **2020**, *10*, 2169.
- [12] W. A. Saidi, W. Shadid, G. Veser, *J. Phys. Chem. Lett.* **2021**, *12*, 5185.
- [13] W. A. Saidi, *J. Phys. Chem. Lett.* **2022**, *13*, 1042.
- [14] W. A. Saidi, I. Nandi, T. Yang, *Electrochim. Sci. Adv.* **2022**, <https://doi.org/10.1002/esa.202100224>.
- [15] X. Wan, Z. Zhang, W. Yu, H. Niu, X. Wang, Y. Guo, *Patterns* **2022**, *3*, 100553.
- [16] J. K. Pedersen, C. M. Clausen, O. A. Krysiak, B. Xiao, T. A. A. Batchelor, T. L  ffler, V. A. Mints, L. Banko, M. Arenz, A. Savan, W. Schuhmann, A. Ludwig, J. Rossmeisl, *Angew. Chem., Int. Ed.* **2021**, *60*, 24144.
- [17] A. S. Nugraha, G. Lombard, J. Na, M. S. A. Hossain, T. Asahi, W. Chaikittisilp, Y. Yamauchi, *J. Mater. Chem. A* **2020**, *8*, 15352.
- [18] Y. Zhang, T. C. Peck, G. K. Reddy, D. Banerjee, H. Jia, C. A. Roberts, C. Ling, *ACS Catal.* **2022**, *12*, 10562.
- [19] M. Kim, M. Y. Ha, W.-B. Jung, J. Yoon, E. Shin, I.-d. Kim, W. B. Lee, Y. Kim, H.-t. Jung, *Adv. Mater.* **2022**, *34*, 2108900.
- [20] T. A. A. Batchelor, T. L  ffler, B. Xiao, O. A. Krysiak, V. Strotk  ter, J. K. Pedersen, C. M. Clausen, A. Savan, Y. Li, W. Schuhmann, J. Rossmeisl, A. Ludwig, *Angew. Chem., Int. Ed.* **2021**, *60*, 6932.
- [21] F. J. Poelwijk, D. J. Kiviet, D. M. Weinreich, S. J. Tans, *Nature* **2007**, *445*, 383.
- [22] I. E. L. Stephens, A. S. Bondarenko, U. Gr  nbj  rg, J. Rossmeisl, I. Chorkendorff, *Energy Environ. Sci.* **2012**, *5*, 6744.
- [23] G. Henkelman, B. P. Uberuaga, H. J  nsson, *J. Chem. Phys.* **2000**, *113*, 9901.
- [24] D. Sheppard, R. Terrell, G. Henkelman, *J. Chem. Phys.* **2008**, *128*, 134106.
- [25] J. A. Garrido Torres, P. C. Jennings, M. H. Hansen, J. R. Boes, T. Bligaard, *Phys. Rev. Lett.* **2019**, *122*, 156001.
- [26] O.-P. Koistinen, F. B. Dabgjartsd  ttir, V. Asgeirsson, A. Vehtari, H. J  nsson, *Holzforschung* **2017**, *147*, 152720.
- [27] F. H. Arnold, *Angew. Chem., Int. Ed.* **2018**, *57*, 4143.
- [28] M. P. Andersson, T. Bligaard, A. Kustov, K. E. Larsen, J. Greeley, T. Johannessen, C. H. Christensen, J. K. Norskov, *J. Catal.* **2006**, *239*, 501.
- [29] P. C. K. Vesborg, T. F. Jaramillo, *RSC Adv.* **2012**, *2*, 7933.

# 5 How did we forget grazing cows that produce milk for the famous Swiss chocolates and cheeses



Even though Bayesian optimization established itself as the primary optimization algorithm it has one major flaw, which I briefly addressed in Chapter 2. Bayesian optimization is designed to work with single experiments in an iterative process. This concept works perfectly in computational studies, however, in the workflow of practical laboratory experiments this creates a severe bottleneck. The acquisition of a single data-point is often limited by preparation and waiting times that cannot be accelerated. For instance, when carrying out a nanoparticle synthesis, the preparation of the precursor solutions can take up to a day, which on top of that will be usable for only the next few days. Moreover, the synthesis itself can take several days, depending on the method. Consequently, laboratory work is most efficiently accelerated by parallelizing experiments and working in batches. Therefore, an ideal optimization algorithm needs to be able to effectively utilize this parallelization.

Searching for alternative algorithms to substitute Bayesian optimization, I ended up in the field of stochastic evolutionary optimization algorithms, many of which draw inspiration from nature. Amidst these evolutionary optimization algorithms, one that particularly captivated my interest was particle swarm optimization. This algorithm is inspired by the collaborative behavior of a herd of animals searching for food in a vast landscape. As the animals traverse the terrain, they exchange information regarding the location of abundant food sources. Food-rich spots act as magnets and attract other animals, whereas food-poor spots may act as repellents. Over the course of the optimization, all animals are expected to end up in the area with the most food.

Now, let's apply this concept to the realm of high entropy alloy research. Here, the animal population represents a single batch of experiments. The position of each animal corresponds to a composition within the high entropy alloy composition space. The amount of food corresponds to the activity of said composition. When initiating the optimization algorithm with the animals in different corners of the composition space, each animal will need to traverse a large distance before it meets another animal. During its journey, it will collect data about the locations it visits. If these locations correspond to an increased activity, the animal will

decelerate and attract other animals. Thus, we can expect that in the first iterations of the optimization process, animals will actively explore the composition space. This exploration should provide an initial data set that can outline the mathematical landscape of the composition-activity space. As the animals gradually convene, they decelerate near local and global optima, homing in on specific regions, resulting in an exploitation phase. This phase refines the most active compositions discovered and finalizes the optimization process.

In contrast to Bayesian optimization, I envisioned that this algorithm allows direct user interference to steer the optimization process. For instance, if the animals converge too fast, the maximum distance they can travel can be reduced. Should the animals converge to a specific value, it is possible to teleport some of them to random positions forcing them to explore new areas of the composition space. Likewise, during the optimization process, it is possible to increase or reduce the size of the batch. Numerous other modifications are possible to aid the optimization process in producing a desired dataset. However, the scientist conducting this optimization needs to understand the algorithm's working principles to successfully implement these dynamic adjustments in a programming language.

We decided to explore the use of particle swarm optimization in a master project that was conducted under my supervision by Ahmad Tirmidzi. In this work, Ahmad programmed a fully informed particle swarm algorithm. However, the particle swarm optimization algorithm utilizes a set of hyperparameters that modulate the optimization process. Consequently, the initial phase of our work focused on determining the optimal hyperparameters. To achieve this, we employed four high entropy alloy composition space models, Clausen and co-workers<sup>9</sup> neural network model and the models from Chapter 3 and 6. Our objective was to identify the hyperparameters that enable the particle swarm optimization to efficiently converge to the global optimum for each model. As a result, we obtained four distinct sets of hyperparameters.

The second objective involved assessing the universal applicability of these sets of hyperparameters and compare them to Bayesian optimization. This was achieved by constructing convergence curves, which show the optimum activity found against the number of iterations or evaluations. Given the distinct batch sizes employed, Bayesian optimization using batches of one and particle swarm optimization using batches of five, the results will differ depending on the normalization. As we are focusing on batch optimization, we normalized the convergence curve to the number of iterations. In this case, particle swarm optimization outperformed the Bayesian optimization for two models. However, when normalizing the convergence curve to the number of evaluations, Bayesian optimization always outperforms particle swarm optimization. This was anticipated given that Bayesian optimization updates its prior and takes decision in iteration cycles of one evaluation, in contrast to particle swarm optimization's updates in batches of evaluations.

The primary objective of the optimization algorithms is to identify the global optimum within the composition spaces. Concurrently, the search process yields a dataset potentially suitable for machine learning application. The ongoing third part of this project involves investigating the quality of the generated dataset for machine learning. This will be achieved by constructing learning curves that demonstrate the convergence of the machine learning model to the ground

truth in relation to the iteration cycle of the optimization process. As a final result, Bayesian optimization and particle swarm optimization will be compared on two dimensions: The efficiency of locating the global optimum and the quality of the generated dataset for machine learning applications.

Based on the current findings, I recommend considering the utilization of a hybrid optimization algorithm employing both Bayesian optimization and particle swarm optimization together. Particle swarm optimization can generate batches of spread-out experiments maximizing exploration. Bayesian optimization, using the data produced by particle swarm optimization, can complement it by identifying poorly explored regions, which require additional attention. Combined, I expect these two algorithms to effectively use the concept of batches to optimize the composition and deliver a dataset well-suited for machine learning modeling.

## Manuscript Outline:

### Investigating Particle Swarm Optimization in High Entropy Alloy Research as an alternative to Bayesian Optimization

A. Tirmidzi, M. Arenz, V.A. Mints

The Manuscript is based on the master thesis titled: "Comparing Performance of Bayesian Optimization and Particle Swarm Optimization on Compositional Search of High-Entropy Alloy" by Ahmad Tirmidzi. Figures presented here are reprinted with permission from this master thesis.

This study investigates the application of particle swarm optimization for high entropy alloy composition optimization. The movement of each particle in the optimization is described by Eq. 1. In this Equation,  $v_i(t)$  is the vector describing the particle's movement, and  $x_i$  represents the current position of the particle. The coefficient  $\phi_{damp}$  governs the inertia of the particles influencing how readily they change trajectory.  $\phi_b$  and  $\bar{\phi}_b$  reflect the impact from the particle's previous best ( $b_i$ ) and worst ( $\bar{b}_i$ ) position, respectively, creating an attractive force from the best and a repelling force from the worst. Similarly,  $\phi_h$  and  $\bar{\phi}_h$  represent the learning from the best ( $h_i$ ) and worst ( $\bar{h}_i$ ) positions in the current iteration, respectively.  $\phi_g$  and  $\bar{\phi}_g$  represent the learning from the globally best ( $g_i$ ) and worst ( $\bar{g}_i$ ) positions, respectively, found throughout the optimization process. The random number  $r$  introduces variability to the optimization process altering the particle's trajectory to allow exploring additional regions. Tuning parameters  $\rho_1$  and  $\rho_2$  affect the value of  $r$ . Finally,  $v_{max}$  defines the maximum magnitude that the velocity vector can attain.

$$v_i(t) = [\phi_{damp} v_i(t-1) + \phi_b(b_i - x_i) + \phi_h(h_i - x_i) + \phi_g(g_i - x_i) - \bar{\phi}_b(\bar{b}_i - x_i) - \bar{\phi}_h(\bar{h}_i - x_i) - \bar{\phi}_g(\bar{g}_i - x_i)]r$$

$$r = \begin{cases} 1 & \text{if } r_1 > \rho_1 \\ -\mu < r < \mu & \text{if } r_1 \leq \rho_1 \end{cases} \begin{cases} r = -r & \text{if } r_1 \leq \rho_1 \times \rho_2 \\ r = r & \text{if } r_1 > \rho_1 \times \rho_2 \end{cases} \quad \text{for } r, r_1 \in [0,1] \quad (1)$$

$$v_i(t) = \begin{cases} v_i(t) & \text{if } |v_i(t)| \leq |v_{max}| \\ \frac{v_i(t)}{|v_i(t)|} |v_{max}| & \text{if } |v_i(t)| > |v_{max}| \end{cases}$$

According to this equation, this model possesses a set of hyperparameters that can be adjusted, thereby influencing the optimization algorithm's behavior. Therefore, we fine-tuned these hyperparameters utilizing Bayesian optimization to produce algorithms that most swiftly can identify the global optimum of four selected models. These selected models all cover the oxygen reduction reaction. The first model is a neural network taken from the work of Clausen et al.<sup>1</sup> The second and third models are density functional theory (DFT) models extracted from the work discussed in Chapter 3. The fourth model is the Gaussian process model from the work presented that will be presented in Chapter 6.

This search for hyperparameters produced multiple combinations yielding similar performance. Using the density-based spatial clustering of applications with noise algorithm

we identified the different combination of hyperparameters that have high performance. Subsequently, we investigated the centroids of the best performing clusters for their universality. Figure 1 shows the values for the centroids of the four best performing clusters. Particle swarm optimization best perform when relying on the positive learning, implying attraction from regions with high activity. Only in case of the DFT model for AgIrPdPtRu, particle swarm optimization prefers negative learning. The anomaly is caused by the global optimum laying in the reverse direction from the starting vector. Consequently, to effectively identify this optimum, the particle needs to reverse its direction.

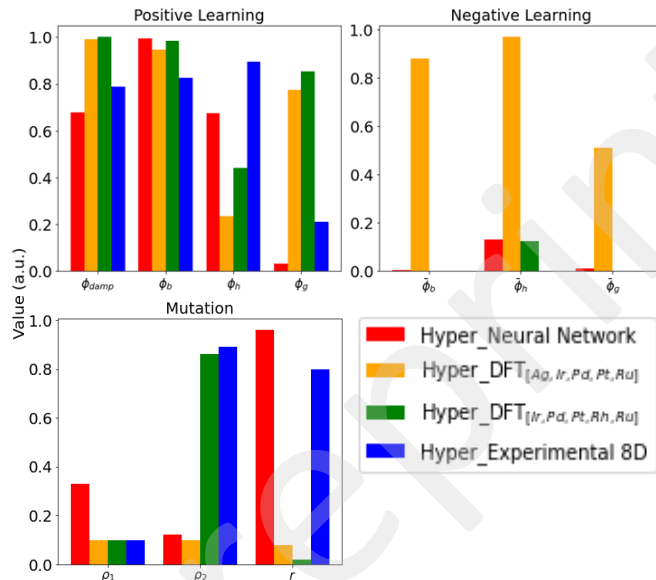


**Figure 1.** Optimal hyperparameter settings for the particle swarm optimization when applied to the four selected known oxygen reduction reaction models.

Subsequently, we investigated if the found sets of hyperparameters can be universally applied to all four models. The results are summarized in Figure 2, which shows the average best activity found per iteration cycle. This figure also compares the performance of particle swarm optimization to Bayesian optimization. In case of the DFT model for IrPdPtRhRu and the Gaussian Process, particle swarm optimization outperforms Bayesian optimization based on the number of iterations. In case of the DFT AgIrPdPtRu model, of the four hyperparameter sets only the one containing negative learning was able to identify the global optimum. However, this set of hyperparameters failed to identify the global optimum of the Gaussian process. Therefore, we conclude that particle swarm optimization does not have a universal set of hyperparameters that will always outperform Bayesian optimization. In addition, if the data is normalized by the number of evaluations, Bayesian optimization will always

outperform particle swarm optimization. The reason for this is the fact that Bayesian optimization updates its prior more frequently compared to particle swarm optimization.

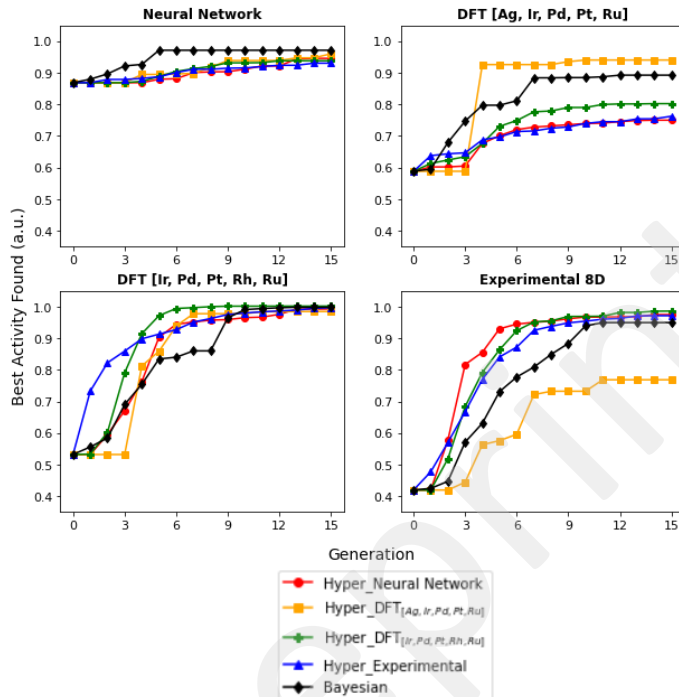


**Figure 2.** The search performance of Bayesian optimization and particle swarm optimization with different hyperparameter settings taken from Figure 1. The search performance is evaluated on four selected models, and the y-axis is normalized by the global best activity in each of the models.

The work will also compare Bayesian optimization and particle swarm optimization based on how well the obtained data sets can be used for machine learning. For this, we will construct machine learning models at each iteration using the sampled data. Subsequently, using parity plots, the machine learning models will be compared to the ground truth. Using the metrics such as the coefficient of determination or mean absolute error learning curves will be constructed.

## References

1. Clausen, C. M., Nielsen, M. L. S., Pedersen, J. K. & Rossmeisl, J. Ab Initio to Activity: Machine Learning-Assisted Optimization of High-Entropy Alloy Catalytic Activity. *High Entropy Alloys & Materials* (2022). doi:10.1007/s44210-022-00006-4

# 6 Don't get lost while traversing multi-dimensional worlds



When we established the benefits of using optimization algorithms and machine learning methods in the Center of High Entropy Alloy Catalysis, we started to receive the following question: How many elements should one study together in a single machine learning study? In other words: What complexity of a high entropy alloy composition space is feasible to study? The answers to this question I will address in this Chapter.

First, we need to define the cost to study a n-element composition space. From the work presented in Chapter 3 we know that around 50 experiments are necessary to obtain a reasonable machine learning model for a 5-element composition space. Employing *the curse of dimensionality* we can scale this number of experiments to composition spaces containing a different number of elements. According to this curse, the number of experiments required to study a space grows exponentially with the dimensions. Thus, we first estimate the number of experiments required for a 1-dimensional system, calculated as  $50^{1/4}=2.66$ . Then if want to calculate the number of experiments required to study a 6-element system, which mathematically is 5-dimensional, we scale it up to 5-dimensions resulting in  $2.66^5 = 133$ . As the complexity of the composition space grows, the number of experiments increases exponentially quickly leading to numbers that cannot be executed within a reasonable timeframe.

Now, let's consider the flip side of this mathematical problem. Once we have constructed a machine learning model for the 6-element space, we also inherited the models for the six underlying 5-element composition spaces. Investigating each of them individually would require a total of  $6 \times 50 = 300$  experiments. Therefore, by going up in dimensions we not only expand the size of the composition space, but we also increase the amount of information contained in a

single experiment. This gives rise to a trade-off rule that can be generally formulated as: the number of experiments required to study a composition space versus the information quantity in a single experiment.

In case of high entropy alloys, our current primary focus lies in 5-element composition spaces. Consequently, we defined the trade-off rule as: number of experiments required to study the complex space against the number of experiments required to study all underlying 5-element composition spaces individually. I would like to point out that this is just one of the possible definitions of the generalized rule in the previous paragraph. Therefore, in a different setting experimental setting this trade-off rule might need to be reformulated to accommodate the interests and specifics of the planned experiments.

Based on these ideas I can now propose a straightforward template for designing a high entropy alloy study. The first step is to consider the number of experiments that can feasibly be conducted within the project's time frame. Based on this, we can estimate the maximum complexity of the high entropy alloy composition space that can be explored using 'the curse of dimensionality'. If the number of experiments required to study this composition space is less than the number of experiments required to study the underlying 5-element spaces individually, then the recommendation is to study this complex space. Otherwise, it is advisable to investigate the underlying 5-element spaces separately. Of course, this template can be expanded to incorporate dynamic constraints, such as when an experiment in a 5-element composition space takes less time than an experiment in an 8-elements space. However, I hope that I could illustrate the train of thought in this process.

Sometimes it is enough to prove a concept mathematically, but in the world of chemistry, experimental validation is often preferred. Therefore, I went on to demonstrate this concept in practice by experimentally studying the AuIrOsPdPtReRhRu composition space. To demonstrate the idea that knowing the model for the composition space of AuIrOsPdPtReRhRu also grants knowledge about the underlying 5-element models, I synthesized 200 nanoparticles with varying compositions within this space and an additional 50 nanoparticles in each of the subspaces AuIrOsPdPt, IrOsPdPtRu, and IrOsPtRhRu. All these particles I evaluated for the electrochemical oxygen reduction reaction and oxygen evolution reaction, which provided me with a large data set for machine learning application. In this chapter the dataset on the oxygen reduction reaction was used to successfully demonstrate that the 8-element model can predict the activity-composition relations of the 5-element models. The oxygen evolution reaction data will be discussed in the Chapter 7.

In this work, we also conducted a qualitative comparison between the machine learning model derived from experimental data and a DFT calculated model of the AuPdPt ternary space. This comparison revealed a high degree of similarity in the center of the composition space strengthening the credibility of the approach. However, a large discrepancy is observed around the edge which can be explained by the low certainty in the machine learning model due to absence of data in these regions. For now, this DFT comparison is limited to the AuPdPt ternary space due to computational constraints, as constructing DFT models for the three selected 5-

element spaces is computationally costly. However, developing DFT models for these three 5-element spaces is not off the table making it a topic for a follow up study.

## Learning in Higher Dimensions: A Strategy for Alloy Electrocatalyst Discovery

Vladislav A. Mints<sup>1,\*</sup>, Jack K. Pedersen<sup>2,\*</sup>, Gustav K. H. Wiberg<sup>1</sup>, Jan Rossmeisl<sup>2\*</sup>, Matthias Arenz<sup>1,2\*</sup>

<sup>1</sup>Department for Chemistry, Biochemistry and Pharmaceutical Sciences, University of Bern, Freiestrasse 3, 3012, Bern, Switzerland.

<sup>2</sup>Center for High Entropy Alloy Catalysis (CHEAC), Department of Chemistry, University of Copenhagen, Universitetsparken 5, 2100 København Ø, Denmark.

\* equally contributing first authors

\* Corresponding authors: [jan.rossmeisl@chem.ku.dk](mailto:jan.rossmeisl@chem.ku.dk); [matthias.arenz@unibe.ch](mailto:matthias.arenz@unibe.ch);

### Abstract

In this work, we propose an inversion to the classical bottom-up approach to identify improved energy conversion electrocatalysts, i.e., one starts with many constituents in a single study and then, based on the obtained data, removes low-performing elements from the alloy. The efficiency of this data-driven approach arises from the fact that when studying many elements together, information is also obtained on all lesser alloys that are part of this complex alloy. Thereby, the number of elements required to study the complex alloy is less than when studying all constituent alloys individually. Furthermore, this approach allows for a new way of comparing activity models constructed from experimental data and theoretical simulations. We demonstrate this approach by studying the AuIrOsPdPtReRhRu high entropy alloy (HEA) composition space for the acidic oxygen reduction reaction (ORR). With 200 experiments we created a machine-learned activity model that spanned the AuIrOsPdPtReRhRu composition space. This model predicted the composition and activity of the optima of all 56 5-element HEA compositions that are contained in the AuIrOsPdPtReRhRu HEA composition space. In relation, the search for the optimum of a single 5-element HEA requires estimated 50 experiments. According to our activity models, the shared optimum of the most active ORR catalyst is composed of AuPdPt.

### Introduction

Design strategies for improved energy conversion electrocatalysts typically follow a bottom-up approach where one or several additional elements are added in single succession to simple model systems of the most active element creating bi-metallic or multi-metallic surfaces. Thereby, the number of alloy constituents and the complexity of the catalyst are gradually increased, and theory is used as a means to rationalize catalyst performance (1). This strategy has been successfully applied to the acidic oxygen reduction reaction which is one of the central electrocatalytic processes for energy conversion with Pt being the element with the highest catalytic performance (2–4). The research to identify improved ORR catalysts is rooted in experimental and theoretical studies of Pt single-crystal surfaces (5, 6). Well-defined bimetallic Pt-single crystals, polycrystalline Pt-alloys, and Pt-alloy nanoparticles were studied in continuation of the early work and showed promising performance (7–12). Theoretical studies on these catalysts lead to the development of the scaling relations theory, which puts a hard limit on the efficiency of metallic ORR catalysts (13, 14). The next level of complexity consists of ternary alloys, for which presently studies are gradually appearing (15). However, it has been pointed out by Cantor that in this approach to catalysis only the corners and edges of an, in principle, multidimensional composition space of catalytic materials are investigated (16). Consequently, in the last years, the topic of high entropy alloy (HEA) catalysts has gained significant attention (17–19). Composed of 5 elements and more, HEAs provide an unexplored class of astronomically many compositions. In addition, based on pioneer work, it was proposed that HEA

catalysts can overcome the limitations of state-of-the-art ORR electrocatalysts and, e.g., break the scaling relations of the ORR (20). As such, there is a probability of finding novel ORR catalysts in the multidimensional composition space. However, using the classical approach to search for the most active 5-element ORR catalyst will probably require years of research, and including more than 5 elements would require even more time.

The classical approach and its combination of experimental and computational investigations originates from the previous century when computational power was severely limited. Hence, there was a preference to simplify models to one- or two-dimensional systems which can be visualized and fitted with simple linear models. Nowadays, computational power has become much more accessible, which facilitates the use of machine learning tools in electrocatalysis (21–25). Machine learning tools assist in the construction of multi-dimensional composition-activity models which allows for studying complex HEA composition spaces (26–28). Also, machine learning has been demonstrated to assist in the characterization of HEAs and aid the search for the most active catalyst composition (29–32). This makes machine learning tools an indispensable aid in HEA research. Nevertheless, remnants of the classical mindset still dictate that HEAs need to be first studied in their least complex shape. As such most HEA research is limited to quinary alloys while only a fraction is exploring more complex HEAs.

Several studies have demonstrated that the most active HEA composition is not necessarily found at the near-equimolar composition (33, 34). Therefore, in pursuit of the most active catalyst, it is crucial to study entire HEA composition spaces. Following our previous study, the number of experiments that are required to study a 5-element HEA composition space is around 50 experiments (28). According to the “curse of dimensionality”, this number grows exponentially when more elements are included in the space (Fig. 1B, SI. II). However, we argue that by going to a 6-element HEA composition space six 5-element HEA composition spaces are automatically being included in the study. Thereby, the number of experiments required to study the combined 6-element HEA composition space is less than when studying all six 5-element HEA composition spaces separately. In addition, the latter do not contain any information about 6-element HEAs. This makes it more favorable to study more elements together than limiting studies to fewer components in the HEA.

In this work, we studied this hypothesis by constructing a data-driven model of the 8-element AuIrOsPdPtReRhRu HEA composition space for the acidic ORR. This model not only contains the role of each of the eight elements for the catalytic reaction, it is also possible to approximate the optima of 56 5-element HEA composition spaces and estimate their activity. This procured a map that categorizes the different HEA compositions into three classes: low activity, medium activity, and high activity composition spaces. Representative for each of the classes, we investigated a single 5-element HEA composition space with 50 experiments. The comparison with the 8-element HEA model showed that the 8-element HEA model learned a very similar composition-activity landscape as compared to the individual 5-element HEA composition spaces. Keeping in mind, that the 8-element HEA model contains also the information for 7-element and 6-element HEAs, our results demonstrate that by studying more elements together, substantially fewer experiments are required to gain knowledge on all underlying catalyst compositions. Furthermore, data-driven models can be compared to models derived from computational simulations offering a unique way of testing theoretical predictions.

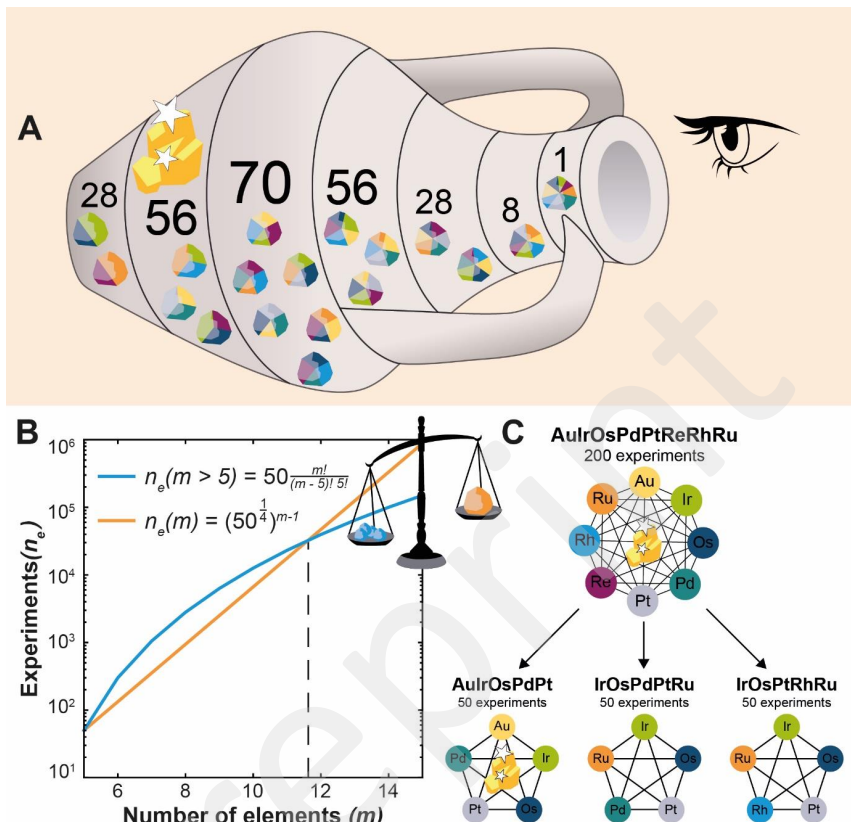


**Fig. 1. Depiction of the benefits of multi-dimensional modeling.** (A) An artistic representation of the concept of multi-dimensional learning applied to this study. The single investigation of the 8-element space produced knowledge on all possible lower lying  $n$ -element spaces. This allowed to directly identify the most active alloy catalyst composition across the entire space, which turns out to be part of a three-element subspace. (B) Modeled information density in disordered alloys. (red) The number of experiments required to achieve the same sample density as with 50 experiments in the 5-element space. (blue) The number of experiments required to study all possible 5-element combinations that are part of a more complex alloy space. (C) Summary of the alloy compositions that were investigated.

## Results and Discussion

The workflow we employed to study the different HEA compositions, is outlined in Fig. 2A. The ORR electrocatalysts were prepared adopting a solvothermal synthesis route that previously was shown to produce HEA nanocatalysts (35). In this synthesis, chloride-based metal precursor salts were dissolved in ethanol and heated up to 20 bar for 30 minutes in a microwave reactor. This produced nanoparticles with a size larger than 100 nm. Therefore, they are not expected to show particle-size effects during catalytic measurements (36). The precursor mixtures were selected using the Sobol sequence generator to create a grid that can be dynamically extended (37). In the end, 200 different

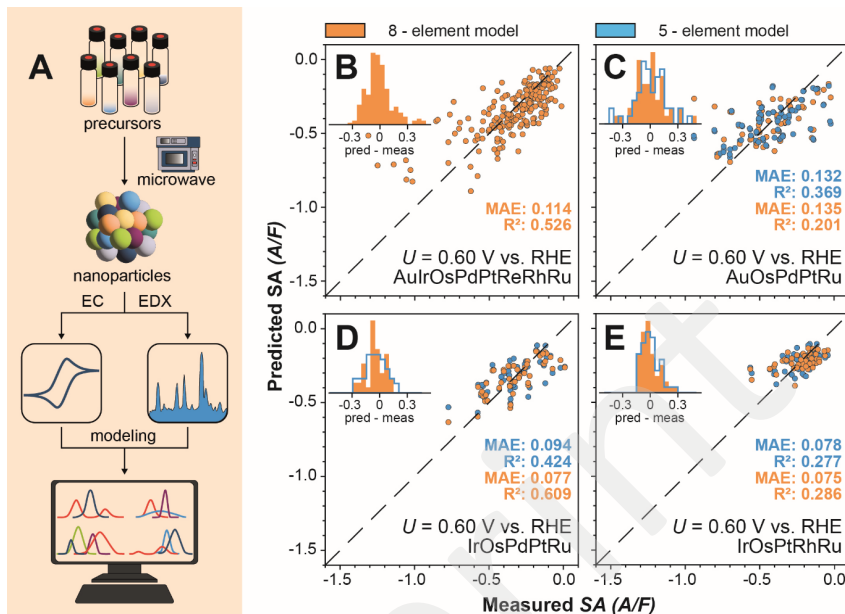


**Fig. 2. Workflow and predictive performance of models.** (A) The workflow for data collection. Starting with the microwave synthesis the obtained nanoparticles were characterized with EDX and evaluated for the electrocatalytic ORR performance. The acquired data was used to train gaussian process models. (B to E) Leave-one-out parity plots showing the measured ORR current density plotted against the prediction of a Gaussian process regressor trained on all samples except the sample being predicted for the AuIrOsPdPtReRhRu 8-element model (B), as well as the AuOsPdPtRu (C), IrOsPdPtRu (D), and IrOsPtRhRu (E) 5-element models. For the 5-element alloys a constant scaling factor was multiplied on the predicted values (Fig. S5 and S6). The measured current density is extracted from the polarization curves at a potential of 0.60 V vs. RHE and divided by the mean capacitance in the potential region from 0.30 to 0.50 V vs. RHE. A/F: amperes per farad. MAE: mean absolute error in A/F.

nanoparticle compositions in the AuIrOsPdPtReRhRu space were synthesized and 50 different compositions in the AuOsPdPtRu, IrOsPdPtRu, IrOsPtRhRu spaces each.

The compositions of the as-synthesized nanoparticles were evaluated with energy dispersive x-ray spectroscopy (EDX). These compositions formed the input for the machine-learned Gaussian processes. Upon inspecting the compositions, we observed that Re had an average concentration of less than 3 atomic percent (at.%) in contrast to the expected 12 at.%. (Fig. S10). Therefore, Re is mostly absent in the HEA particles and no conclusions on its role could be made later on. Using the Pearson correlation coefficients (Fig. S11) it is demonstrated that the elements do not have any strong correlation with each other. Thus, all composition spaces are sampled randomly.

We evaluated the ORR activity of the nanoparticles using a multi-electrode setup (Fig. S1) in a “three-electrode configuration”. The multi-electrode allowed the simultaneous study of six catalytic films.

The measurements started with a cyclic voltammogram (CV) between 0 to 0.6 V vs. reversible hydrogen electrode (RHE). From these measurements, the capacitance was extracted in the potential window of 0.3 to 0.5 V vs. RHE. This capacitance was used to normalize the reaction currents to correct for possible loading and surface area differences. As the specific capacitance for these multi-elemental nanoparticles is unknown, we approximated that all particles have the same specific capacitance. After the CV, the particles were oxidized at 1 V vs. RHE for 20 minutes, while the electrolyte was being saturated with O<sub>2</sub>. Following, the potential was stepped down to 0.6 V vs. RHE with steps of 10 mV each lasting for 20 seconds.

With the obtained experimental data, we constructed gaussian process models for the ORR activity-composition relationship in each of the four composition spaces. The gaussian process models correlated the EDX compositions of the particles with the specific activity at 0.6 V vs. RHE measured at quasi steady-state conditions. The specific ORR activity is thereby defined as the catalytic current divided by the capacitance. The gaussian processes were fitted with a radial basis function kernel with optimized length scales of 0.22, 0.25, 0.28, and 0.13 as well as a white noise kernel with noise values of 0.41, 0.47, 0.45, and 0.40 for AuIrOsPdPtReRhRu, AuOsPdPtRu, IrOsPdPtRu, and IrOsPtRhRu respectively. These length scales and noise levels indicate that the composition-activity relationships are explained by smooth mathematical functions with relatively strong correlations between the activity of compositions at these distances between them. These length scales are comparable to the one observed in our previous study (28). The performance of the gaussian process models was tested with the leave one out cross validation (LOOCV) (Fig 2B-E). The 8-element model predicts the activities with a mean absolute error (MAE) of 0.11 A/F. In a similar way, the mean absolute error can be used to evaluate the prediction of 5-element spaces by the 8-element model. The 8-element model predicts the AuOsPdPtRu space with a MAE of 0.14 A/F, whereas the LOOCV score of the model itself is 0.13 A/F. Thereby a multiplicative bias correction has been applied to the 8-element model prediction. The IrOsPdPtRu space was predicted with a MAE of 0.08 A/F, which is smaller than the LOOCV score of 0.09 A/F. Likewise, the IrOsPtRhRu space is predicted by the 8-element model with a MAE of 0.075 A/F which is similar to the LOOCV score of 0.078 A/F. As the bias correction is multiplicative, the projections of the 5-element spaces maintain their landscapes. In other words, the absolute activity values change but the correlations that influence the predictions as well as the positions of the optima are not altered. Thus, we conclude that the 8-element model learned a very similar landscape for the 5-element spaces as their corresponding 5-element models themselves.

Using the 8-element model, we mapped out all possible optima of the 56 5-element HEA composition spaces (Fig. 3A). These can be classified based on their maximum activity into three classes. The first class has optima with an ORR activity below 0.6 A/F, making them ill-suited for catalytic applications. The second class has optima with activities between 0.6 and 0.8 A/F. Distinctively, these optima contain a combination of Pt with Pd or Au. The third class, composed of optima with the highest ORR activity, is most interesting for catalytic application. Their optima are composed of a combination of Pt, Pd, and Au.

We investigated three 5-element models each representing one of the three separate activity classes. Starting with the low activity class, the IrOsPtRhRu model shows the existence of 2 distinct activity optima at Os<sub>13</sub>Pt<sub>33</sub>Rh<sub>49</sub>Ru<sub>5</sub> and Ir<sub>22</sub>Os<sub>15</sub>Pt<sub>42</sub>Ru<sub>21</sub>. On the other hand, the 8-element model predicts only a single optimum. As the ORR activity of the compositions in this space is low, the fluctuations in the 5-element model are easily overshadowed by major contributions in the 8-element model. Hence, the 8-element model is unable to pinpoint the exact location of both optima but points to the correct region of interest. The IrOsPdPtRu model, which represents the middle activity class, contains an optimum at Os<sub>3</sub>Pd<sub>38</sub>Pt<sub>45</sub>Ru<sub>14</sub>. The 8-element model predicts a similar optimum at Os<sub>17</sub>Pd<sub>33</sub>Pt<sub>41</sub>Ru<sub>9</sub>,

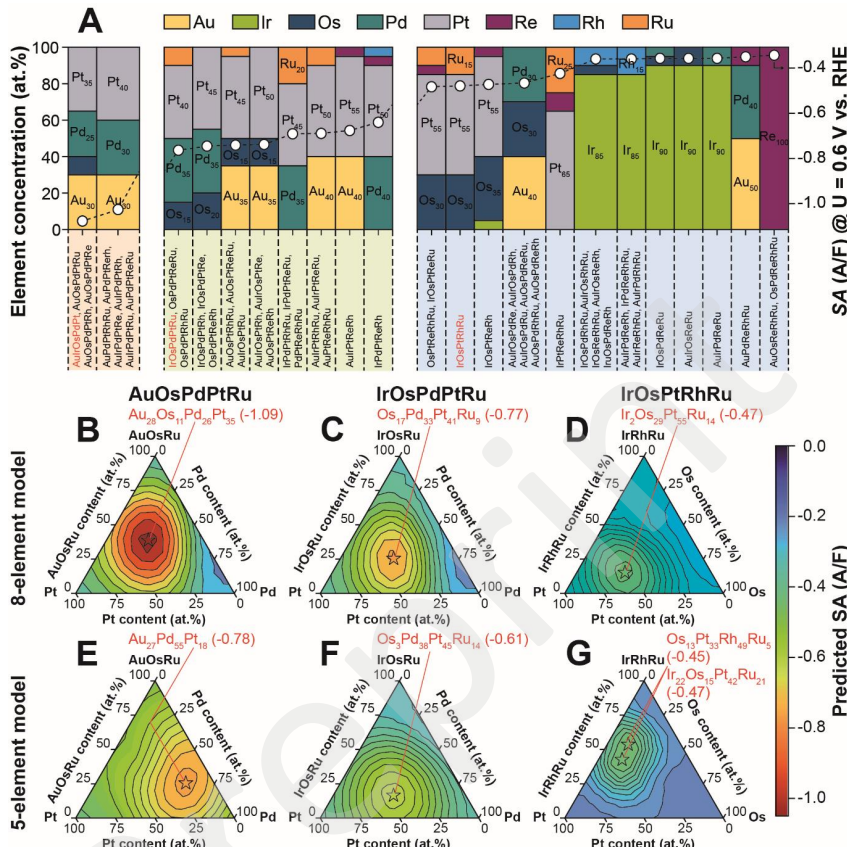


**Fig. 3. Optima in composition spaces.** (A) Optimal compositions for ORR in all of the 56 five-element composition spaces contained in the 8-element composition space as predicted by the 8-element model in a 5 at.% grid scan of the composition space. The three investigated 5-element HEAs are highlighted in red. (B to G) Most active compositions of 5-element HEAs shown as pseudo-ternary plots with the molar concentrations summed for three of the elements. Predictions by the 8-element model (B to D), and the individual 5-element models (E to F) for AuOsPdPtRu (B and E), IrOsPdPtRu (C and F), and IrOsPtRhRu (D and G). The optimal predicted compositions in each composition are annotated in red.

which has a Euclidian distance of 16 at.%. Finally, the AuOsPdPtRu model representing the high active class predicts the optimum at  $\text{Au}_{27}\text{Pd}_{55}\text{Pt}_{18}$ , whereas the global optimum of the 8-element model is  $\text{Au}_{28}\text{Os}_{11}\text{Pd}_{26}\text{Pt}_{35}$ . Further analysis, which is discussed below, shows that the Os content has no distinct correlation to the ORR activity in these HEA catalysts. This suggests that the Os in the global optimum of the 8-element model is an artifact.

Using optimization algorithms on the different spaces we can evaluate the approximate number of experiments required to optimize these HEA composition spaces, see Fig. 4. On average, 16

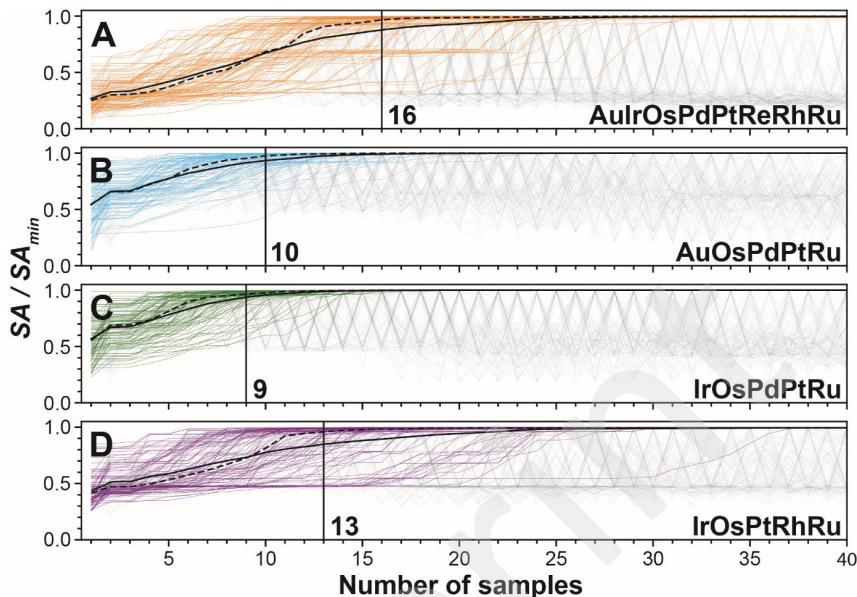


**Fig. 4. Number of experiments needed to obtain the optimal composition.** (A to D) Bayesian optimizations of the number of compositions needed to obtain the optimal composition in the 8-element AuIrOsPdPtReRhRu composition space (A), as well as the 5-element AuOsPdPtRu (B), IrOsPdPtRu (C), and IrOsPtRhRu (D) composition spaces. The optimization is performed on the GPR models of each composition space. Each of the 100 faint, grey lines represents an individual Bayesian optimization initialized with two compositions chosen at random from the composition space. The solid (dashed), black lines show the expectation (median) value of the highest absolute current density found after a given number of samples. The number of samples needed for the median to reach 95% of the value of the current density of the global optimum (i.e. the number of samples where 50% of the optimizations are sufficiently close to the global optimum) are annotated to estimate the number of experiments needed to find the global optimum.

experiments are required to find the global optimum of the 8-element model. For the 5-element models, it took 10 experiments for the AuOsPdPtRu, 9 experiments for the IrOsPdPtRu, and 13 experiments for the IrOsPtRhRu model. Thus, our optimization experiments indicate that the number of experiments required to optimize a model does not scale exponentially with increasing the complexity of the HEA composition space. The latter would be the case for grid search studies according to the “curse of dimensionality”. The reason for this milder scaling is that the optimization algorithms depend mostly on the complexity of the mathematical landscape. In contrast to e.g. drug discovery where large data sets are essential to train a model (38–40), our studies of electrocatalysts require only a limited number of experiments as the composition-activity relationships exhibit smooth landscapes. Thus, we propose that if elements have a minor contribution on the reaction, adding them to an optimization study will marginally increase the experimental demand. Therefore, optimizing HEA

composition spaces with as many elements as possible becomes even more beneficial, when in search of the most active catalyst.

These highly dimensional models can be used to analyze the contributions of the individual elements to the catalytic activity. Using the 8-element model, we evaluated the correlations of the elements to the ORR activity using SHapely Additive explanations (SHAP) (Fig. 5C) (41). The SHAP values show that the element that has the largest positive influence on the ORR is platinum. This result is in agreement with the established conclusion that Pt is the most active element for the ORR (42–45). The next element that according to the SHAP analysis has a strong positive impact on the ORR is Pd. Pd, similar to Pt, lies close to optimum in established ORR volcano plots and is being investigated as a substitute for Pt (6, 46–48). The final element that improves the ORR reaction according to our analysis is Au. While Au itself is not very active for the acidic ORR (49, 50), its alloys with Pt (51–53) and Pd (54, 55) have been reported previously to improve the ORR activity. Together, these three elements are responsible for the optimum of this 8-element HEA composition space. On the other hand, the SHAP analysis suggests that under the chosen experimental conditions Ir, Ru and Rh are the worst elements to promote the ORR. However, this does not concern possible stabilizing effects which were not tested here. Finally, the analysis of Os shows only a weak correlation to the ORR. Therefore, its contributions to the ORR activity have a larger error margin, which explains its artificial presence in the 8-element model optimum, see above.

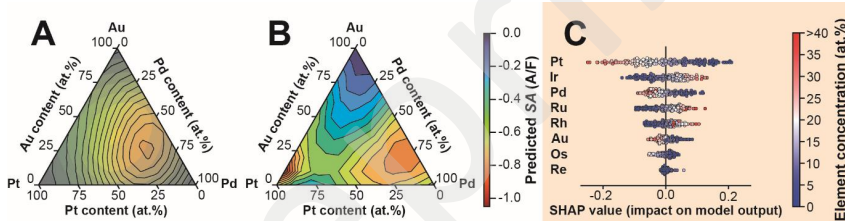


**Fig. 5. Highest activity found in the AuPdPt ternary subspace.** (A and B) ORR catalytic activities in the Au-Pd-Pt composition space as predicted by the 5-element AuOsPdPtRu model (A), and with DFT simulations (B). The coloring of the DFT prediction has been normalized such that the optimum at  $\text{Au}_{26}\text{Pd}_{57}\text{Pt}_{17}$  in A is given the same color in B. (C) The influence of the individual element concentrations on the catalytic activity of each experiment in the 8-element model obtained with a SHAP analysis.

Last but not least, the data-driven models derived from HEA studies allow a unique comparison to computational studies. Typically, a close resemblance between the surfaces studied in computational simulations and experimental studies is only achieved with well-defined single-crystal surfaces and individual activities can be compared. By contrast, comparisons between data-driven models and computational models reveal activity trends and bring a new quality to testing the predictive power of computational simulations. In our specific case, the 8-element model and the AuOsPdPtRu model both agree that the most active subspace is composed of PtPdAu. We visualized the activity of the PtPdAu space in a ternary plot (Fig. 5A). We then performed DFT calculations of this composition space and constructed an equivalent “theory-based” activity model for the ternary PtPdAu composition space (Fig. 5B). This provides a visual comparison between “theory-based” and data-driven activity modeling. It is seen that the data-driven model exhibits an optimum at  $\text{Au}_{26}\text{Pd}_{57}\text{Pt}_{17}$ , with a soft gradient towards the edges. The DFT model, on the other hand, shows a local optimum at  $\text{Au}_{27}\text{Pd}_{72}\text{Pt}_7$ , which is remarkably close to the experimentally predicted  $\text{Au}_{26}\text{Pd}_{57}\text{Pt}_{17}$  optimum. However, the DFT

model also calculates a global optimum at  $\text{Au}_7\text{Pt}_{93}$  with even high ORR activity and a strong minimum at pure Au. Both this optimum and minimum are located near the mono-metallic corners of the composition space. As the data-driven model was built to span a HEA composition space it simply lacks data in these regions, which is reflected in an increased prediction uncertainty. This leads to the observed discrepancy and supports the power of combining computational and experimental studies.

## Conclusion

With our presented work, we propose an inversion of the classical bottom-up approach to studying electrocatalysts. Instead of gradually increasing the complexity of an electrocatalyst, we argue that catalytic information is obtained more efficiently when starting from complex HEA composition spaces. As a complex HEA composition space contains information on all constituent catalysts with fewer components, its optimum will correspond to the global optimum across all its sub-spaces. In addition, the data can be used to produce a map of the optima of its different subspaces and provides argumentation on which element combinations can be ignored in later studies and which are worth investigating further. Furthermore, the data-driven activity models can be compared “theory-based” activity models both testing the predictability of computational simulations with a new quality as well as offering to accelerate catalyst discovery significantly.

We demonstrated this approach of a HEA discovery platform by studying the 8-elemental  $\text{Au}_{17}\text{Os}_{12}\text{Pd}_{12}\text{Pt}_{12}\text{Re}_{12}\text{Rh}_{12}\text{Ru}_{12}$  composition space using microwave-based nanoparticle synthesis and multi-electrode electrochemical activity experiments. The  $\text{Au}_{17}\text{Os}_{12}\text{Pd}_{12}\text{Pt}_{12}\text{Re}_{12}\text{Rh}_{12}\text{Ru}_{12}$  model mapped out effectively the optima of HEA spaces with fewer elements and provided an analysis of the contributions of the individual elements to the catalytic activity. As most contributing elements Pt, Pd and Au are identified. The highest activity is obtained for a combination of all three elements and the comparison of the data-driven model and the DFT model point towards highly active ternary  $\text{Au}_x\text{Pd}_y\text{Pt}_z$  compositions. However, also limitations of the regression models constructing activity maps are highlighted. Extrapolations in data-driven models beyond experimentally sampled compositions are to be avoided. Computational simulations can therefore accelerate the catalyst discovery substantially, but also automated synthesis robots coupled to the demonstrated accelerated electrocatalytic testing will allow experimental sampling of larger areas of interest.

## Acknowledgments

The authors acknowledge support from the Danish National Research Foundation Center for High Entropy Alloy Catalysis (DNRF 149) and Anna Iarchuk for the graphic design.

## References

1. Z. W. Seh, J. Kibsgaard, C. F. Dickens, I. Chorkendorff, J. K. Nørskov, T. F. Jaramillo, Combining theory and experiment in electrocatalysis: Insights into materials design. *Science* (1979). **355** (2017), doi:10.1126/science.aad4998.
2. S. Ott, A. Orfanidi, H. Schmies, B. Anke, H. N. Nong, J. Hübner, U. Gernert, M. Gliech, M. Lerch, P. Strasser, Ionomer distribution control in porous carbon-supported catalyst layers for high-power and low Pt-loaded proton exchange membrane fuel cells. *Nat Mater.* **19**, 77–85 (2020).
3. P. P. Lopes, D. Li, H. Lv, C. Wang, D. Tripkovic, Y. Zhu, R. Schimmenti, H. Daimon, Y. Kang, J. Snyder, N. Becknell, K. L. More, D. Strmcnik, N. M. Markovic, M. Mavrikakis, V. R. Stamenkovic, Eliminating dissolution of platinum-based electrocatalysts at the atomic scale. *Nat Mater.* **19**, 1207–1214 (2020).
4. H. A. Gasteiger, S. S. Kocha, B. Sompalli, F. T. Wagner, Activity benchmarks and requirements for Pt, Pt-alloy, and non-Pt oxygen reduction catalysts for PEMFCs. *Appl Catal B.* **56**, 9–35 (2005).
5. N. Markovic, Surface science studies of model fuel cell electrocatalysts. *Surf Sci Rep.* **45**, 117–229 (2002).
6. J. K. Nørskov, J. Rossmeisl, A. Logadottir, L. Lindqvist, J. R. Kitchin, T. Bligaard, H. Jónsson, Origin of the overpotential for oxygen reduction at a fuel-cell cathode. *Journal of Physical Chemistry B.* **108**, 17886–17892 (2004).
7. R. Chattot, O. le Bacq, V. Beermann, S. Kühl, J. Herranz, S. Henning, L. Kühn, T. Asset, L. Guétaz, G. Renou, J. Drnec, P. Bordet, A. Pasturel, A. Eychmüller, T. J. Schmidt, P. Strasser, L. Dubau, F. Maillard, Surface distortion as a unifying concept and descriptor in oxygen reduction reaction electrocatalysis. *Nat Mater.* **17**, 827–833 (2018).
8. D. Göhl, A. Garg, P. Paciok, K. J. J. Mayrhofer, M. Heggen, Y. Shao-Horn, R. E. Dunin-Borkowski, Y. Román-Leshkov, M. Ledendecker, Engineering stable electrocatalysts by synergistic stabilization between carbide cores and Pt shells. *Nat Mater.* **19** (2020), pp. 287–291.
9. C. Chen, Y. Kang, Z. Huo, Z. Zhu, W. Huang, H. L. Xin, J. D. Snyder, D. Li, J. A. Herron, M. Mavrikakis, M. Chi, K. L. More, Y. Li, N. M. Markovic, G. A. Somorjai, P. Yang, V. R. Stamenkovic, Highly Crystalline Multimetallic Nanoframes with Three-Dimensional Electrocatalytic Surfaces. *Science* (1979). **343**, 1339–1343 (2014).

10. V. R. Stamenkovic, B. Fowler, B. S. Mun, G. Wang, P. N. Ross, C. A. Lucas, N. M. Marković, Improved Oxygen Reduction Activity on Pt<sub>3</sub>Ni(111) via Increased Surface Site Availability. *Science* (1979). **315**, 493–497 (2007).
11. G. W. Sievers, A. W. Jensen, J. Quinson, A. Zana, F. Bizzotto, M. Oezaslan, A. Dworzak, J. J. K. Kirkensgaard, T. E. L. Smitshuyzen, S. Kadkhodazadeh, M. Juelskolt, K. M. Ø. Jensen, K. Anklam, H. Wan, J. Schäfer, K. Čépe, M. Escudero-Escribano, J. Rossmeisl, A. Quade, V. Brüser, M. Arenz, Self-supported Pt–CoO networks combining high specific activity with high surface area for oxygen reduction. *Nat Mater.* **20**, 208–213 (2021).
12. J. Greeley, I. E. L. Stephens, A. S. Bondarenko, T. P. Johansson, H. A. Hansen, T. F. Jaramillo, J. Rossmeisl, I. Chorkendorff, J. K. Nørskov, Alloys of platinum and early transition metals as oxygen reduction electrocatalysts. *Nat Chem.* **1**, 552–556 (2009).
13. A. Kulkarni, S. Siahrostami, A. Patel, J. K. Nørskov, Understanding Catalytic Activity Trends in the Oxygen Reduction Reaction. *Chem Rev.* **118** (2018), pp. 2302–2312.
14. W. Zhou, H. Su, W. Cheng, Y. Li, J. Jiang, M. Liu, F. Yu, W. Wang, S. Wei, Q. Liu, Regulating the scaling relationship for high catalytic kinetics and selectivity of the oxygen reduction reaction. *Nat Commun.* **13** (2022), doi:10.1038/s41467-022-34169-w.
15. J. Kim, Y. Hong, K. Lee, J. Y. Kim, Highly Stable Pt-Based Ternary Systems for Oxygen Reduction Reaction in Acidic Electrolytes. *Adv Energy Mater.* **10** (2020), , doi:10.1002/aenm.202002049.
16. B. Cantor, Multicomponent and high entropy alloys. *Entropy*. **16**, 4749–4768 (2014).
17. Y. Xin, S. Li, Y. Qian, W. Zhu, H. Yuan, P. Jiang, R. Guo, L. Wang, High-Entropy Alloys as a Platform for Catalysis: Progress, Challenges, and Opportunities. *ACS Catal.* **10**, 11280–11306 (2020).
18. Y. Ma, Y. Ma, Q. Wang, S. Schweidler, M. Botros, T. Fu, H. Hahn, T. Brezesinski, B. Breitung, High-entropy energy materials: Challenges and new opportunities. *Energy Environ Sci.* **14** (2021), pp. 2883–2905.
19. Y. Yao, Z. Huang, P. Xie, S. D. Lacey, R. J. Jacob, H. Xie, F. Chen, A. Nie, T. Pu, M. Rehwoldt, D. Yu, M. R. Zachariah, C. Wang, R. Shahbazian-Yassar, J. Li, L. Hu, Carbothermal shock synthesis of high-entropy-alloy nanoparticles. *Science* (1979). **359**, 1489–1494 (2018).
20. T. A. A. Batchelor, J. K. Pedersen, S. H. Winther, I. E. Castelli, K. W. Jacobsen, J. Rossmeisl, High-Entropy Alloys as a Discovery Platform for Electrocatalysis. *Joule*. **3**, 834–845 (2019).
21. A. Mistry, A. A. Franco, S. J. Cooper, S. A. Roberts, V. Viswanathan, How Machine Learning Will Revolutionize Electrochemical Sciences. *ACS Energy Lett.* **6**, 1422–1431 (2021).
22. Z. Yao, Y. Lum, A. Johnston, L. M. Mejia-Mendoza, X. Zhou, Y. Wen, A. Aspuru-Guzik, E. H. Sargent, Z. W. Seh, Machine learning for a sustainable energy future. *Nat Rev Mater* (2022), doi:10.1038/s41578-022-00490-5.
23. F. Dinic, K. Singh, T. Dong, M. Rezagazadeh, Z. Wang, A. Khosrozadeh, T. Yuan, O. Voznyy, Applied Machine Learning for Developing Next-Generation Functional Materials. *Adv Funct Mater.* **31** (2021), doi:10.1002/adfm.202104195.

24. H. Mai, T. C. Le, D. Chen, D. A. Winkler, R. A. Caruso, Machine Learning for Electrocatalyst and Photocatalyst Design and Discovery. *Chem Rev.* **122** (2022), pp. 13478–13515.
25. R. Ding, Y. Chen, P. Chen, R. Wang, J. Wang, Y. Ding, W. Yin, Y. Liu, J. Li, J. Liu, Machine Learning-Guided Discovery of Underlying Decisive Factors and New Mechanisms for the Design of Nonprecious Metal Electrocatalysts. *ACS Catal.* **11**, 9798–9808 (2021).
26. C. M. Clausen, M. L. S. Nielsen, J. K. Pedersen, J. Rossmeisl, Ab Initio to Activity: Machine Learning-Assisted Optimization of High-Entropy Alloy Catalytic Activity. *High Entropy Alloys & Materials* (2022), doi:10.1007/s44210-022-00006-4.
27. V. A. Mints, J. K. Pedersen, A. Bagger, J. Quinson, A. S. Anker, K. M. Ø. Jensen, J. Rossmeisl, M. Arenz, Exploring the Composition Space of High-Entropy Alloy Nanoparticles for the Electrocatalytic H<sub>2</sub>/CO Oxidation with Bayesian Optimization. *ACS Catal.* **12**, 11263–11271 (2022).
28. J. K. Pedersen, C. M. Clausen, O. A. Krysiak, B. Xiao, T. A. A. Batchelor, T. Löfller, V. A. Mints, L. Banko, M. Arenz, A. Savan, W. Schuhmann, A. Ludwig, J. Rossmeisl, Bayesian Optimization of High-Entropy Alloy Compositions for Electrocatalytic Oxygen Reduction\*\*. *Angewandte Chemie - International Edition*. **60**, 24144–24152 (2021).
29. Z. Rao, P.-Y. Tung, R. Xie, Y. Wei, H. Zhang, A. Ferrari, T. P. C. Klaver, F. Körmann, P. T. Sukumar, A. Kwiatkowski da Silva, Y. Chen, Z. Li, D. Ponge, J. Neugebauer, O. Gutfleisch, S. Bauer, D. Raabe, Machine learning–enabled high-entropy alloy discovery. *Science (1979)*. **378**, 78–85 (2022).
30. Y. Yao, Q. Dong, A. Brozena, J. Luo, J. Miao, M. Chi, C. Wang, I. G. Kevrekidis, Z. J. Ren, J. Greeley, G. Wang, A. Anapolsky, L. Hu, High-entre opy nanoparticles: Synthesis-structure-property relationships and data-driven discovery. *Scienc (1979)*. **376** (2022), doi:10.1126/science.abn3103.
31. M. K. Plenge, J. K. Pedersen, V. A. Mints, M. Arenz, J. Rossmeisl, Following Paths of Maximum Catalytic Activity in the Composition Space of High-Entropy Alloys. *Adv Energy Mater* (2022), doi:10.1002/aenm.202202962.
32. C. Chen, L. Ma, Y. Zhang, P. K. Liaw, J. Ren, Accelerating the design of high-entropy alloys with high hardness by machine learning based on particle swarm optimization. *Intermetallics (Barking)*. **154** (2023), doi:10.1016/j.intermet.2022.107819.
33. L. Banko, O. A. Krysiak, J. K. Pedersen, B. Xiao, A. Savan, T. Löfller, S. Baha, J. Rossmeisl, W. Schuhmann, A. Ludwig, Unravelling Composition–Activity–Stability Trends in High Entropy Alloy Electrocatalysts by Using a Data-Guided Combinatorial Synthesis Strategy and Computational Modeling. *Adv Energy Mater.* **12**, 2103312 (2022).
34. S. Schumacher, S. Baha, A. Savan, C. Andronescu, A. Ludwig, High-throughput discovery of hydrogen evolution electrocatalysts in the complex solid solution system Co-Cr-Fe-Mo-Ni. *J Mater Chem A Mater* (2022), doi:10.1039/d2ta01652d.
35. M. Bondesgaard, N. L. N. Broge, A. Mamakhel, M. Bremholm, B. B. Iversen, General Solvothermal Synthesis Method for Complete Solubility Range Bimetallic and High-Entropy Alloy Nanocatalysts. *Adv Funct Mater.* **29** (2019), doi:10.1002/adfm.201905933.

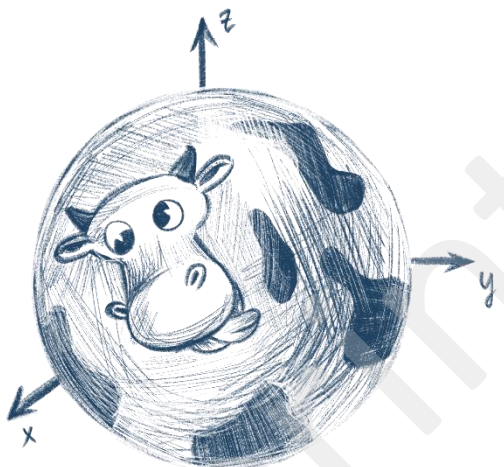
36. M. Inaba, A. Zana, J. Quinson, F. Bizzotto, C. Dosche, A. Dworzak, M. Oezaslan, S. B. Simonsen, L. T. Kuhn, M. Arenz, The Oxygen Reduction Reaction on Pt: Why Particle Size and Interparticle Distance Matter. *ACS Catal.* **11**, 7144–7153 (2021).
37. I. M. Sobol', On the distribution of points in a cube and the approximate evaluation of integrals. *USSR Computational Mathematics and Mathematical Physics*. **7**, 86–112 (1967).
38. J. A. Keith, V. Vassilev-Galindo, B. Cheng, S. Chmiela, M. Gastegger, K. R. Müller, A. Tkatchenko, Combining Machine Learning and Computational Chemistry for Predictive Insights into Chemical Systems. *Chem Rev.* **121** (2021), pp. 9816–9872.
39. L. E. McCoubrey, S. Gaisford, M. Orlu, A. W. Basit, Predicting drug-microbiome interactions with machine learning. *Biotechnol Adv.* **54** (2022), , doi:10.1016/j.biotechadv.2021.107797.
40. M. Bagherian, E. Sabeti, K. Wang, M. A. Sartor, Z. Nikolovska-Coleska, K. Najarian, Machine learning approaches and databases for prediction of drug-target interaction: A survey paper. *Brief Bioinform.* **22** (2021), pp. 247–269.
41. S. M. Lundberg, S. I. Lee, A unified approach to interpreting model predictions. *Adv Neural Inf Process Syst.* **2017-Decem**, 4766–4775 (2017).
42. S. Wang, E. Zhu, Y. Huang, H. Heinz, Direct correlation of oxygen adsorption on platinum-electrolyte interfaces with the activity in the oxygen reduction reaction. *Sci Adv.* **7** (2021), doi:10.1126/sciadv.abb1435.
43. K. Kodama, T. Nagai, A. Kuwaki, R. Jinnouchi, Y. Morimoto, Challenges in applying highly active Pt-based nanostructured catalysts for oxygen reduction reactions to fuel cell vehicles. *Nat Nanotechnol.* **16** (2021), pp. 140–147.
44. C. A. Campos-Roldán, D. J. Jones, J. Rozière, S. Cavalieri, Platinum-Rare Earth Alloy Electrocatalysts for the Oxygen Reduction Reaction: A Brief Overview. *ChemCatChem.* **14** (2022), , doi:10.1002/cctc.202200334.
45. D. Wu, X. Shen, Y. Pan, L. Yao, Z. Peng, Platinum Alloy Catalysts for Oxygen Reduction Reaction: Advances, Challenges and Perspectives. *ChemNanoMat.* **6** (2020), pp. 32–41.
46. T. Wang, A. Chutia, D. J. L. Brett, P. R. Shearing, G. He, G. Chai, I. P. Parkin, Palladium alloys used as electrocatalysts for the oxygen reduction reaction. *Energy Environ Sci.* **14** (2021), pp. 2639–2669.
47. H. Lv, D. Li, D. Strmcnik, A. P. Paulikas, N. M. Markovic, V. R. Stamenkovic, Recent advances in the design of tailored nanomaterials for efficient oxygen reduction reaction. *Nano Energy.* **29** (2016), pp. 149–165.
48. J. A. Zamora Zeledón, G. A. Kamat, G. T. K. K. Gunasooriya, J. K. Nørskov, M. B. Stevens, T. F. Jaramillo, Probing the Effects of Acid Electrolyte Anions on Electrocatalyst Activity and Selectivity for the Oxygen Reduction Reaction. *ChemElectroChem.* **8**, 2467–2478 (2021).
49. W. Jiao, C. Chen, W. You, G. Chen, S. Xue, J. Zhang, J. Liu, Y. Feng, P. Wang, Y. Wang, H. Wen, R. Che, Tuning strain effect and surface composition in PdAu hollow nanospheres as highly efficient ORR electrocatalysts and SERS substrates. *Appl Catal B.* **262** (2020), doi:10.1016/j.apcatb.2019.118298.

50. P. Rodriguez, M. T. M. Koper, Electrocatalysis on gold. *Physical Chemistry Chemical Physics*. **16** (2014), pp. 13583–13594.
51. S. Yin, Z. Xie, X. Deng, W. Xuan, Y. Duan, S. Zhang, Y. Liang, Simple synthesis of ordered platinum-gold nanoparticles with the enhanced catalytic activity for oxygen reduction reaction. *Journal of Electroanalytical Chemistry*. **856** (2020), doi:10.1016/j.jelechem.2019.113707.
52. S. Lankiang, M. Chiwata, S. Baranton, H. Uchida, C. Coutanceau, Oxygen reduction reaction at binary and ternary nanocatalysts based on Pt, Pd and Au. *Electrochim Acta*. **182**, 131–142 (2015).
53. W. Tang, S. Jayaraman, T. F. Jaramillo, G. D. Stucky, E. W. McFarland, Electrocatalytic activity of gold-platinum clusters for low temperature fuel cell applications. *Journal of Physical Chemistry C*. **113**, 5014–5024 (2009).
54. J. Yu, H. Jin, Q. Wang, X. Wei, H. Chen, Y. Wang, Coalescence of Au–Pd Nanoropes and their Application as Enhanced Electrocatalysts for the Oxygen Reduction Reaction. *Small*. **18**, 2203458 (2022).
55. H. Duy Mai, S. Kim, H. Yoo, Controllable growth of palladium on gold multipod nanoparticles and their enhanced electrochemical oxygen reduction reaction performances. *J Catal*. **388**, 20–29 (2020).



# 7

## What is the difference between a Swiss cow and a spherical cow in space?



Investigating the  $\text{AuIrOsPdPtReRhRu}$ ,  $\text{AuIrOsPdPt}$ ,  $\text{IrOsPdPtRu}$ , and  $\text{IrOsPtRhRu}$  compositions spaces provided me with a dataset for the oxygen evolution reaction. In contrast to the oxygen reduction reaction, there is already a DFT model developed that spanned essentially the whole 8-element composition space. This model excluded Au due to surface-related issues during calculations, where Au atoms tend to leave the surface upon structure-relaxation. Additionally, Re was excluded as its presence was not observed experimentally. Therefore, we could fully compare the experimental model with the DFT calculations.

In contrast to the oxygen reduction reaction, this comparison between the DFT calculations and the machine learning models for the oxygen evolution reaction showed an extremely large discrepancy. Here I would like to emphasize that DFT simulations calculate the intrinsic activity of an assumed ideal surface, that is described by the bulk atomic composition. Therefore, this discrepancy highlights that under experimental conditions, the oxygen evolution reaction activity cannot be solely explained by the atomic bulk composition of the as-prepared catalyst. In fact, there are non-negligible effects at play that need to be incorporated into DFT calculations to bring them closer to experimental observations. Identifying these effects opens two important pathways in catalyst discovery. Firstly, it demonstrates how to improve computer simulations to make them more realistic and relevant. Secondly, it shows on which aspects the catalyst can further be improved besides the intrinsic activity.

In this work, we observed that even in short oxygen evolution reaction experiments, which lasted for less than 10 minutes, the performance of the catalyst is strongly influenced by side

effects. Although conclusive evidence regarding the nature of these side effects is not available, we do provide hypotheses concerning which complementary effects are important and their correlation with the bulk atomic composition of the as prepared catalyst. We propose two primary effects that contribute to the activity of the oxygen evolution reaction catalyst which I will briefly summarize in the following paragraphs.

The first effect is related to the electrochemically active surface area. It is well known that the electrochemically active surface area has a detrimental effect on the absolute catalyst activity. Therefore, when it is possible to determine the electrochemically active surface area, we aim to normalize the activity with respect to it to eliminate its contribution. However, in case of the oxygen evolution reaction the catalytic surface is an oxide for which no reliable method is available to determine the surface in the electrochemical setup. Consequently, any changes to the surface due to reconstruction or leaching of elements might affect the effectively observed activity. In the  $\text{AuIrOsPdPtReRhRu}$  system, we can propose that Os, whose oxide is completely acid unstable, leeches out and roughens the surface.

The second effect involves the stability of the nanomaterials. In this experiment the oxygen evolution reaction, which takes place on oxides, was measured in an acidic electrolyte. It is well established fact that oxides dissolve in acidic environments, with varying dissolution rates. For the noble metals Ru, Ir, Pt, and Au, the oxygen evolution reaction activity is inversely correlated to the oxide stability.<sup>10</sup> Consequently, the most active Ru catalyst is also the most unstable. In this context, Ir becomes the most viable catalyst as it provides both enough activity and stability to be industrially relevant. Similarly, we hypothesize that the optimum composition that the machine learning model found, composed of  $\text{AuIrOsPdRu}$ , is a balance between activity and stability.

This work demonstrated that high entropy alloys can be seen as I would term “self-supported catalysts”. In these self-supported catalysts, certain elements are intentionally introduced to engineer the structure. Their functions can consist of enhancing catalyst stability by stabilizing the active sites or providing porosity through leaching out. Also, we can hypothesize that they may be used to enhance the electronic conductivity of the material, which is necessary for certain oxides. As a conclusion, high entropy alloy catalysts may draw interest for their secondary properties rather than their primary catalytic one.

These findings have changed my perspective of the oxygen evolution reaction. Currently, there is a tendency to search for novel oxygen evolution reaction catalysts that can outperform pure Ir based on “initial” activity alone. However, this work demonstrates that even within a 10-minute timeframe, the catalyst stability in acidic conditions is detrimental for the measured activity. This stability is not only affected by the alloyed elements but also on the employed supporting material. Therefore, I believe that for the oxygen evolution reaction system the support should be seen as an integral part of the catalyst system. Consequently, improving the oxygen evolution reaction catalyst stability via investigating catalyst support interaction may advance the development of oxygen evolution reaction catalysts much further than the search for just active catalysts.

Exploring the high entropy oxide composition space: insights through comparing experimental with theoretical models for the oxygen evolution reaction

Vladislav A. Mints<sup>a</sup><sup>§</sup>, Katrine L. Svane<sup>b</sup><sup>§</sup>, Jan Rossmeisl<sup>\*b</sup>, and Matthias Arenz<sup>\*a,b</sup>

<sup>a</sup> Department of Chemistry, Biochemistry and Pharmaceutical Sciences, University of Bern, Freiestrasse 3, 3012 Bern (Switzerland)

<sup>b</sup> Center for High Entropy Alloy Catalysis, Department of Chemistry, University of Copenhagen, Universitetsparken 5, 2100 København K, (Denmark)

<sup>§</sup> These authors contributed equally

\* Corresponding authors emails: [jan.rossmeisl@chem.ku.dk](mailto:jan.rossmeisl@chem.ku.dk) and [matthias.arenz@unibe.ch](mailto:matthias.arenz@unibe.ch)

**Keywords:** Oxygen evolution reaction • High entropy oxides • Electrochemistry • Machine learning • Density functional theory (DFT) calculations

## Abstract

The oxygen evolution reaction (OER) is key for the transition to a hydrogen-based energy economy. The observed activity of OER catalysts arises from the combined effects of surface area, intrinsic activity, and stability. Therefore, alloys provide an effective platform to search for catalysts that balance these factors. In particular, high entropy oxides provide a vast material composition space that could contain catalysts with optimal OER performance. In this work, the OER performance of the AuIrOsPdPtReRhRu composition space was modelled using an experimentally obtained data set of 350 nanoparticles. This machine-learned model based on experimental data found the optimal catalyst to be a mixture of AuIrOsPdRu. However, as “black-box model” it cannot explain the underlying chemistry. Therefore, density functional theory (DFT) calculations were performed to provide a complementary theoretical model with defined assumptions and hence a physical interpretation through comparison with the experimental model. The DFT calculations suggest that the majority of the activity originates from Ru and Ir active sites and that addition of Pd improves the performance of these sites. However, the DFT calculation did not find the experimentally observed beneficial effects of Au and Os. Therefore, we hypothesize that Os contributed to the performance of the tested catalysts by roughening the surface, whereas Au fulfilled the role of a structural support. Overall, it is demonstrated how machine learning not only can help to accelerate catalyst discovery but by combining machine-learned models obtained from experimental data with models based on DFT calculations can provide important insights on the complex chemistry of OER catalysts.

## 1. Introduction

The development of new materials with specific properties is of huge importance to humankind, not least in the transition to a society based on renewable energy sources. As an example, proton-exchange membrane (PEM) electrolyzers are of high interest for industrial

hydrogen production. However, the acidic operating conditions mean that catalysts are mostly limited to elements from the platinum group metals. The sluggish oxygen evolution reaction (OER) at the anode is most efficiently catalysed by oxides of Ru and Ir, but the cost and scarcity of these elements is a bottleneck to the large-scale use of PEM electrolyzers<sup>1,2</sup>. Therefore extensive research efforts are aimed at improving the activity relative to the amount of precious metal or completely replacing them with other materials.<sup>3,4</sup>

Many efforts have explored the alloying of Ir and Ru with other metals.<sup>5-8</sup> The most widely employed method is to increase the activity of the active sites by tuning the electronic structure. Another strategy is aimed at increasing the surface area of the Ir surface by alloying with acid unstable elements.<sup>9</sup> These elements leach out under acidic conditions, which results in porous structures that have a high electrochemically active surface area.<sup>10-12</sup> Finally, research is aimed at improving the stability of the electrochemically active surface. While Ru is more active than Ir, pure Ru nanoparticles are unsuitable for the OER due to their high instability.<sup>13-15</sup> However, when Ru is alloyed with Ir the stability of Ru improves at the cost of lowering the stability of Ir.<sup>16</sup> Therefore, the optimal OER catalyst is obtained by balancing the activity, stability, and surface area.

Recently, the first high entropy oxide (HEO), containing 5 different metals in a single-phase solid solution with oxygen was synthesised and characterised.<sup>17</sup> Since then, HEO's have gained attention for a number of different applications, including as potentially superior catalyst materials.<sup>18,19</sup> The random arrangement of the elements results in surface atoms with different local atomic environments. The neighbouring atoms perturb the binding energy of a catalytic intermediate such that the single value found on a pure oxide surface is replaced by a distribution of energies, some of which may be superior to those of the pure oxide. Furthermore, several studies suggest that the combination of multiple elements can lead to an increased stability under OER conditions.<sup>20-22</sup> Including several elements also results in a huge number of possible compositions,<sup>23</sup> promising rich opportunity to balance out the material properties for OER catalysts.

The large number of possible HEO compositions, however, poses the challenge of how to efficiently identify the optimum composition(s) within the search space. The number of experiments that can be performed manually is limited, and the number of samples required for grid searches thus calls for a partly automated experimental setup.<sup>24,25</sup> Alternatively, the combination of laboratory experiments with computational, and statistical methods can be used to reduce the number of samples that are needed. Presently, Bayesian optimization has been demonstrated to effectively optimize 5-element high entropy alloy (HEA) catalysts compositions with less than 50 experiments.<sup>26,27</sup> Furthermore, we demonstrated that the search for HEA catalysts can be accelerated by including a larger number of elements in the initial composition search space.<sup>28</sup> Finally, a strategy based on density functional theory (DFT) calculations, has been developed to enable computational screening of HEA and HEO catalysts.<sup>29,30</sup> Both experimental and theoretical screening methods procure information about the catalyst from different angles. Therefore, the combination of these two different

approaches provides an important verification of the obtained results and a basis for further improvement of the employed methods.<sup>31</sup>

In this work, we investigated the possible noble metal high entropy oxide combinations, in short the noble metal high entropy oxide space using the strategy described in Mints et al.<sup>28</sup> Using experimentally obtained data of 350 different unsupported nanoparticle catalysts in the AulIrOsPdPtReRhRu composition space, a machine-learned model covering the main relevant noble metal OER catalysts in aqueous electrolysis was constructed. This data-based model correlates the elemental composition with the observed activity. Comparison with a theoretical model based on DFT calculations allows us to propose a physical interpretation of the experimental data. In line with previous literature, Ir and Ru demonstrated to be the main elements responsible for the OER activity. In addition, DFT calculations show that Pd synergistically improves the activity of Ru active sites through a ligand effect. Interestingly, the experimental data-based model observes non-negligible positive contributions originating from the presence of Os and Au that cannot be explained with the DFT calculations. We therefore hypothesize that these contributions do not originate from the intrinsic activity but from structural effects that are not considered in the DFT calculations. Consequently, this work demonstrates how by combining experimental and theoretical studies that construct activity models, OER catalysts can further be improved beyond pure compositional optimization.

## 2. Experimental Part

In the following, the main experimental details are described. More information on the calculations, data treatment, and the machine learning can be found in the electronic supplementary information (ESI).

### Catalyst Synthesis

The catalysts used in this work were the same as described in our previous work Mints et al.<sup>28</sup> The nanoparticles were prepared by a microwave solvothermal synthesis. In this synthesis, the precursors: HAuCl<sub>3</sub> (Alfa Aesar, 99.99%), IrCl<sub>3</sub> (Strem Chemicals, 99.9%), OsCl<sub>3</sub> (Sigma Aldrich), PdCl<sub>2</sub> (Sigma Aldrich, 99%), H<sub>2</sub>PtCl<sub>6</sub> (Alfa Aesar, 99.999%), ReCl<sub>3</sub> (Sigma Aldrich), RhCl<sub>3</sub> (Alfa Aesar and Sigma Aldrich, 99.98%), RuCl<sub>3</sub> (Sigma Aldrich, ReagentPlus) were mixed in stoichiometric ratio to produce 4 mL 5.0 mM solution in ethanol (VWR, AnalaR NORMAPUR ACS). Then the reaction vessel was heated up to 20 bars for 30 minutes in a microwave reactor (CEM, Discover SP). The obtained suspension was centrifuged, washed with ethanol, and dried. Following the particles were redispersed in 3.25 mL 3:1 water:IPA (water: deionized and ultrafiltered by a Millipore MilliQ system; iso-propanol: VW) to produce an ink. Assuming that all precursors did react, the ink had a concentration of 6.15 mM metal. The composition of the nanoparticles was evaluated using energy dispersive x-ray spectroscopy (EDX) using an EDS Photodetector Ultim max 65 (Oxford instruments) in a GeminiSEM450 (Zeiss). The spectra were measured at four different spots with a size of 588 μm<sup>2</sup> at a working distance of 8 mm

and an accelerating voltage of 25kV. The average concentrations observed for each of the subspaces are plotted in Figure S1.

### **Electrochemical measurements**

The electrochemical measurements were carried out using a 6-channel multi-working electrode. Each electrode consisted of a 5mm in diameter glassy carbon disk on which 8.17 ml ink was dropped. A platinum mesh separated by a frit served as the counter electrode whereas a reversible hydrogen was used as a reference electrode. A stirring bar rotating at 1500 revolutions per minute created convection in the electrochemical cell. The water used in these experiments was deionized and ultrafiltered by a Millipore MilliQ system (resistivity > 18.2 MΩ cm, TOC ≤ 5 ppb). The electrolyte consisted of 0.1 M H<sub>2</sub>SO<sub>4</sub> (Merck, Suprapur) and was renewed after each measurement.

The electrochemical measurements started by measuring cyclic voltammograms between 0 to 0.6 V vs. RHE at 100 mV/s, from which the capacitance was extracted between 0.3 and 0.5 V vs. RHE. The capacitance was used to normalize the data for possible differences in electrocatalytic surface area. Following, the solution was saturated with O<sub>2</sub> and the particles were oxidized at 1.5 V vs. RHE for 4 minutes. Then, the potential was stepped up with increments of 10 mV from 1.45 V to 1.65 V vs. RHE which lasted each for 20 seconds. The shown datapoints were created by averaging the current over the last 17 seconds of each potential step. In addition, the averaged current at 1.45 V vs. RHE was used for baseline subtraction. Due to the design of the multi-working electrode, the data was not corrected for the solution resistance. The absence of such a correction, results in a smaller activity spread at large overpotentials. However, trends in catalytic activity with respect to the composition are maintained.

### **Gaussian Process (GP) regression**

The oxygen evolution reaction (OER) in acidic electrolyte has a strong dependence on the electrochemically surface area. In addition, the formation of the oxide is also accompanied with large structural changes. In absence of a method to determine the exact electrochemical surface area, this makes the data in particular sensitive to noise and outliers. For instance, when the activity distributions of the four subspaces at 1.5 V vs. RHE are plotted (see Figure S2), it is evident that in the AuIrOsPtPdReRhRu space 16 out of 200 particles fall in the region larger than two standard deviations. However, assuming that the activity is normal distributed, around 5 samples should have such a high activity. This suggests that a large number of outliers is present. Due to their exceptionally high activity, these outliers have a high leverage on the model. Since we are unable to identify which samples are these outliers to safely remove them, we decided to reduce their leverage by combining all four data sets into a single one. Therefore, in this work, the Gaussian processes were trained using all 350 samples.

At each potential, a separate Gaussian Process was trained. The kernel for each consisted of a radial basis kernel multiplied with a constant kernel and a white kernel:

$$k(x_i, x_j) = c * e^{\frac{-d(x_i, x_j)^2}{2l^2}} + \delta_{ij}\alpha^2 \quad (1)$$

In this equation,  $k$  is the kernel function,  $d$  is the Euclidean distance between parameter  $x_i$  and  $x_j$ ,  $l$  is the fitted correlation length scale  $\delta_{ij}$  is the Kronecker delta which is unity when  $i$  and  $j$  are identical and zero for non-identical  $i$  and  $j$ ,  $\alpha$  is the fitted noise parameter.

All models were fitted with a length scale of around 30 at.% (Figure S3). In our previous works, the Gaussian Processes were fitted on a transformed simplex with unit edge lengths. This work in contrast uses a simplex space with edge length equal to the square root of two. Therefore, to compare the length scales, a correction is necessary which results in a length scale of 21 at.%. This length scale is similar to the previously observed length scales of 40 at.% and 0.25 at.% for the oxygen reduction reaction.<sup>1</sup> Since the activity domain of the models is changing, the mean absolute error (MAE) obtained by the leave-one-out cross-validation (LOOCV) method was normalized by dividing with the average activity observed activity. As a result, MAEs around 0.3 are observed for all the models (Figure S3). In addition, the performance of the models was evaluated using the coefficient of determination ( $R^2$ ) from the LOOCV method. The  $R^2$  values were all above 0.57, indicating that the models have predicting power (Figure S3).

### Computational details

Density functional theory calculations were performed using the grid-based projector augmented wave (GPAW) software,<sup>4,5</sup> using a plane-wave basis with an energy cut-off of 500 eV. The atomic simulation environment (ASE) was used to set up the calculations and analyze the results.<sup>6</sup> The exchange and correlation energy was described by the RPBE functional.<sup>7</sup>

The HEO surface of RuPtIrOsRhPd oxide is modeled by a 1x3 rutile (110) surface with four layers of atoms, of which the bottom two are fixed in the bulk positions. A minimum of 20 Å of vacuum separates the periodic images of the slab, and a dipole correction is used to decouple the electrostatic interactions across the periodic boundary. The metal sites of the slab are randomly occupied by each of the 6 elements with equal probability. The lattice constant is chosen as the average of that calculated for the six pure oxides by DFT (see Table S1). The Brillouin zone was sampled by 2x2 k-points. Adsorbates are placed on a coordinatively unsaturated (cus) site.

To mimic the coverage close to the onset potential, the cus sites that are not the active site are covered by \*O if they are one of the strong-binding metal atoms (Ru, Ir, Os, see section S5 below) and empty otherwise. The adsorption energies are calculated using the computational hydrogen electrode to account for the effect of an applied potential, and free energy corrections of 0.35 eV, 0.05 eV and 0.40 eV are added for the \*OH, \*O and \*OOH adsorbates, respectively, to account for changes in entropy and zero point energy.<sup>8</sup>

### 3. Results and Discussion

#### Analysis of experimental OER activity measurements

The experimental data-based models were constructed from 200 different nanoparticle compositions from the  $\text{AuIrOsPdPtReRhRu}$  composition space, and 50 compositions were taken from each of the  $\text{AuOsPdPtRu}$ ,  $\text{IrOsPdPtRu}$  and  $\text{IrOsPtRhRu}$  subspaces. The evaluation of the obtained nanoparticle compositions with EDX showed the presence of all elements except Re, which was only detected in very small amounts (see Figure S1). The analysis and conclusions on the role of Re are therefore omitted in the following discussion.

An initial analysis of the correlations between composition and OER activity was achieved by calculating the Pearson correlation coefficient. The changes in correlation within the measured potential range, see Figure 1, reflect some key properties of noble metal based OER catalysts. Throughout the investigated potential range, the correlation coefficients of both Ru and Ir are more positive than those of the other elements, consistent with studies in the literature showing Ru and Ir to be the most active OER catalysts.<sup>32–35</sup>

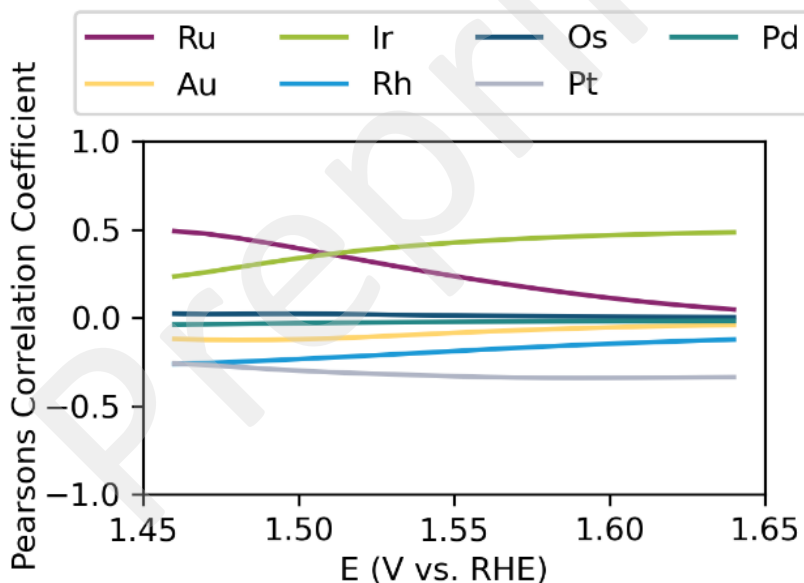
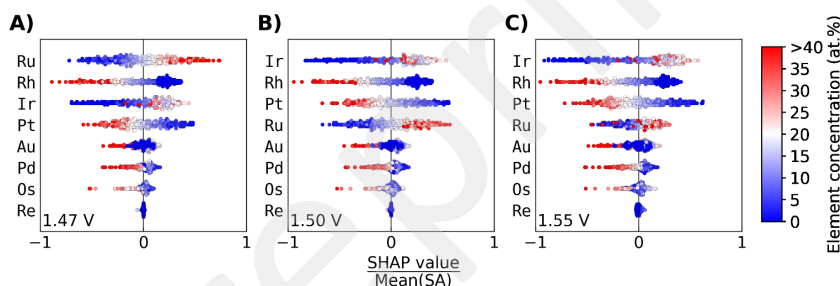


Figure 1: Pearson's correlation coefficients of the elements and activity from the experimental data set at different potentials.

At low overpotentials, Ru displays the largest correlation coefficient to the measured current, however, this correlation coefficient decreases with increasing potential. This indicates that the linear dependency on Ru decreases with increasing potential. The correlation coefficient of Ir shows the opposite behavior, increasing with potential to eventually become larger than

that of Ru, indicating an increasing linear dependency on Ir. Together these results suggest that the optimal composition for an OER catalyst is dependent on the overpotential. The elements Au, Os, and Pd show correlation coefficients near zero for all potentials, indicating an absence of a linear correlation. This implies that these elements are suitable for alloying with Ir and Ru, as increasing their content does not necessarily compromise the activity of the catalyst. On the other hand, Pt and Rh show negative correlation coefficients, meaning that increasing their concentrations leads to a decrease in activity.

The experimental data were further analyzed by constructing GP Regressions at each individual potential. The models predict the experimental data in the leave-one-out cross-validation procedure with  $R^2$  values around 0.6 (see Figure S3). The GPs were fitted with the radial basis function kernel multiplied with a constant kernel and a white noise kernel. For all the models, the radial basis function kernel had optimized lengths scales of ~30 at.% (Figure S3). These long length scales are similar to the length scales of 40 at.% and 25 at.% observed for the ORR models.<sup>26,28</sup> This indicates that also for the OER, the mathematical activity landscapes are relatively smooth.



**Figure 2:** SHAP-values for each of the elements at a potential of a) 1.47 V, b) 1.50 V and c) 1.55 V vs. RHE. Each point represents a measured sample and a positive SHAP value indicates a positive contribution to the current. The color of the points indicates the atomic percentage of the elements as shown in the colorbar on the right.

The correlations within the GP models were evaluated using SHapely Additive exPlanations (SHAP).<sup>36</sup> Selected SHAP analyses at 1.47, 1.50 and 1.55 V vs. RHE are shown in Figure 2. In these figures positive SHAP values are associated with an increase in OER activity. At 1.47 V vs. RHE only a few nanoparticles have a high activity for the OER. As such the model at this potential gives insight into which element(s) are responsible for an “early onset” of the OER. The key element is Ru, which shows the strongest SHAP correlations. Ir has a smaller positive contribution, however, low concentrations of Ir are strongly correlated with a low OER activity. On the other hand, Pt and Rh demonstrate a strong negative contribution to the OER, consistent with their Pearson correlation coefficients. Lastly, Os, Au, and Pd, all three show weak correlations to the OER, yet in moderate quantities they show to improve the activity. At 1.5 and 1.55 V vs. RHE the same trends are observed except that the impact of Ru on the model decreases, while the importance of Ir grows.

Both the SHAP analysis and the Pearson correlation coefficients suggest that the optimum catalyst composition is electrode potential dependent. Figure 3a shows the optimal compositions at different electrode potentials obtained from a 5 at. % atomic grid for each GP regression. Surprisingly, the optimum composition is a combination of AuIrOsPdRu. The optimal content of Ru at the onset is 45 at. %, which steadily decreases to 30 at. % with increasing overpotential while being replaced with Os. On the other hand, the fractions of Au, Pd and Ir remain mostly constant.

### DFT based model

To get a better understanding of the experimental observations, the compositional space, reduced to IrOsPdPtRhRu, was modelled using DFT calculations (see experimental section and ESI for computational details). Re was excluded from the calculations based on the low amounts present in the EDX spectra. Au was excluded because initial attempts to include it resulted in large deviations from the initial structure indicating that it is not favourable for Au to be incorporated in the oxide structure (see section S4 in the ESI). Calculations of the catalytic activity for the pure rutile oxides furthermore reveal that neither  $\text{AuO}_2$  nor  $\text{ReO}_2$  are good catalysts on their own, suggesting that they can only provide indirect contributions to the catalytic activity, e.g., through a ligand effect (see Section S5 in the ESI). The HEO containing the remaining elements were modelled in the rutile oxide structure, which is the most stable oxide for Ru, Ir and Rh, with the coordinatively unsaturated (cus) metal atoms on the 110 surface considered as the catalytically active sites. The computational modelling follows the procedure described in ref.<sup>29</sup> The metal sites are randomly occupied by one of the six elements with equal probability. Two different reaction pathways are considered; the conventional pathway going through the  $^*\text{OH}$ ,  $^*\text{O}$  and  $^*\text{OOH}$  intermediates<sup>37</sup> and an alternative pathway where the proton of the  $^*\text{OH}$  and/or  $^*\text{OOH}$  intermediates are transferred to a neighboring bridging oxygen site to form ( $^*\text{O} + \text{H}_\text{b}$ ) and ( $^*\text{O}_2 + \text{H}_\text{b}$ )<sup>38,39</sup> (See Section S6 in the ESI for further details). The free energies of adsorption of the reaction intermediates are calculated by DFT for a number of randomly generated surface sites. From these energies a linear model, capable of predicting the binding energy based on the local atomic configuration, is constructed (See section S7 in the ESI). This model allows for the fast evaluation of the overpotential on any site,  $i$ , on a macroscopic surface, which can be generated with any ratio of the 6 elements. The current from each site ( $j_i$ ) is calculated as:

$$\frac{1}{j_i} = \frac{1}{j_{k,i}(\eta_i, U)} + \frac{1}{j_d} \quad (2)$$

And the total current from all  $N$  sites on the surface ( $j = \sum_i^N j_i$ ) is used as a measure of the catalytic activity (See section S8 in the ESI). Here  $j_d$  is the diffusion current and  $j_{k,i}$  is the kinetic current which depends on the overpotential of site  $i$  ( $\eta_i$ ) as well as the potential ( $U$ ). We note that the potential in this model is not aligned with the electrode potential in the experiment. This is because the magnitude of the diffusion current relative to the kinetic current in Eq. 2 is unknown. Different choices of  $j_d$  affect the number of sites that have reached the diffusion limited current at a given potential, i.e.,  $j/j_{\max}$ , where  $j_{\max} = N j_d$  is the maximum total current

when all sites are limited by diffusion. Here we arbitrarily choose  $j_d = 100$ ; a different choice would result in a rigid shift of all results along the potential axis. (see Figure S22 In the ESI)

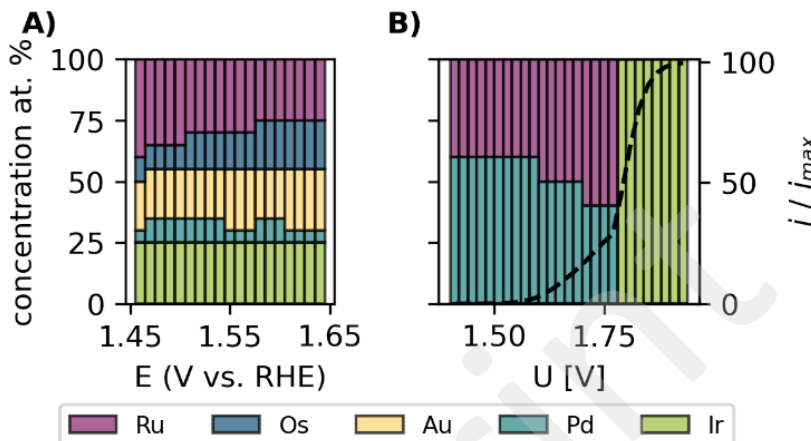


Figure 3: Optimum composition as a function of potential a) obtained from the experimental GP models and b) obtained from the computationally based current model. The black dashed line in b) indicates the fraction of the maximum possible current within the diffusion limitation that has been reached ( $j/j_{max}$ ).

The DFT based model is used to calculate the total current from 100x100 surfaces with compositions on a regular grid with a 10% resolution throughout the 6-element composition space. The resulting map of the activity as a function of composition and potential reveals that the optimum composition is always found within the IrPdRu subspace, which is further investigated with a 5% resolution. The optimum composition as a function of potential is shown in Figure 3b. The fraction of the maximum activity that has been reached at a given potential,  $j/j_{max}$ , is plotted on top as a black line. The plot shows that the most active composition is a mixture of Ru and Pd at low potentials, when only a small fraction of the surface sites are active. Pure  $\text{IrO}_2$  becomes the most active composition at high potential, when approximately 30% of the maximum activity has been reached. The change in optimum composition with potential thus reflects the balance between the overpotential of individual sites and the number of sites that are active. A mixture of Ru and Pd will result in a few sites with an overpotential that is lower than that of  $\text{IrO}_2$ , but also some sites with a higher overpotential. RuPd will therefore have an earlier onset, but as the potential increases the activity of the most active sites becomes limited by diffusion. At some moment, the maximum activity that the catalyst can reach becomes limited by the least active sites. In case of  $\text{IrO}_2$ , all its sites are more active than the least active sites of RuPd. Therefore, even though the OER requires a higher overpotential on  $\text{IrO}_2$ ,  $\text{IrO}_2$  reaches fully diffusion limited activity at a

lower potential than RuPd. This results in an intersection of their activity curve and the resulting change in optimal OER catalyst composition at a certain overpotential.

To understand in more detail how Pd contributes to the catalytic activity, we firstly note that all the Pd cus sites calculated by DFT have large overpotentials (c.f. Figure S13 in the ESI), implying that Pd acts by modifying the energy levels of Ru and Ir cus sites. Figure 4 compares the energy levels of the catalytic intermediates for the two considered reaction pathways on pure  $\text{IrO}_2$  and  $\text{RuO}_2$  with the corresponding average energies for  $\text{Ru}_{0.5}\text{Pd}_{0.5}\text{O}_2$  and  $\text{Ir}_{0.5}\text{Pd}_{0.5}\text{O}_2$  obtained from the DFT-based linear model. The diagrams show that Pd weakens the average binding energy of intermediates on the cus site, and the intermediates that use the bridge site are stabilized relative to  $^*\text{O}$ , in particular if the bridge site consists of two Pd atoms. For pure  $\text{IrO}_2$  the limiting step in OER is the final step, i.e., removal of  $^*\text{O}_2 + \text{H}_\text{b}$ . The average energies of the IrPd and PdPd bridge sites result in an increase in the energy required for this step, while an IrIr bridge will decrease it slightly. Thus, the addition of some Pd will create sites that are more active than pure  $\text{IrO}_2$  but only when Pd is not on the active cus site and neighbouring bridge sites, suggesting that the concentration should be low. For  $\text{RuO}_2$  the situation is different because the largest step for pure  $\text{RuO}_2$  is the conversion of  $^*\text{O}$  to  $^*\text{O}_2 + \text{H}_\text{b}$ . A lowering of the  $^*\text{O}_2 + \text{H}_\text{b}$  energy level reduces  $\Delta G$  for this step, and therefore lowers the overpotential. This is actually the case for the average energies of both RuRu, RuPd and PdPd bridge sites, but in particular the RuPd bridge sites balance  $\Delta G$  for the last two reaction steps favourably. Here, the largest difference between the average energy levels is just 1.54 eV, explaining how RuPd can be more active than pure  $\text{IrO}_2$  or IrPd. However, once a potential is reached where all sites with an RuPd bridge are fully active, the remaining sites with RuRu and PdPd bridges are less active and pure  $\text{IrO}_2$  becomes the most active catalyst.

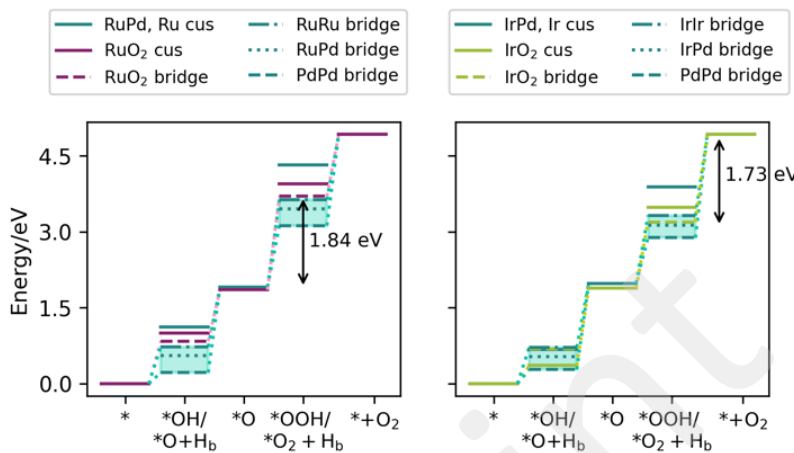


Figure 4: Energy levels for the OER intermediates on pure RuO<sub>2</sub> and average energy levels for Ru<sub>0.5</sub>Pd<sub>0.5</sub>O<sub>2</sub> (left) and corresponding plot for IrO<sub>2</sub> and Ir<sub>0.5</sub>Pd<sub>0.5</sub>O<sub>2</sub> (right). The largest steps for the pure oxides are indicated by arrows. For the oxides containing Pd the bridge adsorbates are represented by three different energy levels, corresponding to the three different possible combinations of metal atoms on the bridge site. The area between these energy levels is shaded as a guide to the eye.

#### Comparison of experimental data-based model with DFT model

We now compare the results obtained with the experimental and DFT based models, keeping in mind that only a qualitative comparison of the electrode potential is possible. Firstly, it is noticed that Ru, Ir and Pd are present in both the experimental and computational optimum, while Os and Au are only found in the experimental model. The computational model predicts the optimum in the RuIrOs subspace to contain little to no Os (c.f. section S9 in the ESI). Thus, it can be excluded that Os improves the *intrinsic* catalytic activity of the optimum in the experimental model and a different explanation on its role is necessary. According to a literature survey, Os has been demonstrated to increase the OER activity by leaching out of the catalyst and thereby increasing its surface area.<sup>40</sup> Since the surface area was approximated using the capacitance at 0.5 V vs. RHE, any roughening of the surface due to element leaching at 1.5 V vs. RHE will contribute to an increase in activity. Therefore, we hypothesize that the contribution of Os in the experimental model is due to an influence on the surface area rather than an improvement in the electronic structure of active sites.

The experimental model also predicts that 20 at. % Au is present in the optimum. This is surprising considering that Au is not known to be a strong OER catalyst.<sup>40</sup> However, it has been shown that in segregated systems, the Au-Ir interface exhibits a higher activity than pure Ir.<sup>41,42</sup> Yet, the large fractions of Au we observe in the current optimum in the experimental model do not fit the small Au quantities required for such an enhancement. Also, gold has

been demonstrated to improve the OER activity of Co catalysts in alkaline media by acting as an electron sink, which can lead to an enhancement in conductivity.<sup>43</sup> Similarly, research has investigated the performance of iridium deposited on gold structures.<sup>44,45</sup> Lastly, Au has also been shown to improve the stability of Ru under OER conditions.<sup>46</sup> In these cases Au is fulfilling the role of a support rather than being a direct participant in the active site. In comparison to Os, Au is stable in acids and thus will have a different role in the catalyst. Based on the comparison of the experimental model with the DFT calculations as well as the findings in literature, we hypothesize that since the particles in this work are unsupported, Au mainly acts as a structural support enhancing the particle stability and/or conductivity. According to the machine-learned experimental model, in this set-up the 20 at. % Au is essential for optimal measurements. Therefore, in other set-ups where particles are supported, the observed importance of gold may change. However, since Au could not be included into the DFT model, we cannot fully exclude possible beneficial effects on the intrinsic activity in a manner similar to Pd.<sup>47</sup>

Having concluded that the positive contributions of Au and Os are most likely non-catalytic, we now focus on the remaining three elements, which are found in the optimum of both models, namely: Ru, Ir, and Pd. Our DFT calculations described above clearly suggest an intrinsically high activity for combinations of these elements. Furthermore, experiments on RuPd and IrPd oxides have previously shown an increased activity compared with pure RuO<sub>2</sub> and IrO<sub>2</sub>, respectively.<sup>48–50</sup> A computational screening study has likewise identified Ir<sub>0.5</sub>Pd<sub>0.5</sub>O<sub>2</sub> as a good catalyst.<sup>51</sup> Still, to our knowledge, the combination of Ru, Ir and Pd has not yet been studied.

The activity within the RuIrPd subspace is visualized in the ternary plots in Figure 5 for both the computational and the experimental models at two different potentials. At low electrode potential the computational model has a global maximum at the RuPd edge which is connected to a local maximum at the IrPd edge. As the potential increases the valley between the two maxima becomes more active, and a third maximum appears at the RuIr edge before IrO<sub>2</sub> becomes the most active catalyst at high potentials.

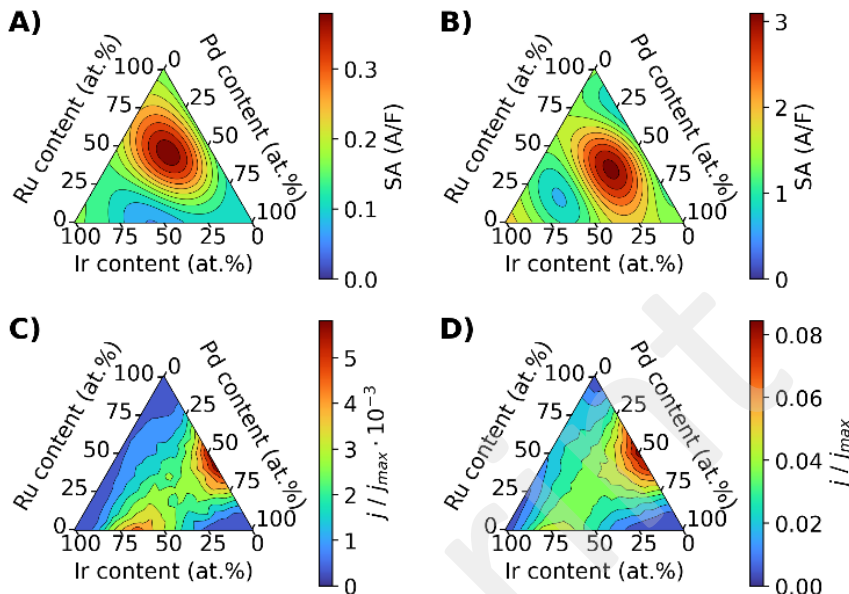


*Figure 5: Catalytic activity within the RuIrPd subspace at different potentials extrapolated from the experimental data in units of A/F a) at 1.5 V vs. RHE and b) at 1.6 V vs. RHE and c) catalytic activity determined from the computational model in units of  $j/j_{max}$  at  $U=1.55$  V and d)  $U=1.65$  V.*

The corresponding experimental model has a single, well-defined maximum at low potentials located in the center of the composition space. At higher potentials, this maximum shifts towards lower Ru and higher Pd content. But within the measured potential range the optimum always contains all three elements (Figure S24) and never a binary combination. This discrepancy in the optimum composition with the DFT prediction is expected based on the complexity of the OER system. The DFT based model is simply a distribution of overpotentials arising from a given compositions. It does not include stability or in-situ structural changes as that would require exhaustive quantum mechanical simulations. On the other hand, the experimental models are based on measured OER data and thus influenced by the structural and stability of the catalysts under reaction conditions. This is especially evident in the catalytic activity of Ru rich nanoparticles, which according to DFT are the catalytic optimum. However, under reaction conditions, Ru rich nanoparticles are acid unstable resulting in the absence of measured OER activity.<sup>13</sup> Consequently, the optimum according to the experimental model is a consequence of a balance of activity and stability, which is achieved by mixing all three elements together.

The above comparison of the experimental data-based and theoretical DFT models highlights how the two approaches complement each other. The experimental model is a black-box model purely based on experimental observations and unable to distinguish between pure

intrinsic activity and activity arising from structural modification. Meanwhile, DFT predicts the intrinsic activity based on well-defined assumptions and explains its origin but does not consider effects of structural changes and stability under experimental conditions. Similarities between these independent models substantially strengthen our conclusions. At the same time, discrepancies highlight the presence of previously ignored effects or material properties. Expanding the machine-learned and theoretical models to include these dimensions will increase their generalization and applicability. On top of that, identifying these dimensions also shows how a catalytic system can further be improved.

#### 4. Conclusion

In this work, we have explored the 8-element composition space of  $\text{AuIrOsPdPtReRhRu}$  experimentally for the OER and performed complementary DFT modelling of the  $\text{IrOsPdPtRhRu}$  subspace. The machine-learned model identified that the optimum catalyst composition is achieved by a combination of  $\text{AuIrOsPdRu}$ . By comparing the machine-learned model with the DFT model, we identify that the performance of  $\text{AuIrOsPdRu}$  is due to the self-supporting property of HEO materials. Namely, DFT calculations show a positive effect of Pd on the activity of Ru active sites, which results in the catalytic activity originating from the  $\text{RuIrPd}$  ternary subspace. Thereby, DFT calculations could not explain the improvement of the catalytic reaction due to the presence of Au and Os. Therefore, we propose that Au and Os, improve the OER indirectly by structural modifications resulting in an enhanced stability and surface area.

Finally, this work demonstrates a synergistic investigation of two different approaches. Significant discrepancies between the two differently obtained models can be used to pinpoint deficiencies in both models and clarify the causation of experimental observations. Meanwhile, when both models arrive at identical results by identifying high-activity domains in similar regions of the compositions space, the confidence in the drawn conclusion substantially increases. Therefore, on the material design quest, theoretical and experimental approaches can be regarded as complementary sources of information. In a continuous feedback loop, this information can be used to develop and refine models of material properties. As demonstrated, for the OER the stability of the nanomaterials is a non-negligible contribution studying which may improve the catalytic performance further compared to searching for novel active catalysts.

#### Acknowledgements

This work is supported by the Danish National Research Foundation Center for High-Entropy Alloy Catalysis (CHEAC) DNRF-149.

#### References

1. Bernt, M. et al. Current Challenges in Catalyst Development for PEM Water Electrolyzers. *Chemie Ingenieur Technik* **92**, 31–39 (2020).

2. Ayers, K., Danilovic, N., Harrison, K. & Xu, H. PEM Electrolysis, a Forerunner for Clean Hydrogen. *Electrochim Soc Interface* **30**, 67–72 (2021).
3. Seh, Z. W. *et al.* Combining theory and experiment in electrocatalysis: Insights into materials design. *Science* (1979) **355**, (2017).
4. An, L. *et al.* Recent Development of Oxygen Evolution Electrocatalysts in Acidic Environment. *Advanced Materials* **33**, 2006328 (2021).
5. Forgie, R., Bugosh, G., Neyerlin, K. C., Liu, Z. & Strasser, P. Bimetallic Ru electrocatalysts for the OER and electrolytic water splitting in acidic media. *Electrochemical and Solid-State Letters* **13**, 36–39 (2010).
6. De Faria, L. A., Boodts, J. F. C. & Trasatti, S. Electrocatalytic properties of ternary oxide mixtures of composition  $\text{Ru}_0.3\text{Ti}(0.7-x)\text{Ce}_x\text{O}_2$ : oxygen evolution from acidic solution. *J Appl Electrochem* **26**, 1195–1199 (1996).
7. Wen, Y. *et al.* Stabilizing Highly Active Ru Sites by Suppressing Lattice Oxygen Participation in Acidic Water Oxidation. *J Am Chem Soc* **143**, 6482–6490 (2021).
8. Gu, X.-K., Camayang, J. C. A., Samira, S. & Nikolla, E. Oxygen evolution electrocatalysis using mixed metal oxides under acidic conditions: Challenges and opportunities. *J Catal* **388**, 130–140 (2020).
9. Collantes Jiménez, P. *et al.* Gas diffusion electrode activity measurements of iridium-based self-supported catalysts produced by alternated physical vapour deposition. *J Power Sources* **569**, (2023).
10. Kim, Y. T. *et al.* Balancing activity, stability and conductivity of nanoporous core-shell iridium/iridium oxide oxygen evolution catalysts. *Nat Commun* **8**, (2017).
11. Kim, K. S. *et al.* Promoting Oxygen Evolution Reaction Induced by Synergetic Geometric and Electronic Effects of IrCo Thin-Film Electrocatalysts. *ACS Catal* **12**, 6334–6344 (2022).
12. Zhu, J. *et al.* Ultrathin-shell IrCo hollow nanospheres as highly efficient electrocatalysts towards the oxygen evolution reaction in acidic media. *Nanoscale* **12**, 24070–24078 (2020).
13. Reier, T., Oezaslan, M. & Strasser, P. Electrocatalytic Oxygen Evolution Reaction (OER) on Ru, Ir, and Pt Catalysts: A Comparative Study of Nanoparticles and Bulk Materials. *ACS Catal* **2**, 1765–1772 (2012).
14. Cherevko, S. *et al.* Oxygen and hydrogen evolution reactions on Ru,  $\text{RuO}_2$ , Ir, and  $\text{IrO}_2$  thin film electrodes in acidic and alkaline electrolytes: A comparative study on activity and stability. *Catal Today* **262**, 170–180 (2016).

15. Danilovic, N. *et al.* Activity-Stability Trends for the Oxygen Evolution Reaction on Monometallic Oxides in Acidic Environments. *J Phys Chem Lett* **5**, 2474–8 (2014).
16. Escalera-López, D. *et al.* Phase- And Surface Composition-Dependent Electrochemical Stability of Ir-Ru Nanoparticles during Oxygen Evolution Reaction. *ACS Catal* **11**, 9300–9316 (2021).
17. Rost, C. M. *et al.* Entropy-stabilized oxides. *Nat Commun* **6**, (2015).
18. Albedwawi, S. H., AlJaber, A., Haidemenopoulos, G. N. & Polychronopoulou, K. High entropy oxides-exploring a paradigm of promising catalysts: A review. *Materials and Design* vol. 202 Preprint at <https://doi.org/10.1016/j.matdes.2021.109534> (2021).
19. Löffler, T., Ludwig, A., Rossmeisl, J. & Schuhmann, W. What Makes High-Entropy Alloys Exceptional Electrocatalysts? *Angewandte Chemie - International Edition* vol. 60 26894–26903 Preprint at <https://doi.org/10.1002/anie.202109212> (2021).
20. Kante, M. V *et al.* A High-Entropy Oxide as High-Activity Electrocatalyst for Water Oxidation. *ACS Nano* **17**, 5329–5339 (2023).
21. Miao, X., Peng, Z., Shi, L. & Zhou, S. Insulating High-Entropy Ruthenium Oxide as a Highly Efficient Oxygen-Evolving Electrocatalyst in Acid. *ACS Catal* **13**, 3983–3989 (2023).
22. Nguyen, T. X., Liao, Y., Lin, C., Su, Y. & Ting, J. Advanced High Entropy Perovskite Oxide Electrocatalyst for Oxygen Evolution Reaction. *Adv Funct Mater* **31**, (2021).
23. Cantor, B. Multicomponent and high entropy alloys. *Entropy* **16**, 4749–4768 (2014).
24. Strotkötter, V. *et al.* Discovery of High-Entropy Oxide Electrocatalysts: From Thin-Film Material Libraries to Particles. *Chemistry of Materials* **34**, 10291–10303 (2022).
25. Banko, L. *et al.* Microscale Combinatorial Libraries for the Discovery of High-Entropy Materials. *Advanced Materials* **35**, (2023).
26. Pedersen, J. K. *et al.* Bayesian Optimization of High-Entropy Alloy Compositions for Electrocatalytic Oxygen Reduction\*\*. *Angewandte Chemie - International Edition* **60**, 24144–24152 (2021).
27. Mints, V. A. *et al.* Exploring the Composition Space of High-Entropy Alloy Nanoparticles for the Electrocatalytic H<sub>2</sub>/CO Oxidation with Bayesian Optimization. *ACS Catal* **12**, 11263–11271 (2022).
28. Mints, V. A., Pedersen, J. K., Wiberg, G. K. H., Rossmeisl, J. & Arenz, M. Backward Elimination: A Strategy for High-Entropy Alloy Catalyst Discovery. *Currently under 2nd review at Nature Materials* doi:10.26434/chemrxiv-2022-78s83.

29. Svane, K. L. & Rossmeisl, J. Theoretical Optimization of Compositions of High-Entropy Oxides for the Oxygen Evolution Reaction\*\*. *Angewandte Chemie International Edition* **61**, (2022).
30. Batchelor, T. A. A. *et al.* High-Entropy Alloys as a Discovery Platform for Electrocatalysis. *Joule* **3**, 834–845 (2019).
31. Batchelor, T. A. A. *et al.* Complex-Solid-Solution Electrocatalyst Discovery by Computational Prediction and High-Throughput Experimentation\*\*. *Angewandte Chemie - International Edition* **60**, 6932–6937 (2021).
32. Lee, Y., Suntivich, J., May, K. J., Perry, E. E. & Shao-Horn, Y. Synthesis and Activities of Rutile IrO<sub>2</sub> and RuO<sub>2</sub> Nanoparticles for Oxygen Evolution in Acid and Alkaline Solutions. *J Phys Chem Lett* **3**, 399–404 (2012).
33. Trasatti, S. Electrocatalysis by oxides — Attempt at a unifying approach. *J Electroanal Chem Interfacial Electrochem* **111**, 125–131 (1980).
34. Cheng, J., Zhang, H., Chen, G. & Zhang, Y. Study of Ir<sub>x</sub>Ru<sub>1-x</sub>O<sub>2</sub> oxides as anodic electrocatalysts for solid polymer electrolyte water electrolysis. *Electrochim Acta* **54**, 6250–6256 (2009).
35. Lyons, M. E. G. & Floquet, S. Mechanism of oxygen reactions at porous oxide electrodes. Part 2—Oxygen evolution at RuO<sub>2</sub>, IrO<sub>2</sub> and Ir<sub>x</sub>Ru<sub>1-x</sub>O<sub>2</sub> electrodes in aqueous acid and alkaline solution. *Physical Chemistry Chemical Physics* **13**, 5314 (2011).
36. Lundberg, S. M. & Lee, S. I. A unified approach to interpreting model predictions. *Adv Neural Inf Process Syst* **2017-Decem**, 4766–4775 (2017).
37. Man, I. C. *et al.* Universality in Oxygen Evolution Electrocatalysis on Oxide Surfaces. *ChemCatChem* **3**, 1159–1165 (2011).
38. Halck, N. B., Petrykin, V., Krtík, P. & Rossmeisl, J. Beyond the volcano limitations in electrocatalysis-oxygen evolution reaction. *Physical Chemistry Chemical Physics* **16**, 13682–13688 (2014).
39. Divanis, S., Frandsen, A. M., Kutlusoy, T. & Rossmeisl, J. Lifting the discrepancy between experimental results and the theoretical predictions for the catalytic activity of RuO<sub>2</sub> (110) towards oxygen evolution reaction. *Physical Chemistry Chemical Physics* **23**, 19141–19145 (2021).
40. Diaz-Morales, O., Calle-Vallejo, F., de Munck, C. & Koper, M. T. M. Electrochemical water splitting by gold: evidence for an oxide decomposition mechanism. *Chem Sci* **4**, 2334 (2013).

41. Chen, P.-C. *et al.* Heterostructured Au–Ir Catalysts for Enhanced Oxygen Evolution Reaction. *ACS Mater Lett* **3**, 1440–1447 (2021).
42. Moon, S. *et al.* Single-Step Electrospun Ir/IrO<sub>2</sub> Nanofibrous Structures Decorated with Au Nanoparticles for Highly Catalytic Oxygen Evolution Reaction. *ACS Appl Mater Interfaces* **11**, 1979–1987 (2019).
43. Yeo, B. S. & Bell, A. T. Enhanced activity of gold-supported cobalt oxide for the electrochemical evolution of oxygen. *J Am Chem Soc* **133**, 5587–93 (2011).
44. Petkucheva, E. *et al.* Gold-supported magnetron sputtered Ir thin films as OER catalysts for cost-efficient water electrolysis. *Int J Hydrogen Energy* **43**, 16905–16912 (2018).
45. Ke, Z., Li, L., Jia, Q., Yang, Y. & Cui, H. Facile synthesis of jagged Au/Ir nanochains with superior electrocatalytic activity for oxygen evolution reaction. *Appl Surf Sci* **463**, 58–65 (2019).
46. Gloag, L. *et al.* Three-Dimensional Branched and Faceted Gold–Ruthenium Nanoparticles: Using Nanostructure to Improve Stability in Oxygen Evolution Electrocatalysis. *Angewandte Chemie International Edition* **57**, 10241–10245 (2018).
47. Frydendal, R. *et al.* Enhancing Activity for the Oxygen Evolution Reaction: The Beneficial Interaction of Gold with Manganese and Cobalt Oxides. *ChemCatChem* **7**, 149–154 (2015).
48. Zhang, T. *et al.* Ir-Pd nanoalloys with enhanced surface-microstructure-sensitive catalytic activity for oxygen evolution reaction in acidic and alkaline media. *Sci China Mater* **61**, 926–938 (2018).
49. Shiva Kumar, S., Ramakrishna, S. U. B., Bhagawan, D. & Himabindu, V. Preparation of Ru<sub>x</sub>Pd<sub>1-x</sub>O<sub>2</sub> electrocatalysts for the oxygen evolution reaction (OER) in PEM water electrolysis. *Ionics (Kiel)* **24**, 2411–2419 (2018).
50. Zhu, J. *et al.* Facile Synthesis and Characterization of Pd@Ir<sub>n</sub>L ( $n = 1–4$ ) Core–Shell Nanocubes for Highly Efficient Oxygen Evolution in Acidic Media. *Chemistry of Materials* **31**, 5867–5875 (2019).
51. Back, S., Tran, K. & Ulissi, Z. W. Discovery of Acid-Stable Oxygen Evolution Catalysts: High-Throughput Computational Screening of Equimolar Bimetallic Oxides. *ACS Appl Mater Interfaces* **12**, 38256–38265 (2020).

# 8 Don't panic, alone



When I was starting my PhD project, there were approximately only 15 publications on the topic of High Entropy Alloy Catalysis. Over the course of my project, the field has gained a lot of attention which is evident from the appearance of multiple reviews<sup>11–25</sup> and an exponential growth in number of publications that mention “High Entropy Alloy” and “Catalyst”. By now I estimate the number of publications between 150 and 250 that are covering this topic. However, giving the exact number of publications is challenging due to variations in the naming conventions used by different researchers, such as: “High-Entropy Alloy”, “High-Entropy Oxide”, “Complex Solid Solutions”. These different naming’s require different queries in the search engine to aggregate these papers. Anecdotally, it’s noteworthy that all papers<sup>26–28</sup> published with the affiliation “Center for High Entropy Alloy Catalysis”, not necessarily on the high entropy alloy topic, involuntary became part of the statistics adding up to the distortion. The citations provided here represent only a randomly selected subset of these “imposters”, however there are many more out there. Combined, all the papers on high entropy alloys have significantly advanced the field with notable advancements occurring across various subdivisions of high entropy alloy catalysis. In this chapter I will aim to outline the major developments in the subdivisions of Synthesis, Characterization, Catalysis, Screening, and Theory.

## Synthesis

The majority of work has focused on synthesis and characterization of high entropy alloy catalysts. After all, studying a material in the lab requires its existence. As the foundation for new synthesis methods older high entropy alloy studies can be used. In the pioneering work of Cantor and co-workers<sup>1</sup>, high entropy alloys were synthesized by melting the pure metals in stoichiometric ratios together to form a single solid sample. Yeh and co-workers<sup>2</sup> applied a similar methodology however after they obtained the high entropy alloy sample, they redeposited it on a substrate using a radio frequency sputtering method. In both cases, the researchers were mostly interested in the characterization of the newly synthesized materials and their mechanical properties. Therefore, their choice of synthesis methods was aimed to produce macroscopic alloys, with a high surface-to-bulk ratio, which can be easily investigated. However, the shift to catalysis studies requires to synthesize materials which have a high activity relative to the amount of materials used. Since the absolute activity has a linear correlation to the exposed surface, catalysts are often designed to have a low surface to bulk ratio, which is obtained for nanomaterials. Consequently, the field of high entropy alloys catalysis had to find ways to synthesize nano high entropy alloys and more importantly prove the successful synthesis.

There are multiple ways to synthesize nano high entropy alloy catalysts, of which I made a small selection that will be discussed in the following paragraphs. Probably the most employed method to synthesize high entropy nanoparticles is the wet-chemical approach.<sup>29–42</sup> In this method, precursors are dissolved together followed by the addition of a reducing agent and/or the sample of the sample. Sealing the reaction mixture in an autoclave and heating it above the boiling point of the solvent results in the solvothermal synthesis<sup>43,44</sup>. Likewise, this method is also widely used.<sup>45–48</sup> In fact, I have used the solvothermal method myself to produce the datasets discussed in Chapter 6 and 7. After the synthesis, the obtained nanoparticles can be annealed to produce crystalline materials.<sup>49</sup> Personally, I think that as these two methods require common laboratory glassware, they can be easily employed facilitating the studies of nanoscale high entropy alloys.

The next synthesis methods that have captured my attention are the carbothermal shock synthesis<sup>50,51</sup> and the incipient wetness impregnation synthesis<sup>52–54</sup>. In both approaches, a support, usually carbon, is impregnated with a precursor solution and subsequently dried, resulting in a support covered in precursor-salt. The difference between the two methods lies in the reduction method of the precursor-salt to nanoparticles. In case of the carbothermal shock synthesis<sup>50,51,55,56</sup>, the carbon support is heated to temperatures above 1000 degrees and rapidly cooled back to room temperature in millisecond pulses. The incipient wetness impregnation method on the other hand, reduces the salts at lower temperatures by pyrolysis in Ar or Ar/H<sub>2</sub> atmosphere. While both methods have demonstrated to reliably produce nanoparticles, it's worth noting that they require a slightly more advanced set-up compared to the wet-chemical method.

The final method I would like to highlight would be the electrochemist preferred one, the electrodeposition method.<sup>57,58</sup> In this method, the precursors are dissolved in an electrolyte in

which the substrate is submerged. Depending on the precursors, the electrolyte does not need to be aqueous.<sup>59</sup> By running a high potential or high current, the precursors get reduced plating the substrate. Depending on the chosen potential, current, and pulsing time, it is possible to make different structures ranging from supported nanoparticles to foams.

## Characterization

After synthesizing the nanomaterial, the next challenge is to characterize the obtained material. Traditionally, the initial step in characterizing nanometer sized high entropy alloys is to investigate them with transmission electron microscopy and energy dispersive X-ray spectroscopy. Transmission electron microscopy produces a visualization of nanoparticles through micrographs. From these images it is possible to extract the nanoparticle size and lattice parameters.<sup>60-63</sup> On the other hand, energy dispersive X-ray spectroscopy evaluates the nanoparticle composition and verifies its homogeneity via elemental maps.<sup>55,61,64-66</sup>

In transmission electron microscopy it is difficult to distinguish between single particles and agglomerates. Likewise, low spatial resolution energy dispersive X-ray spectroscopy does not provide information on local elemental segregation. Therefore, X-ray diffraction is often requested as a complementary method. X-ray diffraction aggregates statistical information of multiple nanoparticles allowing to extract lattice parameters, crystallite size and whether the particles are single or mixed phase. It is claimed that if nanoparticles are single phase, the elements must be homogeneously mixed resulting in a high entropy alloy. However as shown in the work of Yeh<sup>67</sup> the presence of two phases does not exclude the formation of a high entropy alloy.

The methods discussed above asses the bulk structure of high entropy alloys. However, for catalytic applications the surface will be decisive for the catalytic performance. Therefore, there is a demand in characterization methods that probe selectively the surface region. Currently, the primarily choice is X-ray photoelectron spectroscopy.<sup>34,68-72</sup> In X-ray photoelectron spectroscopy, the energy and counts of emitted photoelectrons are measured which originate from a layer of approximately 5 nm in depth.<sup>73</sup> In addition, constructing a depth profile by varying the incidence angle of the X-rays is not possible for a rough surface composed of deposited nanoparticles. Therefore, X-ray photoelectron spectroscopy for nanoparticles will always have a minimum depth at which the surface is probed. Consequently, in case of very small nanoparticles, this method produces an image of the entire structure. A possibility to distinguish between bulk and structure might be to investigate the fraction of oxidized elements on the premise that an oxide layer only present in the first monolayer. Thus, there is still an ongoing search for a characterization method that will allow to probe selectively the surface of high entropy alloy nanoparticles.

## Catalysis

Having synthesized and characterized the material the subsequent step involves testing its catalytic performance for a specific reaction. Before we dive into the catalytic studies, I would like to address the elephants in the room. The first, is the choice of normalization. As stated

previously, the measured catalytic activity is linearly correlated to the surface area of the catalyst. However, for high entropy alloys, due to large mixture of different elements there are probably no reliable *in-situ* methods to assess the electrochemically active surface area without resorting to methods like lead under potential deposition. Consequently, researchers are free to choose their normalization method which often favors the narrative of the paper. The second, is the choice of benchmark catalyst as there is nothing better than showcasing the dominance of a newly synthesized catalyst over a reputable catalyst. Yet, there are multiple different industrial catalysts, each optimized for their own set of specific conditions. As a result, measuring an industrial catalyst in conditions for which it was not designed may create an illusion of superiority. In turn, this illusion can further be amplified by the choice of normalization. Therefore, I recommend paying attention to the benchmark catalyst and normalization methods used in high entropy alloy catalysis literature.

High entropy alloys have been widely studied as catalysts for the classical energy conversion reactions consisting of the hydrogen evolution<sup>74–81</sup>, oxygen reduction<sup>35,64,82–85</sup>, oxygen evolution<sup>33,46,47,68,70,71,86–92</sup>. Primarily these studies have focused on assessing the activity of the newly designed high entropy. However, concerning catalytic strategies, these works did not exploit additional benefits high entropy alloys possess besides the formation of active sites. Nonetheless, there are works that try to utilize additional properties of high entropy alloys, which I will discuss below.

An inherent property of high entropy alloys is the presence of multiple active sites, making them versatile catalysts capable of catalyzing various reaction. Classically, a reversible oxygen evolution and oxygen reduction reaction catalyst is a highly desired bifunctional catalyst. Developing this catalyst would allow to reverse a fuel cell to act as electrolyzer. More importantly, this bifunctional catalyst is essential for the development of metal-air batteries. In the field of high entropy alloys, there are a couple works<sup>34,93–97</sup> that have explored this concept. Additionally, there are works that explore reaction pairs present in electrolyzers or fuel cells with the aim to use the same anode and cathode materials. Examples include the hydrogen evolution and oxygen evolution reaction<sup>57,98–107</sup>, and formic acid oxidation and oxygen reduction reaction<sup>108</sup>. However, when a high entropy alloy catalyst is employed for two parallel reactions, the optimal active sites for each may differ. If the catalyst is balanced, only half of the surface area will be active for either of the reactions. Thus, when a bifunctional catalyst is compared to a benchmark catalyst for a single reaction it becomes crucial to properly normalize the surface area as the bifunctional catalyst might require more material to achieve the same observed activity. Consequently, it might be a better practice to compare bifunctional catalysts to composite catalyst systems rather than pure catalysts.

Another way to exploit the presence of multiple active sites it to employ high entropy alloy catalysts for cascade reactions. In cascade reactions reactants undergo several oxidation or reduction step to reach the final product. For example: the full oxidation of hydrocarbons, such as formic acid oxidation<sup>30</sup>, methanol oxidation<sup>109–111</sup>, ethanol oxidation,<sup>39,112</sup> and ethylene glycol oxidation<sup>49,113</sup> are cascade reactions that should produce CO<sub>2</sub> as final product. Likewise, multiple active sites of a high entropy alloy can be used to catalyze multiple reactions in parallel. For example: CO gas, which is poisonous for platinum and humans, is present in small traces in the

currently produced hydrogen gas. Therefore, a hydrogen oxidation reaction catalyst requires to be resistant to CO poisoning. In case of platinum its CO poisoning resistance can be enhanced by alloying it with additional elements, which results in a bifunctional catalyst capable of oxidizing CO to CO<sub>2</sub>.<sup>114</sup> This idea was also the topic of Chapter 2.

Lastly, as demonstrated in Chapter 7 and supported by research from various groups<sup>58,115</sup>, high entropy alloys can be seen as ‘self-supporting’ catalysts. In this concept, the various elements in the high entropy alloy are not only used to increase the activity but also to provide stability and morphology to the catalyst. For example, in the work of Cui and co-workers<sup>116</sup>, the researchers studied a FeCoNiMoAl alloy for the oxygen evolution reaction. The improved activity of the catalyst was appointed to an enhancement in conductivity of the material. Additionally, there are works that investigated the changes in morphology<sup>60,117–119</sup> of high entropy alloys under catalytic conditions. Typically, the beneficial changes involve an increase in porosity which ultimately lead to an increased activity.

## Screening

The number of possible high entropy alloys reaches astronomically large numbers as discussed in Chapter 2.<sup>7</sup> Therefore, this thesis focused on investigating strategies to quickly screen high entropy alloy composition spaces. However, our laboratory was not the only one engaged in experimental screening of high entropy alloy composition spaces. Notably, The University of Bochum developed a high-throughput setup allowing them to rapidly measure the activity and composition of hundreds of compositions.<sup>120</sup>

In their high-throughput setup, the sample is prepared by sputtering deposition of multiple different elements onto a round substrate. The sputtering targets are aligned in a way to produce a film with a composition gradient. Following, by dividing the substrate into pixels, data for different compositions is quickly obtained by scanning the disk with a probe. Thus, the disk can be scanned with X-ray diffraction and energy dispersive X-ray spectroscopy probes to provide the full characterization of the sample. Complementing with the scanning droplet cell, the electrocatalytic performance is also obtained. As a result, a single sputtered disk produces a slice of the composition space. When this process is repeated for a different permutation of the sputtering targets, a different slice of the composition space is created. Therefore, by measuring a sufficient number of permutations, a highly accurate representation of the composition-activity relationship can be obtained.

This setup allows the researchers to produce multiple screening studies, which presently encompass the exploration of high entropy alloy compositions for the hydrogen evolution<sup>121,122</sup>, oxygen reduction<sup>122,123</sup>, and oxygen evolution<sup>124,125</sup>. Intriguingly, in most of their screening studies the optimal composition is found near the edge of the high entropy alloy composition space. This is in line with my studies where the most active composition was not identified as a high entropy alloy.

## Theory

High entropy alloys gained attention for their four core effects, described in Chapter 1, which were anticipated to positively contribute to the activity of a catalyst. However, upon critical examination, we may conclude that they poorly explain the observed catalytic performances. The high entropy effect allows to synthesize novel unseen materials, but it can't explain why the new material suddenly performs better. The sluggish diffusion might explain the stability of the high entropy alloy core, but it doesn't explain surface dissolution, which has the paramount impact on catalytic performance. The cocktail effect unfortunately is not adding anything new to the table. Only the lattice distortion effect, which changes the d-band structure of the catalyst, might be responsible for changes in catalytic performance. Therefore, developing a theory for high entropy alloy catalysis is essential to explain novel observations.

The most important theoretical paper is the paper from Bachelor<sup>6</sup> and co-workers where they demonstrate how the single descriptor approach can be used to model the activity of a high entropy alloy catalyst. In this paradigm, for a high entropy alloy system the binding energy of the descriptor is described by a distribution rather than a discreet value. After, this distribution is transformed into a single activity, which the authors do by assuming a Koutecky-Levich like model, outlined by Eq. 8.1 and Eq. 8.2. In these equations,  $j_k$  and  $j_l$  represent the kinetic and diffusion limited current respectively.  $\Delta G$  denotes the binding energy of the descriptor, which in case of a distribution is a list of binding energies.  $\Delta G_{opt}$  signifies the optimal binding energy of this descriptor, which can be derived from theory.  $k_B$  and  $T$  stand for the Boltzmann constant and temperature, respectively and  $a$  is a scaling factor, often assumed to be 1. Of all these variables,  $a$ ,  $j_l$ , and  $\Delta G_{opt}$  serve as fitting parameters to which values can be assigned based on prior knowledge. However, as demonstrated in the recent work of Clausen and co-workers,<sup>126</sup> these values can be obtained from fitting the model to an experimentally obtained dataset.

$$j = \sum \frac{a}{\frac{1}{j_k} + \frac{1}{j_l}} \quad (8.1)$$

$$j_k \propto e^{\frac{-|\Delta G - \Delta G_{opt}|}{k_B T}} \quad (8.2)$$

Calculating the activity from the binding energy distribution is a relatively straightforward task, but obtaining the binding energy distributions is a computationally costly challenge. For instance, considering a high entropy alloy of 5 different elements where an active site is composed of 8 atoms, there would be  $5^8 = 390\,625$  different possible active sites. Expanding the active site by including more atoms would lead to an exponential growing number of arrangements. Very quickly it becomes impossible to evaluate all possible active site, and DFT calculations need to resort to statistical tricks to speed up the calculations.<sup>9,127-129</sup> Another strategy is to find the exact number of atoms necessary to describe the binding energy of the active site. Knowing this number would significantly cut down on the number of permutations that need to be evaluated to produce the binding energy distribution. In fact, based on current works, the

binding energy of the active site is mostly influenced by a few atoms. These are the atoms in the first coordination shell<sup>130,131</sup> and several atoms in the bulk that happen to lie in the same 1-dimensional plane as the adsorbing atom.<sup>132</sup> In these studies, the lattice effect, that was initially believed to have major influence on the high entropy alloy catalytic activity, got almost completely overshadowed by the ligand effect of the surrounding atoms.<sup>133</sup> Consequently, I conclude that the catalytic performance of high entropy alloys cannot be explained by any of the four core effects.

An alternative approach to deriving the full binding energy distribution is to derive it from a simulated surface. In this methodology, a high entropy alloy surface of at least 10 000 atoms is simulated, which subsequently is populated with the adsorbing molecules.<sup>120</sup> By introducing constraints, such as that adsorbates cannot bind on neighboring sites and adsorbates preferably bind to strong binding sites, a different binding energy distribution is obtained from an unconstrained simulation. This binding energy distribution is hypothesized to be more realistic, however, the search for the right set of constraints is ongoing.

A large fraction of theoretical work has been carried out on the oxygen reduction reaction. I think that the reason behind it is that this reaction can be described with a single descriptor, simplifying its modeling. However, theoretical models are also being developed for other catalytic reactions, which include the hydrogen oxidation<sup>134</sup>, CO oxidation<sup>135</sup>, formic acid oxidation<sup>136</sup>, nitrogen reduction<sup>128,130,137,138</sup>, nitrate reduction<sup>139</sup>, and CO<sub>2</sub> Reduction<sup>140,141</sup>.

As a final comment on the developments in theory, I would like to explore the use of the Koutecky-Levich approximation in Eq. 8.1. For this investigation, I chose the oxygen reduction reaction on a platinum-based intermetallic binary alloy as a model system. In this system, the kinetic current  $j_k$  is modeled with the Butler-Volmer equation, as outlined in Eq. 8.3. In this equation,  $j_0$  is the exchange current density, set to the value for platinum<sup>142</sup> of  $4.8 \times 10^6$ ,  $n$  is the number of electrons transferred set to 3.7,  $F$  is faraday constant (96 485),  $R$  is the gas constant (8.413) and  $T$  is the temperature at 298 K. The intermetallic alloy features two types of active sites, each occupying the same fraction of the surface with activities of  $1 \times j_0$  and  $0.0001 \times j_0$ .

$$j_k = j_0 \left( -e^{\frac{-0.5nF(E-1.23)}{RT}} + e^{\frac{0.5nF(E-1.23)}{RT}} \right) \quad (8.3)$$

Using Eq. 8.1 and assuming a diffusion limited current  $j$  of -7500 the polarization curve can be modeled as depicted in Figure 8.1. This figure reveals two diffusion limited plateaus, a phenomenon that contradicts experimental observations. The presence of this artifact is attributed to the nature of Eq. 8.1. In this equation, each active site is treated as an independent microelectrode, each having an independent spherical diffusion layer with an associated diffusion-limited current as illustrated in Figure 8.2. In reality, as these sites are neighboring, the diffusion layers of these microelectrodes will overlap creating a planar diffusion layer.

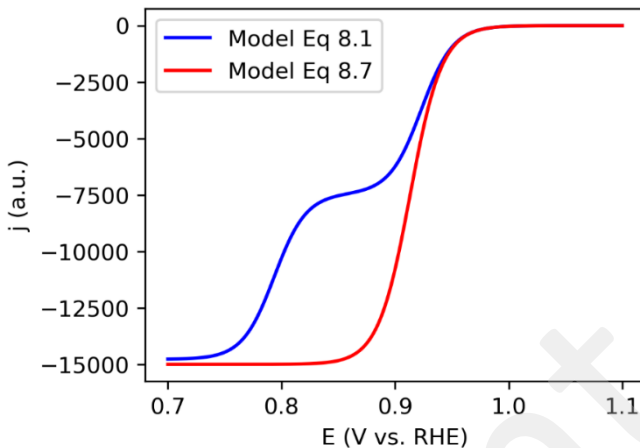


**Figure 8.1.** The modeled polarization curve of an intermetallic alloy that has two sites with the activity of  $1 \times j_0$  and  $0.0001 \times j_0$  respectively. The blue curve is obtained by employing Eq. 8.1. The red curve is obtained by applying Eq. 8.7.



**Figure 8.2.** A schematic depicting the two diffusion modes of a high entropy alloy surface. Top scheme shows the individual spherical diffusion layer. Bottom scheme shows the shared planar diffusion layer.

Consequently, the activity of the entire surface is governed by the competition between the kinetic current, spherical diffusion-limited current and planar diffusion-limited current. Therefore, I propose an initial correction outlined by the model in Eq. 8.4-8.7. In these equations,  $j_k$  is the current of each individual site,  $f$  represents the fraction that the active site with activity  $j_k$  occupies with the sum of all  $f$  equal to one,  $j_{l,sphere}$  is the diffusion-limited current density of the spherical diffusion layer,  $j_{l,planar}$  is the diffusion-limited current of the planar diffusion which via coefficient  $c$  is related to the spherical diffusion limited current  $j_{l,sphere}$ .

$$j_{sites} = \sum f \frac{1}{\frac{1}{j_k} + \frac{1}{j_{l,sphere}}} \quad (8.4)$$

$$j_{HEA}^{-1} = j_{sites}^{-1} + j_{l,planar}^{-1} \quad (8.5)$$

$$j_{l,sphere} = c \times j_{l,planar} \quad (8.6)$$

$$J_{HEA} = \frac{1}{\sum f \frac{1}{\frac{1}{j_k} + \frac{1}{j_{l,sphere}}}} = \frac{1}{\sum f \frac{1}{\frac{1}{j_k} + \frac{1}{c \times j_{l,planar}}}} \quad (8.7)$$

This model is derived based on the following reasoning. Initially, the maximum activity, determined by spherically diffusion-limited current, is calculated for the entire surface using Eq. 8.4. Subsequently, Eq. 8.5 is employed to constrain this total current by the planar diffusion-limited current of the entire surface. The effects of these operations can be visualized by modelling a series of binary platinum alloys with varying platinum content, as shown in Figure 3. In this model, the second element is assumed to have an activity 100 000 times less than the activity of platinum. At high platinum concentrations, the kinetic current scales linearly with the number of platinum active sites and the planar diffusion-limited current is reached before the effects of the spherical diffusion-limited current become evident. In contrast, at low platinum concentrations, where the platinum sites are too widely spread, the activity of individual platinum active sites get first limited by their spherical diffusion-limited current resulting in an intermediate plateau. Only when the active sites of the second metal reach substantial turnover frequencies, the total planar diffusion limited current is reached.

In this proposed model, the final step involves determining coefficient  $c$  by assuming the equations for both the spherical and planar diffusion-limited current. The spherical

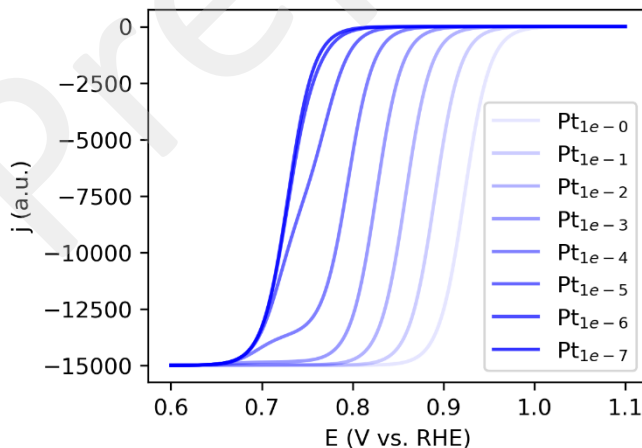


**Figure 8.3.** Modeled polarization curve of a Pt-based binary alloy with two active sites using Eq. 8.7 for different Pt concentrations. The second active site has an activity 100 000 times less than the activity of Pt.  $j_{l,planar}$  and  $c$  are set to -15000 and 100 000, respectively.

diffusion-limited current can be calculated using Eq. 8.8<sup>143</sup> whereas for the planar diffusion-limited current the Levich equation in Eq. 8.9<sup>144</sup> can be assumed. In these equations,  $n$  is the number of electrons transferred,  $A$  is the geometric surface area,  $D$  is the diffusion coefficient of the reactant,  $F$  is the Faraday constant,  $C$  the concentration of the reactant and  $r$  is the radius of the electrode,  $\omega$  is the rotation rate, and  $v$  is the kinematic viscosity of the solvent. Combining both equations results in Eq. 8.10. Solving this system for the oxygen reduction reaction requires to insert values of  $D = 1.9 \times 10^{-5} \text{ cm}^2 \text{ s}^{-1}$ ,  $v = 0.01 \text{ cm}^2 \text{ s}^{-1}$ , and an assumed  $\omega$  of  $104 \text{ rad s}^{-1}$ .<sup>142</sup> In this case,  $r$  is estimated to be the radius of a single atom, which is approximately  $0.2 \times 10^{-7} \text{ cm}$ . As a result, the appropriate value for  $c$  is 100 000. As this value depends only on the diffusion coefficient, kinematic viscosity of the solvent, the rotation rate, and radius of an atom, this value for  $c$  can be used for other reactions in aqueous electrolytes for which the reactant has a similar diffusion coefficient.

$$i_{l_{sphere}} = \frac{nFADC}{r} \quad (8.8)$$

$$i_{l_{planar}} = 0.62nFAD^{\frac{2}{3}}\omega^{\frac{1}{2}}v^{-\frac{1}{6}}C \quad (8.9)$$

$$c = \frac{j_{l_{sphere}}}{j_{l_{planar}}} = \left( \frac{0.62nF^{\frac{2}{3}}\omega^{\frac{1}{2}}v^{-\frac{1}{6}}C r}{nFDC} \right)^{-1} = \left( 0.62D^{-\frac{1}{3}}v^{-\frac{1}{6}}\omega^{\frac{1}{2}}r \right)^{-1} \quad (8.10)$$

This model assumes that the high entropy alloy surface is described by microelectrodes with the size of a single atom. Let's consider the case where instead it is described by a sum of microelectrodes each composed of  $m$  atoms, as schematically depicted in Figure 8.4. In this case, the model takes the shape of Eq. 8.11-8.13. If  $c$  is calculated for a single atom microelectrode according to Eq. 8.10, the radius  $r$  will scale approximately with  $\sqrt{m}$ . In this equation,  $f$  represents the fraction that microelectrodes with identical average  $j_k$  occupy with the sum of all  $f$  equal to one.

$$j_{sites} = \sum f \frac{1}{\frac{1}{\frac{1}{m} \sum_m j_k} + \frac{1}{j_{l_{sphere}}}} \quad (8.11)$$



**Figure 8.4.** A schematic of microelectrodes composed of two active sites sharing one spherical diffusion layer, while the surface shares one combined planar diffusion layer.

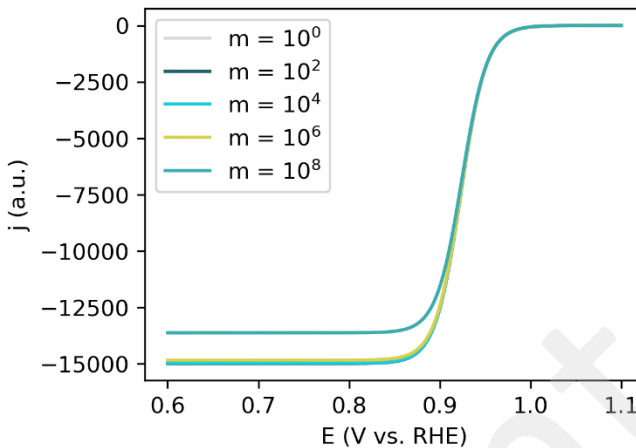


**Figure 8.5.** Modeled polarization curve of Pt based on Eq. 8.13 for different values of  $m$ .

$$j_{l_{sphere}} = \frac{1}{\sqrt{m}} c \times j_{l_{planar}} \quad (8.12)$$

$$j_{HEA} = \frac{1}{\sum f \frac{1}{\frac{1}{\frac{1}{m \sum_m j_k}} + \frac{1}{j_{l_{planar}}}}} \quad (8.13)$$

This model faces two complications. Firstly, when the model in Eq. 8.13 is applied to pure platinum, its solution should be independent of  $m$ . However as shown in Figure 8.4, this is not the case. Since the spherical diffusion-limited current scales with the radius of the microelectrode, at  $m$  larger than  $10^8$  atoms, which is equivalent to a  $13 \mu\text{m}^2$  electrode, the spherical diffusion-limited current gets in the same range as the planar diffusion-limited current. As a result, the system is unable to reach the same current density as set by the planar diffusion, leading to artifacts. Consequently, at large  $m$  it is worth to assume that each microelectrode is limited by its own planar diffusion-limited current transforming Eq. 8.13 into Eq. 8.14.

$$j_{HEA} = \sum f \frac{1}{\frac{1}{\frac{1}{m \sum_m j_k}} + \frac{1}{j_{l_{planar}}}} \quad (8.14)$$

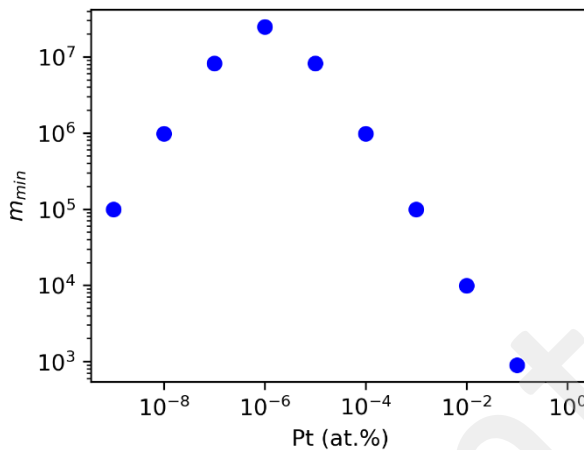


**Figure 8.6.** The  $m_{min}$  as calculated from Eq. 8.18 for the distributions used in the modelling of Figure 8.3. This distribution is composed of Pt and a second element which has an activity 100 000 less than Pt.

The second complication is evaluating the activity of different microelectrodes composed of  $m$  atoms. Considering that the activity distribution of a high entropy alloy is described by 10 000 different active sites, the number of possible microelectrodes is equal to  $10\ 000^m$ . Thus, even if the number of atoms  $m$  is limited to 10, the number of microelectrodes is  $10^{40}$ , which poses a computationally impossible task. Instead, these values can be approximated by employing the bootstrap method. According to the bootstrap method,  $x$  samples of  $m$  atoms are created by sampling  $m$  times the 10 000 different active sites with replacement. By using a large  $x$ , such as  $10^6$ , a decent representation of the activity distributions is obtained. In the bootstrap method, as the number of computations scale with  $x \times m$ , only  $10^7$  evaluations will be necessary accelerating the computation by a factor of  $10^{33}$ .

The bootstrap method also allows to employ the central limit theorem to further simplify the calculation. The average kinetic current of 10 000 different active sites  $m$  can be described by a normal distribution ( $X_{jk}$ ) with an average ( $\mu_{jk}$ ) and standard deviation ( $\sigma_{jk}$ ) (Eq. 8.15). Therefore, applying the central limit theorem to the bootstrap method allows to calculate the standard error ( $\sigma_{bootstrap}$ ) with Eq. 8.15. If  $\sigma_{bootstrap}$  is sufficiently small, for example 10%  $\mu_{jk}$ , the results of the bootstrap method can be approximated with  $\mu_{jk}$ . For this, the minimum number of atoms ( $m_{min}$ ) can be calculated using Eq. 8.18. Thus, if  $m$  is larger than  $m_{min}$  Eq. 8.13 can be transformed into Eq. 8.19. Combining Eq. 8.19 further with Eq. 8.14 creates Eq. 8.20. As an illustration, Figure 8.6 shows the different  $m_{min}$  for the distributions used in Figure 8.3. According to this figure,  $m_{min}$  is for certain systems smaller than 10 000 atoms, equivalent to a  $1300\text{ nm}^2$  microelectrode.

$$X_{jk} \sim N(\mu_{jk}, \sigma_{jk}) \quad (8.15)$$

$$\sigma_{bootstrap} = \frac{\sigma_{jk}}{\sqrt{m}} \quad (8.16)$$

$$\sigma_{bootstrap} = \frac{\sigma_{jk}}{\mu_{jk}\sqrt{m}} < 0.10 \quad (8.17)$$

$$m_{min} = \left( \frac{\sigma_{jk}}{0.10 \times \mu_{jk}} \right)^2 \quad (8.18)$$

$$j_{HEA} = \frac{1}{\sum f \frac{1}{\frac{1}{\mu_{jk}} + \frac{1}{\frac{1}{\sqrt{m}} c \times j_{l_{planar}}}}} + \frac{1}{j_{l_{planar}}} \quad (8.19)$$

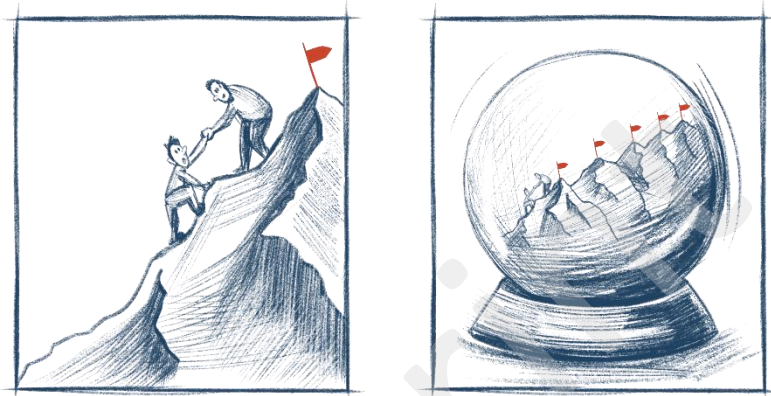
$$= \frac{1}{\frac{1}{\mu_{jk}} + \frac{1}{\frac{1}{\sqrt{m}} c \times j_{l_{planar}}}} + \frac{1}{j_{l_{planar}}} \\ j_{HEA} = \frac{1}{\frac{1}{\mu_{jk}} + \frac{1}{j_{l_{planar}}}} \quad (8.20)$$

In conclusion, modeling the diffusion limited behavior for high entropy alloy catalysts is a complex endeavor for which no conclusive model yet exists. Here, I propose to use the model outlined by Eq. 8.13. However, this model requires to assume the number of active sites ( $m$ ) of a single microelectrode. If the number is set to one, Eq. 8.7 is obtained. However, if the number of active sites is varied, I suggest the use of Eq. 8.14 as its solutions are consistent when tested on a pure metal. If the number of active sites is larger than one but smaller than  $m_{min}$  the system can only be approximated using the bootstrap method. Finally, when the number of active sites becomes larger than  $m_{min}$ , Eq. 8.13 and 8.14 transform into the solvable Eq. 8.19 and 8.20, respectively. Hopefully, computer simulations of the diffusion layer of high entropy alloy catalysts will validate these models.



# Epilogue

When one project ends, other start. Let's see which treasures lie ahead in the fortune-telling glass ball



Before I conclude my thesis, I would like to address one final question: Is it possible to find a high entropy alloy catalyst that is more active than the current state of the art catalysts? The majority of high entropy alloy catalyst studies report that high entropy alloy catalysts outperform benchmark catalysts. This suggests a survivor bias that all billion possible high entropy alloy catalysts are superior catalysts to the existing ones, an improbable statistical scenario. Furthermore, my experimental screening studies, our theoretical models<sup>6,9,126</sup>, and the screening studies of the University of Bochum<sup>120–125</sup> all indicate that starting with an equimolar high entropy alloy, its activity can often be enhanced by tuning its composition. Thereby, the most active composition found may not even meet the basic requirements to be classified as a high entropy alloy. So, our intuition tells us that high entropy alloy catalysts cannot compete in activity with pure metals or bimetallic alloys. In the upcoming paragraphs, I will mathematically proof this intuition right.

The mathematical proof relies on the theoretical framework of high entropy alloy catalysis developed by Thomas Batchelor and co-workers.<sup>6</sup> Using the DFT descriptor-based approach, the activity of a high entropy alloy is calculated by evaluating the binding energy of a catalytic intermediate for each active site. Since a high entropy alloy has many different active sites, it produces a binding energy distribution, which using an Arrhenius type of equation (Eq. 8.2) transforms the binding energy into an activity. This equation into account the Sabatier principle, which states that the ideal binding energy of an intermediate should not be too large nor too small. Therefore, for each reaction there is an ideal binding energy which will correspond to the theoretically maximum activity.

$$\frac{i_{ideal}}{i_{Pt}} = \frac{e^{\frac{-|\Delta G_{Opt} - \Delta G_{opt}|}{k_B T}}}{e^{\frac{-|\Delta G_{Pt} - \Delta G_{opt}|}{k_B T}}} = e^{\frac{0.1}{k_B T}} \approx 48 \quad (9.1)$$

Let's consider the example of the oxygen reduction reaction. The optimum binding energy of OH, relative to the binding energy of OH on platinum is 0.1 eV. We can use this difference of 0.1 eV to calculate the theoretical activity of the ideal catalyst, given that the scaling relations<sup>145</sup> are true. According to Eq. 9.1, the ideal catalyst would be approximately 48 times more active than pure platinum.

When a metal catalyst is alloyed with a second metal, a fraction of the monometallic sites gets substituted with active sites corresponding to the second metal or binary combinations. However, to maintain or enhance the overall activity, the surface loss of the most active pure metal sites needs to be compensated by an increased activity of the binary sites. Failure to achieve this compensation would result in the pure metal being more active than the alloy. This concept extends to ternary, quaternary, and high entropy alloy. I will term this concept, the surface-activity trade-off, which will be quantified using a statistical model described by the assumptions in Table 9.1.

**Table 9.1** List of assumptions of the surface-activity trade-off model

<b>A1</b>	An active site is defined by a center atom and six neighbors.
<b>A2</b>	The activity of an active site is defined by the center atoms and the number of distinct atoms. Thus, all permutations have the same activity.
<b>A3</b>	The activity of the sites increases with increasing the number of distinct atoms in the neighborhood.
<b>A4</b>	The composition should maximize the fraction of the most active sites.
<b>A5.1</b>	Only active sites containing M1 in the center are considered active, the other active sites are assumed inactive.
<b>A5.2</b>	Dead-surface corrected model: Active sites containing M2 in the center are considered 32% less active than the active sites containing M1 in the center. The rest of the sites are assumed to be inactive.
<b>A6</b>	The most complex active sites need to compensate with their activity the loss of the surface area of the less complex and less active sites.

The first step in constructing the surface-activity trade-off involves defining the active sites for which the prevalence will be calculated. In this model, the first assumption (A1) is that an active is defined as an on-top site composed of a single center atom surrounded by six atoms. The second assumption (A2) is that the binding energy and the activity of the active site is defined by the center atom and the total number of distinct atoms it is composed of. A schematic representation of this concept is depicted in Figure 9.1. For example: a binary alloy is described by four types of active sites. The two monometallic sites composed of metal 1 ( $m_1$ ) and metal 2



**Figure 9.1.** Schematic representation the seven atomic active sites as defined for the surface-activity trade-off model. From left to right the models represent the binary, ternary, quaternary, and quinary sites. The colors indicate distinct elements.

( $m_2$ ) and two binary sites ( $m_1, m_2$ ) with either  $m_1$  or  $m_2$  in the center. A three metallic alloy is described by three monometallic sites ( $m_1, m_2, m_3$ ), three binary sites ( $m_1, m_2/m_3; m_2, m_1/m_3; m_3, m_1/m_2$ ), and three trimetallic sites ( $m_1m_2m_3; m_2m_1m_3; m_3m_1m_2$ ). The third assumption (A3) is that the activity of the active sites should increase with respect to complexity. The fourth assumption (A4) is that the considered compositions should maximize the prevalence of the most active site, which according to assumption A3 is the most complex site.

These assumptions achieve one crucial aspect, namely, an overestimation of the prevalence of the most complex sites. In comparison, a bridge site would require the fixation of three elements which statistically will have a lower prevalence than a single fixed center atom, as in A1. Likewise, in a realistic scenario, binary sites containing  $m_1, m_2$  or  $m_1, m_3$  will exhibit different activities, suggesting a lower prevalence of the most active binary sites. Consequently, this model underestimates the activity required to compensate for the surface loss. Therefore, if this model suggests that compensating for surface loss is impossible, it can be reasonably concluded that it is indeed unattainable.

The next assumption (A5.1) is that only active sites with  $m_1$  in the center are considered active and the rest of the surface is considered inactive. The justification of this assumption is based on Eq. 9.2, which quantifies the effective surface loss of the most active site ( $s_1$ ) to a less active site ( $s_2$ ). In this equation,  $e^{0/k_B T} = 1$  corresponds to the activity of  $s_1$ ,  $e^{-\Delta G/k_B T}$  to the activity of  $s_2$  relative to  $s_1$  and  $f_{lost}$  represent the fraction occupied by  $s_2$ . The solution to the effective surface loss is illustrated in Figure 9.2. This figure reveals that when  $s_2$  has a binding energy 0.01 eV smaller than  $s_1$ , the effective loss is 32%, a non-negligible contribution requiring the use of A5.2. However, when the difference is at least 0.06 eV the effective loss is 90%. Differences larger than 0.1 eV correspond to over 98% effective loss, justifying the approximated of 100% loss and supporting the use of A5.1.

$$\eta_{loss} = \frac{\left( e^{\frac{0}{k_B T}} - (1 - f_{lost})e^{\frac{0}{k_B T}} - f_{lost}e^{-\frac{\Delta G}{k_B T}} \right)}{f_{lost}} = 1 - e^{-\frac{\Delta G}{k_B T}} \quad (9.2)$$

In the context of the oxygen reduction reaction, the difference in the binding energy for OH relative to pure platinum is for most elements exceeds 0.1 eV. The only exception is Pd, the

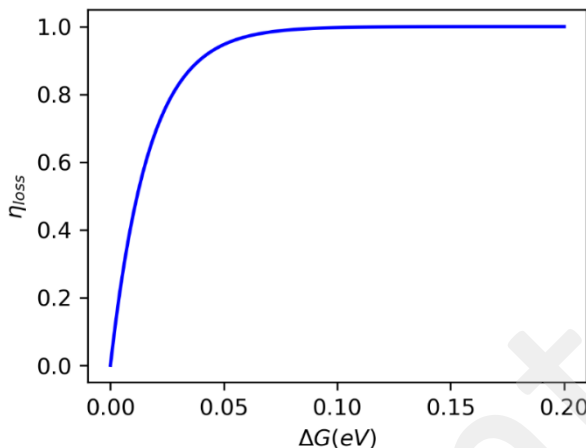


**Figure 9.2.** The effective surface loss as calculated from Eq. 9.2.

second most active catalyst, for which DFT models do not provide a conclusive value.<sup>9,145,146</sup> However, experimental evidence indicates that the oxygen reduction reaction on palladium is highly facet-sensitive. Pd(100) is approximately three times more active than platinum, whereas Pd(111) and Pd(110) are 5 and 10 times less active, respectively.<sup>147</sup> Therefore, palladium forms an exception whose activity cannot be solely described by the OH binding energy. For simplicity, this exception can be neglected, and assumption A5.1 can be applied to the oxygen reduction reaction.

These assumptions allow to calculate the prevalence the prevalence of different active sites for various compositions. While it is theoretically possible to calculate all possible permutations that satisfy A2, the complexity of the calculation increases significantly for a 5-element system, with a total of  $5^6=15625$  permutations, adding the risk of making algebraic mistakes. To mitigate this, I used a simulation approach, generating all possible permutations and selecting the ones that full fill A2. Subsequently, using Eq. 9.3, the prevalence of the different active sites can be computed. In this equation,  $e$  represents the total number of elements in the alloy,  $n$  is the number of elements in the active site,  $x$  is the index of the center atom,  $f_m$  the fraction of the element, and  $c$  the frequency of element  $m$  in the six-atom surrounding.

$$P(e, n, x) = f_{m_x} \sum f_{m_1}^{c_1} f_{m_2}^{c_2} f_{m_3}^{c_3} f_{m_4}^{c_4} f_{m_5}^{c_5} \quad (9.3)$$

The prevalence of the different active sites is calculated for compositions satisfying A4 and the summary of this calculation is schematically visualized in Figure 9.3. In this figure, the binding energies assigned to the different active sites are arbitrarily chosen, yet they conform to the assumptions A3 and A5.1. Due to A5.1, the catalyst's activity is solely described by the activities of active sites contain  $m_1$  in the center. These prevalences are summarized in Table 9.2.

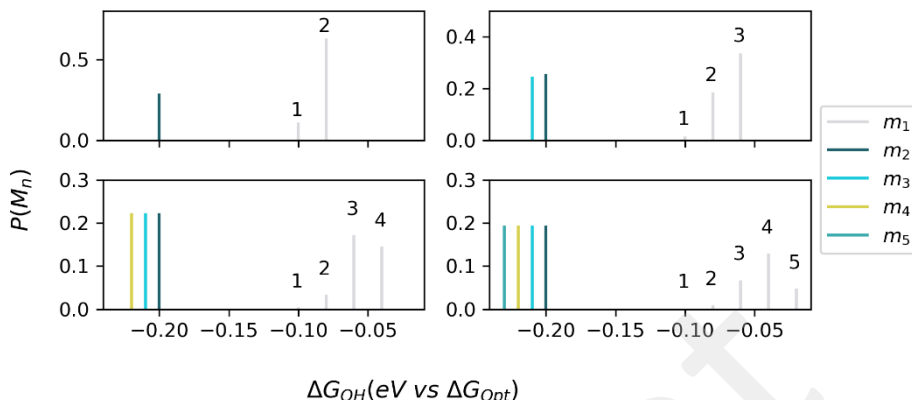


**Figure 9.3.** A schematic representation of the binding energy distributions according to the statistical model using A5.1. The numbers above the distributions represent the number of elements in the active site. The colors represent the metal that is in the center of the active site. The value of  $\Delta G_{OH}$  for the monometallic sites of  $m_1$  is fixed at -0.1 eV equal to the binding energy of platinum. The rest of the binding energies is chosen arbitrary; however, the most active sites are put in the order of increased activity. On the contrary, dead sites are placed at binding energies below -0.2 eV to emphasize their unimportance.

**Table 9.2.** The prevalence of the different active sites for a pure metal, binary alloy, ternary alloy, quaternary alloy, and quinary alloy based on A5.1. The considered compositions maximize the prevalence of their most complex site.

	[1,0,0,0,0]	[0.72,0.28,0,0,0]	[0.51, 0.25, 0.24,0,0]	[0.34, 0.22, 0.22, 0.22,0]	[0.24, 0.19, 0.19, 0.19, 0.19]
<b>1-element</b>	1	0.10031	0.00897	0.00053	0.00005
<b>2-element</b>		0.61969	0.17860	0.02988	0.00588
<b>3-element</b>			0.32993	0.16836	0.06384
<b>4-element</b>				0.14123	0.12556
<b>5-element</b>					0.04464

The prevalence of each active site allows to calculate the surface loss when alloying the catalyst. For example, alloying a pure metal to a 5-element alloy results in the removal 99.995 % of the pure metallic surface. Similarly, alloying a binary alloy to a 5-element alloy results in the loss of 62% of the surface dedicated to the binary active sites. This loss for each active site depending on the degree of alloying is displayed in Table 9.3.

**Table 9.3.** The surface loss of the most active n-element site when alloying it further based on A5.1.

	Binary alloy	Ternary alloy	Quaternary alloy	Quinary alloy
<b>1-element</b>	0.89969	0.99103	0.99947	0.99995
<b>2-element</b>		0.44109	0.58981	0.61381
<b>3-element</b>			0.16157	0.26609
<b>4-element</b>				0.01567

The lost surface needs to be compensated with the most active site, leading to the final assumption (A6). In case of an alloy, this needs to be the most complex site according to A3. Thus, by dividing the lost surface by the gained surface, we can determine the breaking point at which the alloy starts surpassing its separate components. These breaking points are listed in Table 9.4 for A5.1. Let's consider the results for a 5-element high entropy alloy: the 4.5% 5-element active sites need to compensate 99.9995% of the lost mono-metallic sites, requiring them to be 22.4 times more active than the mono-metallic sites. Additionally, the 5-element active site needs to outperform its most active binary component by 13.8 times, the most active 3-element component by 6.0 times, but not necessarily the 4-element sites. However, the latter is an artifact due to A2, which results in the loss of 4-element sites to be less than introduced from the 5-element sites. If one of these rules is not fulfilled, the 5-element alloy will fall short to the alloy that maximized that site.

**Table 9.4.** The break-even activity of the most complex site of an alloy relative to the activity of its 1-element, 2-element, 3-element, 4-element site based on A5.1.

	Binary alloy	Ternary alloy	Quaternary alloy	Quinary alloy
<b>1-element</b>	1.45	3.00	7.08	22.40
<b>2-element</b>		1.34	4.18	13.75
<b>3-element</b>			1.14	5.96
<b>4-element</b>				0.35

Returning to the example of the oxygen reduction reaction and OH binding energy as the descriptor of the catalyst. The activity of an ideal catalyst is 48 times the activity of pure platinum. According to Table 9.4, a 5-element active site needs to be 22 times more active than pure platinum to outcompete it. Given that 22 is less than 48, high entropy alloys can indeed surpass the performance of pure platinum for the oxygen reduction reaction. Now, turning to the next comparison with binary alloys, which the 5-element sites need to outperform by 13.8 times. In the paper of Bachelor and co-workers<sup>6</sup>, the authors report the Ir<sub>17.5</sub>Pt<sub>82.5</sub> is 28 times more active than pure platinum. Using Table 9.2, the activity of the binary sites can be estimated to be 28/0.62 = 45 times the activity of platinum, which is very close to the theoretical maximum. Consequently, a 5-element alloy would require 5-element sites with an activity of 45×13.8 = 621 times the activity of platinum, which is impossible according to theory.

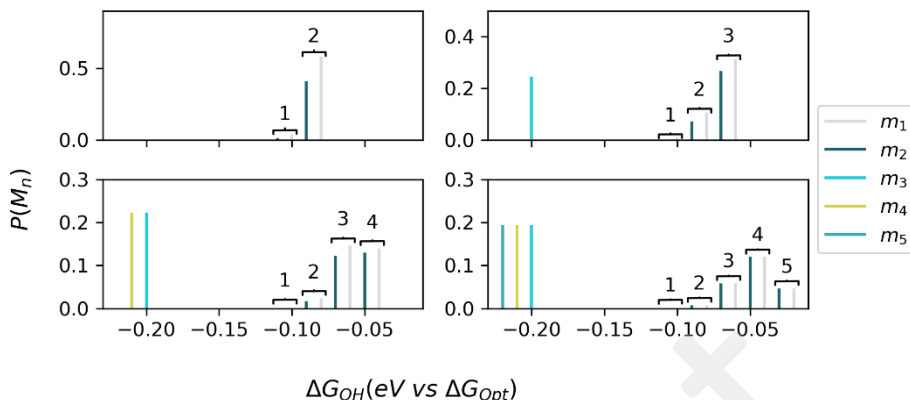


**Figure 9.4.** A schematic representation of the binding energy distributions assuming that the catalysis takes place on two very active elements ( $m_1, m_2$ ) following A5.2. The numbers represent the complexity of the active sites, whereas the colors represent the metal which is in the center of the active site. The OH binding energy of the  $m_1$  is fixed at -0.1 eV. The second-best element has an activity 0.01 eV less than the most active element. This effect propagates in the ordering of the different active sites. The active sites of  $m_3, m_4$ , and  $m_5$  are considered inactive which is emphasized by them having a binding energies less than -0.2 eV.

This statistical model also allows to calculate the maximum increase in activity assuming that all 5-element sites have ideal activities. In the case of oxygen reduction reaction, this would correspond to a  $48 \times 0.045 = 2.2$  increase in activity relative to platinum. As a result, if there is a binary, ternary, or quaternary alloy that has an activity higher than 2.2 times pure platinum, a 5-element alloy won't be able to compete with it.

Let's consider a system where the active sites of the second element have binding energies 0.01 eV less than those of the primary element. According to Eq. 9.2, in this system, the effective loss to the second element amount to 32%, which cannot be neglected requiring a dead-surface correction (A5.2). This dead-surface correction results in a change of distribution depicted in Figure 9.3 to the distribution depicted in Figure 9.5. The surface prevalence of the most active sites can then be calculated with Eq. 9.4 resulting in Table 9.5. In this equation  $P(e,n,1)$  and  $P(e,n,2)$ , correspond to the surface prevalence of  $m_1$  and of  $m_2$  sites respectively.  $C$  represents the effective surface area factor, calculated from Eq. 9.5, yielding a value of 0.68 in the case of a 32% effective surface loss. Subsequently, the breaking-point factors can be calculated using the same method as for the model using A5.1 leading to the values in Table 9.6.

$$P(e, n, C) = P(e, n, 1) + P(e, n, 2)C \quad (9.4)$$

$$C = 1 - \eta_{loss} \quad (9.5)$$

**Table 9.5.** The prevalence of the different active sites for a pure metal, binary alloy, ternary alloy, quaternary alloy, and quinary alloy based on A5.2. The considered compositions maximize the prevalence of their most active site based on Eq. 9.4.

	[1,0,0,0,0]	[0.6,0.4,0,0, ,0]	[0.41, 0.33, 0.26,0,0]	[0.30, 0.26, 0.22, 0.22,0]	[0.22, 0.22, 0.18, 0.19, 0.19]
<b>1-element</b>	1	0.02911	0.00224	0.00027	0.00004
<b>2-element</b>		0.84289	0.14625	0.03007	0.00754
<b>3-element</b>			0.48591	0.22385	0.09276
<b>4-element</b>				0.22261	0.19605
<b>5-element</b>					0.07320

**Table 9.6.** The break-even activity of the most complex site of an alloy relative to the activity of its 1-element, 2-element, 3-element, 4-element site based on A5.2.

	Binary alloy	Ternary alloy	Quaternary alloy	Quinary alloy
<b>1-element</b>	1.15	2.05	4.49	13.66
<b>2-element</b>		1.43	3.65	11.41
<b>3-element</b>			1.18	5.37
<b>4-element</b>				0.36

This dead-surface corrected model further overestimates the prevalence of the active sites, and accordingly reduces the demands on the activity even more. However, when this model is applied to the oxygen reduction reaction it leads a consistent outcome. The binary site of Ir<sub>17.5</sub>Pt<sub>82.5</sub> now has an estimated activity of 28/0.84 = 33.4 times the activity of platinum. 5-element sites would require an activity of 33.3×11.4 = 380 times the activity of platinum to compete with it, which is still theoretically impossible. Therefore, I can safely conclude that, given that this statistical model is correct, 5-element active site can compete with pure platinum for the oxygen reduction reaction, but they can never compete with the optimized binary alloys. Furthermore, this model indicates that the maximum increase in activity originating from the 5-element sites is 2.2 or 3.5 depending on the use of the dead-surface correction. Consequently, reports of high entropy alloys strongly outperforming platinum for the oxygen reduction reaction most likely lend their activity from their binary components or an increased electrochemical surface area. Less likely can their enhanced activity be explained by the high performance of the newly formed 5-element sites.

This analysis should be repeated for other reactions, with or without dead-surface correction. Considering that both models are designed to overestimate the surface area and thereby favor complex sites, I think it is applicable as an approximation for other reactions, including reactions that take place at bridging sites. It remains a possibility that for specific reactions, high entropy alloys could emerge as the most active catalyst. However, as there are four to be met, each amplifying the demands of the others, my intuitions says that the likelihood is close to zero.

This analysis concludes the search for novel active high entropy alloy catalysts. Nonetheless, this certainly does not mean the end of high entropy alloy catalyst studies as there are still multiple research questions left unanswered. As discussed in Chapter 7, high entropy alloys can contribute secondary effects to a catalytic system such as templating and stabilizing the structure, making them interesting for further studies on the morphology control of catalysts. This also includes investigating high entropy alloys for their stability and degradation pathways, providing numerous opportunities for novel research questions. For instance, within a high entropy alloy, each element has a different dissolution rate potentially correlated to the elemental composition. Fast dissolution rates can be exploited to hollow the catalyst increasing its catalytic surface. Slower leaching elements, on the other hand, could compensate for loss of active sites due to dissolution by steadily revealing new ones from a protected core. Personally, I would propose to evaluate the derivative functions of high entropy alloy compositions with respect to time. Specifically: Do all high entropy alloy compositions within a single composition space converge to the same composition and therefore activity, after which they follow the same degradation pathway? However, considering the costs to evaluate this derivative function, the cost of this research project might be on the expensive side.

Additionally, this statistical analysis demonstrates the possibility of creating 5-element alloys that have a similar activity as pure platinum for the oxygen reduction reaction. Therefore, the possibility of designing a platinum free high entropy catalyst with similar activity remains theoretically still possible. Moreover, the identification of multiple high entropy alloy compositions with identical activities can be used to mitigate the fluctuating market prices. However, this reiterates the importance of investigating stability as to make these alloys truly interchangeable, they must also exhibit comparable stabilities.

On this note, I would like to conclude this thesis. This thesis explored strategies to investigate high entropy alloy catalysts by successfully implementing machine learning approaches to optimize the compositions and to study correlations in them. It showcased empirically and mathematically, that high entropy alloys might not rank as the most active catalysts. Therefore, it recommends the research field to shift focus towards investigating stability. As the investigations continue, I expect machine learning methods to maintain their critical role, especially in modeling the multi-dimensional dissolution of high entropy alloys.



## Acknowledgements

This work, like any scientific work, could not have been achieved without help, support, and collaborations. Likewise, this project would not have been possible without a certain prehistory. Therefore, I would like to start with thanking my former master thesis supervisor Prof. Dr. Marc Koper, who not only thought me the fundamentals of electrochemistry, but more importantly, thought me to solve research questions using mathematics and logic, which formed backbone of this thesis.

The next most important person in this project would be my supervisor Prof. Dr. Matthias Arenz, to whom I'm eternally grateful. Matthias Arenz provided me with scientific freedom to shape my project, while at the same time he provided a safety net to resort to in times of difficulty. This way, I build confidence and experience to build and shape research projects, an essential skill for my future academic career.

Also, I would like to express my gratitude to Prof. Dr. Jan Rossmeisl for his support of my project. In particular, I would like to thank him for hosting a two weeks visit to the University of Copenhagen. These two weeks strongly improved my understanding of the DFT calculations on high entropy alloys and the descriptor-based approach. One of the results from this visit is the surface-activity trade-off model, presented in this thesis. Yet I believe there will be more works originating from this visit.

A special thanks goes to Ahmad Tirmidzi, for carrying out the particle swarm optimization study.

I would like to thank all members of the Center for High Entropy Alloy Catalysis and Arenz group for their scientific support. Among them, I would like to highlight the support of Dr. Jack Pedersen for his assistance in understanding machine learning, high entropy alloy catalysis theory and for his assistance in improving my Python code. Also, I would like to highlight the scientific support of Dr. Alexander Bagger, Dr. Gustav K. H. Wiberg, Etienne Berner, and Sven Nösberger.

Furthermore, I would like to thank my family and friends for their support during this PhD journey. Especially, I express deep gratitude to my wife Anna Iarchuk for her unconditional support, helping me design scientific figures and presentations and for making the illustrations in this thesis.

In addition, I would like to acknowledge that the unpublished works in this thesis are based on discussions with Prof Dr. Matthias Arenz, Prof Dr. Jan Rossmeisl, Dr. Gustav K. H. Wiberg, Dr. Soren Scott, and Dr. Jack Pedersen.

Lastly, I would like to thank the University of Bern for the funding of my PhD project. I would like to thank the Young Academics: Open Round 2023 and the Danish National Research Foundation (DNRF 149) for financing the research stays at the University of Copenhagen.



**Supporting Information to:**

**“Exploring the Composition Space of High Entropy Alloy Nanoparticles for the  
Electrocatalytic H<sub>2</sub>/CO Oxidation with Bayesian Optimization”**

Vladislav A. Mints,<sup>a</sup> Jack K. Pedersen,<sup>b</sup> Alexander Bagger,<sup>b</sup> Jonathan Quinson,<sup>b</sup><sup>‡</sup> Andy S. Anker,<sup>b</sup> Kirsten M. Ø. Jensen,<sup>b</sup> Jan Rossmeisl,<sup>b</sup> and Matthias Arenz <sup>\*a</sup>

<sup>a</sup> University of Bern, Department of Chemistry, Biochemistry and Pharmaceutical Sciences,  
Freiestrasse 3, 3012 Bern, Switzerland

<sup>b</sup> University of Copenhagen, Department of Chemistry, Universitetsparken 5, 2100  
Copenhagen Ø, Denmark

<sup>‡</sup> current address: Department of Biological and Chemical Engineering, Hangøvej 2  
8200 Aarhus N, Denmark

\* corresponding author, matthias.arenz@unibe.ch

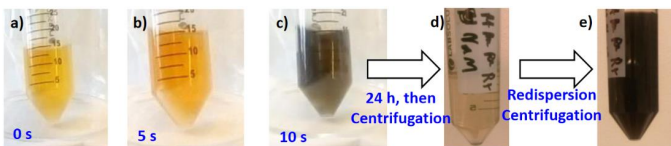


Figure S1: Time series photographs of  $H_2PtCl_6$ ,  $IrCl_3$ ,  $RuCl_3$  and  $PdCl_2$  in alkaline  $NaOH$  methanol under stirring at room temperature a) before, b) 5 s and c) 10 s after addition of  $HAuCl_4$ . d) is the same solution after 24 hours of synthesis and after centrifugation whereas e) is the same solution as d) after removing the supernatant, redispersion in methanol and a new centrifugation cycle. This reaction is for illustration purposes of the simplicity of the general synthesis approach and no carbon support was used to more clearly observe the speed of the reaction (in presence of support the reaction mixture is completely black). The final metal concentration for each element is here 0.5 mM and the final  $NaOH$  concentration is here 48 mM.

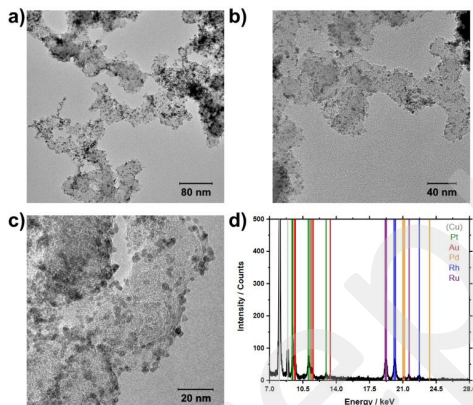


Figure S2: a-c) TEM and d) EDX characterization of the sample  $Pt_{12}Ru_{39}Pd_8Rh_{41}Au_1$  with the expected intensity peaks positions for different elements as indicated in colour in d) where the spectrum is in dark. The copper signal (Cu) comes from the TEM grid

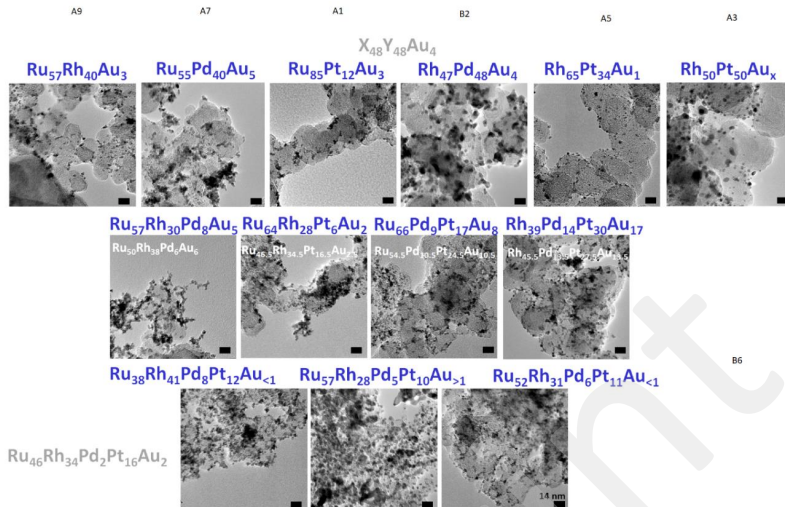


Figure S3: TEM images of ternary and quaternary alloys that were synthesized as control experiments.

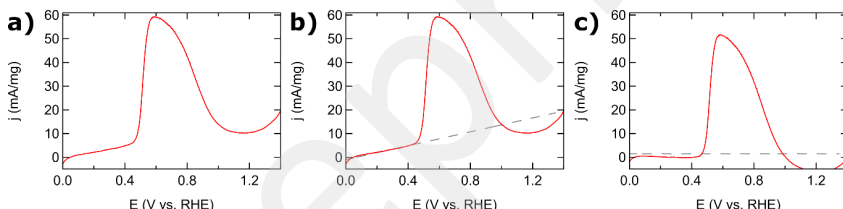


Figure S4: Example of how the data was obtained. a) Raw data as measured experimentally. b) Dashed line shows the linear fit through the capacitance. c) Dashed line indicates the current density at which the CO oxidation onset potential is defined.

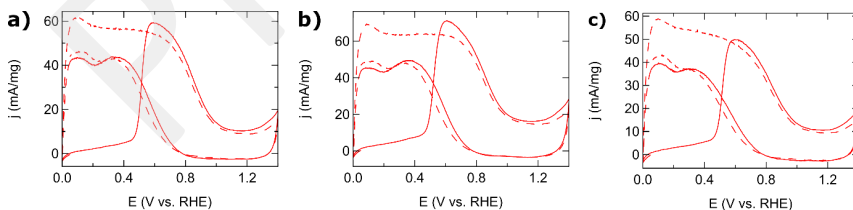
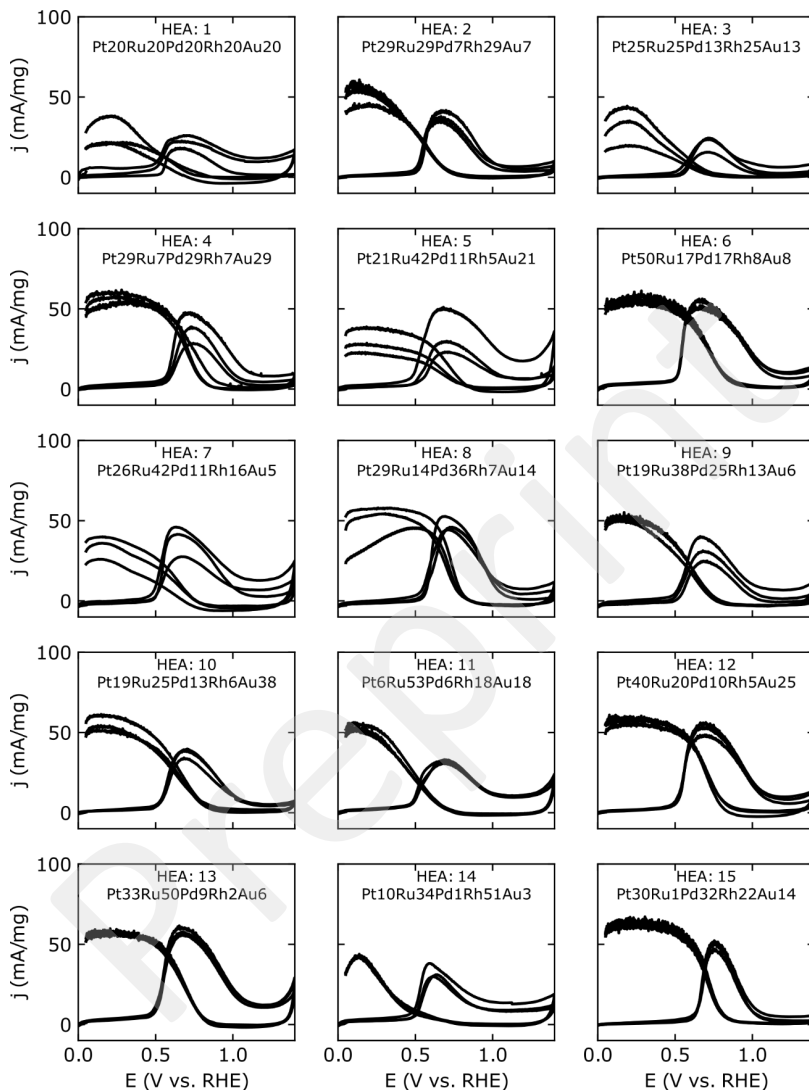


Figure S5: The CO monolayer oxidation on a  $35 \mu\text{g cm}^{-2}$   $\text{Pt}_{12}\text{Ru}_{38}\text{Pd}_8\text{Rh}_{41}\text{Au}_1$  film. a-c) CVs were recorded in  $\text{H}_2$  atm after a CO monolayer was adsorbed on the surfaces at  $10 \text{ mV s}^{-1}$  from 0 to  $1.4 \text{ V}$  vs. RHE. The solid line represents the first cycle, the dashed line represents the second cycle.



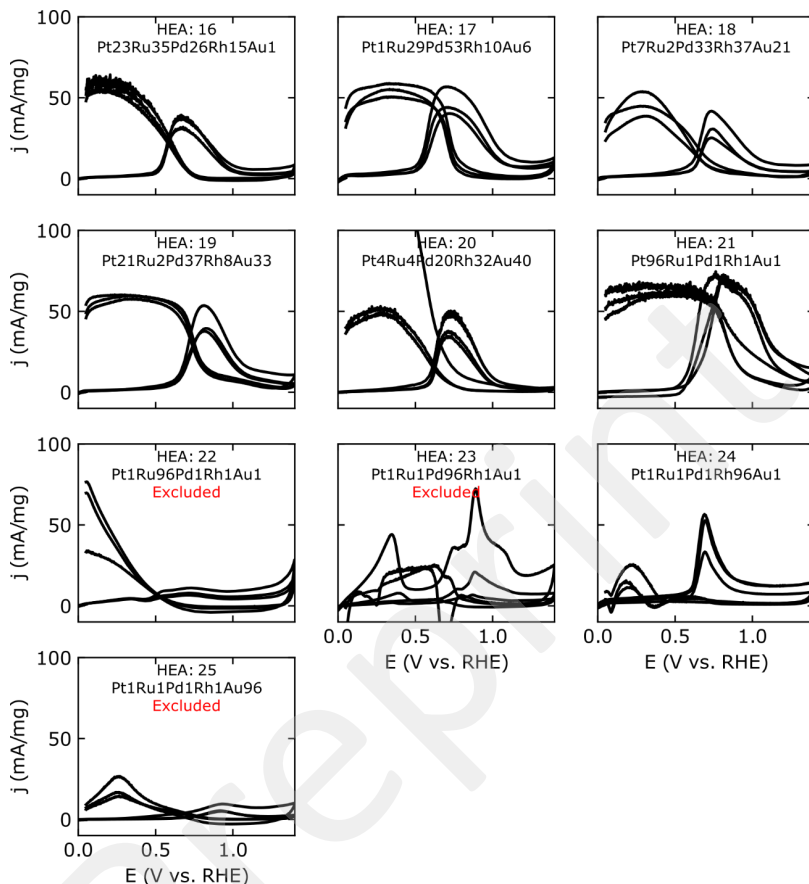


Figure S6: CO monolayer oxidation experiments of the 25 experiments that formed the initial data. CVs were recorded in  $H_2$  atm after a CO monolayer was adsorbed on the surfaces at  $10 \text{ mV s}^{-1}$  from 0 to  $1.4 \text{ V}$  vs. RHE. The shown composition refers to the precursor ratio in the synthesis mixtures.

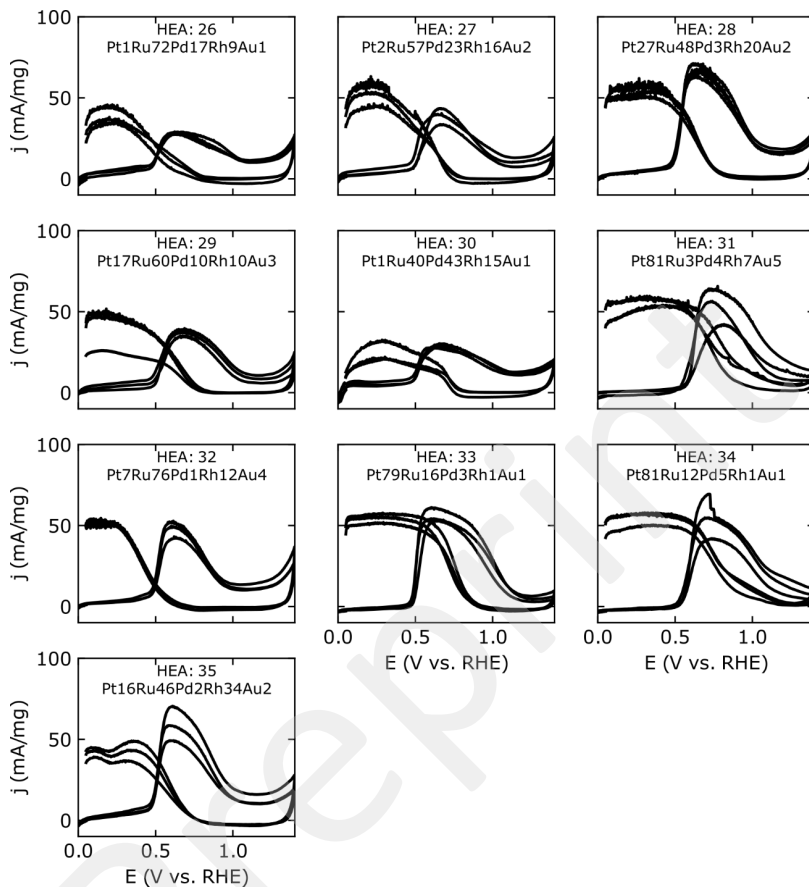


Figure S7: CO monolayer oxidation experiments of the 10 experiments that were suggested in the first Bayesian optimization cycle. CVs were recorded in  $\text{H}_2$  atm after a CO monolayer was adsorbed on the surfaces at  $10 \text{ mV s}^{-1}$  from 0 to 1.4 V vs. RHE. The shown composition refers to the precursor ratio in the synthesis mixtures.

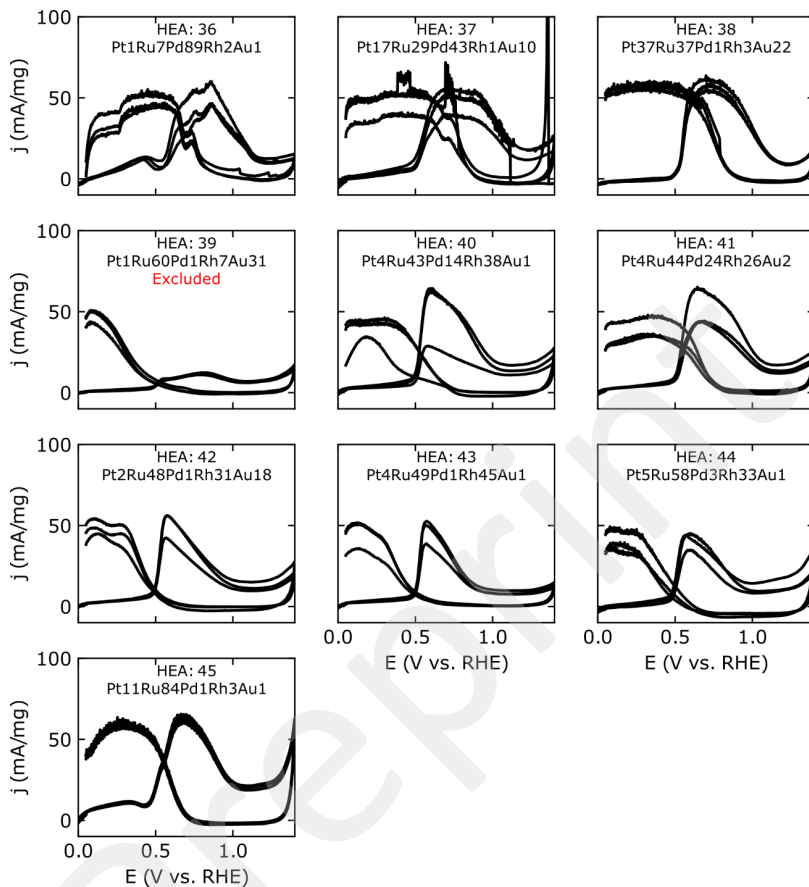


Figure S8: CO monolayer oxidation experiments of the 10 experiments that were suggested in the second Bayesian optimization cycle. CVs were recorded in  $H_2$  atm after a CO monolayer was adsorbed on the surfaces at  $10 \text{ mV s}^{-1}$  from 0 to 1.4 V vs. RHE. The shown composition refers to the precursor ratio in the synthesis mixtures.

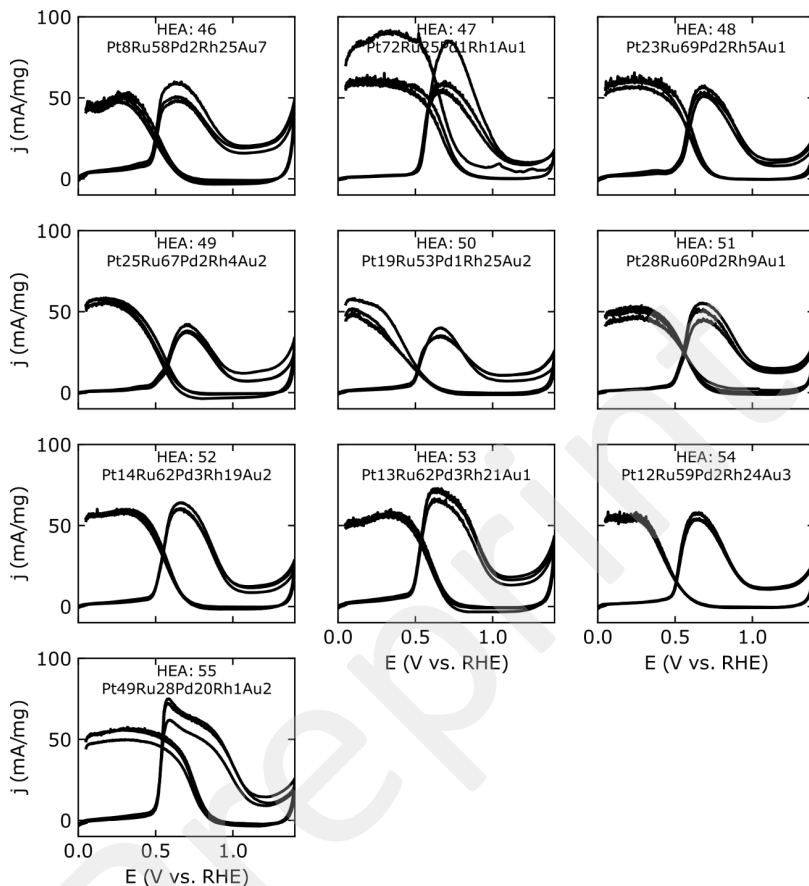


Figure S9: CO monolayer oxidation experiments of the 10 experiments that were suggested in the third Bayesian optimization cycle. CVs were recorded in  $\text{H}_2$  atm after a CO monolayer was adsorbed on the surfaces at  $10 \text{ mV s}^{-1}$  from 0 to 1.4 V vs. RHE. The shown composition refers to the precursor ratio in the synthesis mixtures.

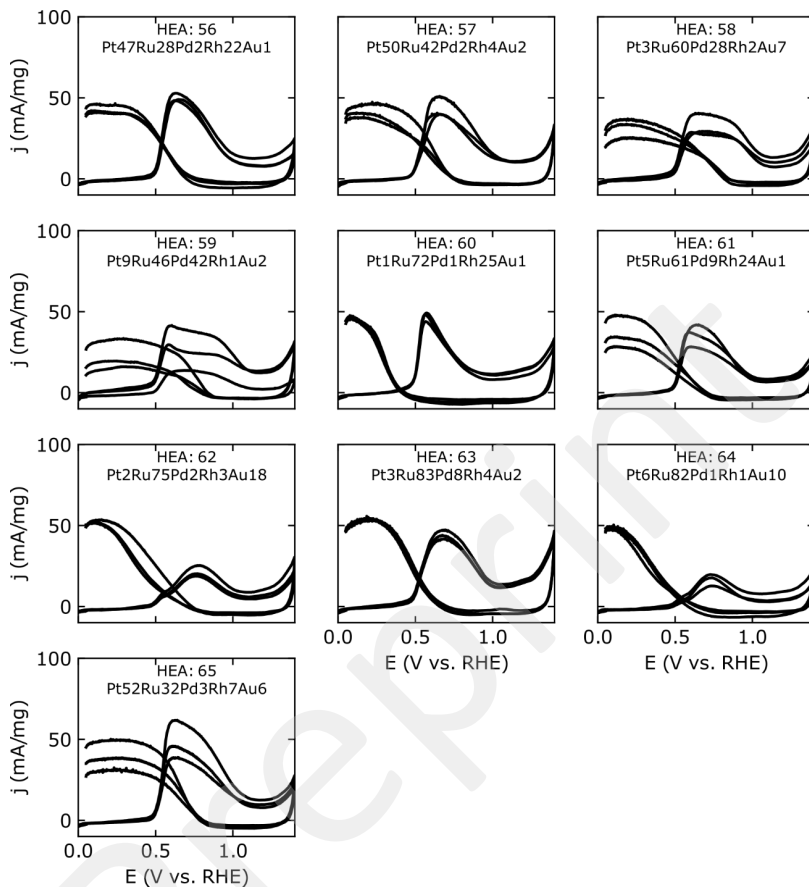


Figure S10: CO monolayer oxidation experiments of the 10 experiments that were suggested in the fourth Bayesian optimization cycle. CVs were recorded in  $\text{H}_2$  atm after a CO monolayer was adsorbed on the surfaces at  $10 \text{ mV s}^{-1}$  from 0 to  $1.4 \text{ V}$  vs. RHE. The shown composition refers to the precursor ratio in the synthesis mixtures.

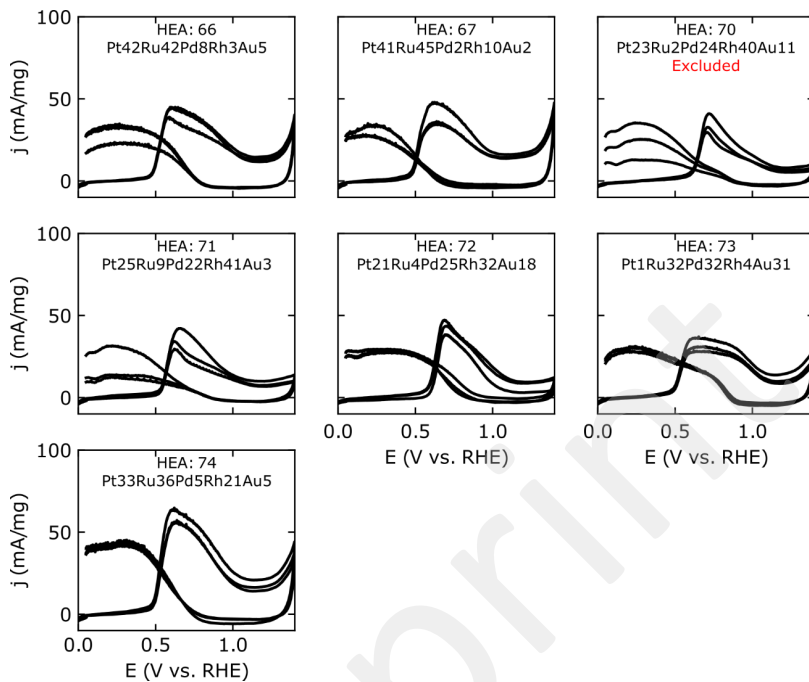


Figure S11: CO monolayer oxidation experiments of the 7 experiments that were suggested in the final Bayesian optimization cycle. CVs were recorded in  $H_2$  atm after a CO monolayer was adsorbed on the surfaces at  $10\text{ mV s}^{-1}$  from 0 to  $1.4\text{ V}$  vs. RHE. The shown composition refers to the precursor ratio in the synthesis mixtures. Samples number 68 and 69 were excluded from the measurements due to Pd amounts larger than 85%.

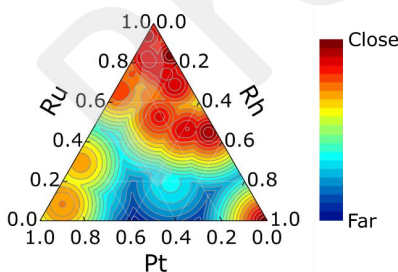


Figure S12: The distance of the grid points for the EDX models in the ternary plots Figure 4 a-b of Ru, Pt, Rh to the closest measured experimental data point in the five dimensional space of RuPtRhPdAu.

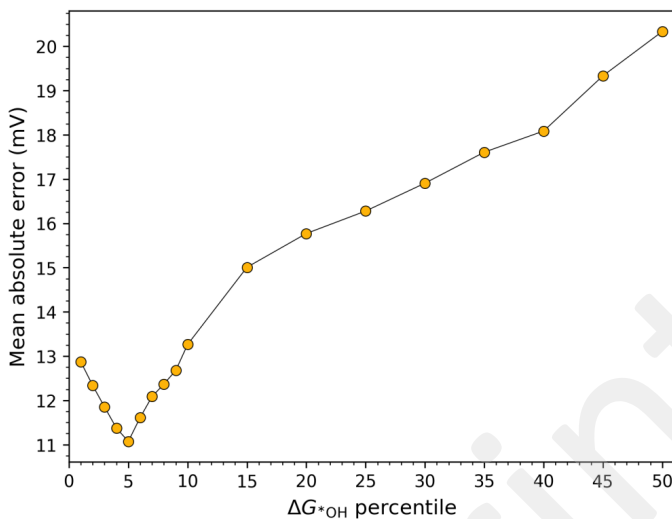


Figure S13: The mean absolute error between the predicted and measured onset potentials as a function of the percentile of the most strongly adsorbing OH sites. The 5 percentile is observed to constitute a minimum in the prediction error, and was hence used in the analysis in Figure 5.



## Supporting Information

### Bayesian Optimization of High-Entropy Alloy Compositions for Electrocatalytic Oxygen Reduction\*\*

Jack K. Pedersen, Christian M. Clausen, Olga A. Krysiak, Bin Xiao, Thomas A. A. Batchelor, Tobias Löffler, Vladislav A. Mints, Lars Banko, Matthias Arenz, Alan Savan, Wolfgang Schuhmann, Alfred Ludwig, and Jan Rossmeisl\*

anie\_202108116\_sm\_miscellaneous\_information.pdf

## SUPPORTING INFORMATION

WILEY-VCH

**Computational Procedures**

All simulated structures, data and scripts necessary for reproducing the simulations herein have made freely accessible at <https://nano.ku.dk/english/research/theoretical-electrocatalysis/katlab/bayesian-optimization-of-hea/>

**Density functional theory simulations**

Density functional theory using the revised Perdew-Burke-Ernzerhof (RPBE) exchange-correlation functional<sup>[1]</sup> as implemented in the GPAW code<sup>[2,3]</sup> was used to obtain \*OH and O\* adsorption energies on fcc (111) 2x2-atoms-sized, four-layered surface slabs that were periodically repeated in the direction parallel to the slab. The structures were set up and manipulated in the Atomic Simulation Environment (ASE)<sup>[4]</sup>. The slabs were constructed with an fcc lattice constant set to the weighted average of the calculated fcc lattice constants of the elements in the surface layer, a vacuum of 7.5 Å was added above and below the slab, and the atoms in the two bottom layers were held fixed during geometry relaxations at which the structures were optimized until the maximum force on any atom was below at least 0.1 eVÅ<sup>-1</sup>. The wave functions were expanded in plane waves with an energy cutoff set to 400 eV, and the Brillouin zone was sampled with a Monkhorst-Pack grid of 4x4x1 k-points. For training the Ag-Ir-Pd-Pt-Ru quinary alloy adsorption energy regressor, a total of 1304 \*OH and 1768 O\* adsorption energies were simulated on slabs where the metals in the structure were randomly sampled from an equimolar ratio. Equivalently for the Ir-Pd-Pt-Rh-Ru system where 856 \*OH and 997 O\* adsorption energies were simulated. The 2x2-atoms-sized, four-layered slabs for the binary alloy systems (Ag-Pd, Ir-Pt and Pd-Ru) were calculated with a similar computational setup with the exception of 10 Å added vacuum. In addition to slabs sampled from equimolar ratios, 25% of the slabs were sampled from a 3:1 ratio e.g. Ag<sub>75</sub>Pd<sub>25</sub> and 25% from a 1:3 ratio e.g. Ag<sub>25</sub>Pd<sub>75</sub> in order to more sensibly span the compositions of the binary alloy systems.

**Adsorption energy prediction**

The DFT calculated \*OH and O\* adsorption energies were used to train a regressor for predicting the \*OH and O\* adsorption energy at any conceivable on-top and fcc hollow site of an fcc (111) surface. To this end, we applied our previously developed scheme<sup>[5]</sup> for mapping structures into machine readable features simply by one-hot encoding the identity of the adsorption site ensemble and by counting the number of each element in equidistant positions from the adsorption site. For \*OH on-top adsorption the atoms included in our description was the on-top adsorbing atom itself, the surface and subsurface neighboring atoms, and the second-nearest atoms in the third layer as we suggested recently<sup>[6]</sup>. For O\* fcc hollow site adsorption the three-atom site ensemble as well as its surface and subsurface neighboring atoms were included in the description of the site (for an example see Figure S3). These features were used to fit a linear model for each on-top \*OH adsorption site, i.e. one for on-top Ag, one for on-top Ir, etc. containing 15 fitted parameters each, as well as a single linear model for fcc hollow adsorbing O\*, containing 55 fitted parameters (the fitted linear parameters are shown in Table S2-S5). For the investigated binary alloys a gradient boosted regressor was used on a more elaborate description of the surface site including the neighboring atomic environment up to the third or fourth closest atoms of each layer in order to improve on the prediction accuracy. Since the 2x2-atoms-sized DFT simulated slabs are periodically repeated this will include some zones without any additional information, however all available atoms will be included in the site features. In addition, a gradient boosted model was fitted to each O\* adsorption site, i.e. one model for Ag<sub>3</sub>, Ag<sub>2</sub>Pd, AgPd<sub>2</sub> and Pd<sub>3</sub>, respectively. Furthermore, when training the gradient boosted regressor the samples of binary alloys were weighted to enhance their representation of the composition span. Thus, each data set of a binary alloy contained two pure metal samples with assigned weights of 1000, approximately 1000 samples drawn equally from the 1:3 and 3:1 molar ratios with assigned weights of 2 and approximately 1000 samples drawn from the equimolar ratio with assigned weights of 1. Linear and gradient boosted regression algorithms were used as implemented in scikit-learn<sup>[7]</sup> with default hyperparameters.

**Current density modeling**

The current density predicted by simulations was predicted using equations 1-3. Equation 3 predicts the per site current density based on an Arrhenius-like rate expression and takes as input the difference in the \*OH or O\* adsorption energy to an optimal value, determined as 0.1 eV<sup>[8]</sup> and 0.2 eV<sup>[9]</sup> weaker than on Pt(111). The theoretical framework behind these experimentally validated optimal adsorption energies is a kinetic model that involves the associative mechanism for the ORR. Initially, the electrochemical adsorption-reduction step of O<sub>2</sub> to \*OH must be facilitated, and finally the desorption-reduction steps of \*OH or O\* to H<sub>2</sub>O. We note that other pathways, including the dissociative ORR mechanism, could also contribute to the produced current density. However, we expect these contributions to be minor. In case of the dissociation of O<sub>2</sub> to form adsorbed O\* on the surface, the argument is that this reaction becomes increasingly less relevant compared to the associative mechanism as the overpotential increases. Already at about 0.8 V vs. RHE the effect of the dissociative mechanism is minor.<sup>[10]</sup>

In order to improve on the model's predictive trend, a simple adsorbate interaction between adsorbed \*OH and O\* was included.<sup>[11]</sup> This interaction works by ensuring that no two neighboring on-top and hollow sites can adsorb reaction intermediates at the same time. To calculate the current density using equation 1-3, the net coverage and corresponding net adsorption energies were used by accounting for this interaction. In practice these *net* adsorption energies were achieved by predicting the \*OH and O\* *gross* adsorption energies on all on-top and fcc hollow sites on a randomly constructed surface with a desired composition and measuring 100x100 atoms (the dependence of the predicted current density on the surface size is shown in Figure S1). The surface was then filled with \*OH on-top and O\* fcc hollow adsorbates starting at the strongest adsorbing sites and filled using the rule that no neighboring on-top and hollow sites can adsorb at the same time, until no more free surface sites remained. The net coverage and

## SUPPORTING INFORMATION

WILEY-VCH

net adsorption energies of  $\text{OH}$  and  $\text{O}^*$  achieved in this way would then act as the input for equation 1-3 when calculating the predicted current density for the given composition.

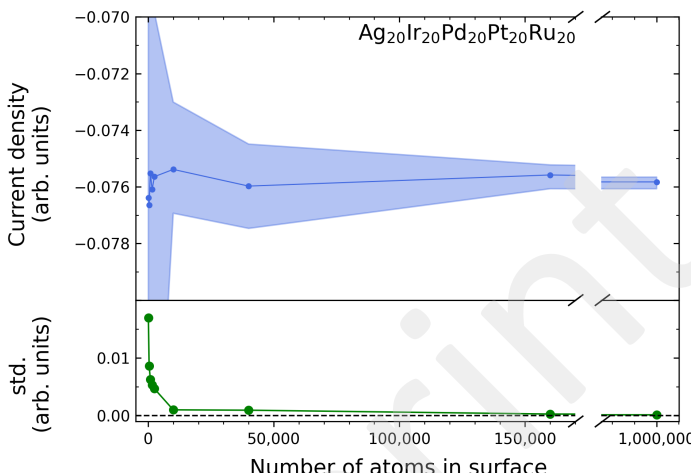


**Figure S1.** The predicted current density vs. the number of atoms of the simulated surface sampled for at least five random surfaces of equimolar  $\text{AgIrPdPtRu}$  at each of the sampled sizes. The standard deviation (std.) of the five sampled points are shown in green in the lower plot. At 10,000 atoms in the surface (100x100 atoms) the variation in the simulated current density is appreciably low compared to the variation between compositions (see for instance Figure 3 in the main text).

**Gaussian Process**

A Gaussian process regressor as implemented in scikit-learn<sup>[7]</sup> was constructed by setting the prior mean to zero everywhere, and defining the kernel (or covariance function) as shown in Equation 4 in the main text. This choice of kernel and prior mean is often a standard choice in machine learning applications, because of its general applicability and limited prior knowledge about the function being estimated. However, the squared exponential kernel does guarantee continuity and differentiability of the realizations of the Gaussian process, which we would also expect for the current densities of a composition space. It therefore forms a natural starting point for the present implementation.

When training the Gaussian process on the sampled compositions, the hyperparameters  $C$  and  $\ell$  were updated as implemented with the default choice of parameters in scikit-learn. The evolution of the hyperparameters as more samples were added are shown for illustration in Figure 2 in the main text.

**Bayesian Optimization**

In order to find optimal compositions with Bayesian inference, the Gaussian process regressor was initially trained on two randomly selected molar fractions along with their corresponding simulated current densities obtained with the kinetic model. The Gaussian process regressor was then used to predict current densities and surrogate model uncertainties at 1000 randomly selected molar fractions in order to span the quinary composition space in an approximate manner. The selection of the most optimal composition to sample next was performed with the *expected improvement* acquisition function. The principle of this acquisition function is to evaluate the expectation value of the improvement function,<sup>[12]</sup>

$$E[I(x)] = E[\max(y_{\min} + \xi - Y, 0)] \quad (\text{S1})$$

at a molar fraction  $x$  for randomly distributed current densities  $Y$  and for the highest absolute value of the current density  $y_{\min}$  sampled by the kinetic model so far.  $\xi$  is a tunable parameter that effectively adjusts  $y_{\min}$ . If  $\xi$  is chosen to be greater than zero, the minimum found so far is effectively increased making molar fractions with greater probability of having current densities below the minimum have larger expected improvements and are therefore more likely to be compositions that could further minimize the current density. Assuming that the current densities at  $x$  are normally distributed with mean and standard deviation given by the prediction of the surrogate Gaussian process regressor, the expected improvement can be evaluated as

**SUPPORTING INFORMATION****WILEY-VCH**

$$E[I(x)] = (y_{min} + \xi - \mu(x))\Phi\left(\frac{y_{min} + \xi - \mu(x)}{\sigma(x)}\right) + \sigma(x)\phi\left(\frac{y_{min} + \xi - \mu(x)}{\sigma(x)}\right), \quad (S2)$$

where  $\mu(x)$  and  $\sigma(x)$  are the mean and standard deviation supplied by the Gaussian process regressor, respectively, and  $\phi(t) = (1/\sqrt{2\pi})\exp(-t^2/2)$  and  $\Phi(t) = \int_{-\infty}^t \phi(t')dt'$  are the standard normal probability and cumulative distributions, respectively. The expected improvement was evaluated at the same 1000 compositions as the Gaussian process regressor, and the composition with the maximum acquisition value was further optimized by sampling the expected improvement around the composition in molar fraction steps of 0.005 until a maximum was found that was then selected for sampling by the kinetic model. A  $\xi$ -value of 0.01 was used throughout. A  $\xi$ -value of zero was found to potentially discover the locally optimal compositions very quickly. However, discovery of the global optimum was not guaranteed with 150 samples as was the case for  $\xi=0.01$ .

## SUPPORTING INFORMATION

WILEY-VCH

## Experimental Procedures

## Electrochemical characterization

Binary thin-film composition spreads were analyzed using a high-throughput scanning droplet cell (SDC) coupled with a Jaissle potentiostat/galvanostat. The teflon tip forming the head of the SDC had an opening of 1 mm in diameter, which formed the working electrode in each of the measurement areas (MAS) with a size of  $7.35 \cdot 10^{-3}$  cm<sup>2</sup>, allowing local characterization of the samples. Particular MAS on all of the samples were separated from each other by 2.25 mm, which corresponds to composition changes of ca. 1.5 at.% per element. All electrochemical measurements were conducted in 0.1 M HClO<sub>4</sub> electrolyte in a three-electrode system with a Ag|AgCl|3M KCl and a Pt wire as a reference and counter electrode, respectively. Linear sweep voltammetry was performed between 1 V and 200 mV vs. the reversible hydrogen electrode (RHE) with a scan rate of 10 mV s<sup>-1</sup>. All potentials are reported versus the RHE calculated according to the following equation:

$$U_{RHE} = U_{Ag|AgCl|3M\text{KCl}} + 0.210 \text{ V} + 0.059 \text{ V} \cdot pH \quad (S3)$$

where  $U_{Ag|AgCl|3M\text{KCl}}$  is the potential measured vs. the Ag|AgCl|3M KCl reference electrode, 0.210 V is the standard potential of the Ag|AgCl|3M KCl reference electrode at 25 °C, 0.059 V is the result of  $\ln(10)RT/nF$ , where  $R$  is the gas constant,  $T$  is the temperature (298 K),  $F$  is the Faraday constant and  $n$  (=1) is the number of electrons transferred during the reaction.

## Composition analysis

The elemental compositions of all MAs in the MLs were determined using automated energy dispersive X-ray spectroscopy (EDX) at 20 kV acceleration voltage in a scanning electron microscope (SEM, JEOL 5800) using a detector (INCA Xact, Oxford Instruments).

## Surface roughness analysis by AFM

Topographical images of the Ag-Pd, Pd-Ru, Ir-Pt and Ir-(H) Pt thin film libraries were measured by atomic force microscopy (AFM, Bruker Dimension Fastscan) using Fastscan mode. For surfaces, whose roughness is characterized by a single length scale, roughness parameters were calculated by the arithmetic mean roughness Ra.

## Phase analysis from XRD

The crystallographic phase analysis was performed using X-ray diffraction (XRD). A Bruker D8 Discover with a Vantec-500 2D-detector in Bragg–Brentano geometry and Cu K $\alpha$  X-ray source was used. To avoid Si-substrate peaks, measurements were performed in 0–20 mode with a 2.5° offset on 0. Five frames were taken stepwise at every MA with an increment of 0/20 7.5°/15°, starting at 10°/25° and finishing at 40°/85°. In this way an angular 20 range from approximately 10° to 100° was covered.

## Thin-film fabrication Pd-Ru, Ir-Pt, and Ag-Pd

The Pd-Ru and Ir-Pt libraries were fabricated by a combinatorial magnetron sputtering system (DCA Instruments, Finland) equipped with five cathodes. Two of these five cathodes were positioned at 144° form each other to create composition gradients. High purity (Ir: 99.9%, Pt: 99.99%) 100 mm diameter single-element targets were used. A confocally-placed 100 mm diameter sapphire wafer (c-plane) was used as a substrate for the Ir-Pt system. It was patterned with small numbered crosses by a photolithographic lift-off process to serve as a reference grid and for making local thickness measurements by stylus profilometry. All of the depositions were carried out without intentional heating. Prior to the deposition, the chamber vacuum was on the order of 10<sup>-5</sup> Pa. During deposition, the pressure was set to 0.667 Pa using Ar (99.999%) at a flow rate of 60 sccm, and the substrate was kept stationary to obtain continuous compositional gradients. The type of power supply used for each library and sputter powers are listed in Table S1.

The Ag-Pd system was deposited in an alternate vacuum chamber, where cathodes with 38 mm diameter targets (Ag: 99.99%, Pd: 99.95%) are positioned 180° to each other. The substrate used was an approximately 1 cm wide strip cleaved from a 100 mm diameter <100> Si wafer, which was thermally oxidized as a diffusion barrier. The chamber base vacuum was 10<sup>-4</sup> Pa and deposition was done at an Ar pressure of 0.5 Pa. The 100 mm diameter (100) Si substrate with a 500 nm SiO<sub>2</sub> barrier layer was stationary at the confocal point of the tilted cathodes so that composition gradients were obtained.

**SUPPORTING INFORMATION****WILEY-VCH****Table S1.** Sputter parameters for the Pd-Ru, Ir-Pt and Ir-(High)Pt, respectively.

		Deposition power (W)			
		Pd	Ru	Ir	Pt
Libraries	(RF) <sup>[a]</sup>	(DC) <sup>[b]</sup>	(DC) <sup>[b]</sup>	(RF) <sup>[a]</sup>	
	Pd-Ru	182	44	-	-
Ir-Pt	-	-	70	194	
Ir-(High)Pt	-	-	40	239	

[a] RF: Radio frequency. [b] DC: Direct current.

## SUPPORTING INFORMATION

WILEY-VCH

## Results and Discussion

Number of samples in a grid search of an N-component composition space

The number of combinations of alloy compositions in steps of molar fractions of s are given by equation S4.

$$N = \frac{\left(\frac{1}{s} + N_{\text{elems}} - 1\right)!}{\left(\frac{1}{s}\right)! (N_{\text{elems}} - 1)!} \quad (\text{S4})$$

where  $N_{\text{elems}}$  is the number of metals in the alloy system. For example, to uniformly span the composition space of a quinary alloy in 5% intervals 10,626 points are needed. Figure S2 shows the number of combinations needed to span the composition space for various steps of molar fractions. It is observed that as the number of elements increases, the exploration of the composition space becomes increasingly infeasible as the number of samples needed increase combinatorially.

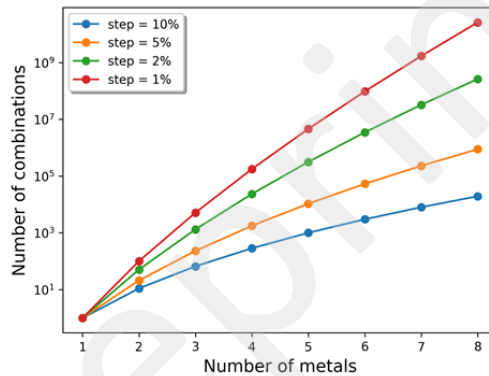


**Figure S2.** Number of samples needed to span the composition space. Shown for molar fraction step sizes of 1, 2, 5 and 10% as a function of the number of metals in the alloy.

## SUPPORTING INFORMATION

WILEY-VCH

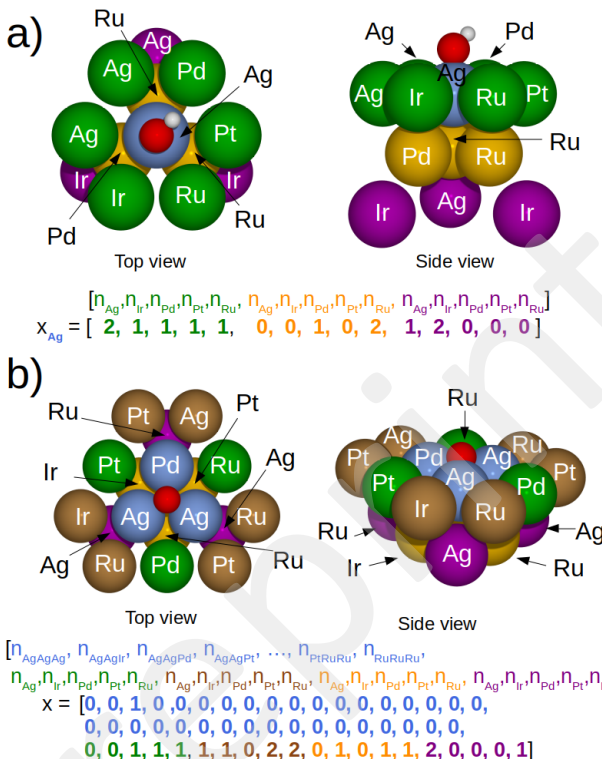


**Figure S3.** Examples of encoding the features of a structure. Shown in a) for an OH on-top site with a set of features for each possible on-top site element (exemplified for an Ag on-top site) with a total of 15 parameters, and in b) for an fcc hollow site with one-hot encoding of the adsorption site ensemble (here exemplified for the AgAgPd ensemble) with a total of 55 parameters. The color of the text matches the corresponding colors of the atoms in the structure.

## SUPPORTING INFORMATION

WILEY-VCH

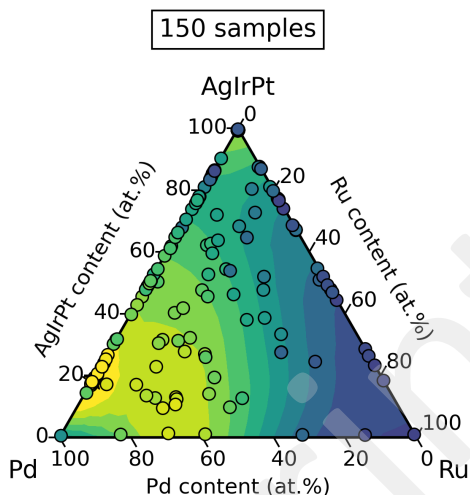


**Figure S4.** Pseudo-ternary plot of the Ag-Ir-Pd-Pt-Ru modeled current densities after sampling of 150 samples with Bayesian optimization. The Ag, Ir, and Pt concentrations have been grouped into one to highlight the plateau of similar current densities when the binary  $Pd_{1-x}Ru_x$  is mixed with other elements in trace amounts. Yellow colors correspond to regions with high absolute values of the current density and blue colors to correspondingly low values. The projection of the current density from the quinary to the pseudo-ternary composition space was accomplished by showing the maximal absolute value of the current density possible for compositions that would otherwise be overlapping.

**SUPPORTING INFORMATION****WILEY-VCH**

**Table S2.** Linear parameters used for on-top \*OH adsorption energy prediction on the Ag-Ir-Pd-Pt-Ru system. The parameters will give the electronic energy in eV relative to \*OH on Pt(111). The order of the parameters, after the intercept, follows the features given in Figure S3a. In the labels of the parameters the number refers to the layer, and the letter to the proximity to the adsorption site, e.g. "3a Pd" refers to the influence of Pd in the nearest atoms in the 3rd layer below the surface. The intercept has been chosen to yield the prediction for the pure element, since this value is obtained by setting the respective parameters for that element in each zone to zero.

Ag-Ir-Pd-Pt-Ru (eV relative to *OH@Pt(111))					
	@Ag	@Ir	@Pd	@Pt	@Ru
<b>Intercept</b>	0.262515	-0.363696	0.075474	-0.023367	-0.604279
<b>1b Ag</b>	0	-0.074370	-0.025064	-0.065560	-0.026962
<b>1b Ir</b>	0.124874	0	0.044604	0.014894	0.025734
<b>1b Pd</b>	0.055553	-0.057413	0	-0.042658	-0.021608
<b>1b Pt</b>	0.106736	-0.016379	0.040827	0	0.021586
<b>1b Ru</b>	0.083629	-0.019943	0.007435	-0.016870	0
<b>2a Ag</b>	0	0.020613	0.022701	0.076312	-0.097415
<b>2a Ir</b>	-0.103170	0	-0.050573	-0.022161	-0.022948
<b>2a Pd</b>	-0.025039	0.008149	0	0.046161	-0.070458
<b>2a Pt</b>	-0.057300	-0.012203	-0.032788	0	-0.059442
<b>2a Ru</b>	-0.121723	0.031539	-0.051361	-0.014583	0
<b>3a Ag</b>	0	-0.036480	-0.015738	-0.022794	-0.025380
<b>3a Ir</b>	0.019881	0	0.035545	0.032103	0.013630
<b>3a Pd</b>	-0.001190	-0.014928	0	-0.006961	-0.000195
<b>3a Pt</b>	0.005926	-0.012114	0.000055	0	0.008633
<b>3a Ru</b>	0.023315	-0.002794	0.033945	0.039372	0

## SUPPORTING INFORMATION

WILEY-VCH

**Table S3.** Linear parameters used for fcc hollow O\* adsorption energy prediction on the Ag-Ir-Pd-Pt-Ru system. The parameters will give the electronic energy in eV relative to O\* on Pt(111). The order of the parameters follows the features given in Figure S3b. In the labels of the parameters the number refers to the surface layer, and the letter to the proximity to the adsorption site, e.g. "2b Pd" refers to the influence of Pd in the next nearest atoms in the subsurface layer.

Ag-Ir-Pd-Pt-Ru (eV relative to O*@Pt(111))						
<b>AgAgAg</b>	0.823301	<b>AgAgIr</b>	-0.470179	<b>AgAgPd</b>	0.612573	<b>AgAgPt</b>
<b>AgAgRu</b>	-0.869420	<b>AgIrIr</b>	-0.603051	<b>AgIrPd</b>	-0.386478	<b>AgIrPt</b>
<b>AgAgRu</b>	-0.971134	<b>AgPdPd</b>	0.417371	<b>AgPdPt</b>	0.226634	<b>AgPdRu</b>
<b>AgPtPt</b>	0.231177	<b>AgPtRu</b>	-0.677207	<b>AgRuRu</b>	-1.168980	<b>IrIrIr</b>
<b>IrIrPd</b>	-0.791251	<b>IrIrPt</b>	-0.645038	<b>IrIrRu</b>	-1.154468	<b>IrPdPd</b>
<b>IrPdPt</b>	-0.435780	<b>IrPdRu</b>	-1.101158	<b>IrPtPt</b>	-0.331185	<b>IrPtRu</b>
<b>IrRuRu</b>	-1.396306	<b>PdPdPd</b>	0.142790	<b>PdPdPt</b>	0.030062	<b>PdPdRu</b>
<b>PdPtPt</b>	0.073705	<b>PdPtRu</b>	-0.771205	<b>PdRuRu</b>	-1.356419	<b>PtPtPt</b>
<b>PtPtRu</b>	-0.617444	<b>PtRuRu</b>	-1.178394	<b>RuRuRu</b>	-1.654559	-
<b>1b Ag</b>	-0.081909	<b>1c Ag</b>	0.028809	<b>2a Ag</b>	-0.040527	<b>2B Ag</b>
<b>1b Ir</b>	0.062988	<b>1c Ir</b>	-0.020630	<b>2a Ir</b>	0.030518	<b>2b Ir</b>
<b>1b Pd</b>	-0.047180	<b>1c Pd</b>	0.014160	<b>2a Pd</b>	-0.022949	<b>2b Pd</b>
<b>1b Pt</b>	0.025269	<b>1c Pt</b>	0.002563	<b>2a Pt</b>	-0.011230	<b>2b Pt</b>
<b>1b Ru</b>	0.040649	<b>1c Ru</b>	-0.025635	<b>2a Ru</b>	0.042969	<b>2b Ru</b>
						0.040405

**SUPPORTING INFORMATION****WILEY-VCH**

**Table S4.** Linear parameters used for on-top \*OH adsorption energy prediction on the Ir-Pd-Pt-Rh-Ru system. The parameters will give the electronic energy in eV relative to \*OH on Pt(111). The order of the parameters, after the intercept, follows the features given in Figure S3a: In the labels of the parameters the number refers to the layer, and the letter to the proximity to the adsorption site, e.g. "3a Pd" refers to the influence of Pd in the nearest atoms in the 3rd layer below the surface. The intercept has been chosen to yield the prediction for the pure element, since this value is obtained by setting the respective parameters for that element in each zone to zero.

Ir-Pd-Pt-Rh-Ru (eV relative to *OH@Pt(111))					
	@Ir	@Pd	@Pt	@Rh	@Ru
<b>Intercept</b>	-0.324264	0.044878	-0.008922	-0.323476	-0.639564
<b>1b Ir</b>	0	0.045847	0.011095	0.037634	0.040998
<b>1b Pd</b>	-0.067114	0	-0.041923	-0.012061	-0.024511
<b>1b Pt</b>	-0.022217	0.041869	0	0.028185	0.018334
<b>1b Rh</b>	-0.048245	0.006241	-0.030170	0	-0.002666
<b>1b Ru</b>	-0.026561	0.001899	-0.020977	0.002107	0
<b>2a Ir</b>	0	-0.034497	-0.013930	-0.007092	-0.018194
<b>2a Pd</b>	0.017262	0	0.030018	-0.006571	-0.047992
<b>2a Pt</b>	-0.006588	-0.027407	0	-0.014891	-0.037786
<b>2a Rh</b>	0.009353	-0.020069	0.021633	0	-0.022024
<b>2a Ru</b>	0.021847	-0.030915	0.002223	0.005128	0
<b>3a Ir</b>	0	0.034227	0.029385	0.006703	0.004741
<b>3a Pd</b>	-0.026733	0	-0.016174	-0.021482	-0.015521
<b>3a Pt</b>	-0.016911	0.012355	0	-0.006625	-0.000825
<b>3a Rh</b>	-0.005591	0.015988	0.015289	0	-0.003526
<b>3a Ru</b>	0.006793	0.035460	0.039082	0.007343	0

## SUPPORTING INFORMATION

WILEY-VCH

**Table S5.** Linear parameters used for fcc hollow O\* adsorption energy prediction on the Ir-Pd-Pt-Rh-Ru system. The parameters will give the electronic energy in eV relative to O\* on Pt(111). The order of the parameters follows the features given in Figure S3b. In the labels of the parameters the number refers to the surface layer, and the letter to the proximity to the adsorption site, e.g. "2b Pd" refers to the influence of Pd in the next nearest atoms in the subsurface layer.

Ir-Pd-Pt-Rh-Ru (eV relative to O*@Pt(111))					
IrIrIr	-0.802671	IrIrPd	-0.698724	IrIrPt	-0.549723
IrIrRu	-1.039895	IrPdPd	-0.490209	IrPdPt	-0.372960
IrIrRu	-1.023565	IrPtPt	-0.244375	IrPtRh	-0.585337
IrRhRh	-0.894818	IrRhRu	-1.128900	IrRuRu	-1.293938
PdPdPt	0.096998	PdPdRh	-0.273295	PdPdRu	-0.866591
PdPtRh	-0.252892	PdPtRu	-0.716471	PdRhRh	-0.602280
PdRuRu	-1.262522	PtPtPt	0.183877	PtPtRh	-0.153542
PtRhRh	-0.506731	PtRhRu	-0.874115	PtRuRu	-1.077222
RhRhRu	-1.144941	RhRuRu	-1.392573	RuRuRu	-1.563099
1b Ir	0.045966	1c Ir	-0.020285	2a Ir	0.026245
1b Pd	-0.061963	1c Pd	0.029724	2a Pd	-0.040319
1b Pt	0.006466	1c Pt	0.012666	2a Pt	-0.022935
1b Rh	-0.011702	1c Rh	0.000303	2a Rh	0.007976
1b Ru	0.021233	1c Ru	-0.022409	2a Ru	0.029033
				2b Ru	0.060954

## SUPPORTING INFORMATION

WILEY-VCH

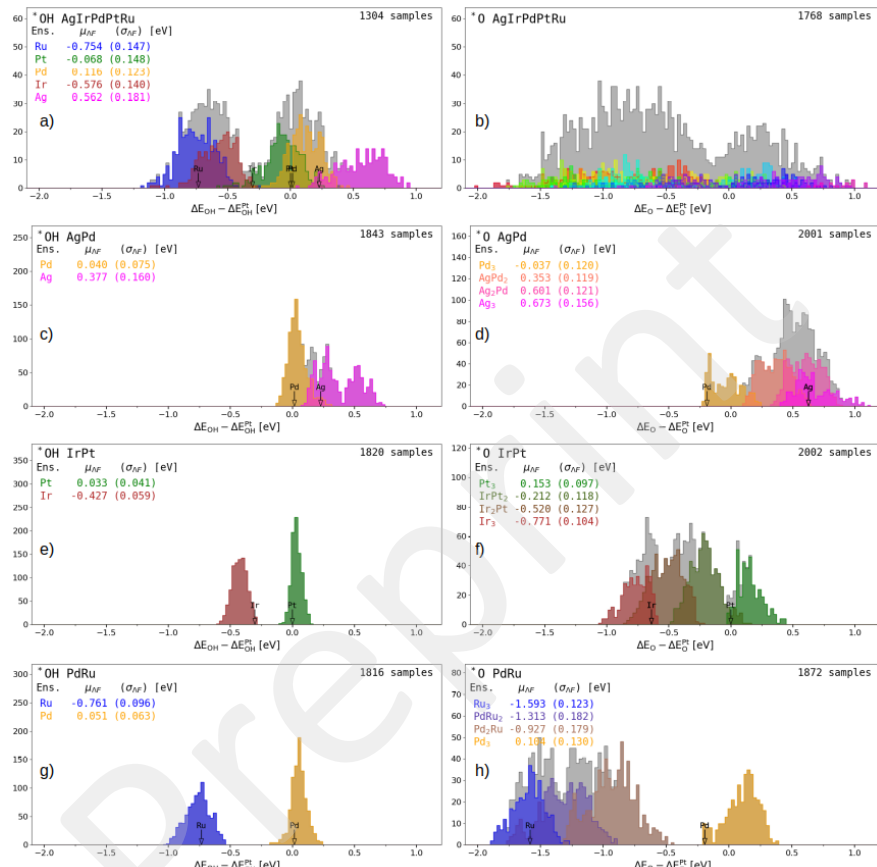


**Figure S5.** Histograms of DFT calculated adsorption energies of \*OH and \*O on the quinary alloy and the three binary alloys. Adsorption ensembles are distinguished by different colors with the mean adsorption energy ( $\mu_{AE}$ ) and standard deviation ( $\sigma_{AE}$ ). Adsorption energies of the pure metal fcc(111) surfaces are marked with black arrows.

## SUPPORTING INFORMATION

WILEY-VCH

**Table S6.** Mean absolute errors (MAEs) in units of eV of several regression algorithms predicting adsorption energies of \*OH and O\* on the quinary and binary alloys using truncated site features as displayed in Figure S3. 20% of the samples were selected for testing with the remaining samples used to train the regression model. The standard deviations on the last digit(s) of the MAEs are displayed in parentheses.

## \*OH adsorption energies - Truncated adsorption site features

Regressor type	Ag-Pd (1843 samples)	Ir-Pt (1820 samples)	Pd-Ru (1816 samples)	Ag-Ir-Pd-Pt-Ru (1304 samples)
Dummy (mean)	0.09(7)	0.05(4)	0.06(5)	0.12(9)
Linear regr.	0.04(3)	0.02(2)	0.05(4)	0.06(5)
Ridge regr.	0.04(3)	0.02(2)	0.05(4)	0.06(5)
Gradient Boosting	0.03(2)	0.018(14)	0.03(3)	0.07(6)
Random Forest	0.03(2)	0.018(15)	0.04(3)	0.07(6)

## \*O adsorption energies - Truncated adsorption site features

Regressor type	Ag-Pd (2001 samples)	Ir-Pt (2002 samples)	Pd-Ru (1872 samples)	Ag-Ir-Pd-Pt-Ru (1768 samples)
Dummy (mean)	0.11(8)	0.10(8)	0.15(10)	0.5(4)
Linear regr.	0.05(4)	0.04(3)	0.08(6)	0.09(7)
Ridge regr.	0.05(4)	0.04(3)	0.08(5)	0.11(8)
Gradient Boosting	0.04(3)	0.04(3)	0.05(4)	0.11(8)
Random Forest	0.03(3)	0.04(3)	0.05(4)	0.10(8)

## SUPPORTING INFORMATION

WILEY-VCH

**Table S7.** Mean absolute errors (MAEs) in units of eV of several regression algorithms predicting adsorption energies of \*OH and O\* on the quinary and binary alloys using extended site features (up to fourth-nearest neighboring atoms for all layers). 20% of the samples were selected for testing with the remaining samples used to train the regression model. The standard deviations on the last digit(s) of the MAEs are displayed in parentheses.

## \*OH adsorption energies - Extended adsorption site features

Regressor type	Ag-Pd (1843 samples)	Ir-Pt (1820 samples)	Pd-Ru (1816 samples)	Ag-Ir-Pd-Pt-Ru (1304 samples)
Dummy (mean)	0.09(7)	0.05(4)	0.06(5)	0.12(9)
Linear regr.	0.04(3)	0.020(17)	0.05(4)	0.08(7)
Ridge regr.	0.03(3)	0.020(19)	0.04(3)	0.06(5)
Gradient Boosting	0.017(16)	0.012(9)	0.03(2)	0.07(5)
Random Forest	0.015(13)	0.011(10)	0.03(2)	0.07(6)

## \*O adsorption energies - Extended adsorption site features

Regressor type	AgPd (2001 samples)	IrPt (2002 samples)	PdRu (1872 samples)	AgIrPdPtRu (1768 samples)
Dummy (mean)	0.11(8)	0.10(8)	0.15(10)	0.5(4)
Linear regr.	0.04(4)	0.02(2)	0.06(4)	0.09(7)
Ridge regr.	0.05(3)	0.026(19)	0.06(4)	0.10(8)
Gradient Boosting	0.024(19)	0.021(17)	0.04(3)	0.08(6)
Random Forest	0.020(18)	0.024(19)	0.03(3)	0.09(8)

## SUPPORTING INFORMATION

WILEY-VCH

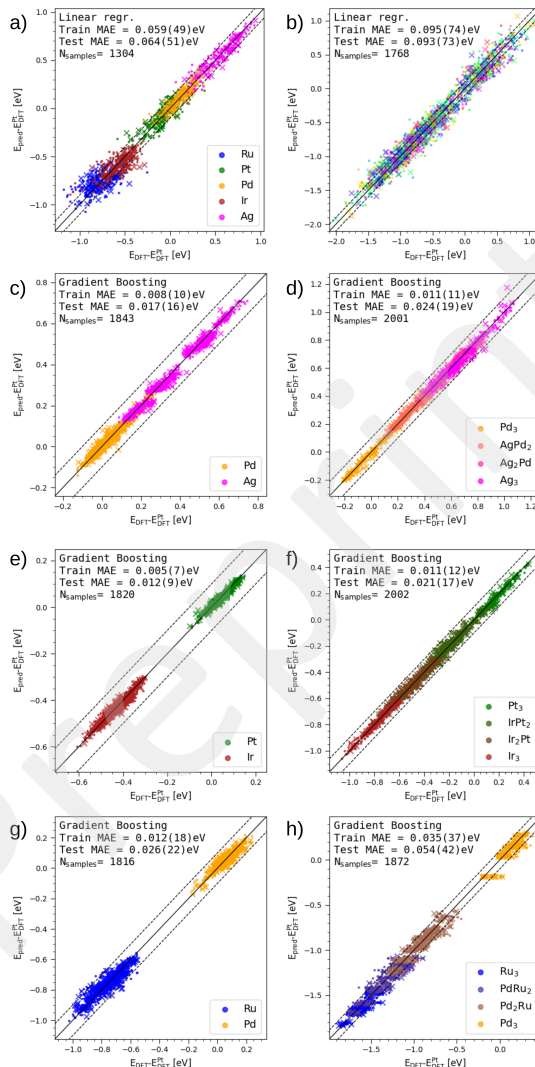


**Figure S6.** Predicted adsorption energy plotted against DFT calculated adsorption energy for the Ag-Ir-Pd-Pt-Ru linear model (a,b), Ag-Pd (c,d), Ir-Pt (e,f), and Pd-Ru (g,h) gradient boosted models for on-top "OH (a,c,e,g) and fcc hollow O<sup>+</sup> (b,d,f,h) adsorption on fcc(111) surfaces. The colors indicate the identity of the adsorption site as shown in the legend. Mean absolute errors with standard deviations are displayed for both training and test set. 20% of the samples were selected for testing (crosses) with the remaining samples used to train the model (circles). For the quinary alloy the results of the linear regression model trained on the truncated site features are displayed, while for the binary alloys the results of the gradient boosted model trained on the extended site features are displayed.

## SUPPORTING INFORMATION

WILEY-VCH

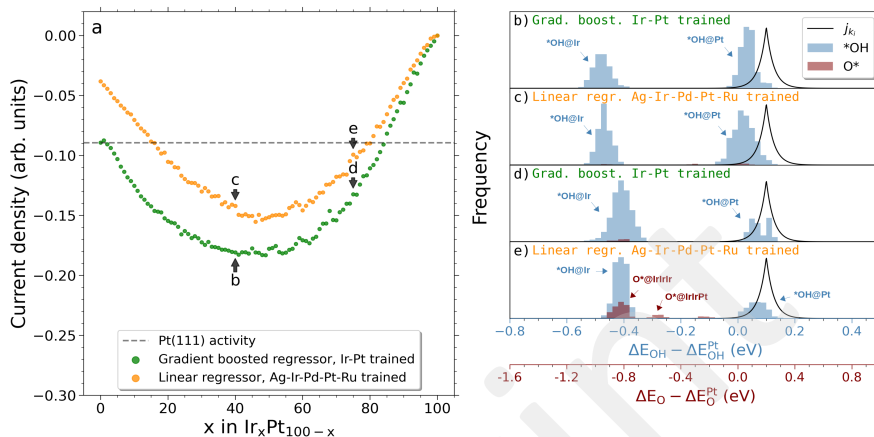


**Figure S7.** a) Simulated current densities of the Ir-Pt binary system shown as a scan from pure Pt to pure Ir with 1 at.% increments. A linear regression model trained on the DFT calculated samples of the quinary alloy is used alongside a gradient boosted model trained on DFT calculated samples of Ir-Pt to predict the adsorption energies of the simulated surface. These predictions serve as input for Equations 1-3 which yield the resulting current densities. b-e) \*OH and O\* net adsorption energy distributions (after intersite blocking) for selected compositions corresponding to the annotations in a). A scaled visualization of the modeled current density in Equation 3 is shown (black solid line).

## SUPPORTING INFORMATION

WILEY-VCH

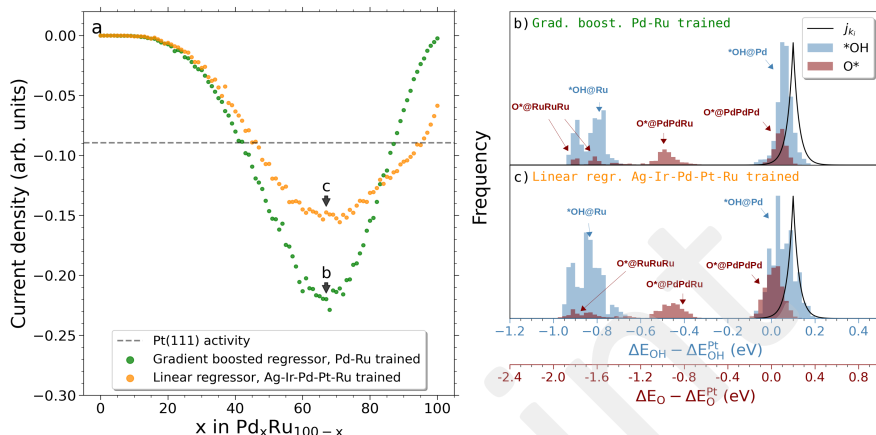


**Figure S8.** a) Simulated current densities of the Pd-Ru binary system shown as a scan from pure Ru to pure Pd with 1 at.% increments. A linear regression model trained on the DFT calculated samples of the quinary alloy is used alongside a gradient boosted model trained on DFT calculated samples of Pd-Ru to predict the adsorption energies of the simulated surface. These predictions serve as input for Equations 1-3 which yield the resulting current densities. b,c)  ${}^*\text{OH}$  and  $\text{O}^*$  net adsorption energy distributions (after intersite blocking) for selected compositions corresponding to the annotations in a). A scaled visualization of the modeled current density in Equation 3 is shown (black solid line).

## SUPPORTING INFORMATION

WILEY-VCH

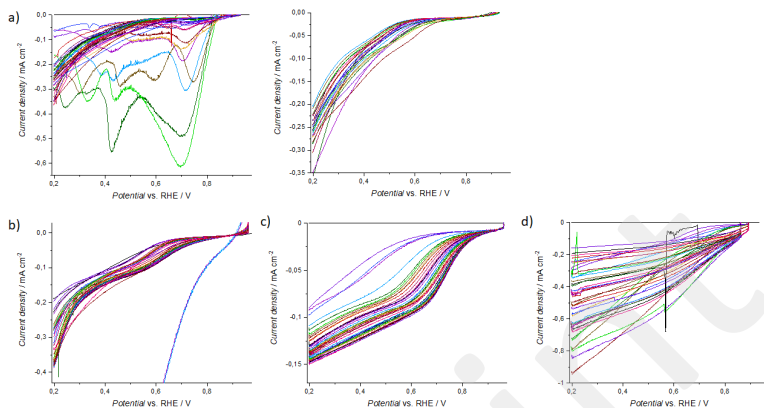


**Figure S9.** All automatically measured LSV curves. **a)** Ag-Pd (right side: LSV plots from the low-Ag part of the sample, without visible film corrosion), **b)** Pd-Ru, and **c)** and **d)** Ir-Pt binaries.

## SUPPORTING INFORMATION

WILEY-VCH

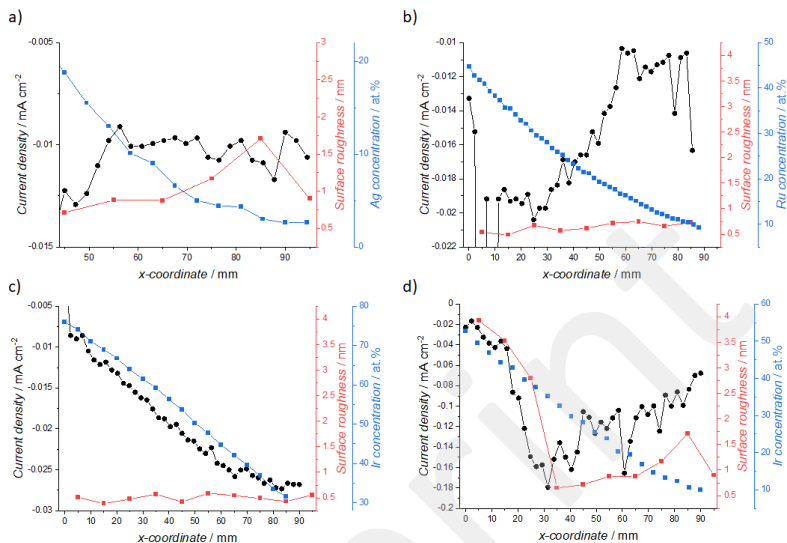


**Figure S10.** Comparisons of measured ORR current densities (black curve) with sample composition (blue curve) and surface roughness (red curve) for synthesized thin-films of a) Ag-Pd, b) Pd-Ru, c) Ir-Pt, and d) Ir(High)Pt.

## SUPPORTING INFORMATION

WILEY-VCH

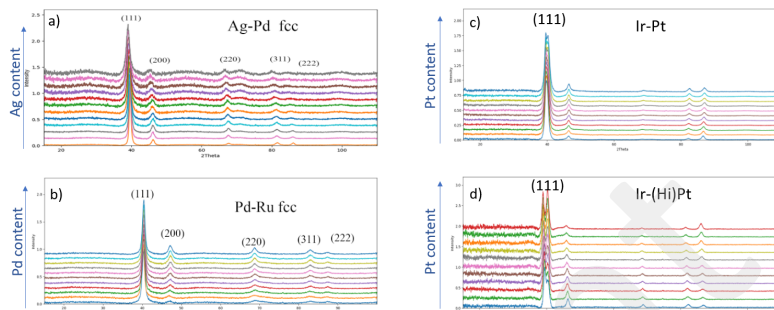


**Figure S11.** XRD profiles for a) Ag-Pd, b) Pd-Ru c) Ir-Pt, and d) Ir-(High)Pt binaries. A single fcc phase is observed for both the Ag-Pd and Pd-Ru systems, regardless of composition, while a dual phase is found for the Ir-Pt system.

## References

- [1] B. Hammer, L. B. Hansen, J. K. Nørskov, *Phys. Rev. B* **1999**, *59*, 7413.
- [2] J. Mortensen, L. B. Hansen, K. W. Jacobsen, *Phys. Rev. B* **2005**, *71*, 035109.
- [3] J. Enkovaara, C. Rostgaard, J. J. Mortensen, J. Chen, M. Dulak, L. Ferrighi, J. Gavnholt, C. Glinsvad, V. Haikola, H. A. Hansen, et al., *J. Phys.: Condens. Matter* **2010**, *22*, 253202.
- [4] A. H. Larsen, J. J. Mortensen, J. Blomqvist, I. E. Castelli, R. Christensen, M. Dulak, J. Friis, M. N. Groves, B. Hammer, C. Hargus, et al., *J. Phys.: Condens. Matter* **2017**, *29*, 273002.
- [5] T. A. A. Batchelor, J. K. Pedersen, S. H. Winther, I. E. Castelli, K. W. Jacobsen, J. Rossmeisl, *Joule* **2019**, *3*, 834.
- [6] C. M. Clausen, T. A. A. Batchelor, J. K. Pedersen, J. Rossmeisl, *Adv. Sci.* **2021**, , 2003357.
- [7] F. Pedregosa, G. Varoquaux, A. Gramfort, V. Michel, B. Thirion, O. Grisel, M. Blondel, P. Prettenhofer, R. Weiss, V. Dubourg, et al., *J. Mach. Learn. Res.* **2011**, *12*, 2825.
- [8] I. E. L. Stephens, A. S. Bondarenko, U. Grønbjerg, J. Rossmeisl, I. Chorkendorff, *Energy Environ. Sci.* **2012**, *5*, 6744.
- [9] J. Greeley, I. E. L. Stephens, A. S. Bondarenko, T. P. Johansson, H. A. Hansen, T. F. Jaramillo, J. Rossmeisl, I. Chorkendorff, J. K. Nørskov, *Nat. Chem.* **2009**, *1*, 552.
- [10] J. K. Nørskov, J. Rossmeisl, A. Logadóttir, L. Lindqvist, J. R. Kitchin, T. Bligaard, H. Jonsson, *J. Phys. Chem. B* **2004**, *108*, 17886.
- [10] T. A. A. Batchelor, T. Löffler, B. Xiao, O. A. Krysiak, V. Strotkötter, J. K. Pedersen, C. M. Clausen, A. Savan, Y. Li, W. Schuhmann, et al., *Angew. Chem. Int. Ed.* **2021**, *60*, 6932.
- [11] D. R. Jones, M. Schonlau, W. J. Welch, *J. Global Optim.* **1998**, *13*, 455.

## Supporting Information

for *Adv. Energy Mater.*, DOI: 10.1002/aenm.202202962

Following Paths of Maximum Catalytic Activity in the Composition Space of High-Entropy Alloys

*Mads K. Plenge, Jack K. Pedersen, Vladislav A. Mints,  
Matthias Arenz, and Jan Rossmeisl\**

**Supporting Information for****Following Paths of Maximum Catalytic Activity in the Composition Space of High-Entropy Alloys**

Mads K. Plenge, Jack K. Pedersen, Vladislav A. Mints, Matthias Arenz and Jan Rossmeisl\*

M. K. Plenge, J. K. Pedersen, M. Arenz, J. Rossmeisl  
Center for High Entropy Alloy Catalysis (CHEAC)  
Department of Chemistry  
University of Copenhagen  
Universitetsparken 5, 2100 København Ø, Denmark  
E-mail: jan.rossmeisl@chem.ku.dk

V. A. Mints, M. Arenz  
Department for Chemistry, Biochemistry and Pharmaceutical Sciences  
University of Bern  
Freiestrasse 3, 3012, Bern, Switzerland

All calculations and simulations were done in Python. All data and scripts necessary for reproducing the results presented in this work can be found at <https://nano.ku.dk/english/research/theoretical-electrocatalysis/katladb/he-a-ridges/>

**Contents**

S1 Kinetic model . . . . .	S2
S2 Revised nudged elastic band to obtain the maximum activity pathway . . . . .	S3
S3 Gaussian process regression . . . . .	S13
S4 Machine learning nudged elastic band to obtain the maximum activity pathway	S15
S5 Ridge detection . . . . .	S22
S6 Artificial elements . . . . .	S30
S7 Directed evolution to obtain the maximum activity pathway . . . . .	S32
S8 Pareto analysis . . . . .	S33
S9 Methods comparison . . . . .	S34

## S1 Kinetic model

Simulation of the catalytic activity is achieved by applying an Arrhenius-like rate expression (Eq. S1) combined with the Koutecký–Levich equation (Eq. S2) for each individual catalyst surface site, considering a face-centered cubic (fcc) (111) surface. These equations together enable the modeling of a linear sweep voltammogram on which an electrochemical potential can be selected to compare catalytic activities. The individual contributions to the catalytic activity from 10,000 surface sites with the frequency of the elements given by the composition being simulated are then averaged to give the resulting catalytic activity in terms of a measure of current density (Eq. S3).

$$j_{k,i} = \exp\left(-\frac{|\Delta G_i - \Delta G_{opt}| - 0.86 \text{ eV} + eU}{k_B T}\right) \quad (\text{S1})$$

$$\frac{1}{j_i} = \frac{1}{j_D} + \frac{1}{j_{k,i}} \quad (\text{S2})$$

$$j = \frac{1}{N} \sum_i^{N_{ads}} j_i \quad (\text{S3})$$

Here,  $j_{k,i}$  is the kinetic catalytic activity at surface site  $i$ ,  $\Delta G_i$  is the adsorption energy of either  $^*\text{OH}$  or  $^*\text{O}$  at site  $i$ ,  $\Delta G_{opt}$  is the optimal adsorption energy of either  $^*\text{OH}$  or  $^*\text{O}$  (set to 0.1 eV<sup>[1]</sup> and 0.2 eV<sup>[2]</sup> higher than for Pt(111) for  $^*\text{OH}$  and  $^*\text{O}$  respectively),  $e$  is the elementary charge,  $U$  is the electrochemical potential applied relative to the reversible hydrogen electrode (RHE),  $k_B$  is the Boltzmann constant,  $T$  is the absolute temperature (set to 300 K),  $j_i$  is the (kinetic and diffusion limited) catalytic activity of site  $i$ ,  $j_D$  is the diffusion limited reaction rate that serves to limit the modeled activity as the potential increases (set to 1 corresponding to the kinetic activity at  $U = 0.86$  V vs. RHE for an optimal site with  $\Delta G_i = \Delta G_{opt}$ ),  $j$  is the resulting catalytic activity,  $N$  is the number of surface sites in the simulation (set to 10,000), and  $N_{ads}$  is the number of sites to which the  $^*\text{OH}$  or  $^*\text{O}$  have adsorbed in the simulation after a simple competitive co-adsorption between the two.

The adsorption energies used in Eq. S1 are estimated from a linear model that was trained on 1304 and 1768 density functional theory (DFT) simulated adsorption energies of  $^*\text{OH}$  and  $^*\text{O}$  respectively on randomly generated surface slabs of AgIrPdPtRu. The linear model as well as the data used to train it are taken from ref. [3] where elaborate descriptions are also given.

## S2 Revised nudged elastic band to obtain the maximum activity pathway

The Nudged Elastic Band (NEB) algorithm is traditionally used to determine minimum energy reaction pathways in atomic configuration space to determine reaction rates and transitions states.<sup>[4,5]</sup> It functions by creating an elastic band from spring forces between images, i.e. points, between initial and final state in an energy landscape. The images are nudged downhill by forces, given by the gradient orthogonal to the path.<sup>[4]</sup> In order to follow the ridges, the NEB method was modified to make the images, go up the orthogonal gradient instead of down. This allows to pick an initial point and a final point. Between these points the images will then be nudged by the gradient while being kept in order by springs between them. Thus, the images form a path along the ridge connecting the initial and final point. The NEB was also modified to work in the composition space, so that it works on the activity function modeled by the Gaussian process regressor (GPR). The composition space resides in simplex space, where all coordinates, i.e. molar fractions, sums to one. The Cartesian coordinates of the simplex space are of one dimension lower. The NEB method is also made to work in n-dimensions for  $n \geq 2$  in Cartesian coordinates, i.e. from a ternary alloy and up. Here there is only investigated up to the quinary composition of Ag-Ir-Pd-Pt-Ru. It was also done with linear interpolation from the grid data.

First a path of  $N + 1$  images is interpolated between a starting point and an end point. For each iteration the force is calculated for  $N - 1$  images, i.e. all images but the initial- and final image. The force on the  $i$ th image at position  $R_i$  is described by Eq. S4 and the spring force by Eq. S5.

$$F_i = F_{si\parallel} + \nabla A(R_i)_\perp \quad (\text{S4})$$

$$F_{si\parallel} = k(|R_{i+1} - R_i| - |R_i - R_{i-1}|)\hat{\tau} \quad (\text{S5})$$

$F_{si\parallel}$  is the spring force given by from the springs between the images and  $A(R_i)_\perp$  is the orthogonal activity gradient. The difference from Henkelman et al.<sup>[4]</sup> is the positive sign on the gradient term and that the surface function is no longer energy but catalytic activity. The used algorithm also uses climbing image (CI). However, instead of accelerating the image along the tangent of the path while also moving down the energy gradient<sup>[4]</sup>, here the image is accelerated up the activity gradient. The force on a CI is given by Eq. S6.

$$F_{CI} = 2\nabla A(R_{max}) \quad (\text{S6})$$

Given that there can be multiple maxima along the path, the climbing image method has here been expanded to allow, if desired, climbing image of more images. An image is then

selected to be a CI if it is greater than its surrounding images.

To allow for a higher density of images close to maxima or more evenly spread images, variable spring constants are used as described by Henkelman et al.<sup>[4]</sup> Here the spring constants are linearly dependent on the activity with greater spring forces at greater activity. The spring constant  $k$  on the  $i$ -th image is given by Eq. S7.  $k_{max}$  is the maximum spring constant  $\Delta k$  denotes the possible variation.  $A_i$  is the greater of image  $i$  or  $i - 1$ .<sup>[4]</sup>

$$k_i = \begin{cases} k_{max} - \Delta k \left( \frac{A_{max} - A_i}{A_{max} - A_{ref}} \right) & \text{if } A_i > A_{ref} \\ k_{max} - \Delta k & \text{if } A_i \leq A_{ref} \end{cases} \quad (\text{S7})$$

The tangent unit vector is calculated as described by Koehl<sup>[6]</sup>. However, since the objective here is to go up the gradients, the conditions are reversed. The non-normalized tangent vector is thus given by Eq. S8, which is then normalized to give  $\hat{\tau}$ .

$$\tau_i = \begin{cases} R_{i+1} - R_i & A_{i+1} < A_i < A_{i-1} \\ R_i - R_{i-1} & A_{i+1} > A_i > A_{i-1} \\ R_{i+1} - R_{i-1} & \text{otherwise} \end{cases} \quad (\text{S8})$$

The used optimization algorithm is the simple steepest descend method<sup>[5]</sup>, which here is altered to ascend. The change in image position  $R$  from the  $j$ -th iteration to the  $j + 1$ -th iteration is given by Eq. S9, where  $\alpha$  is a learning rate.

$$R_{j+1} = R_j + \alpha F_j \quad (\text{S9})$$

The standard used parameters in simulations were  $k = 10$ ,  $\Delta k = 9$ ,  $A_{ref} = 0.1$  and  $\alpha = 0.01$ .

The GPR function and thereby the NEB is described in Cartesian space. In order to keep the images inside the simplex, i.e. within composition space, a function was made to return any images that has been pushed outside by a force to the nearest edge. To proactively prevent as many cases of this as possible and to make convergence of the force (see section S2.1) even possible, each image under each iteration is checked to be on the edge. If an image is on the edge, its calculated force will be checked if it points out of the simplex. If it does, the force is projected along the simplex edge.

## S2.1 Revised nudged elastic band convergence

The NEB algorithm changes the location of the images in the compositions space via the calculated force on each image. As the algorithm progresses the forces should in general be decreasing. At a certain point the forces should reach a magnitude where it becomes negligible. At this point the NEB should be stopped and the NEB would be said to have converged. To

get an understanding of when this convergence point is reached the NEB was run for 100,000, 50,000 and 20,000 iterations for the ternary (Ag–Ir–Pd), quarternary Ag–Ir–Pd–Ru and the quinary composition, respectively. All from Ag to Ir. For each iteration, the maximum force on the images is plotted in Figure S1 along with the activity of all the images added together.

In the ternary composition the maximum force is continuous and the summed activity is always increasing although flattening in the end (Figure S1a). This is not a general trend. For the quarternary and quinary, the maximum force is discontinuous and the summed activity decreases after a local minimum in the maximum force is reached. From this point the quarternary and quinary seems to converge with the force approaching 0 while the summed activity flattens as with the ternary. The reason for the decrease in summed activity seems to be due to several images converging to the maximum, and afterwards spreading out due to the spring forces, leaving only one image on the top and thereby decreasing the summed activity.

From these tests a general convergence criteria of 0.001 in the magnitude of the forces were chosen.

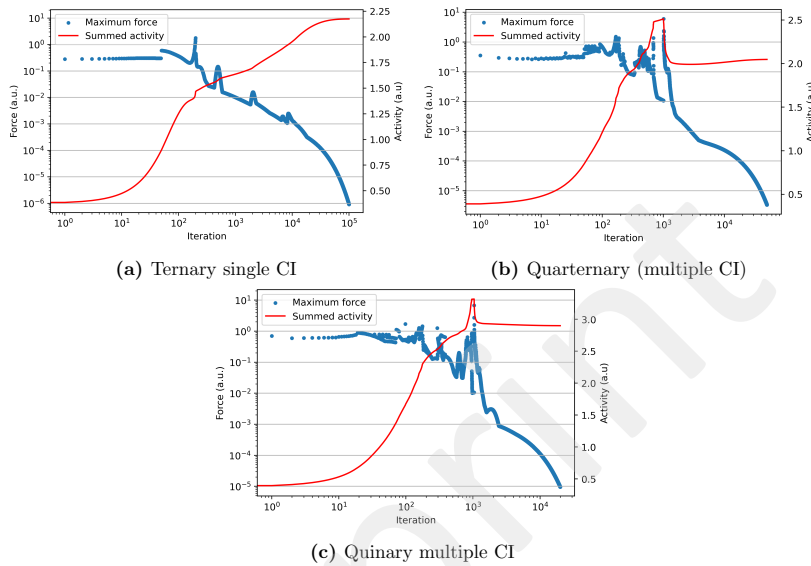


**Figure S1:** The maximum force calculated at each iteration and the activity of all images summed. (a) is the ternary composition Ag-Ir-Pd, (b) is the quarternary composition Ag-Ir-Pd-Ru and (c) and (d) is the quinary Ag-Ir-Pd-Pt-Ru composition. All have pure Ag and Ir as initial and final composition, respectively.

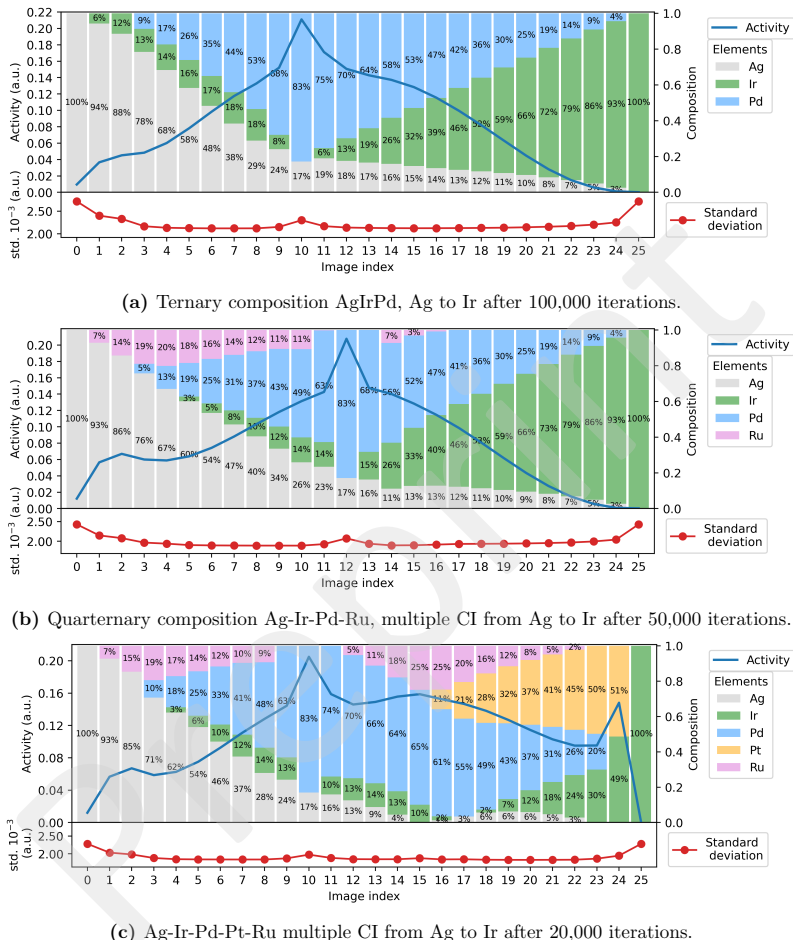


**Figure S2:** Activity height profiles of the images at the end of the force convergence test described in section S2.1.

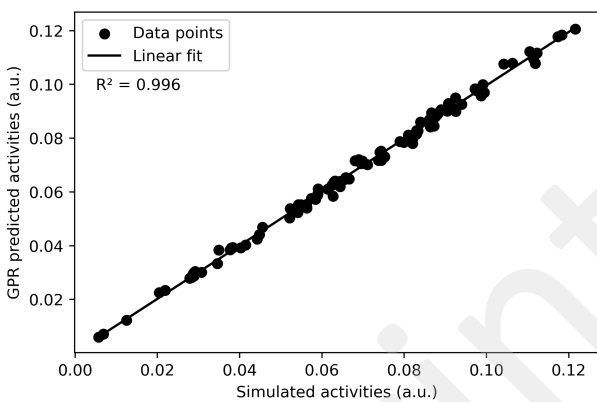


**Figure S3:** Parity plot of 100 quinary random samples' simulated activities vs predicted activities with GPR.

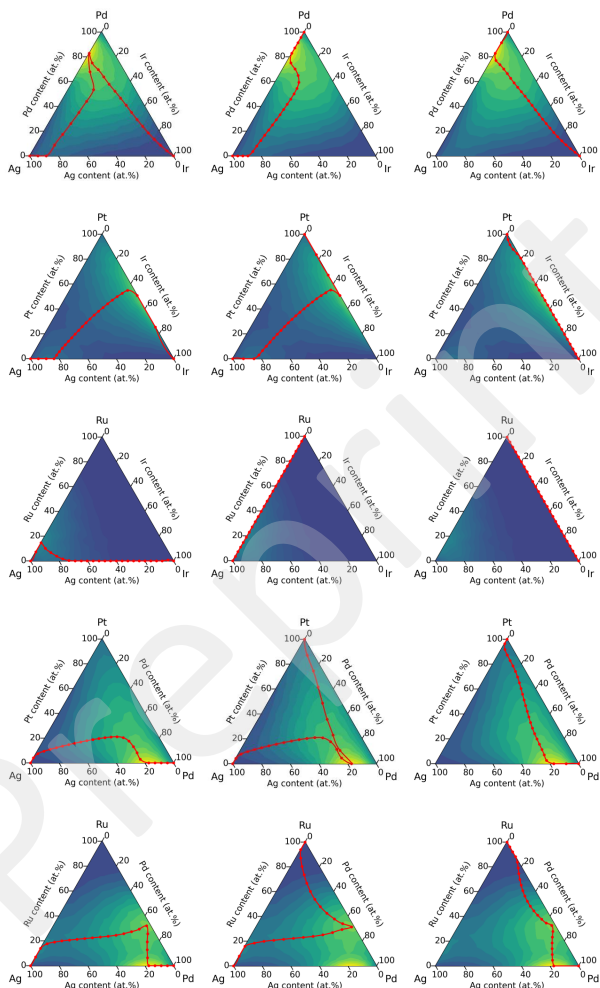


**Figure S4:** All monometals connected via NEB.

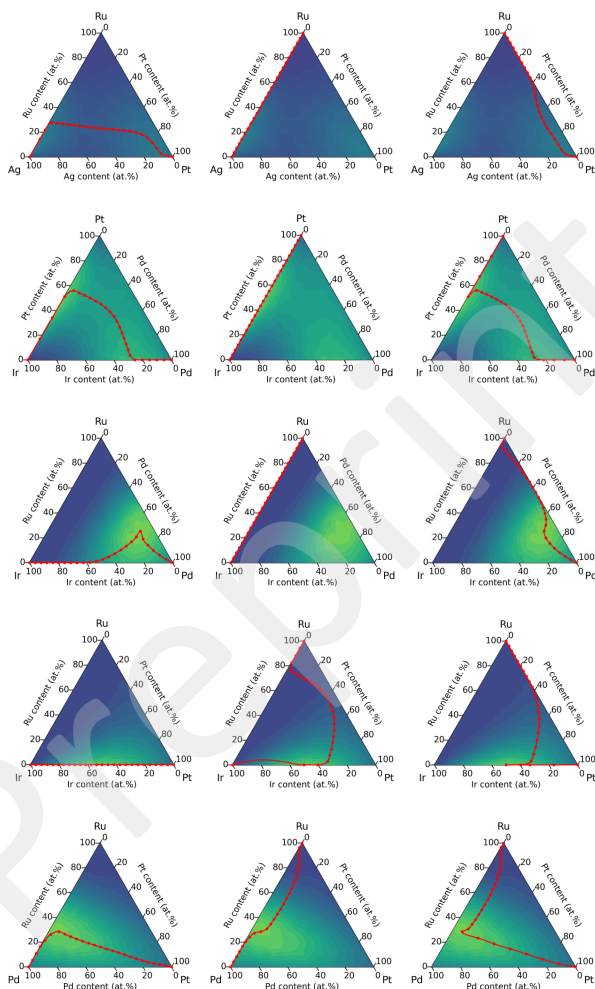


**Figure S4:** (Continued) All monometals connected via NEB.

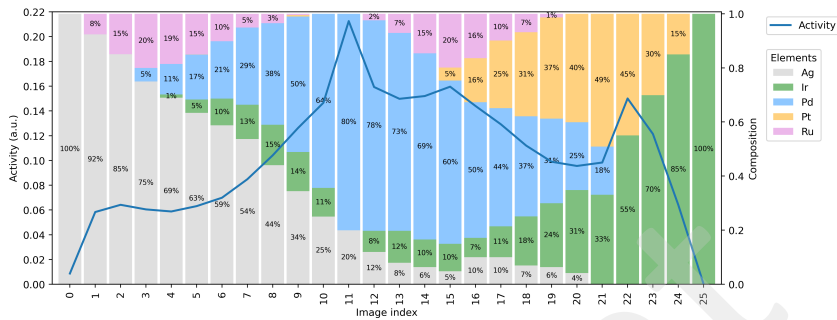


**Figure S5:** Height profile of the activity of the images obtained with linear interpolation NEB in quinary Ag-Ir-Pd-Pt-Ru composition space. Here the gradient is calculated numerically.

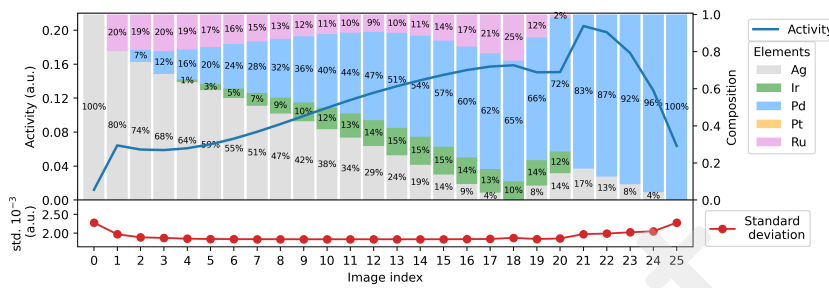


Figure S6: Classic NEB for quinary Ag-Ir-Pd-Pt-Ru from Ag to Pd.

### S3 Gaussian process regression

In Pedersen et al.<sup>[3]</sup> every activity on a 5 at.% molar fraction grid for the Ag–Ir–Pd–Pt–Ru HEA is calculated. In this current work this data set is used to train a Gaussian process regressor (GPR). This is done to create a differentiable surrogate function, which models the activity function, in order to determine the ridges and predict gradients. The kernel used in the GPR is given in Equation S10, where the first term is the product of a constant and the squared exponential kernel and the second term is the white noise kernel. The optimized hyperparameters are the constant  $C$ , the length scale  $l$ , and the noise (or variance)  $\sigma^2$ .  $\delta_{ij}$  is the Kronecker delta.

$$k(\mathbf{x}_i, \mathbf{x}_j) = C^2 \exp\left(-\frac{|\mathbf{x}_i - \mathbf{x}_j|^2}{2l^2}\right) + \sigma^2 \delta_{ij} \quad (\text{S10})$$

GPR is a non-parametric kernel machine that can achieve non-linear regression<sup>[7]</sup>. A Gaussian process is described by a prior mean function and a covariance (i.e. kernel) function which defines a distribution over functions. The GPR is trained by optimizing the hyperparameters in the kernel, given training points<sup>[7]</sup>.

GPR is used used on the data generated in Pedersen et al.<sup>[3]</sup> to model the whole composition space in Ag–Ir–Pd–Pt–Ru and to make predictions in the machine learning algorithm. The Gaussian process is implemented in Python via the module scikit-learn<sup>[8]</sup>. The used kernel, Eq. S10, is the constant kernel multiplied on the radial basis function (RBF) plus a white noise kernel (WhiteKernel). The white noise kernel is added because the calculated activity contains some uncertainty coming from the randomness in the brute force method<sup>[3]</sup>. It estimates the noise level in the data<sup>[8,9]</sup>. The RBF kernel is used because it is a standard kernel that fits many applications<sup>[9]</sup>.

The gradient of the activity function is used in the NEB algorithm and in the ridge detection algorithm. The first derivative of the kernel is used to find the predicted gradient of the activity function, which is given by Eq. S11, where  $\nabla \mathbf{K}$  is a vector containing the derivatives of the kernel function<sup>[10]</sup>. The partial derivative of the kernel between a point  $\mathbf{x}_*$  and training point  $\mathbf{x}_i$  is given by Eq. S12

$$\nabla A = (\nabla \mathbf{K})^\top \cdot \boldsymbol{\alpha} \quad (\text{S11})$$

$$\frac{\delta k(\mathbf{x}_*, \mathbf{x}_i)}{\delta \mathbf{x}_*} = k(\mathbf{x}_*, \mathbf{x}_i) \frac{\mathbf{x}_i - \mathbf{x}_*}{l^2} \quad (\text{S12})$$

To create the Hessian matrix, used in the ridge detection, the second-order partial derivatives of the kernel are used (Eq. S14 and S15). Each element in the matrix is calculated as in Eq. S13.<sup>[10]</sup>

$$H_{i,j} = \frac{\partial^2 A(\mathbf{x})}{\partial x^j \partial x^k} = (\partial_j \partial_k \mathbf{k}(\mathbf{x}))^\top \cdot \boldsymbol{\alpha} \quad (\text{S13})$$

$$\frac{\partial^2 k(\mathbf{x}_*, \mathbf{x}_i)}{\partial \mathbf{x}^j \partial x^2} = k(\mathbf{x}_*, \mathbf{x}) \frac{(\mathbf{x}_* - \mathbf{x}_i)^2}{l^4}, \quad \text{for } j = k \quad (\text{S14})$$

$$\frac{\partial^2 k(\mathbf{x}_*, \mathbf{x}_i)}{\partial x^j \partial x^k} = k(\mathbf{x}_*, \mathbf{x}_i) \frac{(\mathbf{x}_*^k - \mathbf{x}_i^k)(\mathbf{x}_*^j - \mathbf{x}_i^j)}{l^4}, \quad \text{for } j \neq k \quad (\text{S15})$$

#### S4 Machine learning nudged elastic band to obtain the maximum activity pathway

For this NEB method to be applicable in practice, where the space is not already known, it must directly calculate the activity from the molar fraction in the given point. In order for this to be done within a realistic and useful time frame, a Machine Learning NEB (ML NEB) algorithm was integrated as described by Torres et al.<sup>[11]</sup>

In order to make fewer evaluations machine learning NEB has been developed. The overall workflow of the ML-NEB algorithm is that the Gaussian process samples the image that has the greatest uncertainty<sup>[11,12]</sup>. After added and trained on this sample the NEB algorithm is run again. In the initializing process the initial-, final- and equimolar composition is sampled. The algorithm runs until every image's uncertainty is below a given threshold and the NEB has converged given a max force criteria as described in section S2.1. The GP model trained to the data set is considered to provide a relatively accurate description of the composition. Therefore, the criteria for the maximum uncertainty has been chosen from the results of the force convergence test, which are shown in Figure S2. Here the uncertainty of the images are plotted underneath the activity. There is a greater uncertainty on the edges and it's even higher for the mono-metallic composition. This makes sense since there are fewer data points near the edge and corner points as well as they are not surrounded by data points. Since the initial and final composition will be sampled and they are on the edges or corners in the applications used in this work, they don't need to be regarded when determining the image with the highest uncertainty. The ternary results, shown in Figure S2a, have the highest uncertainties. When disregarding the initial and final image they are all below  $2.5 \cdot 10^{-3}$ . Thus, this is chosen as the uncertainty criteria. The quarternary and quinary results, in Figure S2b and S2c, are only slightly below in uncertainty.

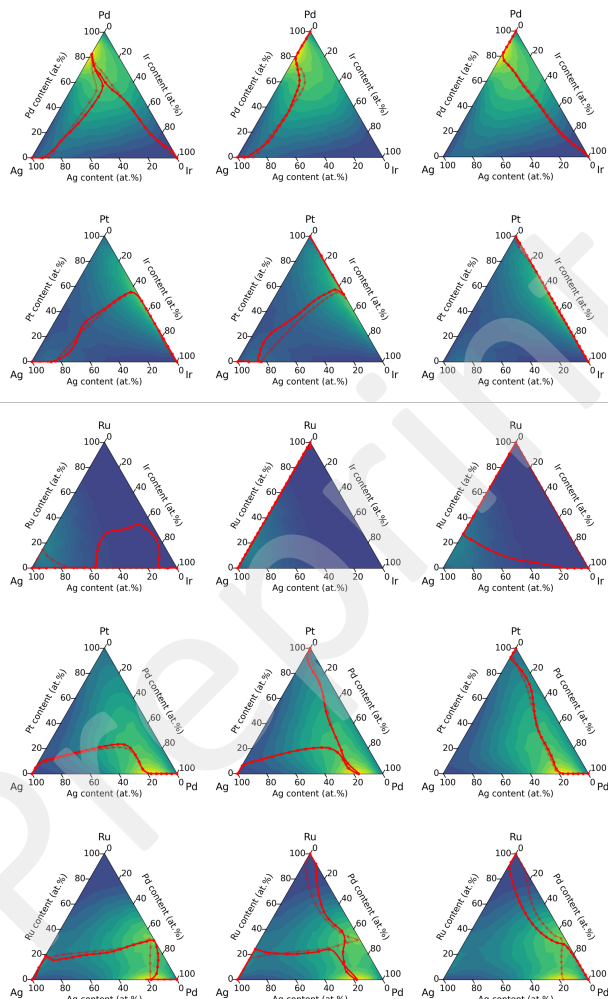


**Figure S7:** Connecting pure metals via ML NEB as shown in red. The results are compared to the classic NEB path, which is shown in faded red.

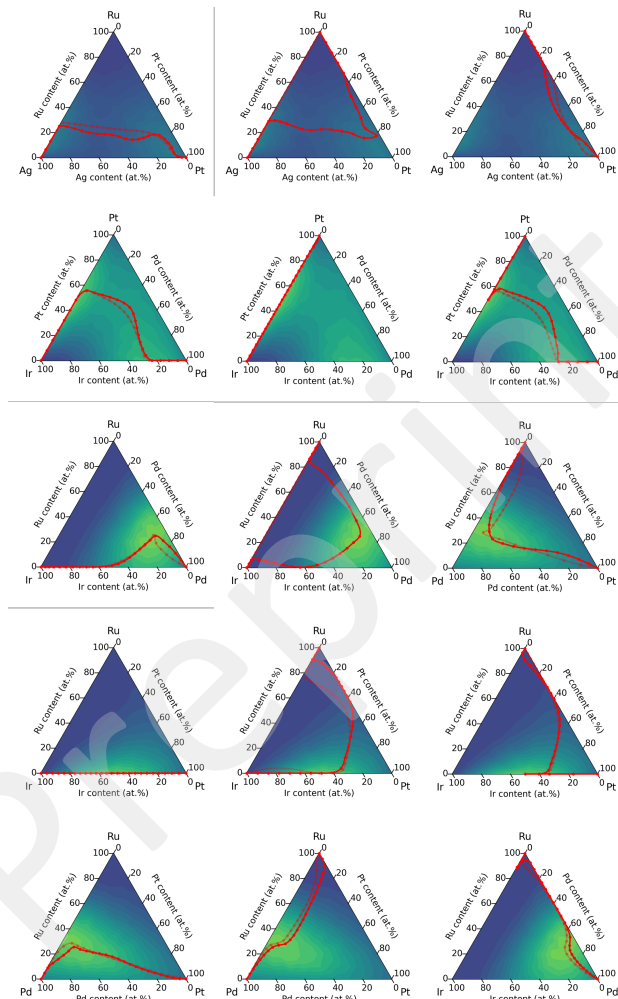


**Figure S7:** (Continued) Connecting pure metals via ML NEB as shown in red. The results are compared to the classic NEB path, which is shown in faded red.

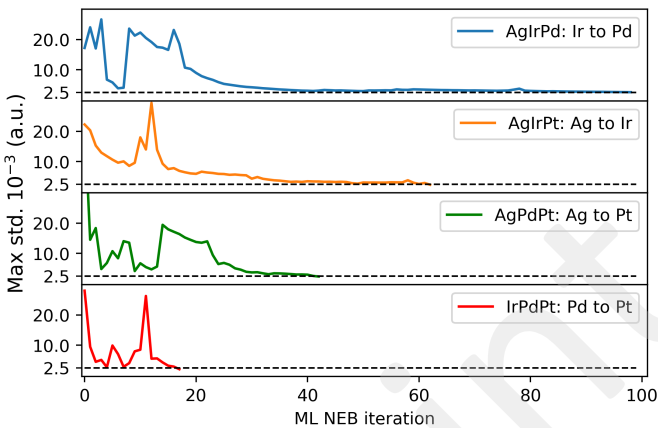


**Figure S8:** The maximum standard deviation from the GPR on the images in each iteration of ML NEB on four ternary compositions from Figure S7. The four compositions are compared because they represent different convergence behaviours

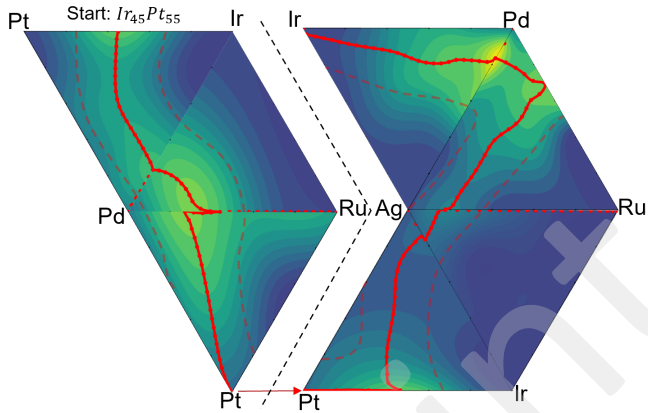


**Figure S9:** Ternary substitution using ML NEB through the same ternary composition spaces as in Figure 1 in the main text. The contour plots show the catalytic activity function predicted by the Gaussian process regressor fitted on the training samples in each ternary composition space. The dashed lines are a guide to the eye to where the activity function within each composition should be comparable to Figure 1.

**Table S1:** Start, finish and number of samples in each composition space in the ML NEB ternary substitution (Figure S9). A minimum of 10 samples and a maximum of 100 NEB iterations was set.

\*Did not converge as it reached maximum in ML NEB iterations. The resulting images from this was taken from the connecting mono-metallic data via ML NEB (Figure S7).

Composition	Start	Finish	nr. of samples
IrPdPt	Ir <sub>45</sub> Pt <sub>55</sub>	Pd	15
IrPdRu	Ir <sub>23</sub> Pd <sub>77</sub>	Ru	10
PdPtRu	Pd <sub>56</sub> Ru <sub>44</sub>	Pt	15
AgIrPt	Pt	Ag	102*
AgPdRu	Ag <sub>82</sub> Ru <sub>18</sub>	Pd	54
AgIrPd	Ag <sub>17</sub> Pd <sub>83</sub>	Ir	23
End: Ag <sub>3</sub> Ir <sub>97</sub>	Total samples: 219		

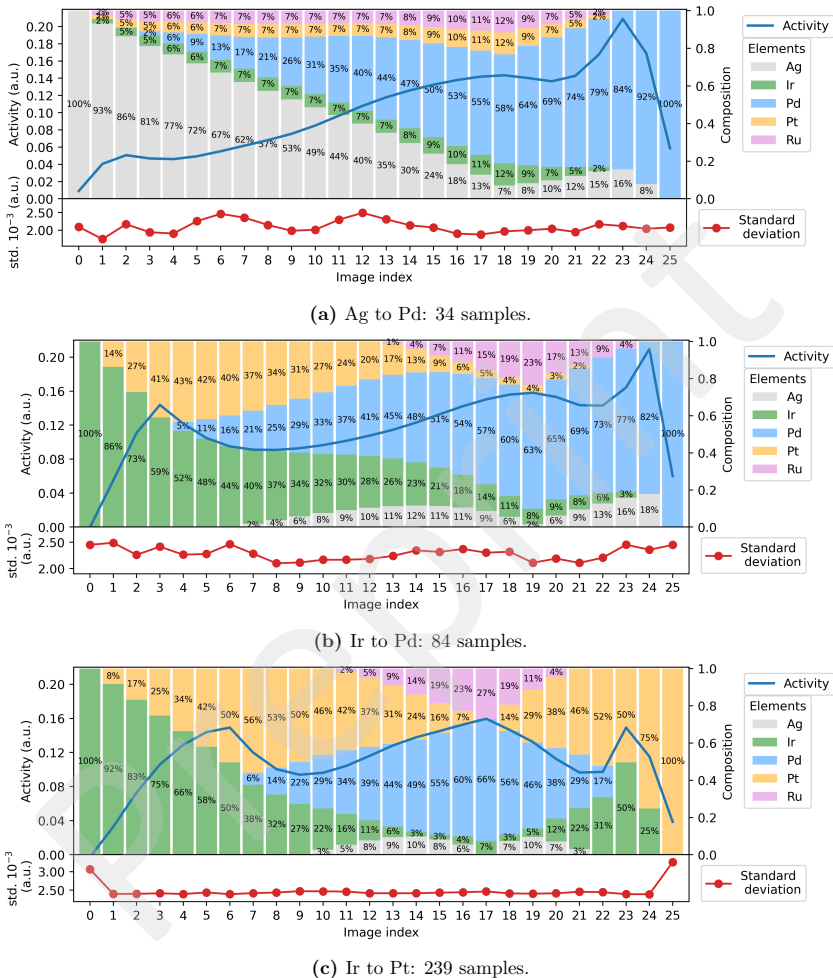


**Figure S10:** Examples of ML NEB in quinary Ag-Ir-Pd-Pt-Ru composition space.

## S5 Ridge detection

In attempt to evaluate if all ridges were found via NEB or just that it indeed converges to ridges; a ridge detection algorithm was made. A ridge in any dimension is characterized by being a maximum orthogonal to the path direction. Determining if a point is on a ridge can therefore be done by looking at the curvature in the point. It is evaluated using the eigenvalues and -vectors of the Hessian matrix in the specific point<sup>[13]</sup>. The ridge detection is done on the GPR predicted function, since it gives a model of the true activity surface and the kernel is infinitely differentiable<sup>[9]</sup>.

In  $n$ -dimensions, the  $k$ -dimensional ridge, meaning the point is a maximum in  $n - k$  dimensions, is defined by<sup>[13]</sup>:

1. The  $n - k$ 'th eigenvalue of the Hessian matrix is negative:  $\lambda_{n-k} < 0$ , where  $\lambda_1 \leq \lambda_2 \leq \dots \leq \lambda_n$
2. The dot product of the gradient with the eigenvectors up to the  $n - k$ 'th eigenvector of the Hessian matrix, where their eigenvalues obey the above condition, must be zero:  $\nabla f(\mathbf{x}) \cdot \mathbf{e}_i$  for  $i = 1, 2, \dots, n - k$

When checking which points in a grid is on a ridge there is little likelihood the point is exactly on the ridge given a dot product of exactly zero. Therefore, the point is accepted as a ridge if its absolute value is close to zero by some margin, typically 0.001.

The results from the ridge detection algorithm on ternary compositions are shown in Figure S11 and they are put together in a big map in Figure S12. Overall, the ridges in Figure S11 resembles the paths found via the NEB and ML NEB methods, see Figure S4 and S7. There is also a small ridge detected with a surprising shape. Many such features are seen in the different compositions in Figure S11. In Figure S15 the predicted surfaces outside the simplex is plotted. This shows how the GPR models the surface by making maxima outside the simplex space when the maximum or maxima in the data is on the edge. In the map in Figure S12, for most part, the ridges somewhat continue in the neighboring composition space. Some discrepancies are due to the fact that the GPR is trained to each composition individually and other are due the way the Gaussian Process has created the surfaces as discussed above and illustrated in Figure S15. However, overall the map shows that the ridges are connected in the ternary compositions.

In Figure S13 is an example of ridges in higher dimensions shown. A  $k$ -dimensional ridge is a maximum in  $d - k$  dimensions, where  $d$  is the Cartesian dimensions of the surface<sup>[13]</sup>. So, a ridge known from a mountain landscape or the ones seen in the ternary composition are

1D-ridges. From Figure S13 it is visible that the 2-dimensional ridges are like sheets while the 1-dimensional ridges are lines within these sheets. The known maxima in this subspace, shown in yellow, are not connected via 1D ridges, as one would suspect. Only the maximum  $\text{Ir}_9\text{Pd}_{64}\text{Ru}_{27}$  lies on a 1D ridge. However, the maxima are still connected via the 2D ridges. The NEB path, shown in green, connects the maxima successfully and lies, mostly, on the ridge points. From Figure S13a it is clear that there are two separate ridges. In Figure S14 the faces of the 4-element simplex are shown. One face, Ag-Ir-Ru (Figure S14c), has no ridges detected. For the other sides, some ridges or features are recognizable from the ridges detected in the ternary space (Figure S11). This shows that when adding elements and therefore adding dimensions, what is seen as a ridge may alter. This may be due to the Gaussian Process now having new nearby points in other directions that it has to fit to. In all, this indicates that there might be more ridges when navigating in higher elemental composition spaces, but still suggest that several maxima can be connected through the same ridge. Indeed, here the known maxima were all connected through a single, although higher dimensional ridge.

The ridge detection algorithm works in all dimensions from ternary (2D) and up. However, there seems to be some problems both in scaling in dimensions and in reliability of the predicted ridges. The scaling problem is due to the fact that it can only test if a point is on a ridge and not predict which points are on a ridge. Especially because a relatively fine grid is needed to make accurate predictions to which points are on ridges. Furthermore, the algorithm has to solve  $d \times d$  Hessian matrices for their eigenvalues, where  $d$  is Cartesian dimensions. However, there is also a problem with the multidimensional ridges. Finding paths via the ridges only really makes sense for 1D ridges, but the way the Gaussian process works, makes maxima outside the simplex, when the maximum in the training data is on an edge (illustrated in Figure S15). This could potentially be resolved if the Gaussian process could be constrained to only define its function to be described inside the simplex. A solution to this has not been found. The problem with the predicted maxima being outside the simplex, is that it predicts a point that actually is a maximum to be on a 2- or higher dimensional ridge, whereas it should be on a 1D ridge. This is for example the case with two of the three maxima in Figure S13, namely  $\text{Ag}_{17}\text{Pd}_{83}$  and  $\text{Ag}_{85}\text{Ru}_{15}$ . Another problem in higher dimensions is that it is difficult to plot in any intuitive way.

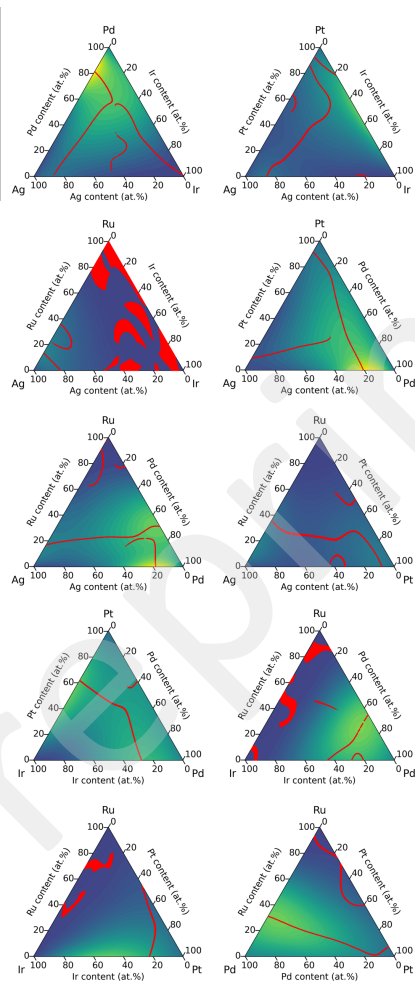


**Figure S11:** Ridges detected (shown in red) in all ternary sub-compositions of Ag-Ir-Pd-Pt-Ru.

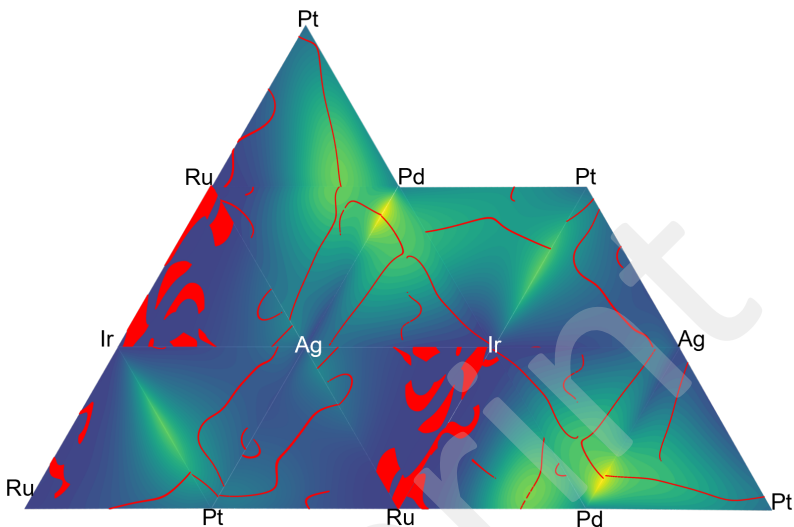


**Figure S12:** Map of all ten ternary compositions (from Figure S11) stitched together with the ridge detection. Some composition are used twice in order to use all. The contour plots are the surface predicted by the GPR in each composition, which is why there is not always perfect accordance between two compositions.

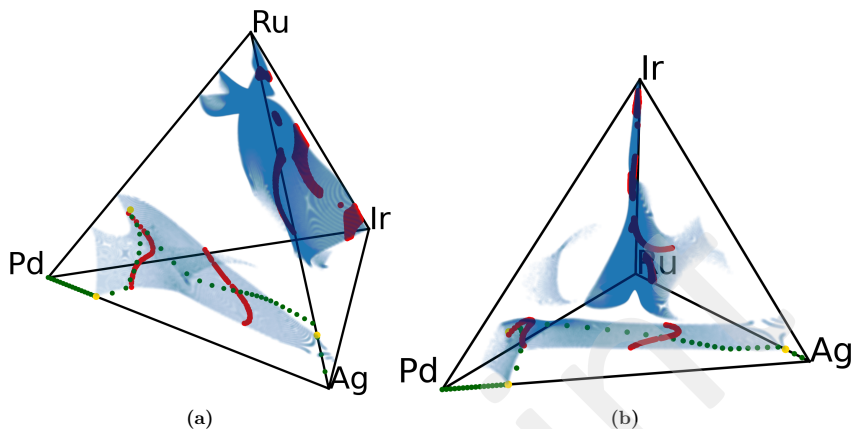


**Figure S13:** Simplex illustrating the Ag-Ir-Pd-Ru quaternary composition space from two different angles (a,b). The figure shows 1D ridges (red), 2D ridges (blue), converged NEB path between Ag and Pd (green) and known maxima within this subspace (yellow).

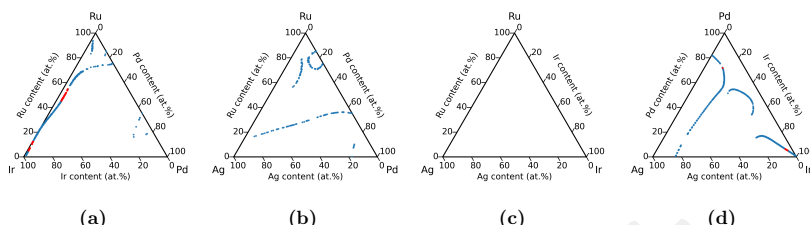


**Figure S14:** The sides of the Ag-Ir-Pd-Ru simplex. 1-dimensional ridges in blue and 2-dimensional ridges in red.

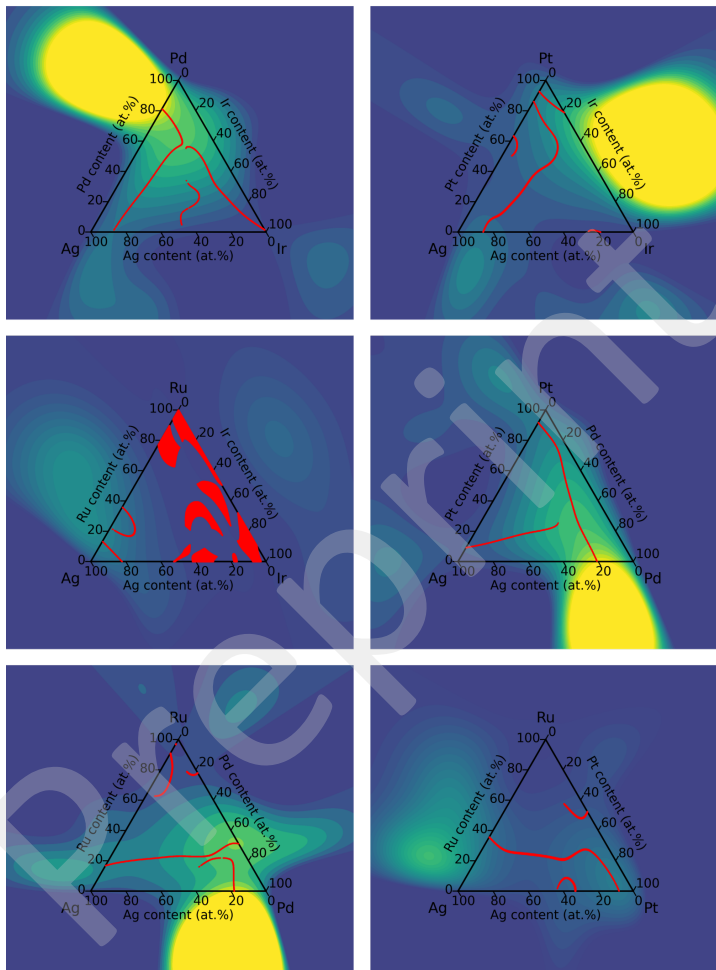


**Figure S15:** The Gaussian process predicted activity function plotted outside simplex and shown with detected ridges in red.

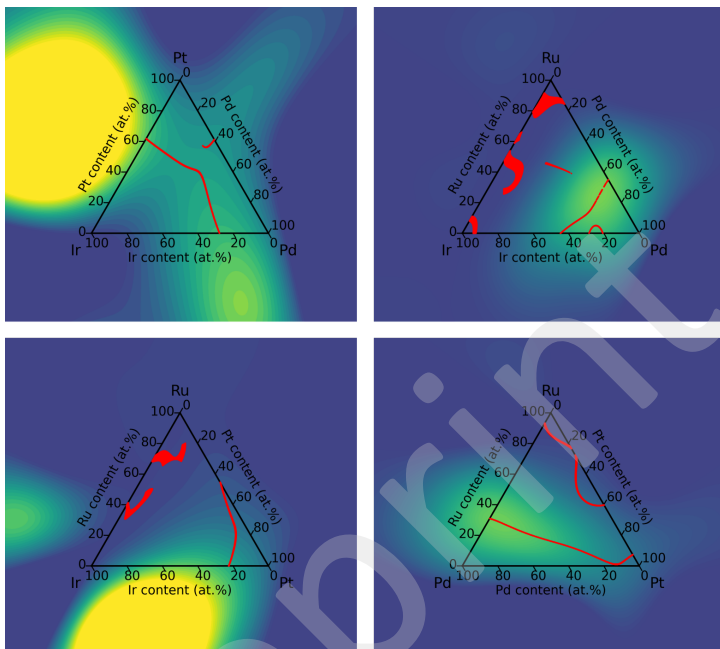


**Figure S15:** (Continued) The Gaussian process predicted activity function plotted outside simplex and shown with detected ridges in red.

## S6 Artificial elements

To get a greater understanding of the nature of this activity landscape and the behavior of the model in general, it is interesting to investigate, what in this work will be called, “artificial elements”. That is, elements which parameters does not describe any actual element. The idea is to see if the activity function show the same behavior when given a different input. Thus, studying an arbitrary activity function of a composition space. The artificial elements are named A, B, C, D and E (B and C, not to be confused with boron and carbon). This new composition space was investigated via the ML NEB using the substituting strategy, described in the previous section. In Figure S16 is shown four out of twenty ternary spaces that the iterative substitution went through in this simulation. There are ten different ternary composition spaces. Already in the second composition, namely ABD, the maximum, within this search, is found:  $B_{83}D_{17}$ . Interestingly, the maximum is again binary and with the same molar fraction as  $Ag_{17}Pd_{83}$ . To test if this is in fact the global maximum, Bayesian optimization using scripts from Pedersen et al.<sup>[3]</sup> was run. The  $\xi$  parameter, which adjusts the exploration vs exploitation level, in the expected improvement acquisition function was set to -0.01. The found maximum was  $B_{82}D_{18}$ , which is indeed the same maximum. This begs the question if there is something inherently within the model that favors binary alloys and possibly this specific molar fraction. The results do show that even though the activities here are much smaller, there are still ridges to walk on and follow through compositions to find maxima.

Further investigation of the model was done by creating “artificial elements”. This was done by replacing the machine learned parameters of the elements with random numbers. For each data set with parameters (found in code of Pedersen et al.<sup>[3]</sup>), the random parameters were set to be between the smallest and greatest value within the data set. Thereby creating random parametric values that are in a realistic range.

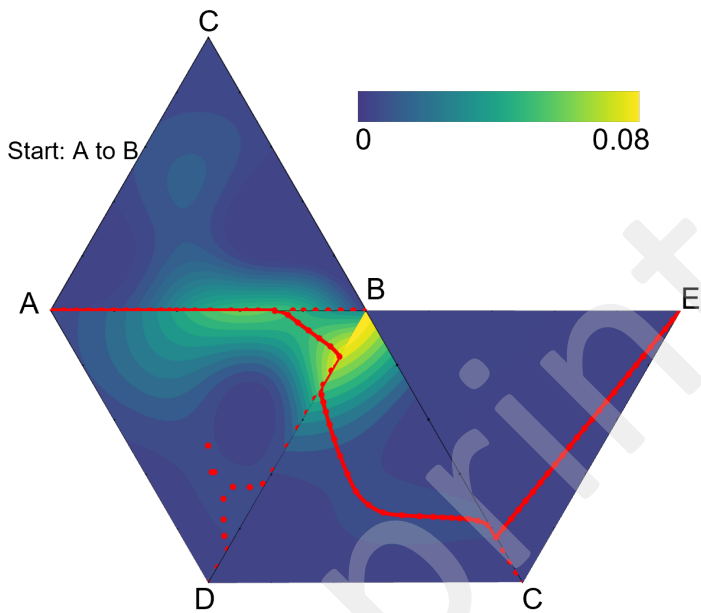


**Figure S16:** A snippet of the ridge walk by substituting artificial elements in ternary space using ML NEB. The simulation start with pure A going to B. The color scale is in arbitrary units.

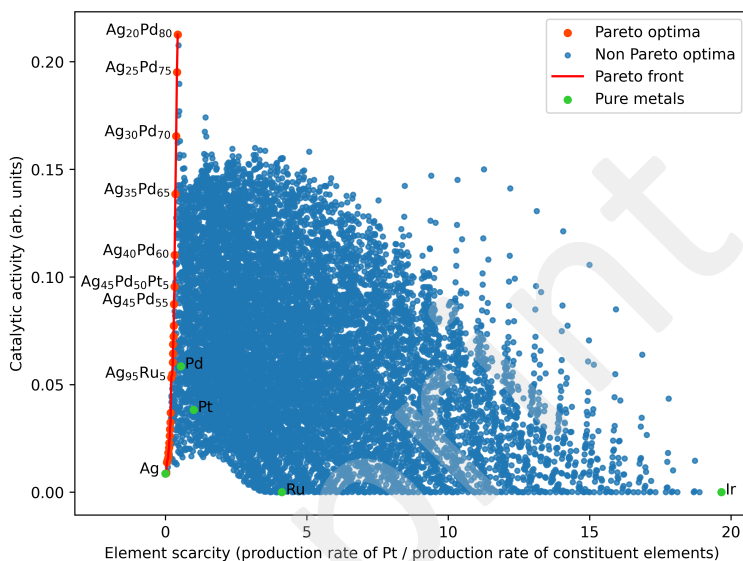
### S7 Directed evolution to obtain the maximum activity pathway

The Machine Learning NEB method requires a chosen end point, which influences the path found. Since the results in this paper indicates that the landscape behaves analogous to an evolutionary landscape, a strategy to experimentally navigate the landscape could also be to use directed evolution.

The directed evolution is implemented, in this work, by drawing samples in a step radius around the previous point. To guide the path along the ridge, in order to walk between maxima, each point is compared to its neighboring mutation points. If a mutation is greater than its two neighbors, it will be seen as a ridge and be favored over a potential mutation with greater activity. It has been found that using this strategy it becomes easier to leave a maximum, whereas by simply choosing the best mutation the algorithm often turns back around.

Following this strategy, the mutations that are treated as ridge points are only a good guess for the actual ridge for two reasons: Firstly, it is unlikely that the mutation will fall precisely on the ridge unless many mutations are made. Secondly, a point is a ridge if it is a maximum orthogonal to the path and by drawing the samples along a radius does not fulfill this definition.

However, by choosing a larger step length, i.e., a higher percentage change in the molar fractions of the mutations, the approximation becomes more accurate given a high enough density of mutations. A way to circumvent this is to make extra samples which give the orthogonal gradient; however, this costs  $2n + 1$  samples instead of just  $n$ . Because of higher simplicity the first described strategy is used in this paper with a mutation change (step length radius) of 0.25 in composition space.

**S8 Pareto analysis**

**Figure S17:** Full scale of Pareto plot of activity vs price in terms of annual Pt production where all 5 at.% grid points are included.

### S9 Methods comparison

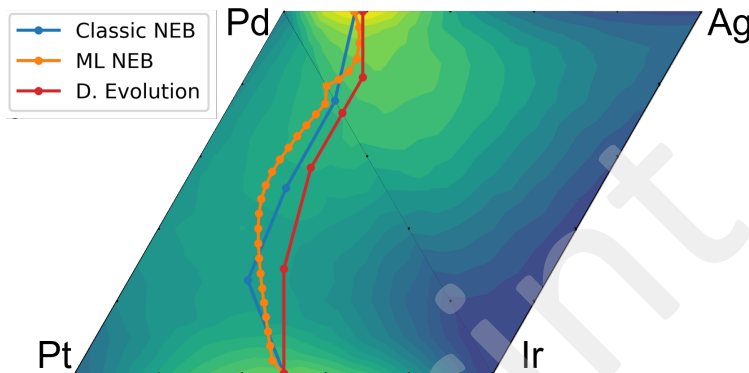


**Figure S18:** Comparing the different methods for going from one optimum ( $\text{Ir}_{50}\text{Pt}_{50}$ ) to another ( $\text{Ag}_{17}\text{Pd}_{83}$ ). The classic NEB is chosen to only include 5 compositions to lower the amount of samples needed as much as possible while still being functional.

**Table S2:** Number of samples needed to converge to the paths in figure S18. For ML NEB and Directed Evolution the samples are calculated with the kinetic model. The Classic NEB is run on the fitted GPR with the number of samples calculated from the number of images and iterations used. It is calculated as three samples per moveable image per iteration: One for activity and two for gradient (The gradient would need to be calculated numerically).

	Classic NEB	ML NEB	Directed Evolution
Number of samples	4717	112	52
Final composition	$\text{Ag}_{17}\text{Pd}_{83}$	$\text{Ag}_{17}\text{Pd}_{83}$	$\text{Ag}_{19}\text{Pd}_{81}$

## References

- [1] I. E. L. Stephens, A. S. Bondarenko, U. Grønbjerg, J. Rossmeisl, I. Chorkendorff, *Energy Environ. Sci.* **2012**, *30*, 6744.
- [2] J. Greeley, I. E. L. Stephens, A. S. Bondarenko, T. P. Johansson, H. A. Hansen, T. F. Jaramillo, J. Rossmeisl, I. Chorkendorff, J. K. Nørskov, *Nat. Chem.* **2009**, *1*, 552.
- [3] J. K. Pedersen, C. M. Clausen, O. A. Krysiak, B. Xiao, T. A. A. Batchelor, T. Löfller, V. A. Mints, L. Banko, M. Arenz, A. Savan, et al., *Angew. Chem. Int. Ed.* **2021**, *60*, 24144.
- [4] G. Henkelman, B. P. Uberuaga, H. Jónsson, *J. Chem. Phys.* **2000**, *113*, 9901.
- [5] D. Sheppard, R. Terrell, G. Henkelman, *J. Chem. Phys.* **2008**, *128*, 134106.
- [6] P. Koehl, *J. Chem. Phys.* **2016**, *145*, 184111.
- [7] C. E. Rasmussen, *Gaussian Processes in Machine Learning*, 63–71, Lecture Notes in Computer Science, **2004**.
- [8] F. Pedregosa, G. Varoquaux, A. Gramfort, V. Michel, B. Thirion, O. Grisel, M. Blondel, P. Prettenhofer, R. Weiss, V. Dubourg, J. Vanderplas, A. Passos, D. Cournapeau, M. Brucher, M. Perrot, E. Duchesnay, *J. Mach. Learn. Res.* **2011**, *12*, 2825.
- [9] C. E. Rasmussen, C. K. I. Williams, *Gaussian processes for machine learning.*, Adaptive computation and machine learning. MIT Press, **2006**.
- [10] J. E. Johnson, V. Laparra, A. Pérez-Suay, M. D. Mahecha, G. Camps-Valls, *PLOS ONE* **2020**, *15*, e0235885.
- [11] J. A. Garrido Torres, P. C. Jennings, M. H. Hansen, J. R. Boes, T. Bligaard, *Phys. Rev. Lett.* **2019**, *122*, 156001.
- [12] O.-P. Koistinen, F. B. Dagbjartsdóttir, V. Ásgeirsson, A. Vehtari, H. Jónsson, *J. Chem. Phys.* **2017**, *147*, 152720.
- [13] D. Eberly, *Ridges in Image and Data Analysis*, Kluwer Academic Publishers, **1996**.

Supplementary Materials for  
**Learning in Higher Dimensions: A Strategy for Alloy  
Electrocatalyst Discovery**

V. A. Mintz *et al.*

Corresponding authors: Jan Rossmeisl, [jan.rossmeisl@chem.ku.dk](mailto:jan.rossmeisl@chem.ku.dk); Matthias Arenz,  
[matthias.arenz@unibe.ch](mailto:matthias.arenz@unibe.ch)

## I. Materials and Methods

### Synthesis

The particles were synthesized using a solvothermal based synthesis.<sup>1</sup> The precursors, H<sub>2</sub>PtCl<sub>6</sub> (Alfa Aesar, 99.999%), HAuCl<sub>3</sub> (Alfa Aesar, 99.99%), RuCl<sub>3</sub> (Sigma Aldrich, ReagentPlus), RhCl<sub>3</sub> (Alfa Aesar and Sigma Aldrich, 99.98%), IrCl<sub>3</sub> (Strem Chemicals, 99.9%), OsCl<sub>3</sub> (Sigma Aldrich), ReCl<sub>3</sub> (Sigma Aldrich), PdCl<sub>2</sub> (Sigma Aldrich, 99%) were dissolved in EtOH (VWR, AnalaR NORMAPUR ACS) to form 20 mM precursor solution. Following, a 1 ml stoichiometric mixture of these precursor solutions were added together with 3 ml EtOH to the microwave vessel. The stoichiometric mixtures were selected using a Sobol Sequence generator.<sup>2,3</sup> This produced a 5 mM reaction mixture. This mixture was heated up till 20 bars for a duration of 30 minutes in the microwave (CEM, Discover SP). The resulting colloidal suspension was centrifuged, washed with EtOH, and air dried. Following, it was dissolved in 3.25 ml water:iso-propanol (3:1) (Water: deionized and ultrafiltered by a Millipore MilliQ system; iso-propanol: VV) to produce the catalyst ink, with an assumed concentration of 6.15 mM metal. The Energy Dispersive X-Ray spectra of the particles were measured using the EDS Photodetector Ultim max 65 (Oxford instruments) in a GeminiSEM450 (Zeiss). The spectra were taken at 4 different spots, each with a size of 588  $\mu\text{m}^2$  at a working distance of 8 mm and an accelerating voltage of 25 kV.

### Electrochemistry

Electrochemical experiments were conducted in a three-electrode cell utilizing a multi working electrode (MWE) (Fig. S1). The MWE contained 6 glassy carbon disks, each of 5 mm in diameter. 8.181 ml of ink was deposited on each of the disk to produce a catalyst loading of 256 nmol cm<sup>-2</sup>. The reference electrode constituted of a reversible hydrogen electrode. The counter electrode was a platinum wire, which was separated from the main compartment with a frit. The mass transport during the measurements was controlled using a magnetic steering rod, which rotated at 1500 revolutions per minute (RPM). All water used in these experiments was deionized and ultrafiltered by a Millipore MilliQ system (resistivity > 18.2 M $\Omega$  cm, TOC  $\leq$  5 ppb). The electrolyte used in the experiments was 0.1 M H<sub>2</sub>SO<sub>4</sub> (Merck, Suprapur) and was renewed after each measurement.

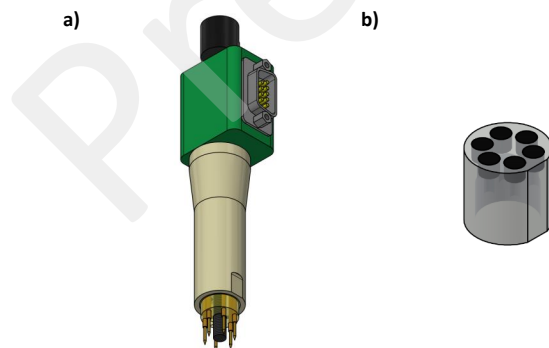


**Fig S1. Electrode in the experimental setup.** (a-b) A rendering of the multi-working-electrode shaft (a) and sample holder (b). The shaft fits to standards glass fittings for an air-tight fit to the electrolyte enclosure. The sample holder has 6 glassy carbon disks, onto which the different catalyst samples can be drop casted. The sample holder and the shaft are keyed so that each sample can easily be related to the acquired current signal.

First, 10 cyclic voltammograms were measured between 0.00 and 0.60 V vs. RHE at a scan rate of 100 mV s<sup>-1</sup>. In the last cycle, the average capacitance was determined in the potential window from 0.3 to 0.5 V vs. RHE. Afterwards, the electrolyte was saturated with O<sub>2</sub> for 20 minutes while the electrode was kept at 1.00 V vs. RHE. Following, the potential was stepped down to 0.60 V vs. RHE in steps of 10 mV, which lasted for 20 seconds. The current was averaged over the last 17 seconds of each time step to produce a single data point.

### Machine learning

For each set of measurements for each of the four alloy systems (AuIrOsPdPtReRhRu, AuOsPdPtRu, IrOsPdPtRu, and IrOsPtRhRu) a Gaussian process regressor was trained on the Cartesian coordinates of the averaged EDX measured compositions and their corresponding ORR cathodic currents at 0.60 V vs. RHE divided by the average capacitance in the region between 0.30 and 0.50 V vs. RHE. The Cartesian coordinates of the compositions were used to eliminate a redundant feature from the compositions (because compositions are constrained to sum to unity). The transformation of compositions into  $m - 1$  dimensional Cartesian coordinates in the composition space with  $m$  being the number of elements was done by converting the barycentric coordinates of a regular simplex with unit side length using the matrix product between the simplex vertices and the composition,

$$\mathbf{r} = \mathbf{V}\mathbf{f}$$

Here,  $\mathbf{r}$  is the  $(m - 1)$ -dimensional Cartesian coordinates of the  $m$ -dimensional molar fractions in  $\mathbf{f}$  (i.e.  $m = 8$  for an eight-metal alloy),  $\mathbf{V}$  is the  $([m - 1] \times m)$  matrix whose columns are the Cartesian coordinates of the  $m$  vertices of the  $(m - 1)$ -dimensional simplex.  $\mathbf{V}$  was obtained by setting the first vertex at the origin  $(0, 0, \dots, 0)$ , the second vertex one unit of distance away at the Cartesian coordinate  $(1, 0, \dots, 0)$  (forming a straight line of unit length), the third vertex one unit away from each of the two first vertices at coordinate  $(1/2, 3^{1/2}/2, 0, \dots, 0)$  (forming an equilateral triangle), etc. for  $m - 1$  dimensions.

For the Gaussian process, the target currents per capacitance were shifted to a mean of zero and scaled to unit variance prior to training. For predictions this scaling and shift was reversed. A zero mean prior and a squared exponential kernel with fitted white noise (Eq. S1) was used for the Gaussian process regressors to model the correlation between experimental measurements,

$$k(\mathbf{r}_i, \mathbf{r}_j) = \exp\left(-\frac{(\mathbf{r}_i - \mathbf{r}_j)^T(\mathbf{r}_i - \mathbf{r}_j)}{2l^2}\right) + \delta_{ij}\alpha^2 \quad (\text{Eq. S1})$$

Here  $k$  is the kernel function,  $\mathbf{r}_i$  and  $\mathbf{r}_j$  are the Cartesian coordinates of the composition indexed  $i$  and  $j$ ,  ${}^T$  denotes the transpose vector,  $l$  is the fitted correlation length scale hyperparameter,  $\delta_{ij}$  is the Kronecker delta which is unity when  $i$  and  $j$  are identical and zero for non-identical  $i$  and  $j$ .  $\alpha$  is the standard deviation of the fitted white noise (independently and identically normally-distributed noise) hyperparameter.

The hyperparameters of the kernel function,  $l$  and  $\alpha$ , were chosen so that they would maximize the log marginal likelihood of the Gaussian process regressor<sup>4</sup>. Or put in other words, the hyperparameters were chosen to maximize the probability of the observed data given the Gaussian process regressor with the kernel in Eq. S1. Plots of the log marginal likelihoods as a function of  $l$  and  $\alpha$  are shown in Fig. S2.

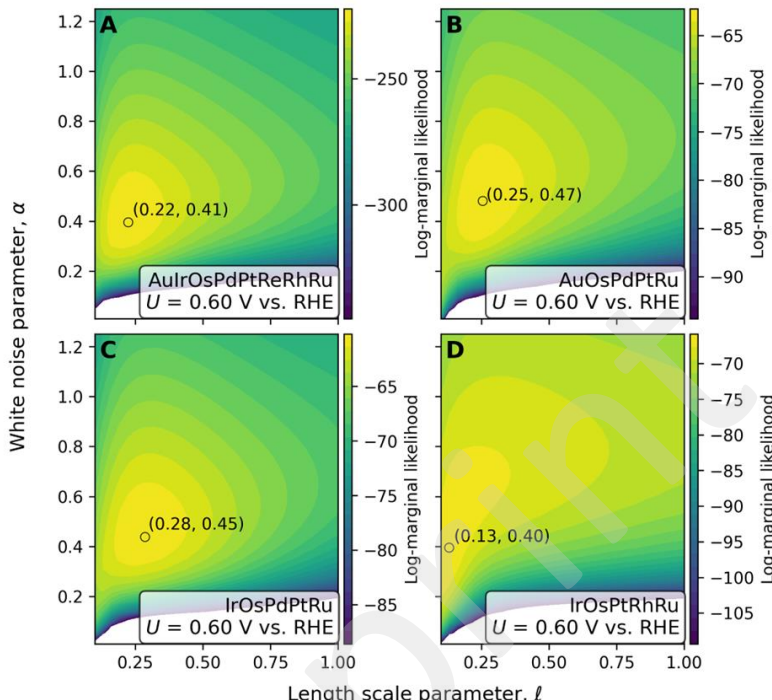


**Fig. S2. Gaussian process regressor (GPR) hyperparameter optimization.** (A-D) Log-marginal likelihood contour plots used to optimize the two hyperparameters for the GPRs of the four alloy systems. Log-marginal likelihoods are shown as a function of the length scale,  $\ell$ , and the white noise,  $\alpha$ , hyperparameters. The three alloy systems AuIrOsPdPtReRhRu (A), AuOsPdPtRu (B), and IrOsPdPtRu (C) show similar optimal length scales and white noises of  $\sim 0.25$  and  $\sim 0.45$ , respectively, whereas IrOsPtRhRu (D) has a log-marginal likelihood optimum at a shorter length scale of 0.13. The IrOsPtRhRu system (D) shows a rather flat plateau of log-marginal likelihoods when going to length scales comparable to the other alloy systems, however, at the cost of higher white noise levels.

For the Bayesian optimization the maximum of the expected improvement acquisition function in Eq. S2 was used to evaluate the next point to sample.

$$\begin{aligned} E[I(\mathbf{r})] &= \int_{-\infty}^{y_{\min}} (y_{\min} - y) N(y; \mu(\mathbf{r}), \sigma(\mathbf{r})) dy \\ &= (y_{\min} - \mu(\mathbf{r})) \Phi\left(\frac{y_{\min} - \mu(\mathbf{r})}{\sigma(\mathbf{r})}\right) + \sigma(\mathbf{r}) \phi\left(\frac{y_{\min} - \mu(\mathbf{r})}{\sigma(\mathbf{r})}\right) \end{aligned} \quad (\text{Eq. S2})$$

Here  $E$  is the expectation value,  $I(\mathbf{r})$  the improvement function at a point  $\mathbf{r}$ ,  $y_{\min}$  is the lowest current sampled so far in the optimization,  $y$  is the current being integrated over,  $N$  is the normal distribution function, the mean of which,  $\mu(\mathbf{r})$ , is the Gaussian process predicted current at the point  $\mathbf{r}$ , and whose standard deviation  $\sigma(\mathbf{r})$  is the uncertainty predicted by the Gaussian process at the same point,  $\Phi$  is the cumulative distribution function of the standard normal distribution (i.e. with  $\mu = 0$  and  $\sigma = 1$ ), and  $\varphi$  is the standard normal distribution function.

## II. Equation for the information density of a composition

The volume of a simplex space with ridge length  $a$  and  $m$  different metals is given by Eq. S3. A high-entropy alloy composition space is described by a simplex with vertices at  $(1,0,0\dots)$   $(0,1,0\dots)$  etc. and a ridge length of  $a = \sqrt{2}$ . When this space is uniformly studied, each experimental sample occupies a fraction of the volume equal to  $V(m, \sqrt{2}) / n_e$ . This fraction of the volume we describe as a simplex with length  $a$  (Eq. S4). The sample density is inversely proportional to the size of the simplex volume. Therefore, the sample density can be estimated using Eq. S5.

$$V(m, a) = \frac{\sqrt{m-1+a}a^{m-1}}{(m-1)!\sqrt{2^{m-1}}} = V(m, 1)a^{m-1} \quad (\text{Eq. S3})$$

$$a(m, n_e) = \left(\frac{V(m, \sqrt{2})}{V(m, 1)n_e}\right)^{\frac{1}{m-1}} = \left(\frac{V(m, 1)\sqrt{2^{m-1}}}{V(m, 1)n_e}\right)^{\frac{1}{m-1}} = \sqrt{2}\left(\frac{1}{n_e}\right)^{\frac{1}{m-1}} \quad (\text{Eq. S4})$$

$$\rho(m, n_e) \propto \frac{1}{a(m, n_e)} = \frac{1}{\sqrt{2}}n_e^{\frac{1}{m-1}} \quad (\text{Eq. S5})$$

Not all simplex geometries can be uniformly filled with the same geometry of smaller simplexes. Therefore, an alternative equation to Eq. S5 can be used which describes the median between the origin and the closest data point in a unit cube (Eq. S6), as described by Hastie et al.<sup>5</sup> Since a simplex geometry is a slice of a unit cube, we assume that the relations in this equation also hold true for a simplex space. Independent of whether Eq. S5 or Eq. S6 are used to determine the number of experiments in higher dimensions, both lead to the identical conclusion that a region exists where studying the combined higher-dimensional system is more efficient (Fig. S2).

$$d(m, n_e) = \left(1 - \left(\frac{1}{2}\right)^{\frac{1}{n_e}}\right)^{\frac{1}{m-1}} \quad (\text{Eq. S6})$$

The number of experiments that are required to study all possible compositions containing  $m_2$  metals from a pool of  $m_1$  metals can be calculated using Eq. S7. In this equation  $m_1$  is the number of metals in the overarching composition space,  $m_2$  the number of elements of a given subspace, and  $n_{e2}$  the number of experiments that are necessary to study that given subspace.

$$n_e(m_1, m_2, n_{e2}) = \frac{m_1!}{(m_2-m_1)!m_1} n_{e2} \quad (\text{Eq. S7})$$

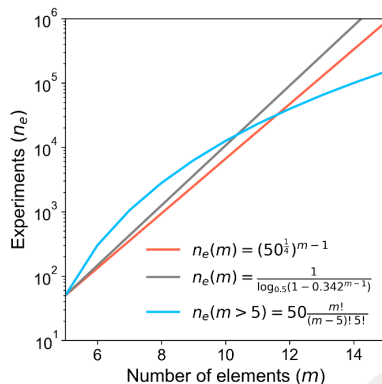


**Fig. S3. Modeled information density in disordered alloys.** (red, grey) The number of experiments required to achieve the same sample density as with 50 experiments in the 5-element space. (blue) The number of experiments required to study all possible 5-element combinations that are part of a more complex alloy space.

According to Eq. S5, 940 experiments in the 8-element space are required to get the same sample density as with 50 experiments in the 5-element space. However, we made the trade-off to do 200 experiments based on Fig. S3. With 200 experiments a normalized sample density of 0.8 is achieved, while a sample density of 1 is desired. To achieve this sample density increase of around 25%, around four times more experiments would be required.

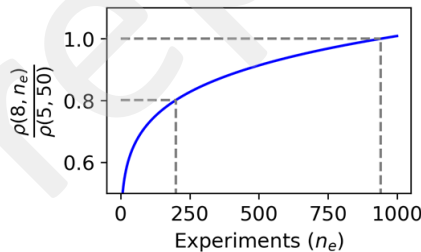


**Fig. S4. Sample density for an 8-element composition space with  $n_e$  experiments.** The dashed lines show the normalized sample density of 0.8 at 200 experiments and 1 at 940 experiments.

### III. Model comparison and bias correction

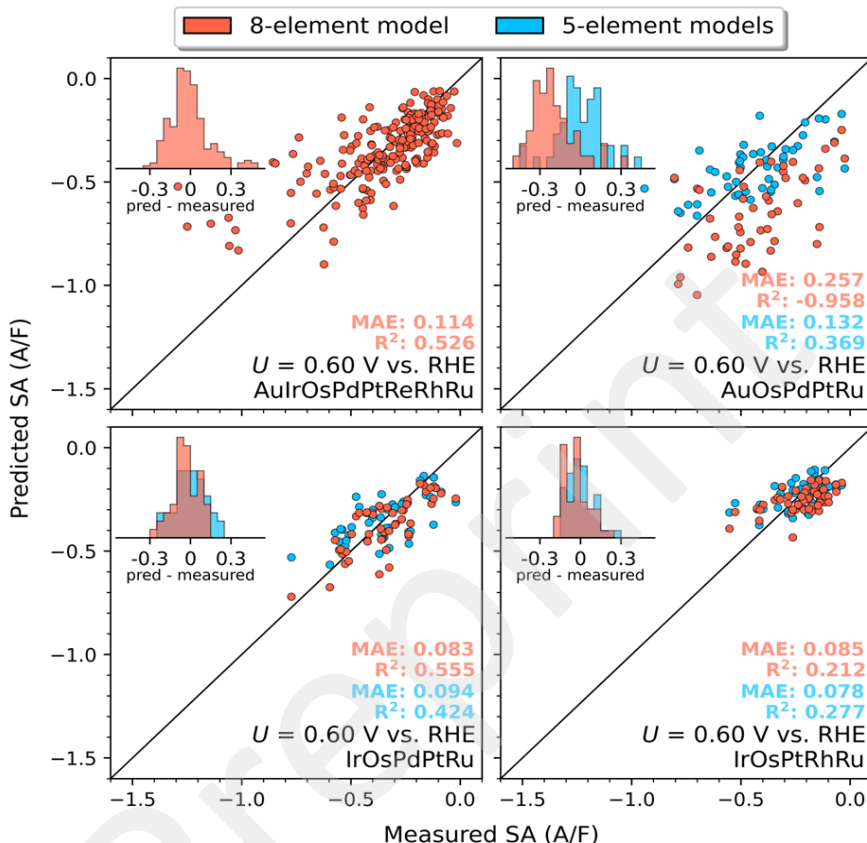


**Fig. S5. Parity plots without bias correction.** Predicted vs. measured current per capacitance for each of the four investigated alloy systems. The prediction was evaluated using the leave-one-out cross-validation. In addition, the subplots with the 5-element models show how the 8-element model is predicting the same data points. The 8-element model is observed to perform similarly to the 5-element model for IrOsPdPtRu and IrOsPdRhRu having approximately the same error metrics. The 8-element model, however, shows a systematic bias for AuOsPdPtRu, resulting in poor prediction in absolute terms, but fair in relative terms. Multiplying by a constant factor corrects this systematic bias as shown in Fig. 2 in the manuscript. The reason for the systematic shift in this part of the composition space is unknown, but undersampling of this region by the 8-element experiments is likely to play a role.

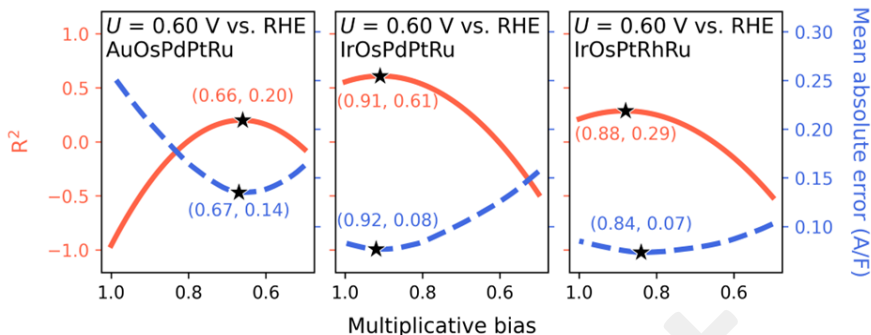


**Fig. S6. Selection of optimal multiplicative bias.** Multiplicative bias of the 8-element model vs. coefficient of determination ( $R^2$ , red solid lines) and mean absolute error (blue, dashed lines) for the three 5-element alloy systems. The star markers indicate the optimal values of the multiplicative bias. The  $R^2$  value assumes its maximum value for a multiplicative bias of 0.66, 0.91, and 0.88 for AuOsPdPtRu, IrOsPdPtRu, and IrOsPtRhRu respectively which has been used to produce the 8-element predictions in Fig. 2 in the manuscript.

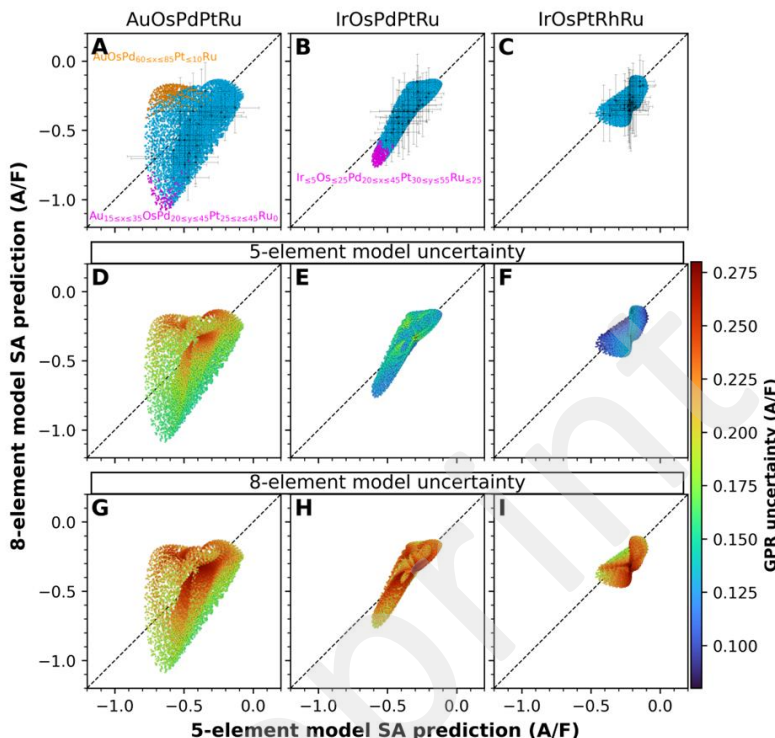


**Fig. S7. Predictions in all of the quinary composition spaces without bias correction.** (A-I) Parity plots comparing the prediction of the 8- and 5-element models on all compositions of the quinary composition spaces taken in steps of 5 at.%. The 8-element predictions have not been corrected for any bias. Each column correspond to a quinary alloy system as labeled in the top. (A-C) Regions of the composition space have been highlighted where the predictions between the 8-element and 5-element models differ: The 8-element model overestimates the activity of compositions with intermediate Au, Pd, and Pt concentrations when ruthenium is absent (magenta points in A) as well as Pd-Pt rich compositions in IrOsPdPtRu (magenta points in B), and underestimates certain Pd-rich compositions in AuOsPdPtRu (orange points in A). Error bars corresponding to the uncertainty of the Gaussian process regressor (GPR) have been shown for a random selection of points. (D-F) Same plots with the color coding illustrating the GPR uncertainty of the 5-element models (the x direction error bars in A-C). (G-I) Same plots with the color coding illustrating the GPR uncertainty of the 8-element model (the y direction error bars in A-C). The GPR uncertainties of the 8-element model are generally larger than for the 5-element models, and the uncertainties are observed to show correlation.

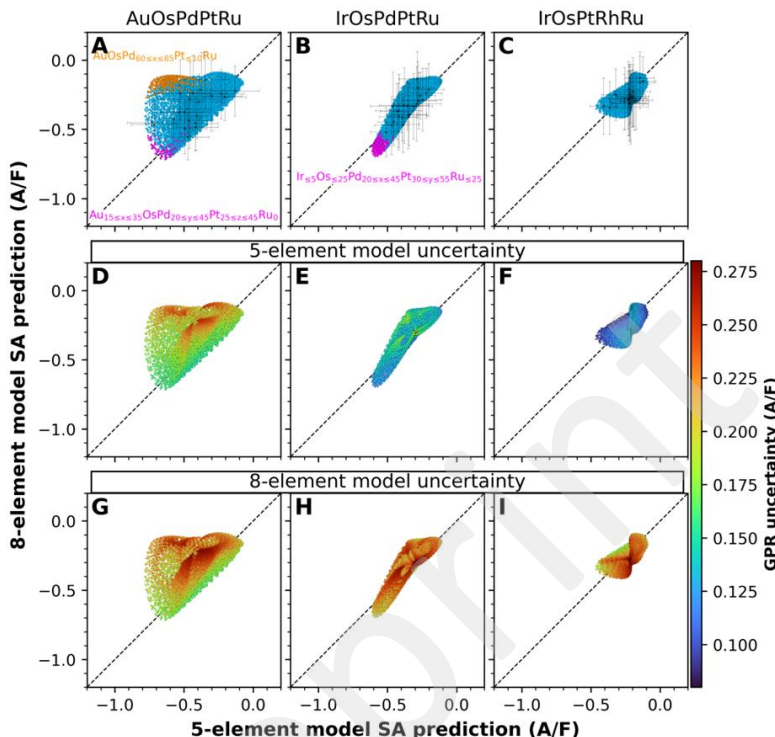


**Fig. S8. Predictions in all of the quinary composition spaces with bias correction.** (A-I) Parity plots comparing the prediction of the 8- and 5-element models on all compositions of the quinary composition spaces taken in steps of 5 at.%. The 8-element predictions have been corrected with a constant multiplicative factor of 0.66, 0.89, and 0.89 for AuOsPdPtRu, IrOsPdPtRu, and IrOsPtRhRu respectively (from Fig. S5). Each column correspond to a quinary alloy system as labeled in the top. (A-C) Regions of composition space identical to those in Fig. S6 have been highlighted. Error bars corresponding to the uncertainty of the Gaussian process regressor (GPR) have been shown for a random selection of points. (D-F) Same plots with the color coding illustrating the GPR uncertainty of the 5-element models (the x direction error bars in A-C). (G-I) Same plots with the color coding illustrating the GPR uncertainty of the 8-element model (the y direction error bars in A-C).

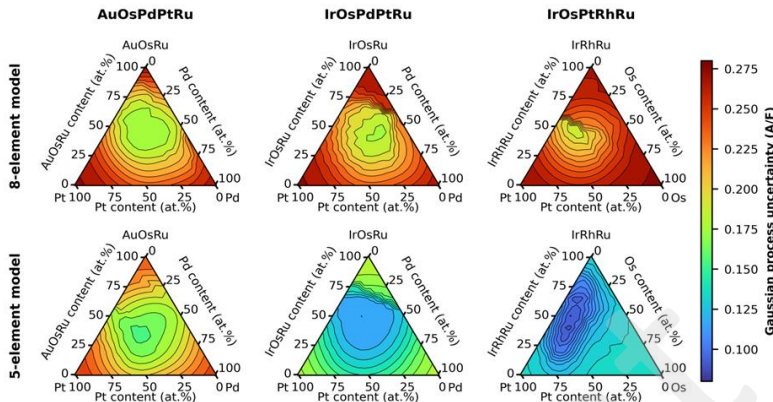


**Fig S9. Model uncertainties around the optima.** Gaussian process regression uncertainties around the optimal compositions in each 5-element composition space for the 5-element and 8-element models. The pseudo-ternary plots are equivalent to those in Fig. 3, B-G in the manuscript in the sense that the uncertainties of the most active compositions are shown on-top of other compositions at the same position in the pseudo-ternary plots. As expected, model uncertainties are observed to increase as the composition approaches binary and unary alloys.

## IV Alloy composition analysis

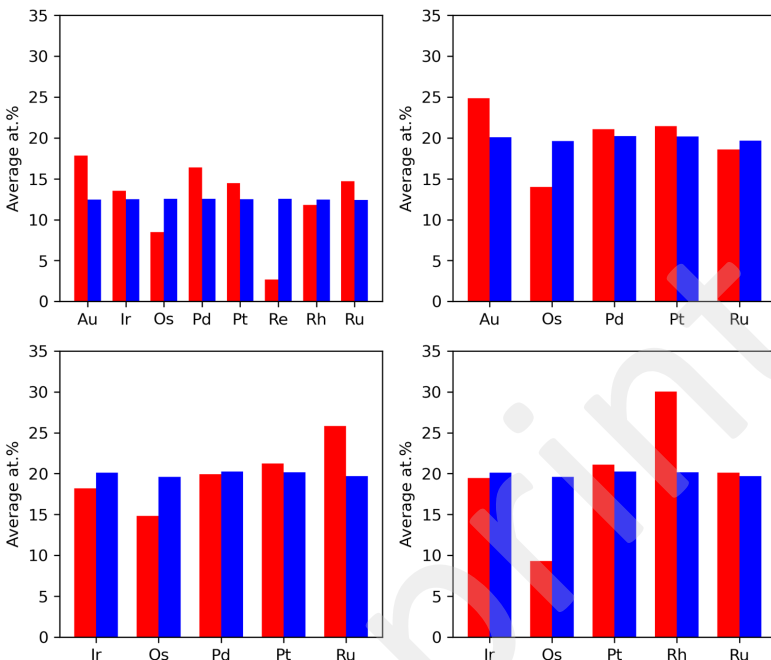


**Fig. S10. Averaged location in composition space.** (red) The average atomic presence of an element in the experimental samples within a catalytic space. (blue) The expected average atomic presence based on the precursor ratios during the synthesis.

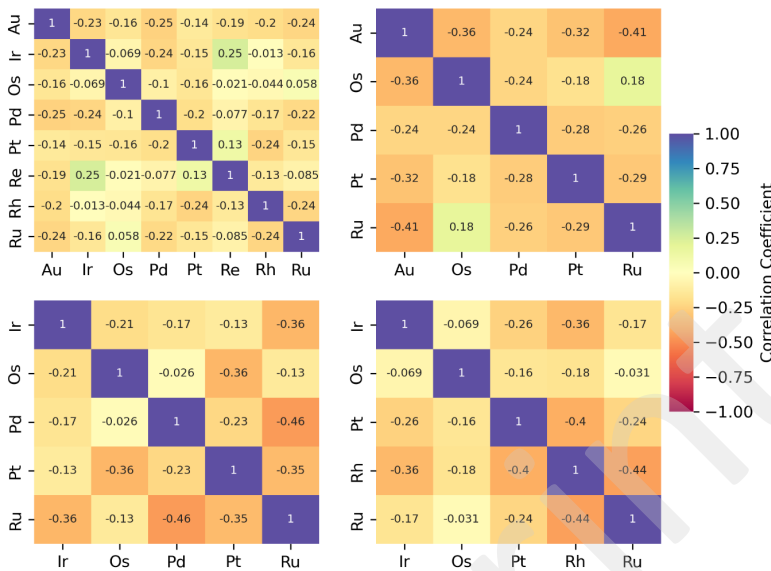
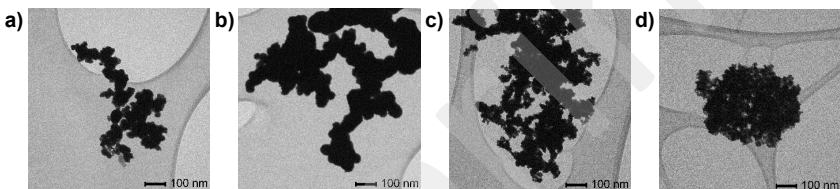


**Fig. S11. Correlation matrixes of molar fractions.** The correlation matrixes for each of the experimental spaces are composed of the Pearson correlation coefficients.

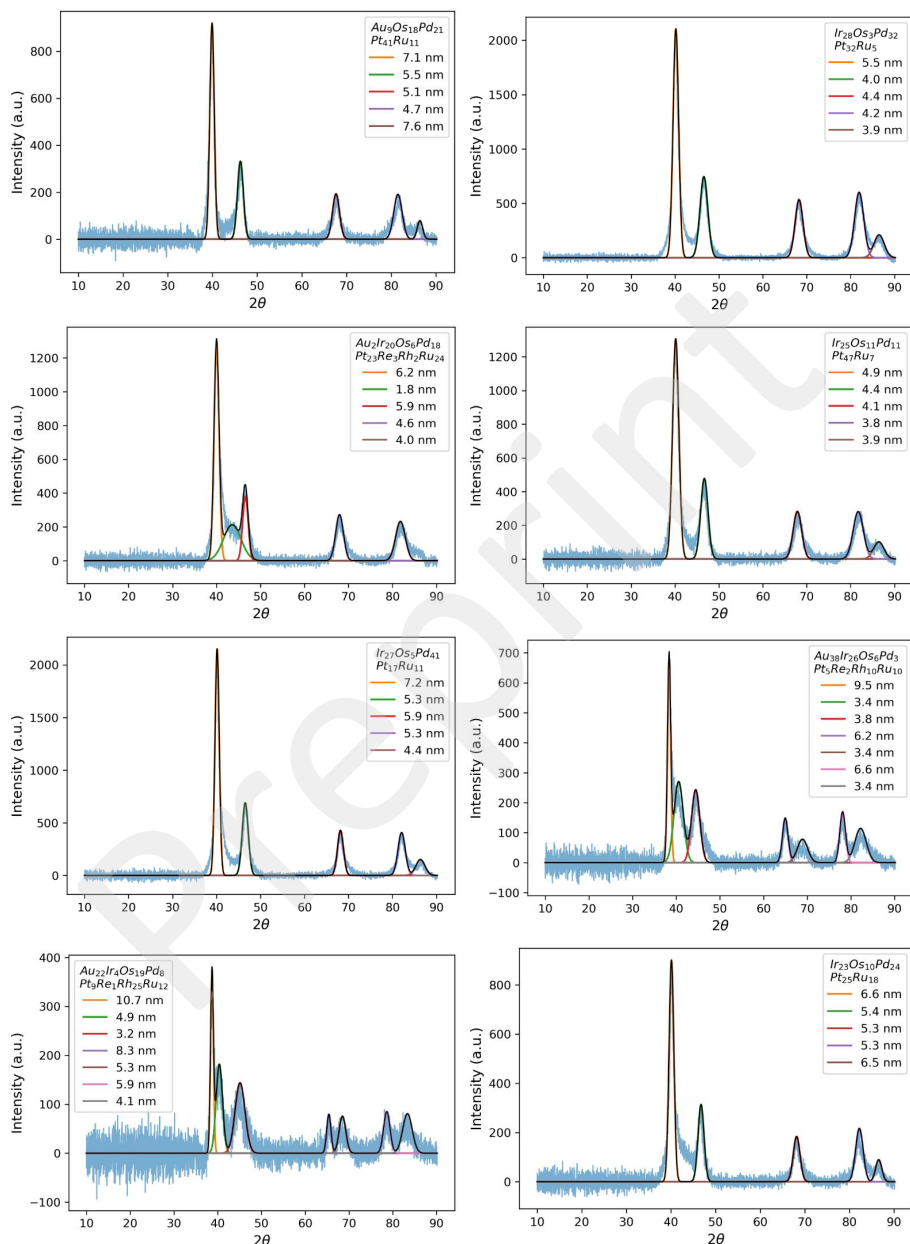
## V Complementary XRD measurements

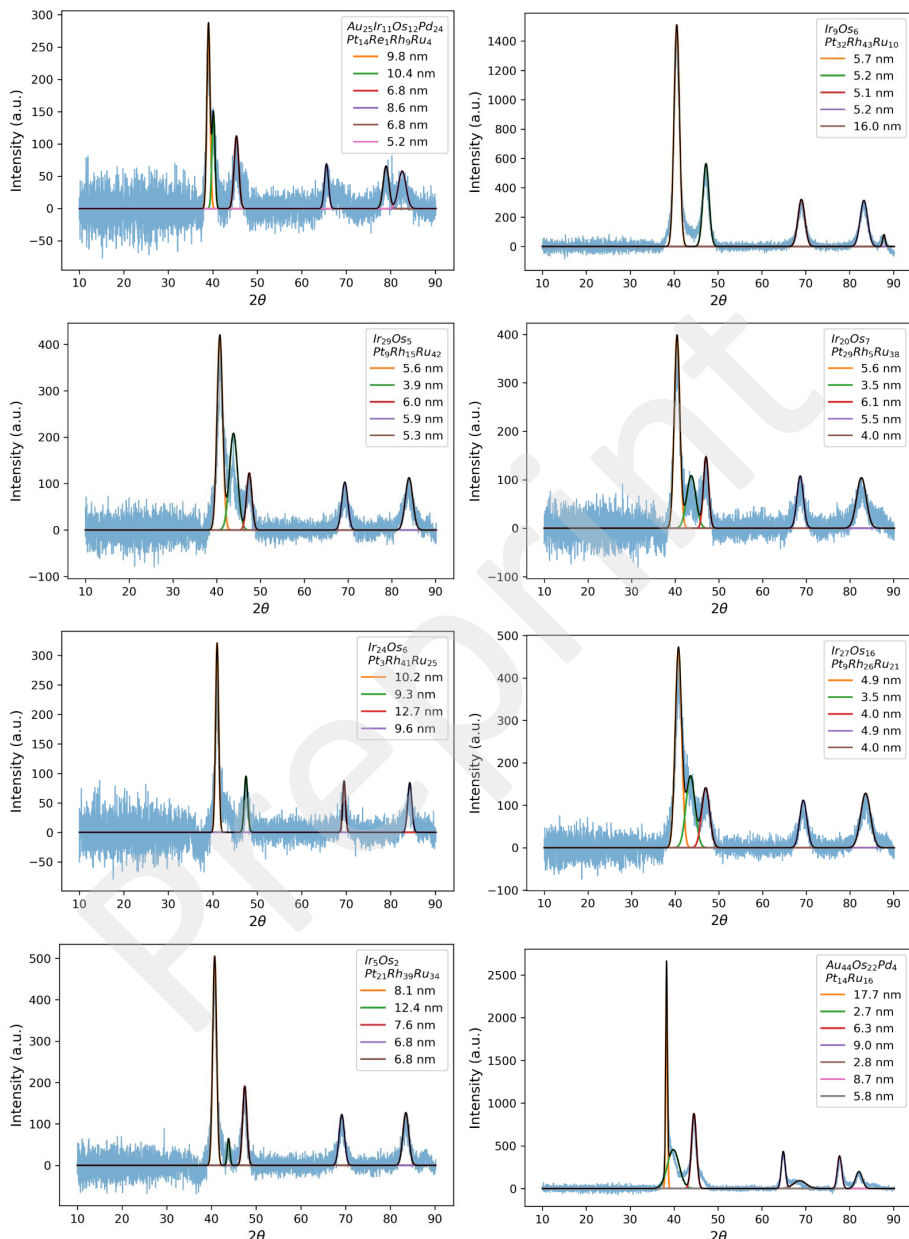
Complementary XRD experiments on randomly selected samples were measured using a STOE StadiP with a Cu K $\alpha$  X-ray source in transmission geometry. TEM images were recorded at the Microscopy Imaging Center of the University of Bern by Dr. Jia Du with a FEI Tecnai Spirit transmission electron microscope at 80 kV with an Olympus-SIS Veleta CCD Camera. In most samples, multiple phases are observed, yet as shown in the work of Yeh this does not exclude the presence of high entropy alloys.<sup>1</sup> However, the presence of these multiple phases significantly complicate the Rietveld refinement of the XRD structure. Therefore, we performed a gaussian fit of the identifiable peaks. These peaks we used to estimate the crystallite size with the Scherrer Equation (Eq. S8). In this Equation K equals the shape factor assumed to 0.89,  $\lambda$  the wavelength of 0.154 nm,  $\beta$  the broadening at half maximum intensity and  $\theta$  the Bragg angle. For most samples, we observe peaks corresponding to crystallite sizes of around 5 nm. This indicates that the particles we observed in the TEM correspond to large agglomerates. In a few samples, such as Ir<sub>4</sub>Os<sub>19</sub>Pd<sub>16</sub>Pt<sub>37</sub>Ru<sub>24</sub>, a broad peak is fitted corresponding to small particles with a size around 2 nm. However, we cannot conclude with certainty whether that broad peak is an artifact of the fitting or a linear combination of several slim peaks.

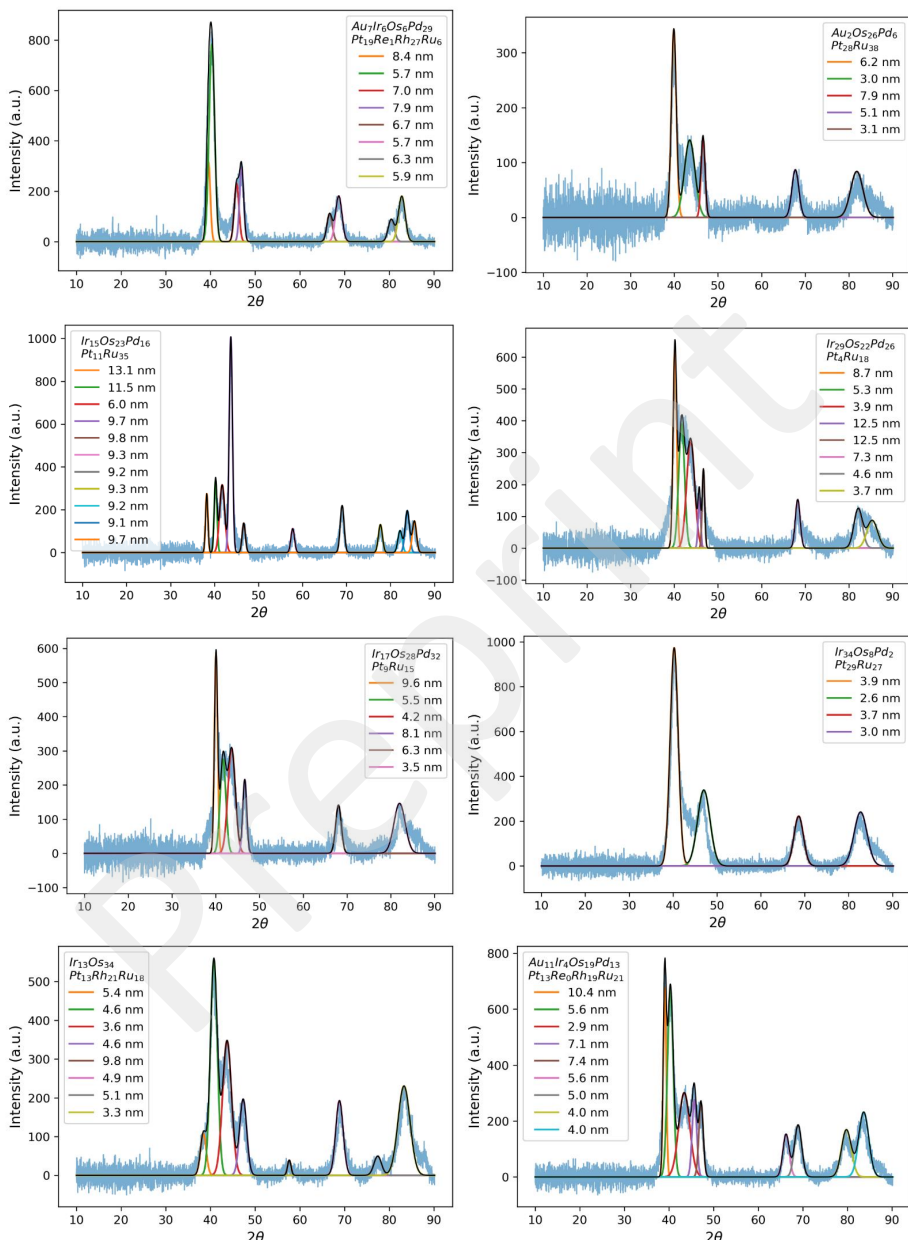
$$\tau = \frac{K\lambda}{\beta \cos \theta} \quad (\text{Eq. S8})$$



**Fig S12. TEM characterization of the selected nanoparticles** (a) Sample: Au<sub>16</sub>Ir<sub>15</sub>Os<sub>16</sub>Pd<sub>16</sub>Pt<sub>11</sub>Re<sub>1</sub>Rh<sub>11</sub>Ru<sub>14</sub>, (b) Sample: Au<sub>25</sub>Os<sub>14</sub>Pd<sub>21</sub>Pt<sub>19</sub>Ru<sub>21</sub>, (c) Sample: Ir<sub>23</sub>Os<sub>10</sub>Pd<sub>24</sub>Pt<sub>25</sub>Ru<sub>18</sub>, (d) Sample: Ir<sub>13</sub>Os<sub>34</sub>Pt<sub>13</sub>Rh<sub>21</sub>Ru<sub>18</sub>.







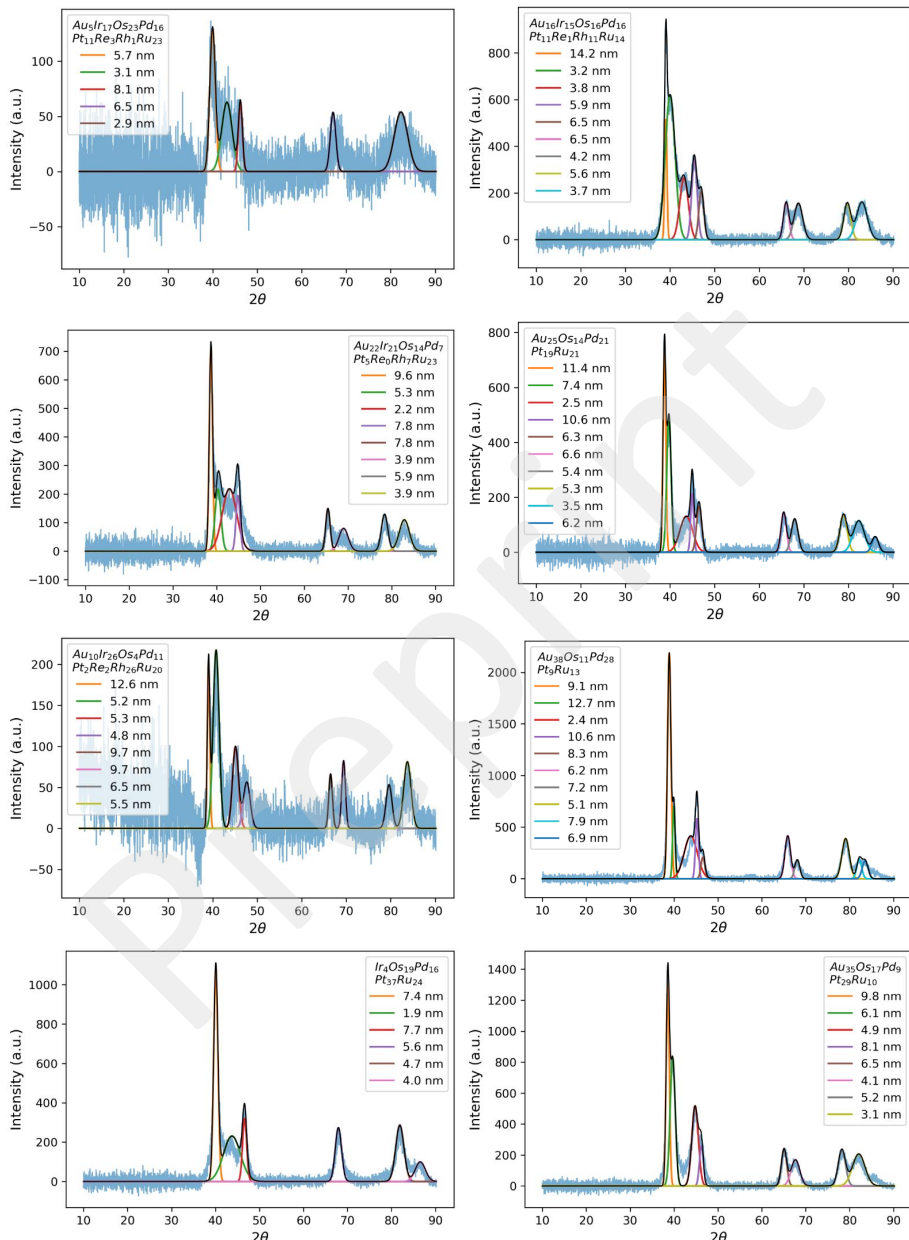


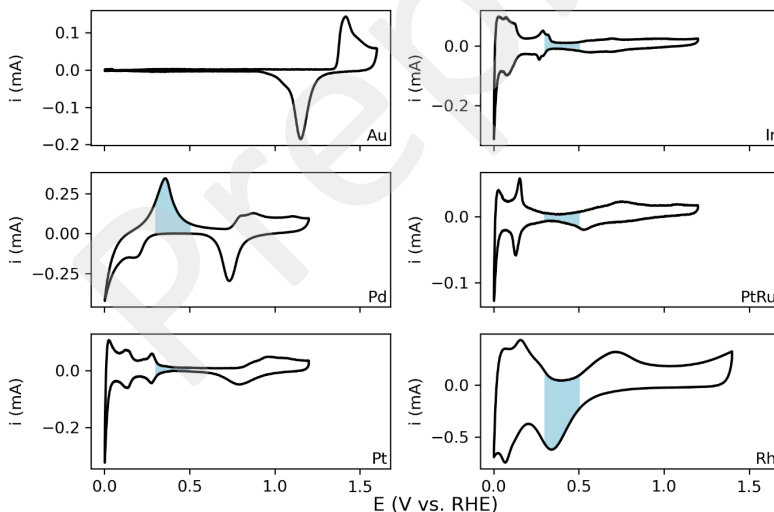
**Fig S13. XRD measurements.** Complementary XRD measurements.

## VI Capacitance measurements

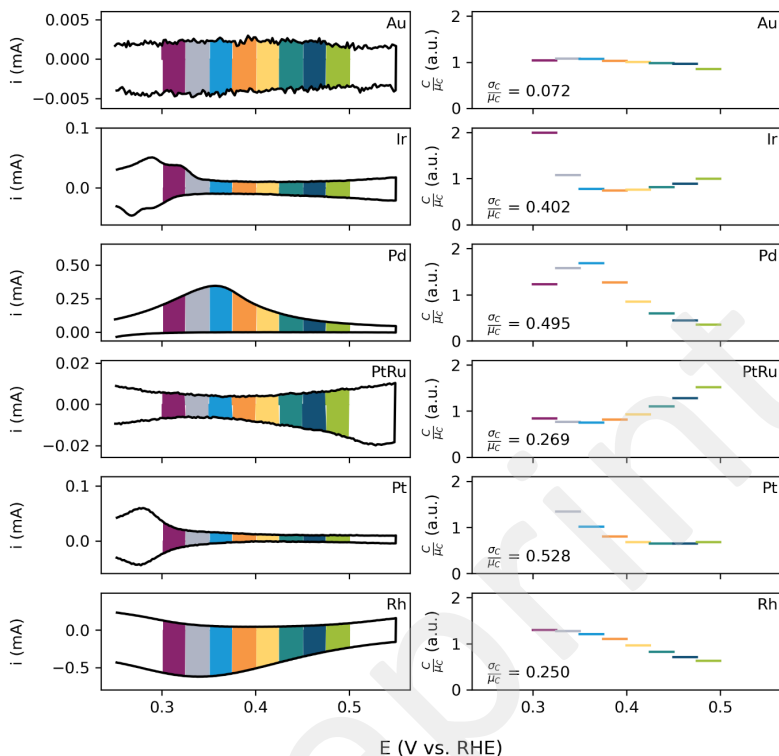
The capacitance of the nanoparticles was determined using the current difference between the anodic and cathodic sweep in the potential window between 0.3 to 0.5 V vs. RHE. To demonstrate that mostly capacitive contributions are present in this potential window, the CVs of pure metals were measured. These CVs show that only Au has no Faradaic contribution in the utilized potential window. Pt, Ir, and PtRu show minor contributions from the hydrogen under potential depositions and the RuO<sub>x</sub> reduction. On top of that Pd and Rh, show very large Faradaic contributions leading to erroneous errors in capacitance when that window is taken.

To estimate the error introduced by the faradaic contributions, we performed the following analysis. The potential window between 0.3 to 0.5 V vs. RHE was segmented into parts of 250 mV. In each of these smaller windows, the capacitance was evaluated. From these 8 capacitances, the standard deviation and the average was obtained. The average was used to normalize the standard deviation to bring them to the same order of magnitude. Results for the single metals are shown in Figure S15. For Au a normalized standard deviation  $\sigma C/\mu C$  of 0.072 indicating a relatively flat double layer. Ir, Pt, PtRu, Rh and Pd each containing faradaic processes in said window which is reflected in  $\sigma C/\mu C$  values larger than 0.25. In comparison our nanomaterials almost all exhibit  $\sigma C/\mu C$  values < 0.2 with the majority being even below 0.1. This indicates that the window between 0.3 to 0.5 V vs. RHE for most nano material samples is flat.

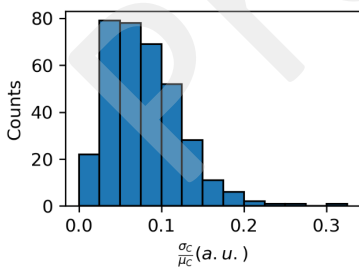
The only two samples with values  $\sigma C/\mu C$  above 0.23 are samples 104, 428, and 384. Sample 104 contains large oscillatory noise waves from the instrument, which did not influence the catalytic measurement. On the other hand, samples 384 and 428 do contain some visible faradaic contributions. However, we expect that the error that arises from these three samples was smoothed out by the Gaussian Process fit.



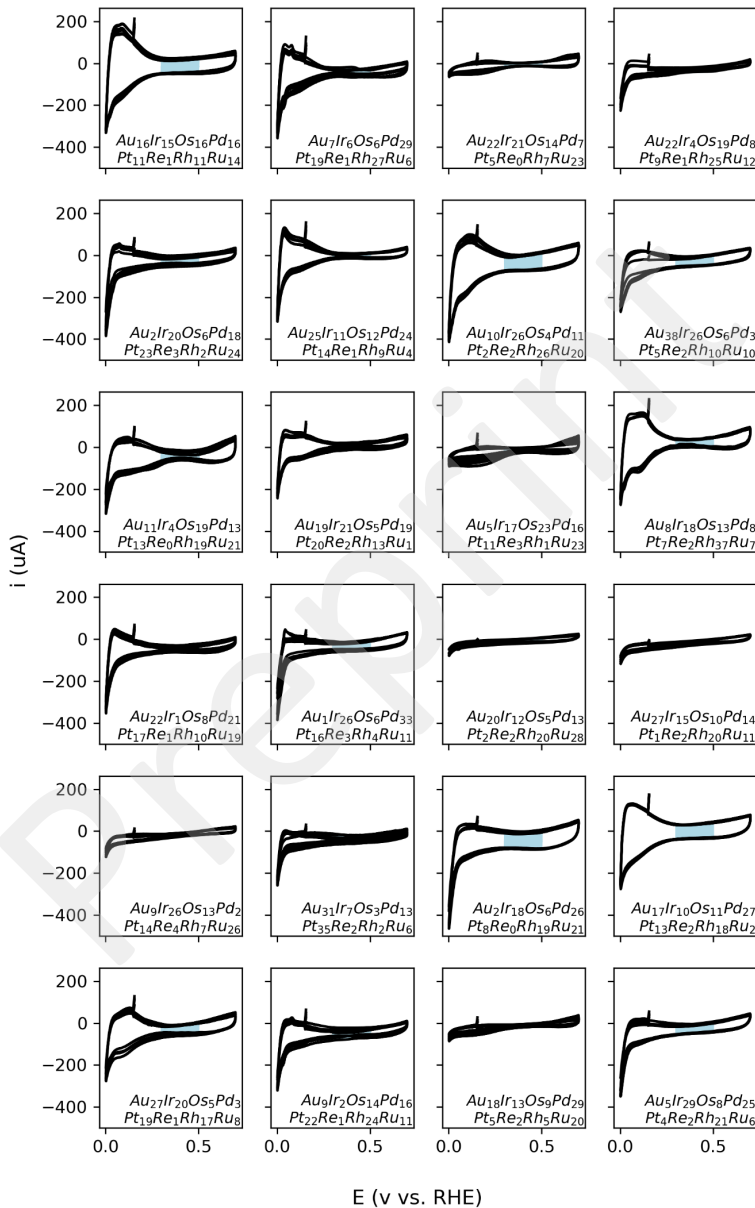
**Fig S14: CVs of the individual metals in Ar.** The measurements were recorded at 200 mV/s in 0.1 M H<sub>2</sub>SO<sub>4</sub>. The blue filled area is the area where the capacitance was determined for the nanomaterials.



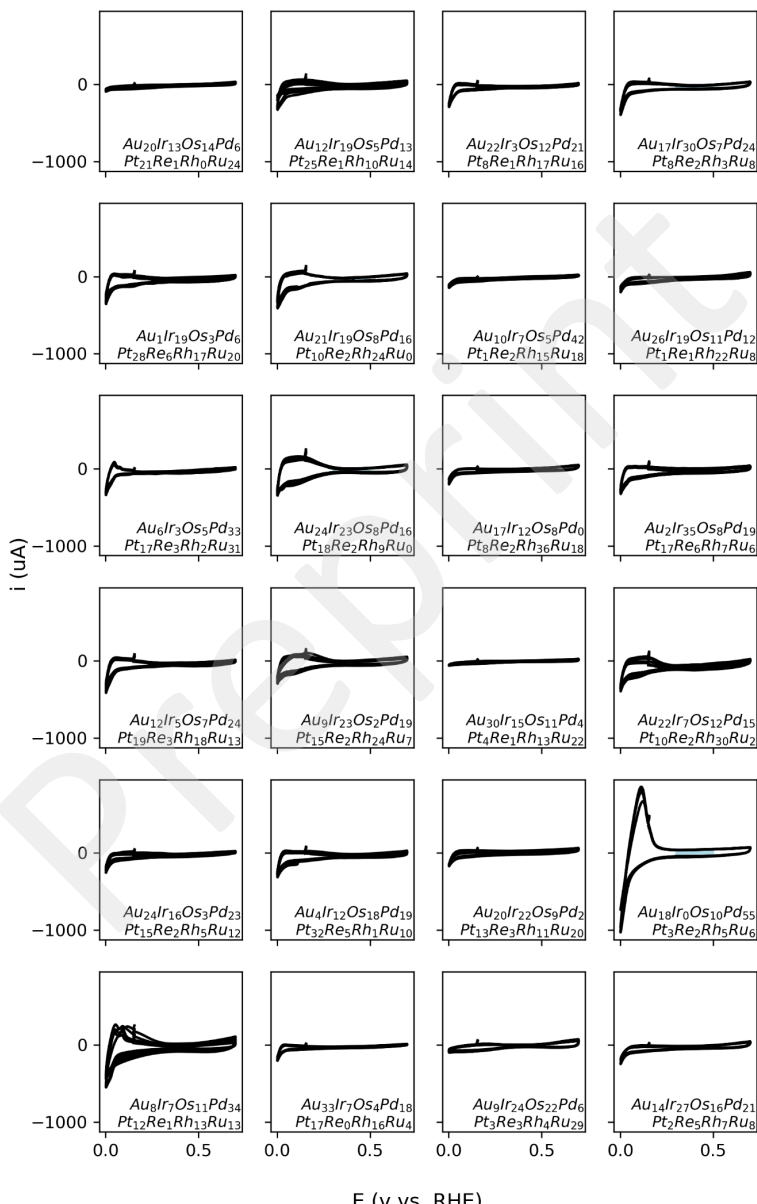
**Fig S14. Capacitance measurements for the pure metals.** The capacitance of the pure metals segmented over different potential windows.

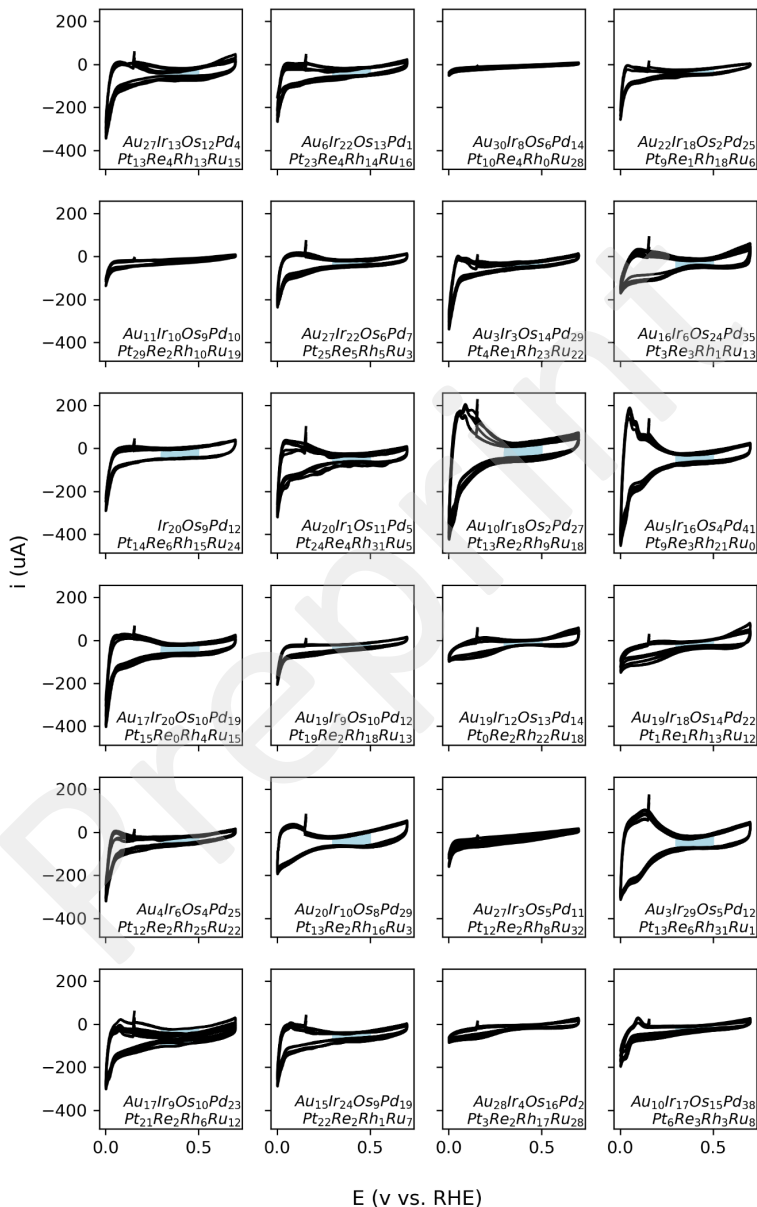


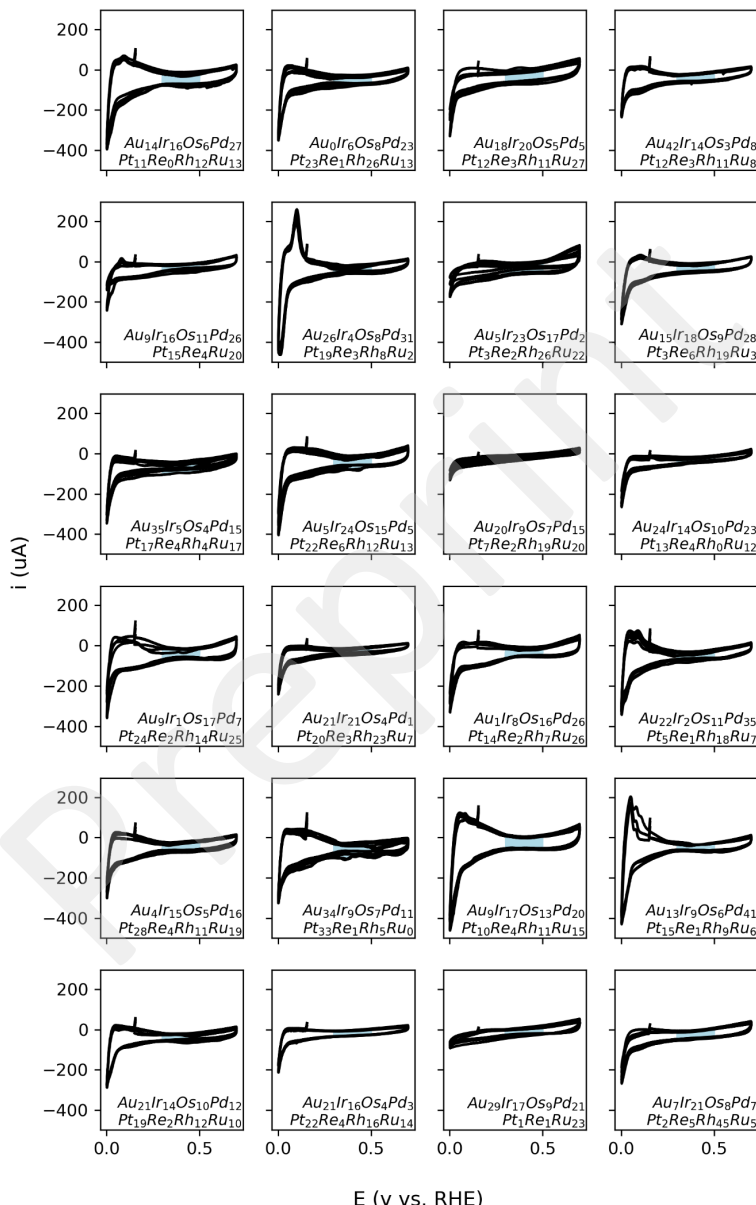
**Fig S15. Standard deviation for the determined capacitance.** The distribution of the standard deviation of the determined capacitance of the investigated nano materials. The standard deviation is normalized by the average capacitance of the investigated particle.



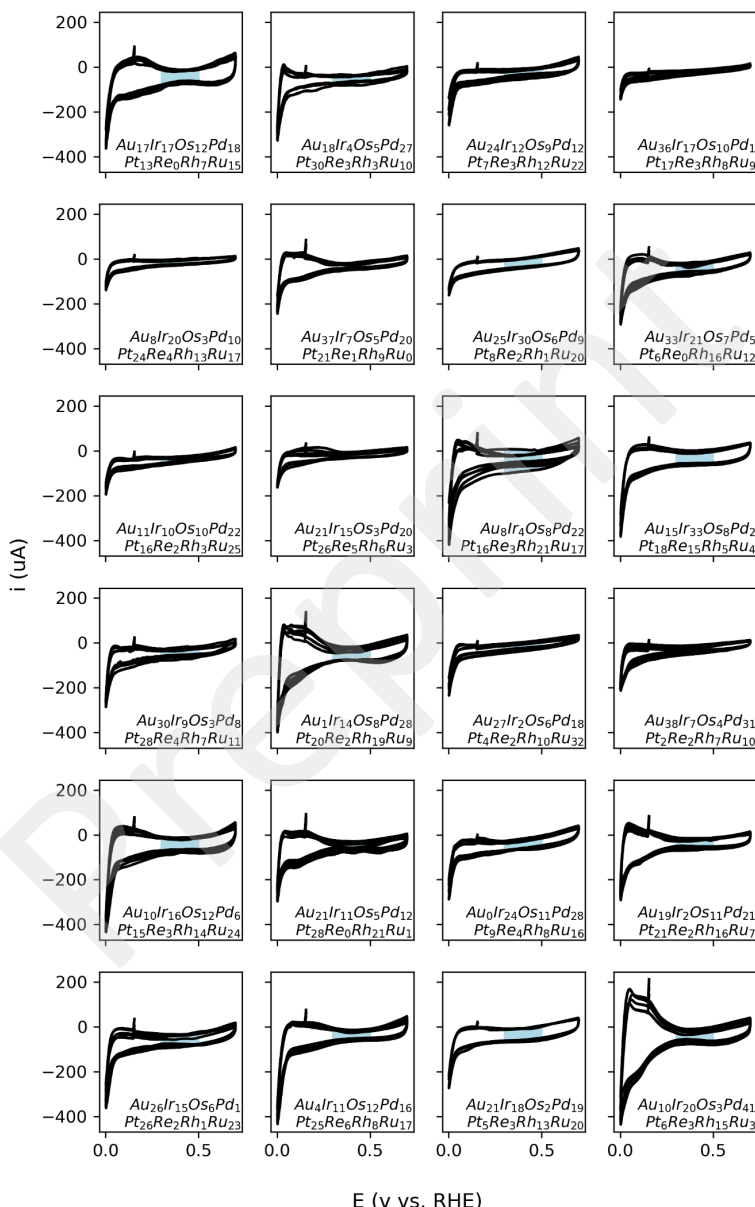
E (v vs. RHE)



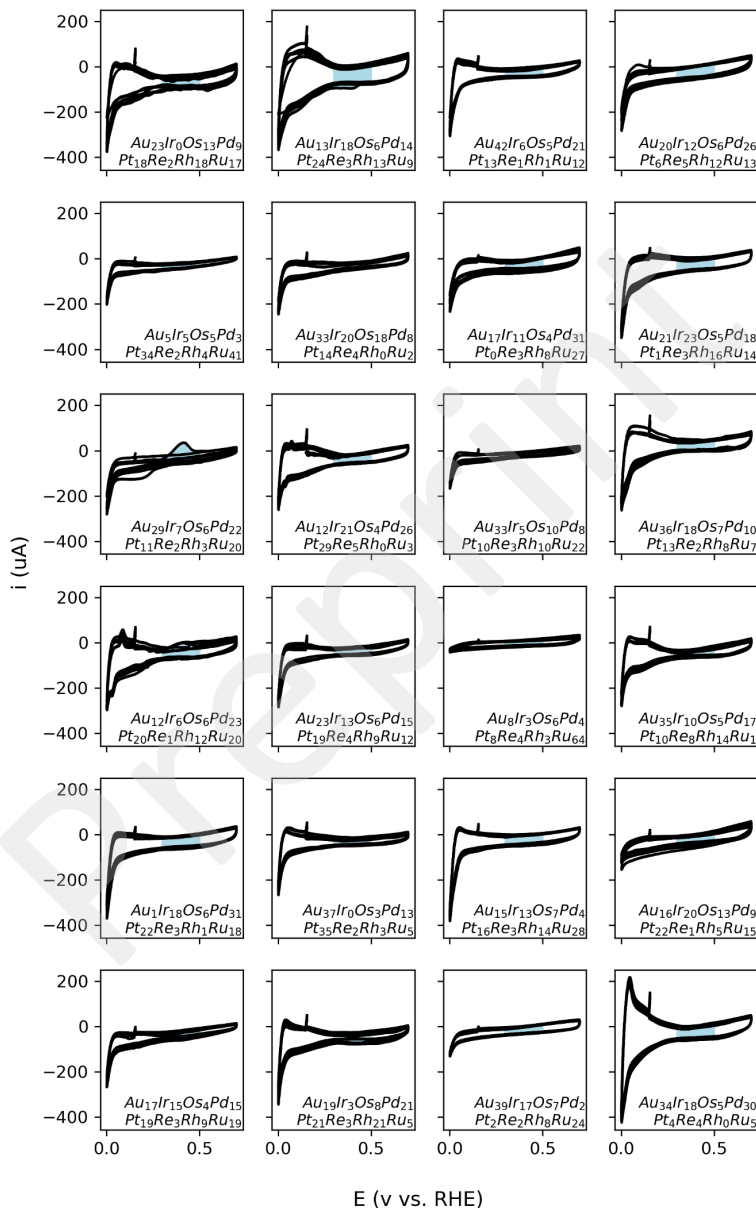
 $E$  (v vs. RHE)

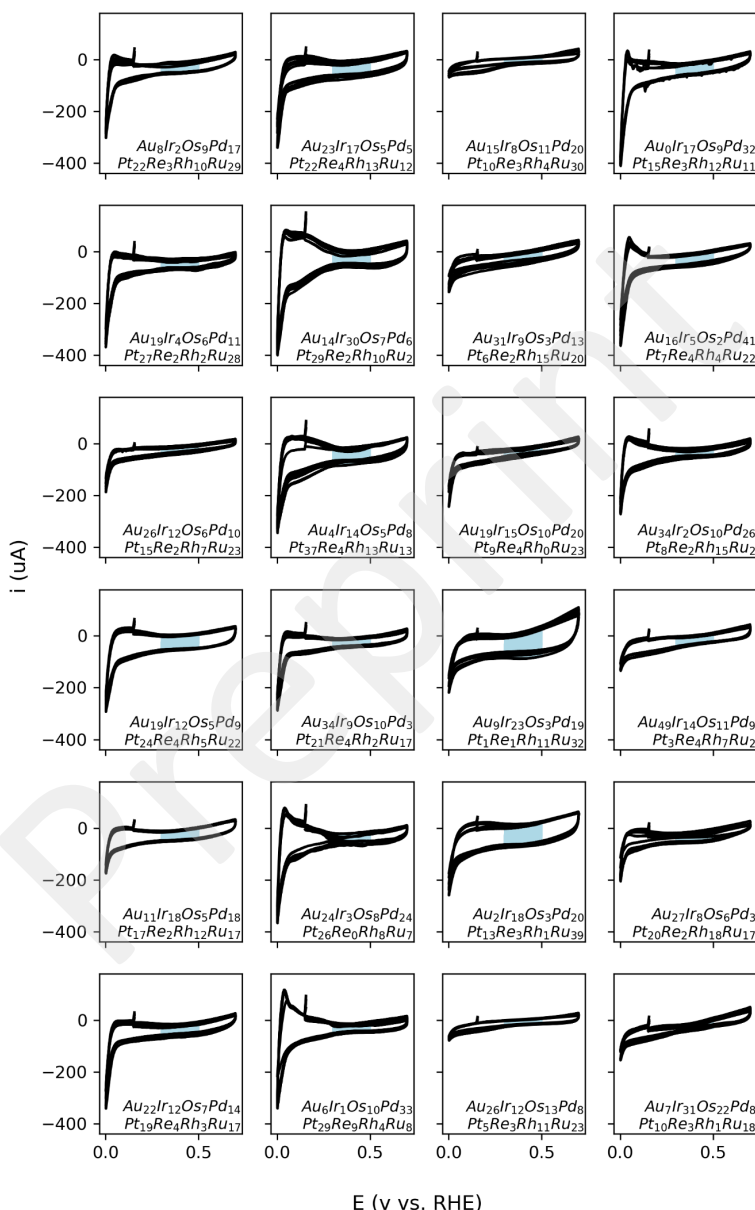


E (v vs. RHE)

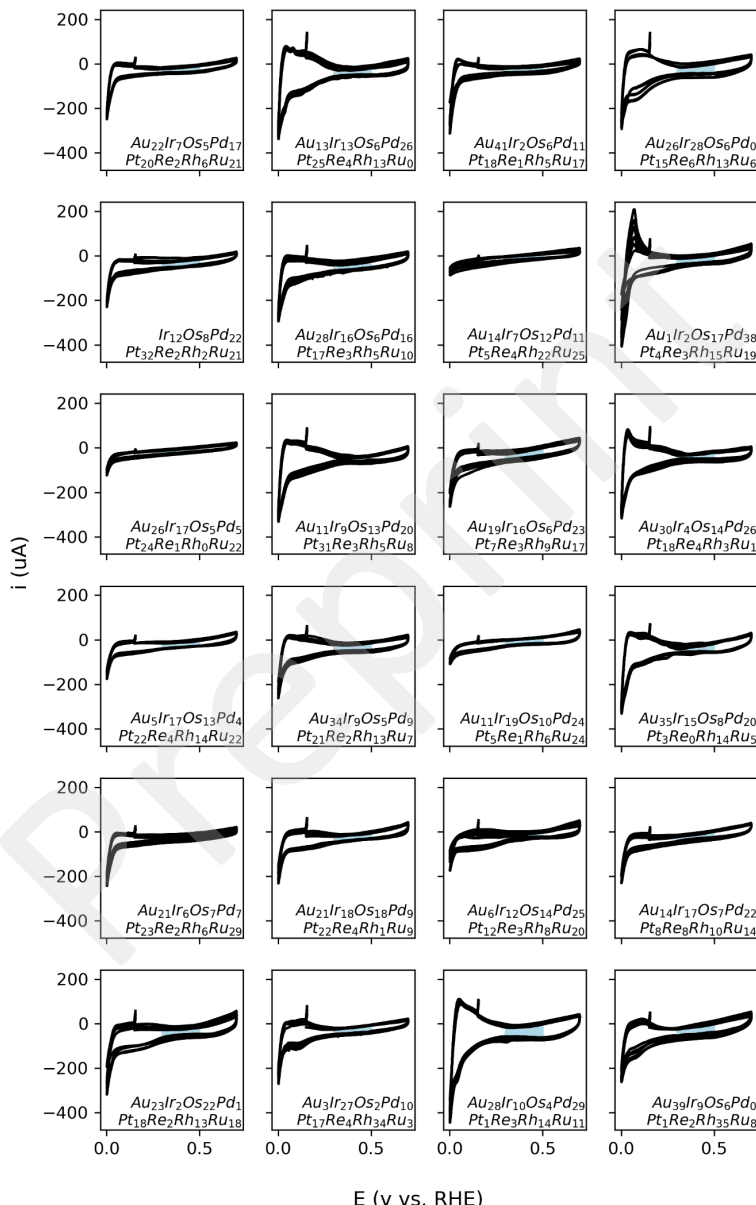


E (v vs. RHE)

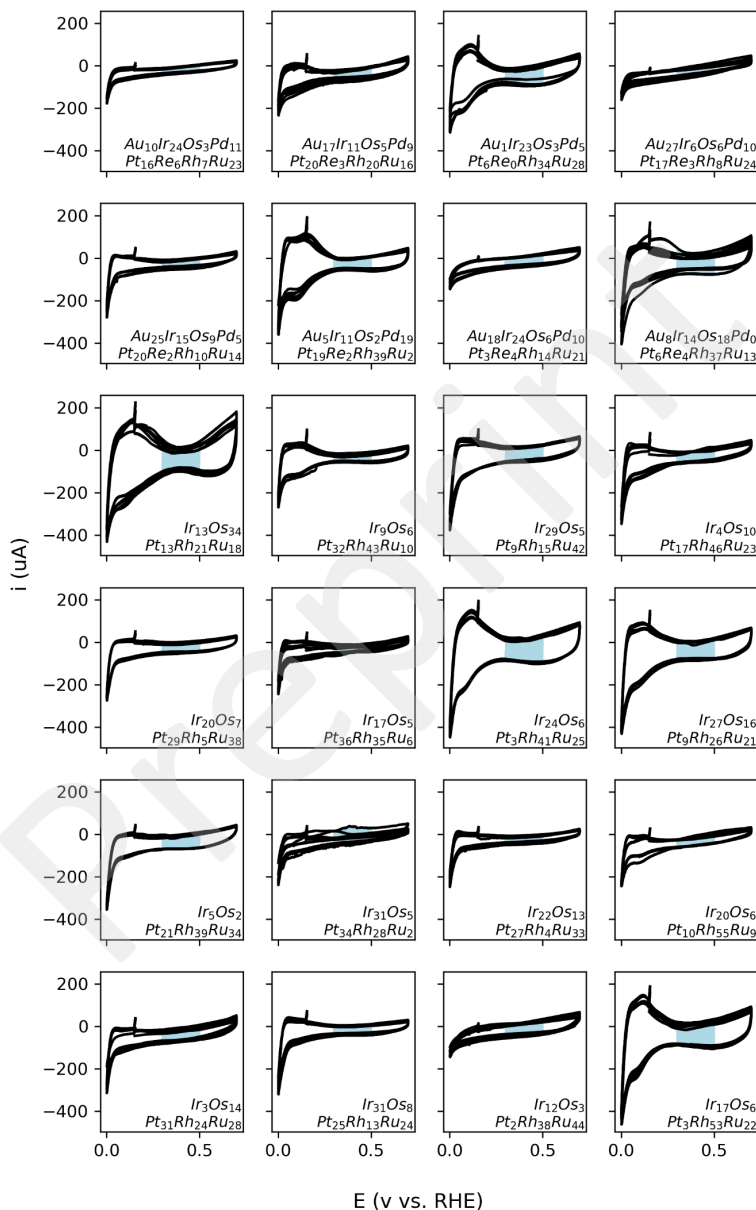
 $E$  (v vs. RHE)

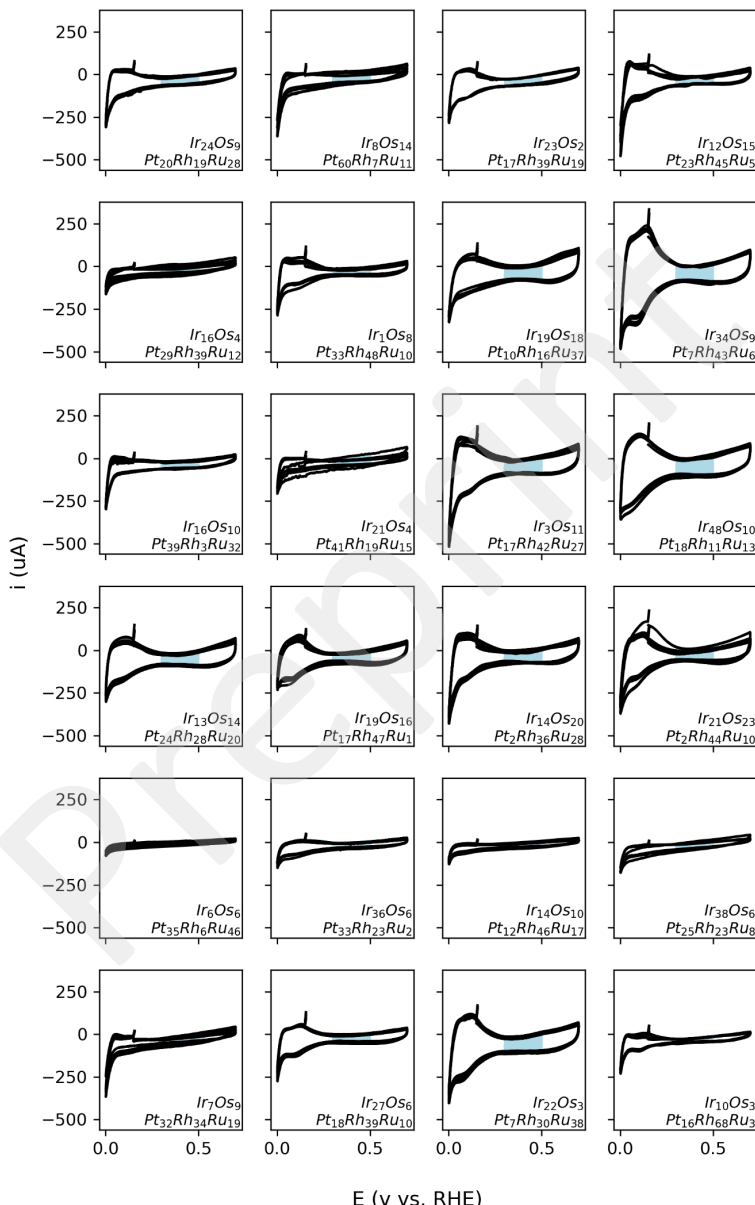


E (v vs. RHE)

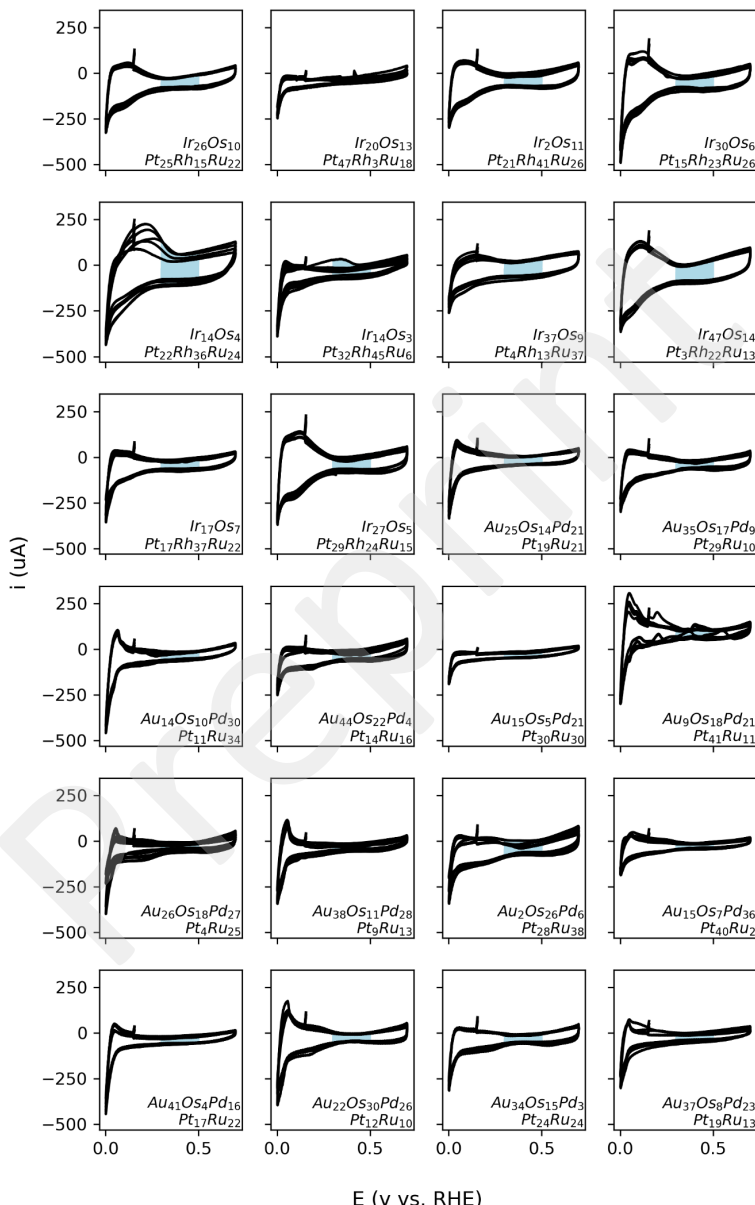


E (v vs. RHE)

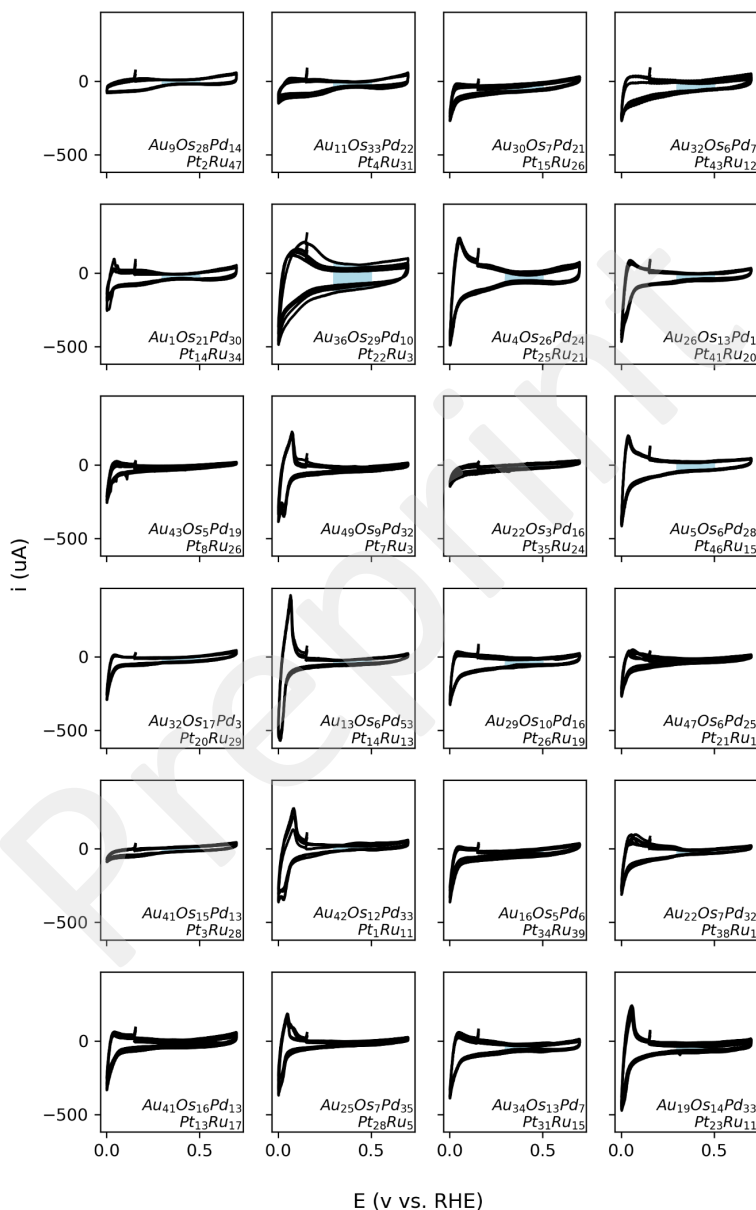


 $E$  (v vs. RHE)

S30

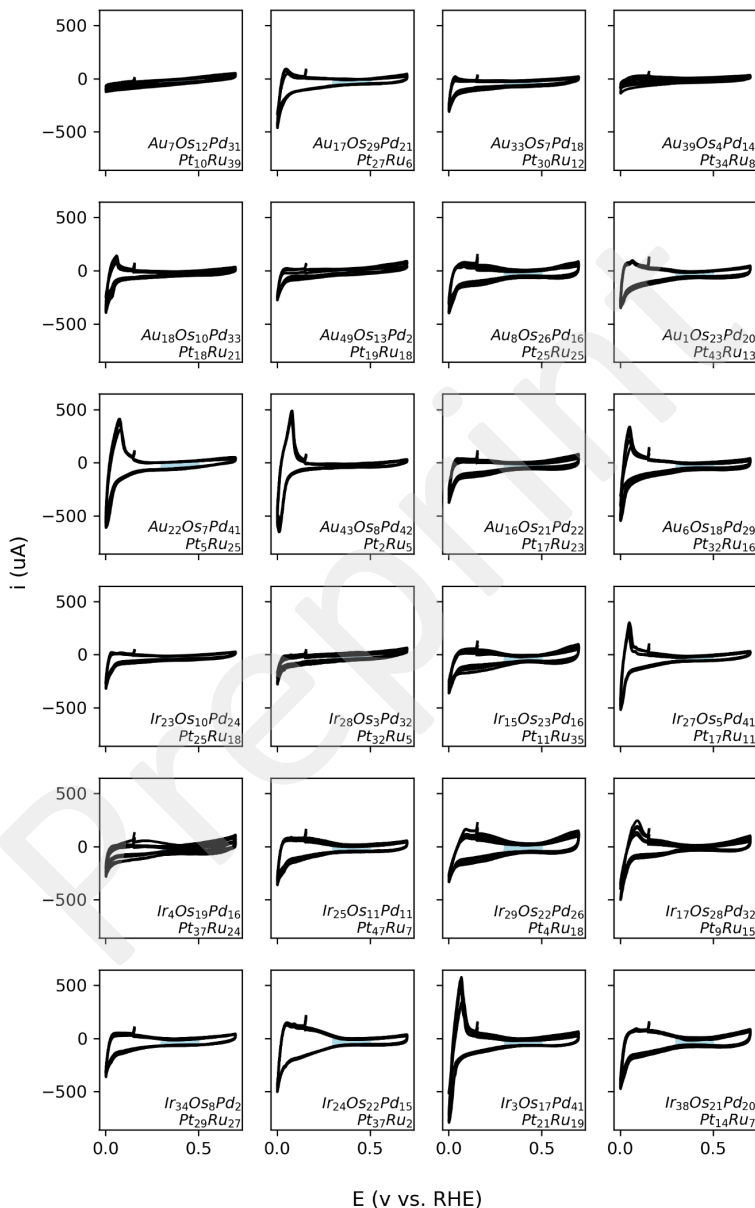


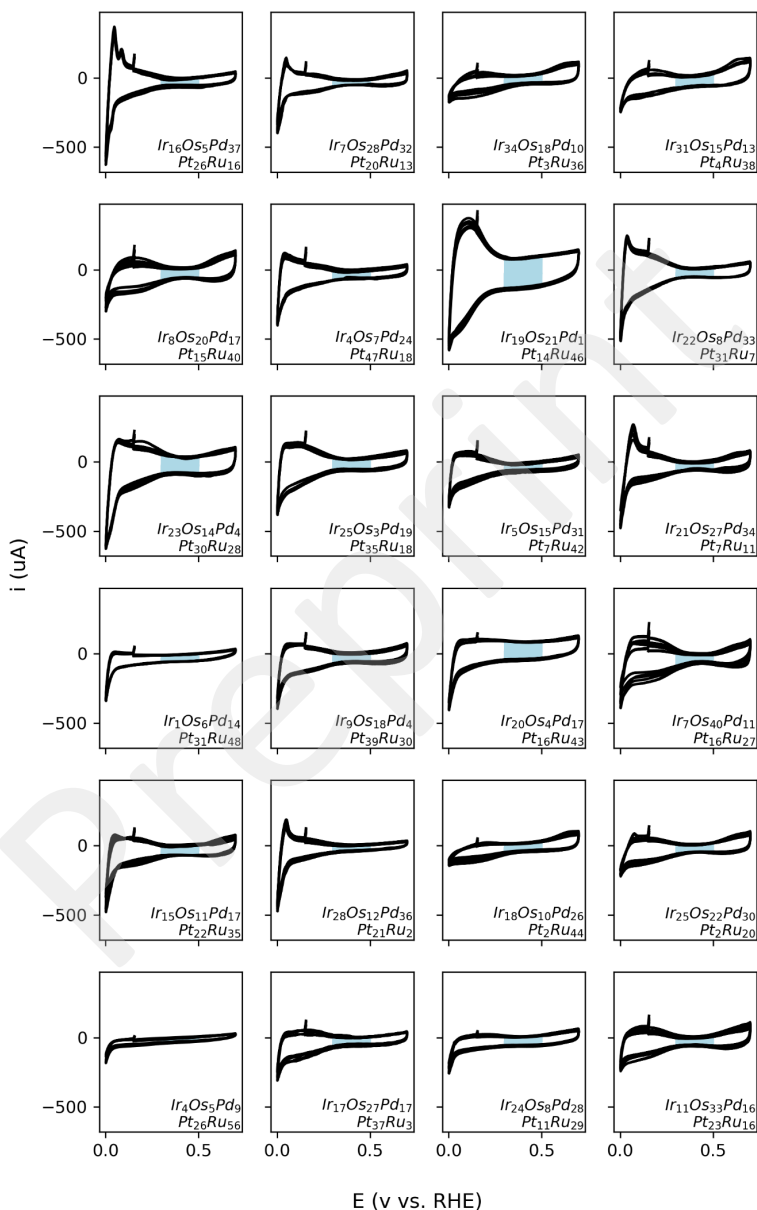
E (v vs. RHE)



$E$  (v vs. RHE)

S32

 $E$  (v vs. RHE)



E (v vs. RHE)

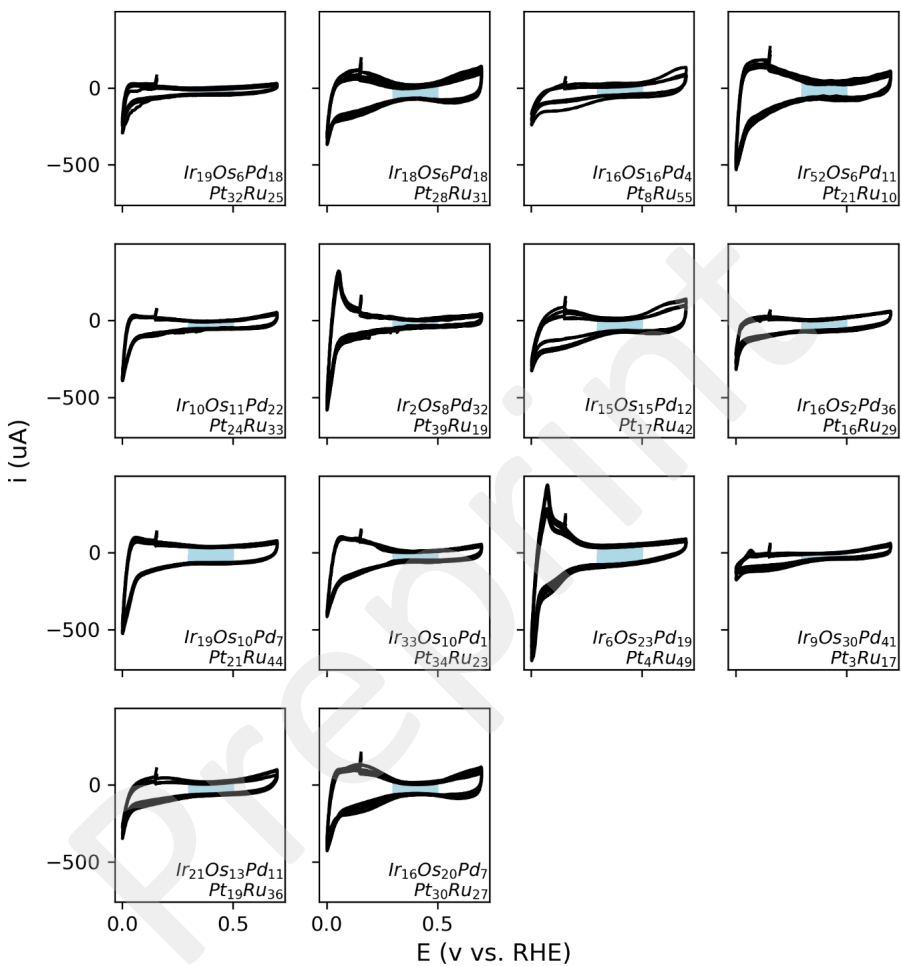


**Fig S16. Cyclic voltammograms of the nanoparticles.** All the CVs for the measured nanoparticle composition as determined with EDX.

## References

1. Bondesgaard, M., Broge, N. L. N., Mamakhel, A., Bremholm, M. & Iversen, B. B. General Solvothermal Synthesis Method for Complete Solubility Range Bimetallic and High-Entropy Alloy Nanocatalysts. *Adv Funct Mater* **29**, (2019).
2. Sobol', I. M. On the distribution of points in a cube and the approximate evaluation of integrals. *USSR Computational Mathematics and Mathematical Physics* **7**, 86–112 (1967).
3. I. M. Sobol. On the distribution of points in a cube and the approximate evaluation of integrals. *Zhurnal Vychislitelnoi Matematiki i Matematicheskoi Fiziki* **7**, 784–802 (1967).
4. C. E. Rasmussen & C. K. I. Williams, Gaussian Processes for Machine Learning, Chapter 5: *Model Selection and Adaptation of Hyperparameters*, the MIT Press, 2006, ISBN 026218253X. © 2006 Massachusetts Institute of Technology. [www.GaussianProcess.org/gpml](http://www.GaussianProcess.org/gpml)
5. Trevor Hastie, Robert Tibshirani & Jerome Friedman. Local Methods in High Dimensions. in *The Elements of Statistical Learning* 22–27 (Springer Science+Business Media, 2017).

## **Supplementary information**

### **"Exploring the high entropy oxide composition space: insights through comparing experimental with theoretical models for the oxygen evolution reaction"**

Vladislav A. Mints<sup>a</sup>, Katrine L. Svane<sup>b</sup>, Jan Rossmeisl<sup>b</sup> and Matthias Arenz<sup>a</sup>

<sup>a</sup> Department of Chemistry, Biochemistry and Pharmaceutical Sciences, University of Bern, Freiestrasse 3, 3012 Bern (Switzerland)

<sup>b</sup> Center for High Entropy Alloy Catalysis, Department of Chemistry, University of Copenhagen, Universitetsparken 5, 2100 København K (Denmark)

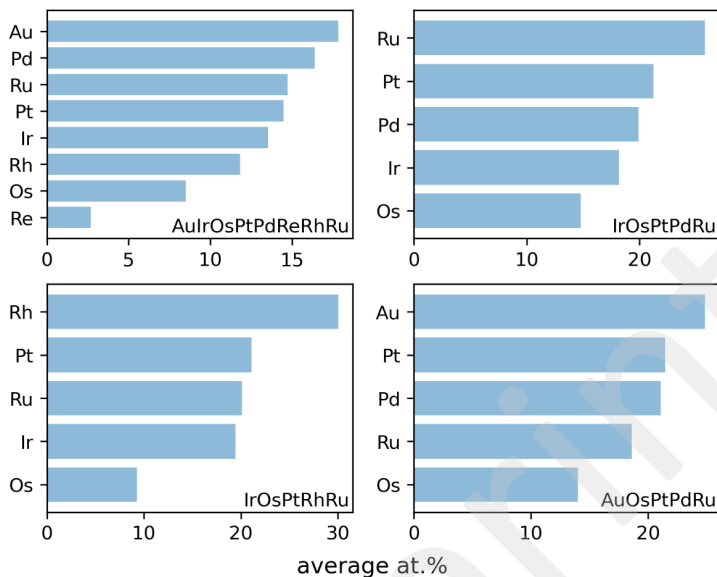
**Section S1: Average Elemental concentrations obtained from EDX**

Figure S1: Average elemental concentrations obtained from EDX data in the four investigated sub-spaces.

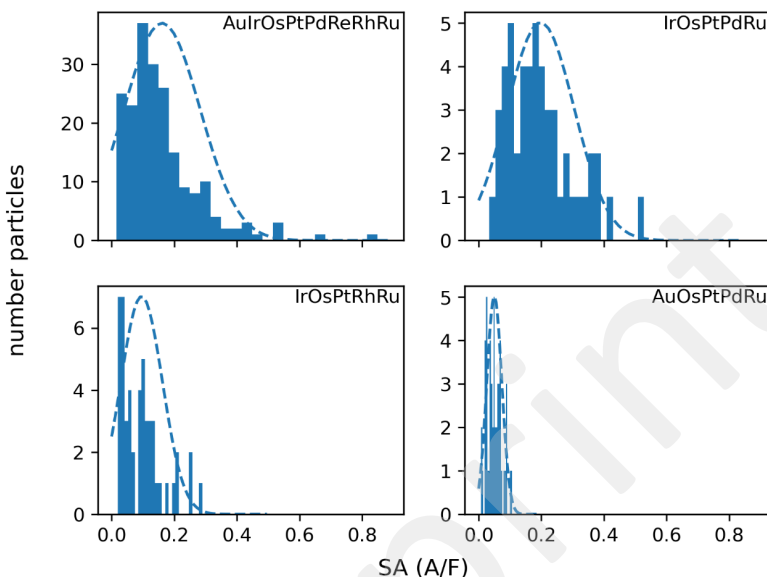
**Section S2.1: Gaussian process regression, fit evaluation.**

Figure S2: The activity distributions of the nanoparticles at 1.5 V vs. RHE sorted by their corresponding subspace. The dashed line shows a fitted Gaussian Distribution.

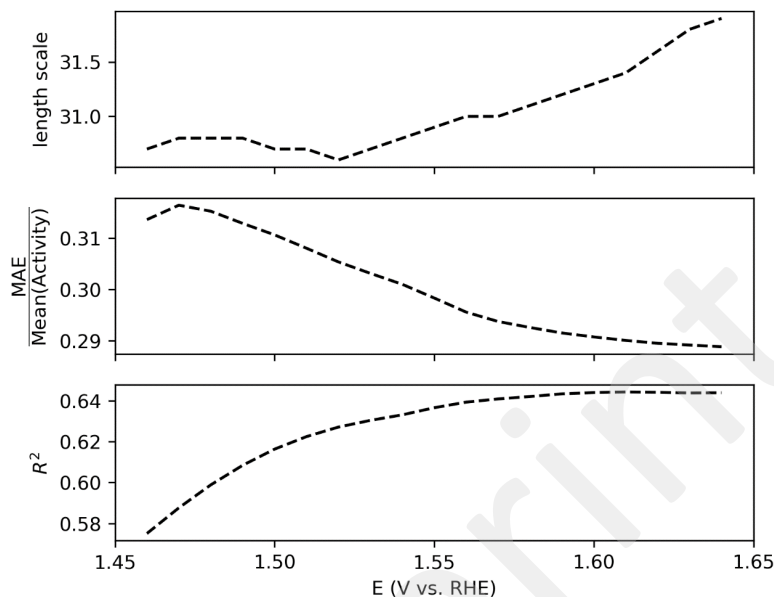


Figure S3: The metrics of the Gaussian Process regression. The length scale is the optimal length scale obtained from the hyperparameter tuning. The MEA was obtained from the LOOCV procedure and normalized with the average measured activity. The  $R^2$  values were obtained from the parity plots in Figure S4.

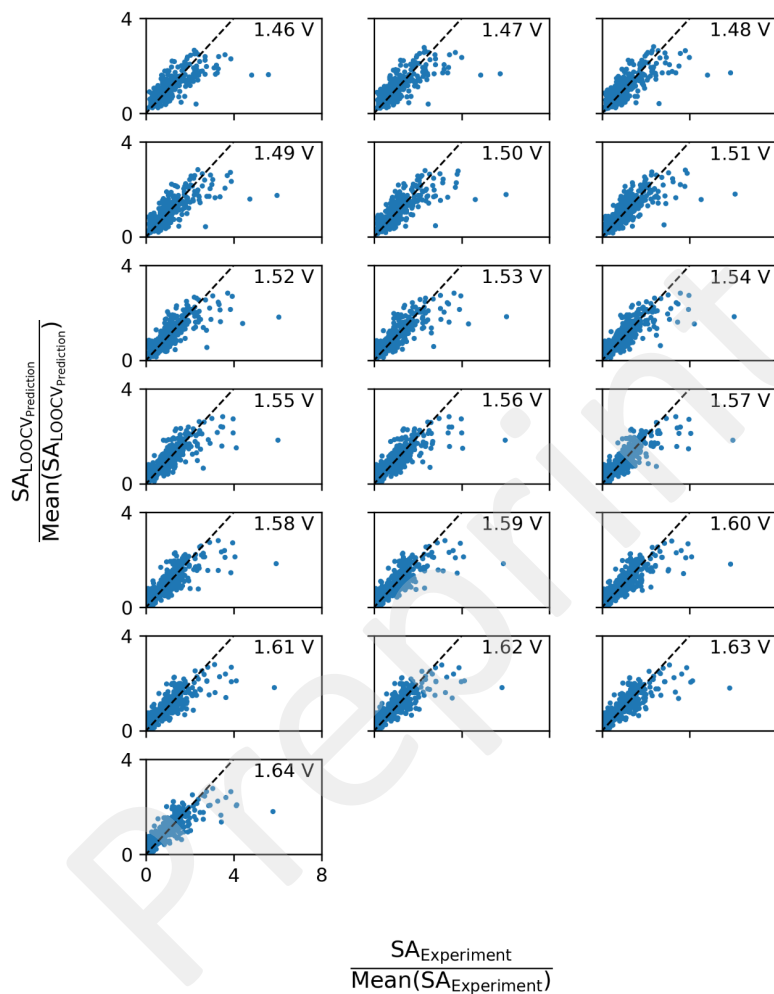


Figure S4: The parity plots of the LOOCV performance for each of the Gaussian Processes. The axes are normalized by the average predicted current and average measured current. As the models are unbiased, the average predicted current is approximately the average measured current.

### Section S2.2: The influence of outliers and the role of osmium

Figure S2, shows that some particles in the 8-element data set exhibit erroneous activities. This is a first indication for the presence of outliers and noise in the data. In this section we explore in further detail the nature of this noise. For this four gaussian process models are trained at 1.5 V vs. RHE. The first was fitted using the 200 nanoparticles of the 8-element space. The second model was fitted using the same data set but excluding the most active data points. The third model is trained on 50 experiments from the IrOsPdPtRu space, which is the only space with the most important geometrical faces. Lastly, the fourth model is trained on the entire data set of 350 particles.

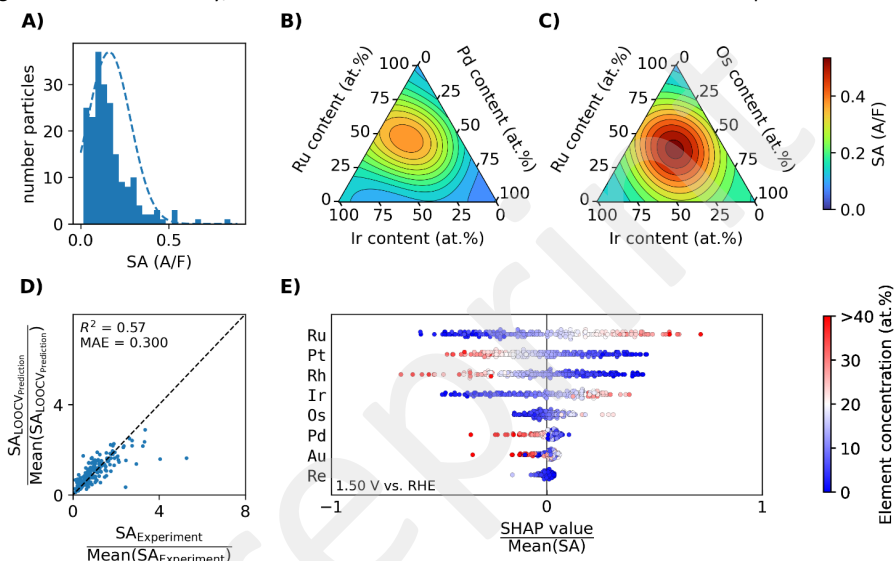


Figure S5: The summary of the Gaussian Process fitted at 1.5 V vs. RHE based on 200 samples in the 8-element space. A) The activity distribution. B) The ternary plot of the activity of the IrPdRu space. C) The ternary plot of the activity of the IrOsRu space. D) The normalized parity plot. E) The SHAP analysis normalized by the average measured activity.

The investigation started by analysing the data of the 8-element model using all data (Figure S5). The SHapely Additive exPlanations (SHAP)<sup>1</sup> demonstrate that Ru and Ir have a strong positive influence on the OER, which is in line with the general expectation. Likewise, Pt and Rh show to have a strong negative influence on the reaction. In contrast to most expectations Os shows to have also a drastic improvement on the reaction, which is in strong disagreement with DFT calculations. This improvement is large enough to create a stronger optimum in the RuIrOs plane than in the RuIrPd plane. Initially this was attributed to the leaching of Os and increase in surface area, however further data analysis shows this Os contribution is amplified due to the presence of outliers.

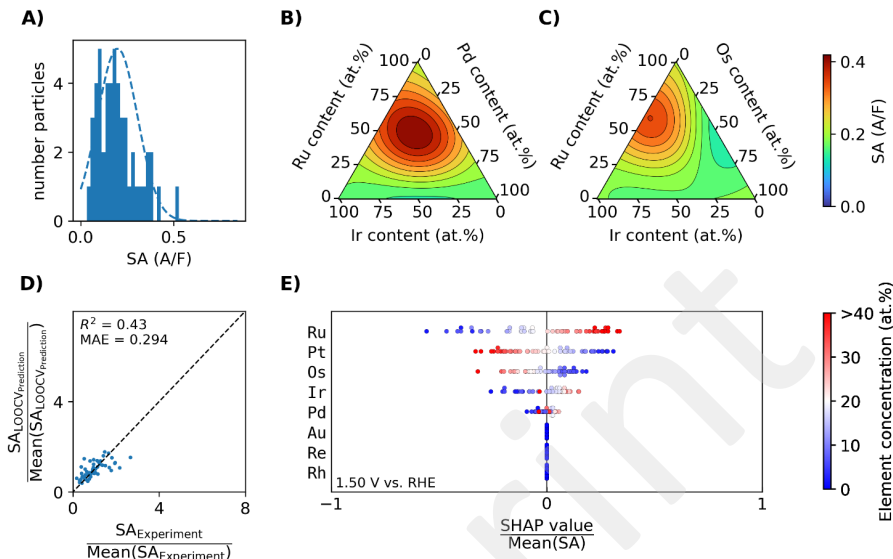


Figure S6: The summary of the Gaussian Process fitted at 1.5 V vs. RHE based on 50 samples in the IrOsPdPtRu space. A) The activity distribution. B) The ternary plot of the activity of the IrPdRu space. C) The ternary plot of the activity of the IrOsRu space. D) The normalized parity plot. E) The SHAP analysis normalized by the average measured activity.

The hypothesis that Os improves the reaction was tested by analysing the model in the IrOsPdPtRu space. This model was trained on 50 experiments (Figure S6). Since this space contains the combined IrPdRu and IrOsRu planes, it is expected to show similar results as the 8-element model. On the contrary, in this model the significance of Os is significantly reduced and the IrRuPd optimum dominates. Also, the SHAP analysis now shows that large quantities of Os are harming the performance. This suggests that the Os role in the 8-element model might be an artifact from the data.

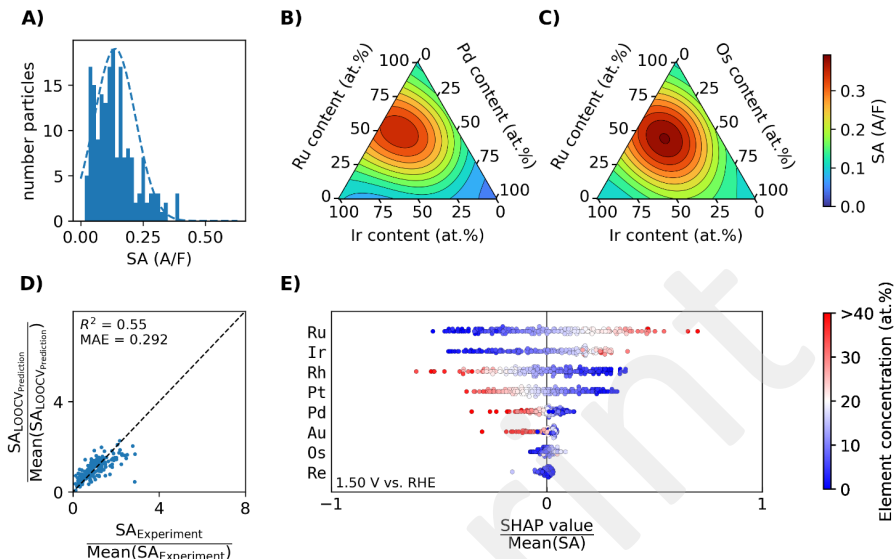


Figure S7: The summary of the Gaussian Process fitted at 1.5 V vs. RHE based on 184 samples in the 8-element space. In this data set, the 16 most active samples from the original 20 samples were removed. A) The activity distribution. B) The ternary plot of the activity of the IrPdRu space. C) The ternary plot of the activity of the IrOsRu space. D) The normalized parity plot. E) The SHAP analysis normalized by the average measured activity.

Statistical analysis of the 200 samples in the 8-element space demonstrated that there is an excess of highly active samples. The effect of these samples was explored by excluding them from them from the training data. The resulting gaussian process model is summarized in Figure S7. According to the SHAP analysis, the removal of the high active samples removes the positive contribution of Os on the OER. Likewise, the previously observed optimum in the IrOsRu plane is shifted from Os at 50 at. % to 25 at.%. Thus, the removed samples, besides being very active, had a large content of Os. However, the optimum is not completely shifted towards the IrPdRu plane indicating that there are still samples present which are responsible for this artificial Os optimum. Therefore, it can be concluded that this data set is composed of two distributions. The first distribution is showing the major OER correlations. On the other hand, the second distribution is inflating the performance of Os rich nanoparticles and therefore most likely noise.

Since we are unable to identify the noisy samples, we decided to dilute their fraction by adding more data into the model. As a consequence, the models discussed in the paper were fitted with all 350 samples. The resulting model at 1.5 V vs. RHE is summarized in Figure S8. From the SHAP analysis, the effect of Os now more closely resembles the correlation observed for the IrOsPdPtRu model. In large quantities, Os shows to harm the performance of the catalyst. However, as the outliers are not removed but suppressed, an optimum in the IrOsRu plane is still present albeit lower in activity compared to the optimum in the IrPdRu plane. On the other hand, the SHAP analysis of Ir, Ru, Pt, Rh, and Au show a similar behaviour as in the 8-element and 5-element model. Therefore, it can be concluded that the combining of the 4 data sets mostly affects the conclusions on the role of Os and does not change the conclusions on the other elements and alloys.

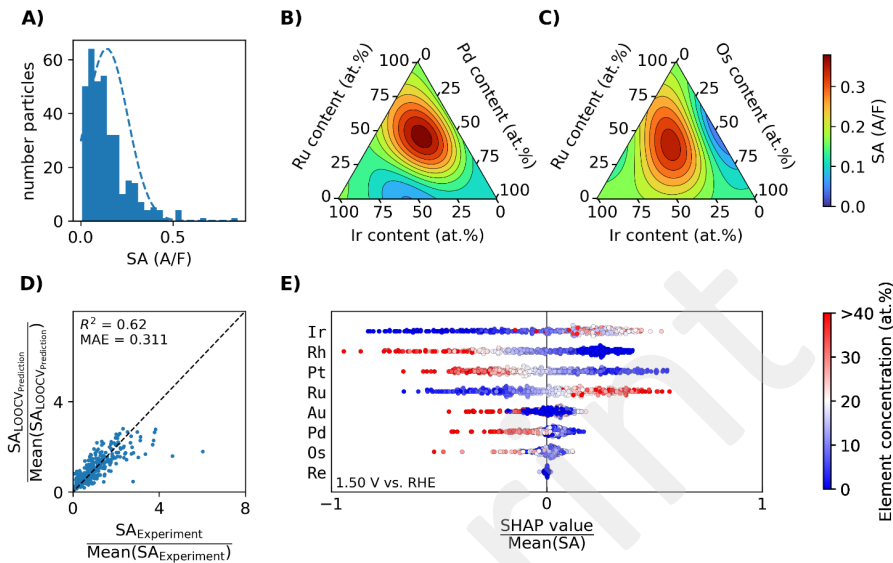


Figure S8: The summary of the Gaussian Process fitted at 1.5 V vs. RHE based on all the 350 samples. A) The activity distribution. B) The ternary plot of the activity of the IrPdRu space. C) The ternary plot of the activity of the IrOsRu space. D) The normalized parity plot. E) The SHAP analysis normalized by the average measured activity.

**Section S3: Lattice constants**

Table S1: Experimental and calculated lattice constants for individual rutile oxides and the HEO. Exp. data is taken from ref<sup>2</sup> for all elements except Pd which is taken from <sup>3</sup>.

		Ir	Os	Pd	Pt	Rh	Ru	HEO (av.)
A (DFT)		4.59	4.56	4.67	4.65	4.59	4.57	4.60
A (Exp.)		4.50	4.50	4.46	4.49	4.49	4.49	-
B (Exp.)		-	-	-	4.54	-	-	-
C (DFT)		3.19	3.19	3.21	3.23	3.19	3.14	3.18
C (Exp.)		3.15	3.18	3.10	3.14	3.09	3.11	-

#### Section S4: Enthalpy of mixing

To assess the stability of the oxides we calculate the energy of replacing 1/12 of a pure oxide with another element for all of the eight oxides considered in the experiment. The results are plotted in Figure S9a, showing that mixing is favourable for most combinations of the elements considered here. Au has a positive energy with several of the other elements, suggesting that it might be difficult to incorporate in the structure. This is consistent with initial calculations of slabs containing Au, which showed a tendency for Au to pop out of the surface. An example of such a structure is shown in Figure S9b. Since this behaviour increases the calculation time and introduces uncertainties in the calculated adsorption energies we decided to exclude Au from the further calculations. We furthermore note that the +4 oxidation state of Au has not been confirmed in its compounds, suggesting that it is unlikely to be found in the rutile structure.

An element showing favourable mixing with most of the other elements does not guarantee that it will be incorporated in the structure. In particular, for elements which prefer an oxide with a different oxidation state than +4, the segregation into different oxides might be preferred. This is probably the case for Re, which has  $\text{Re}_2\text{O}_7$  as the most stable oxide form. The very favourable mixing of  $\text{ReO}_2$  with Au and Pd thus reflects that both of these elements prefer a lower oxidation state, however segregation might still be the most stable situation.

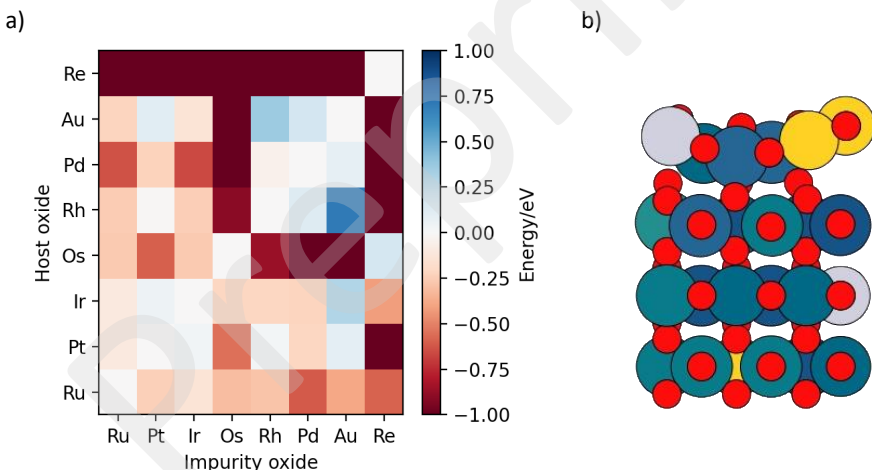


Figure S9: a) Enthalpy of replacing 1/12 atoms in one oxide with another element for the eight metals considered experimentally. B) Example of a slab containing Au where the Au relaxes out of the surface.

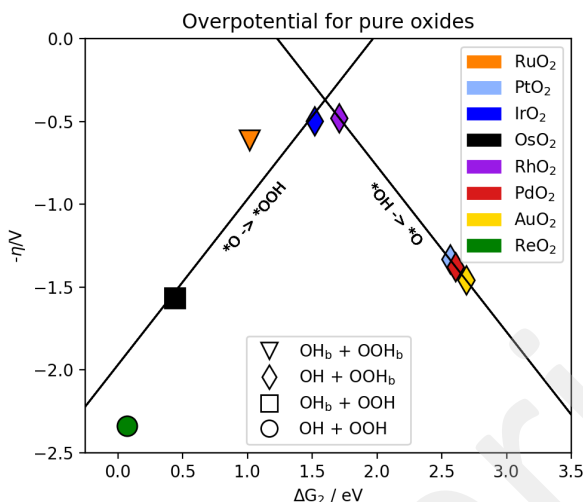
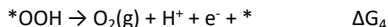
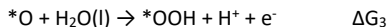
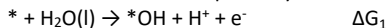
**Section S5: Overpotential of the pure rutile oxides**

Figure S10: Overpotential for the pure rutile metal oxides. Oxides on the left side of the volcano are modeled with  $*\text{O}$  on the cus sites next to the active site while oxides on the right side are modeled with empty neighbouring cus sites. The shape of each marker indicates the preferred reaction pathway (see section S6 below)

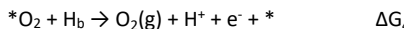
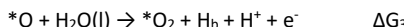
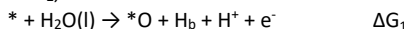
### Section S6: Reaction pathways and scaling relations

The two reaction pathways for the OER considered in this work are illustrated for IrO<sub>2</sub> in Figure S11. The conventional pathway consists of four proton-coupled electron transfers:



Where \* represents the active site, which is the coordinatively unsaturated site (cus) on the rutile (110) surface. The conventional pathway is limited by the scaling relations between the binding energies of the \*OH and \*OOH intermediates ( $\Delta G(\text{OOH}) \approx \Delta G(\text{OH}) + 3.2\text{ eV}$ ) which implies that a minimum potential of 1.6 V is required to run the reaction.<sup>4</sup>

An alternative pathway, in which the proton of the \*OH and \*OOH intermediates are transferred to a neighbouring bridging oxygen has been shown to compare favourably with experimental data on RuO<sub>2</sub>,<sup>5-7</sup> and is therefore also considered:



It is assumed that the reaction always goes via the intermediate with the lowest energy and since both pathways share the \*O intermediate a combination of them is also possible. The scaling relation between the (\*O + H<sub>b</sub>) and (\*O<sub>2</sub> + H<sub>b</sub>) intermediates depends on the element on the cus site (see below). Using the (\*O + H<sub>b</sub>) and/or (\*O<sub>2</sub> + H<sub>b</sub>) intermediates thus makes it possible to circumvent the conventional scaling relation, although this will not necessarily lead to a better overpotential.

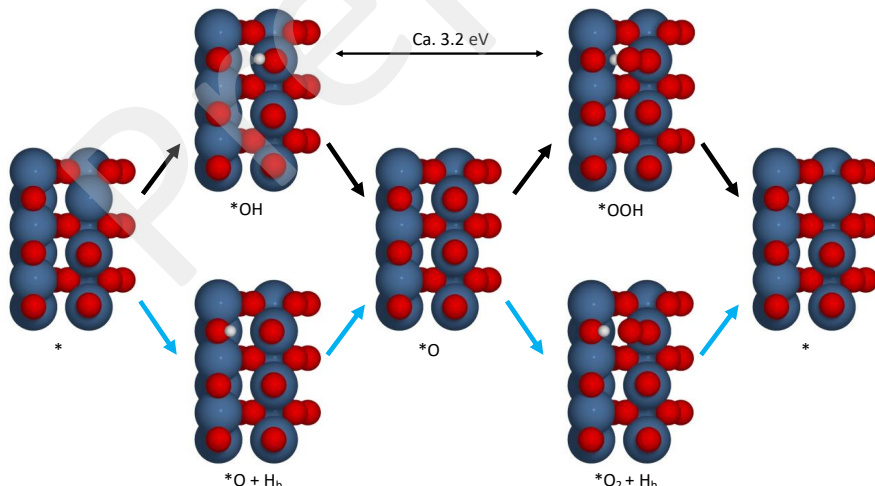


Figure S11: Illustration of the two considered reaction pathways; the conventional pathway indicated with black arrows and the alternative pathway involving proton transfer to the bridge site, indicated with blue arrows.

To determine the scaling relations for both the conventional and the bridge pathways, 30 slabs with \*OOH and \*O<sub>2</sub>+H<sub>b</sub> are calculated (i.e. a total of 90 adsorption energies of which some are discarded because the proton has jumped to a different oxygen). Figure S12a shows the scaling between the \*OH and \*OOH intermediates. Fitting to a linear function with a slope of 1 we find the scaling relation  $G(\text{OOH}) \approx G(\text{OH}) + 3.0 \text{ eV}$ , which is slightly lower than the scaling relation previously found for various oxides.<sup>4</sup> We note that the actual slope appears to be slightly lower than 1, and if the Pd data is removed the scaling constant becomes 3.1 eV.

The corresponding scaling relation between the \*O + H<sub>b</sub> and \*O<sub>2</sub> + H<sub>b</sub> intermediates is also shown in Figure S12. Here individual scaling relations are found for each element on the cus site as shown with the fitted lines, varying between 1.5 eV for Pd and 3.6 eV for Os, with Ir (2.6 eV) being closest to the ideal value of 2.46 eV.

The preferred reaction pathway is found by calculating the adsorption energies of \*O, \*OH and \*O+H<sub>b</sub> by DFT and using the scaling relations to calculate the energies of \*OOH and \*O<sub>2</sub> + H<sub>b</sub>. The resulting overpotentials for ca. 600 sites are plotted in a volcano plot in Figure S13a. A histogram of the overpotentials is shown in Figure S13b revealing that, for the calculated sites, Ir sites have the lowest overpotentials, closely followed by Ru and Rh sites.

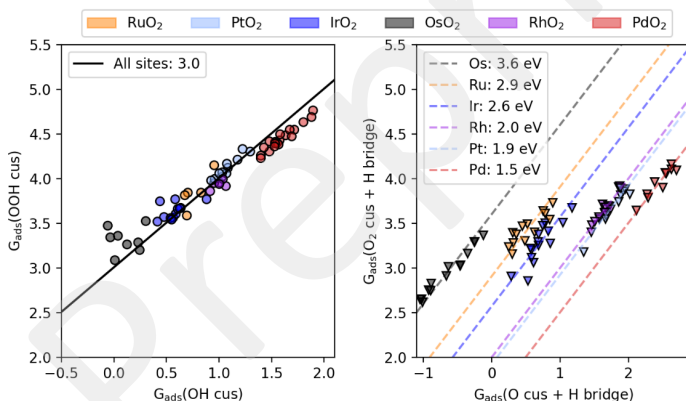


Figure S12: Scaling relation between the adsorption energies of \*OH and \*OOH (left) and \*O+H<sub>b</sub> and \*O<sub>2</sub>+H<sub>b</sub> (right). Colors of the markers indicate the element on the cus site and lines represent the best fit with a slope of 1.

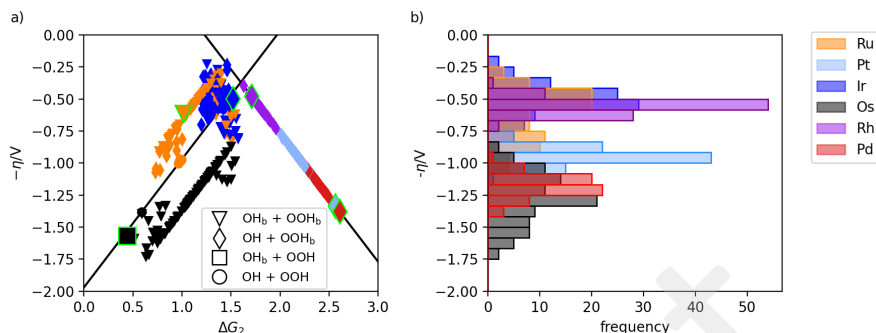


Figure S13: a) Volcano plot showing the activity for all the sites calculated by DFT. Colors indicate the element on the cus site and the shape of the markers indicate the preferred reaction pathway. Large markers with green edges represent the overpotentials for the pure metal oxides. Black lines show the volcano for the conventional reaction pathway, defined by the scaling relation between  ${}^*\text{OH}$  and  ${}^*\text{OOH}$ . b) histogram of overpotentials from the sites plotted in a).

### Section S7: Linear Fit

The sites calculated by DFT only reflect a fraction of the many different possible local atomic environments. A cus site has eight nearest neighbour (NN) metal atoms, which results in a total of  $6^9=10.1*10^6$  different sites (of which some will be equivalent by symmetry), while a bridge has more than a billion different possible sites. Since this is clearly too many sites to be calculated by DFT, instead the calculated adsorption energies for each intermediate are used to fit a linear model that can predict the adsorption energies for all possible local atomic environments.

#### Fitting coefficients

The fitting procedure is similar to that described in ref<sup>8</sup> i.e. the calculated adsorption energies are fitted to a linear model using ridge regression. Only NN metal atoms are assumed to influence the adsorption energies, which was found to be a reasonable approximation in ref.<sup>8</sup>

The adsorption energy on a cus site,  $i$ , ( $E_{ads,i}$ ) can be written as:

$$E_{ads,i} = C_0 + \sum_k^{metals} C_{cus,k} N_{cus,k}^i + \sum_k^{metals} C_{b,k} N_{b,k}^i + \sum_k^{metals} C_{sub,k} N_{sub,k}^i$$

Where  $N_{cus,k}^i$ ,  $N_{b,k}^i$  and  $N_{sub,k}^i$  are the number of atoms of element ( $k$ ) that are present in each of the three types of NN sites around site  $i$  (see Figure S14a) and  $C_{x,k}$  are the coefficients to be fitted. The expression does not consider the relative position of the elements, and thus there are 333396 different types of sites within our model, while the total number of sites will be  $6^9=10.1*10^6$  (of which some will be equivalent by symmetry). Individual fits are made according to the identity of atom  $i$ .

The bridge adsorption site consists of two metal atoms resulting in a total of 21 different combinations. Since the bridge site has five different types of NN atoms (see Figure S14b), the expression for the adsorption energy is:

$$E_{ads,i} = C_0 + \sum_k^{metals} C_{cus1,k} N_{cus1,k}^i + \sum_k^{metals} C_{cus2,k} N_{cus2,k}^i + \sum_k^{metals} C_{sub1,k} N_{sub1,k}^i \\ + \sum_k^{metals} C_{sub2,k} N_{sub2,k}^i + \sum_k^{metals} C_{b,k} N_{b,k}^i$$

Which has a total of 31 coefficients to be fitted for each of the 21 types of bridge sites. Within our model there are  $14.7*10^7$  sites, while the total number of different sites (disregarding symmetry) is  $6^{13}=13.1*10^9$ .

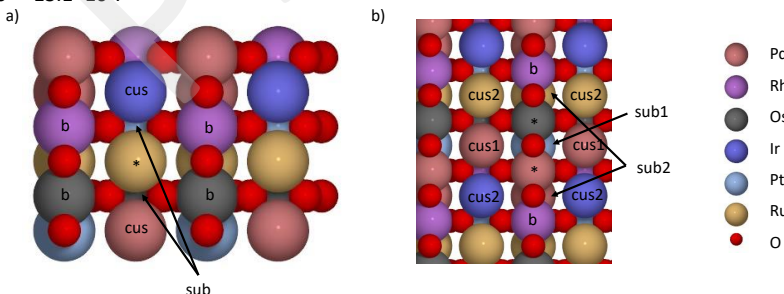


Figure S14: a) Cus adsorption site (\*) on the rutile (110) surface and the three types of nearest neighbour (NN) metal atoms considered in the linear model; cus, bridge (b) and subsurface (sub) and b) bridge adsorption site with the five types of different NN sites marked.

### *Excluding structures from fits*

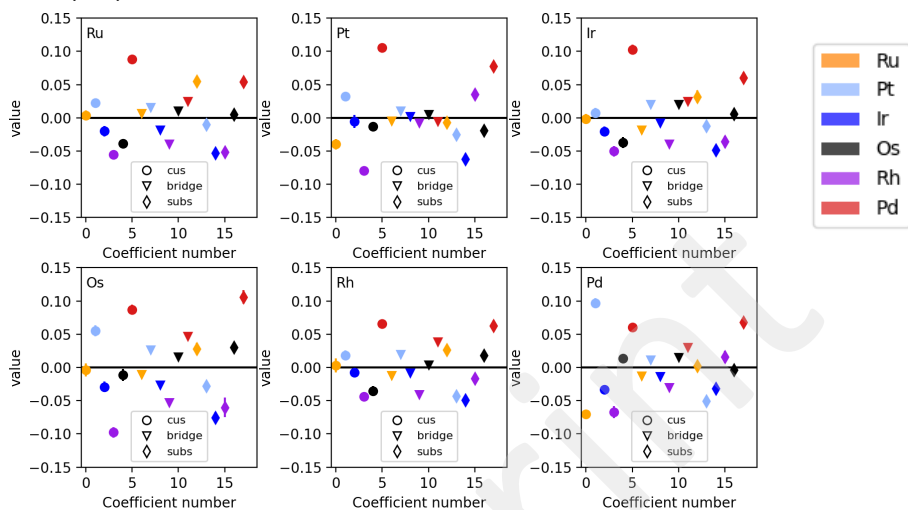
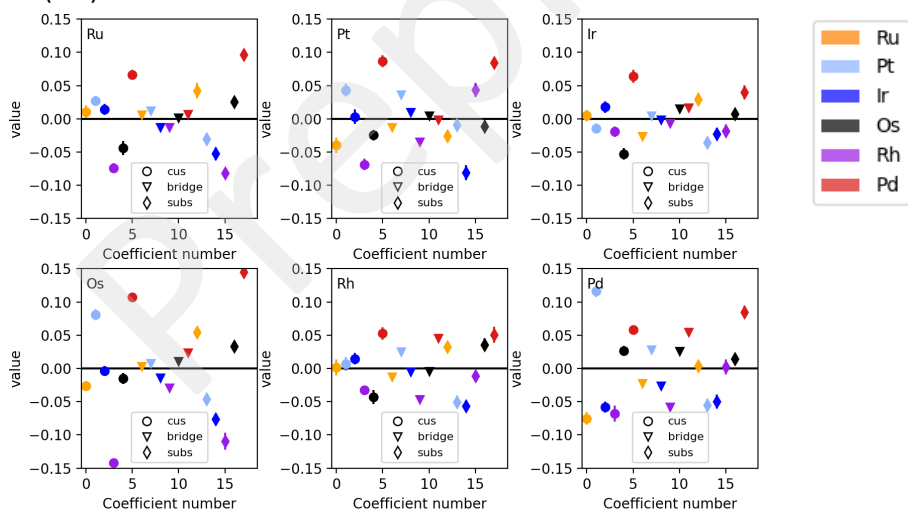
Structures are excluded from the fits if they relax away from the intended structure, or in a way that is significantly different to the reference structure. More specifically, three different types of structures are removed:

- 1) \*OH and \*O + H<sub>b</sub> structures where the proton has jumped to another oxygen atom.
- 2) For some structures, a bridging oxygen between Pd and Os will relax to reside mostly on the Os atom. Such structures are discarded if the M-O bond length in the structure with adsorbate and the reference differ by more than 0.5 Å.
- 3) Structures where two \*O atoms on neighbouring cus sites have moved such that they are separated by less than 1.8 Å.

Adsorption energies on the pure oxides are not included in the fit, as the electronic structure of the pure oxides might be significantly different to that of the HEO.

### *Fitting procedure and results on cus sites*

The calculated adsorption energies are randomly split into a training set (80%) and a test set (20%) and 100 different fits are performed. The average value of each of the fitting coefficients is plotted in Figure S5 for each element for \*OH and \*O adsorbed on the cus site. The fit is performed with adsorption energies from 200 different slabs (corresponding to ca. 600 adsorption energies, since a few are removed). The error bars in Figure S15 indicate the standard deviation calculated from the 100 different fits and clearly they are small when this number of structures is included. The model is used to predict the energies for the ca. 600 sites included in the fit + an additional ca. 150 sites, the results are plotted in Figure S16. The calculated RMSE is below 0.11 eV for the structures included in the test set and slightly larger for the remaining structures (max 0.15 eV), with the \*OH adsorption energies generally predicted slightly better than the \*O energies.

**OH (cus) coefficients****O (cus) coefficients**

**Figure S15:** Fitting coefficients for \*OH cus (top) and \*O cus (bottom) with the element in the top left as the adsorption site. The colour of each point indicates the element and the shape indicates which of the NN positions the coefficient relates to, i.e., coefficient 1-6 represent the influence of NN cus sites, coefficient 7-12 represent the influence of NN bridge sites and coefficient 13-18 represent the influence of NN subsurface atoms. Error bars on each coefficient indicate the standard deviation from the 100 fits with different splitting of training and test data.

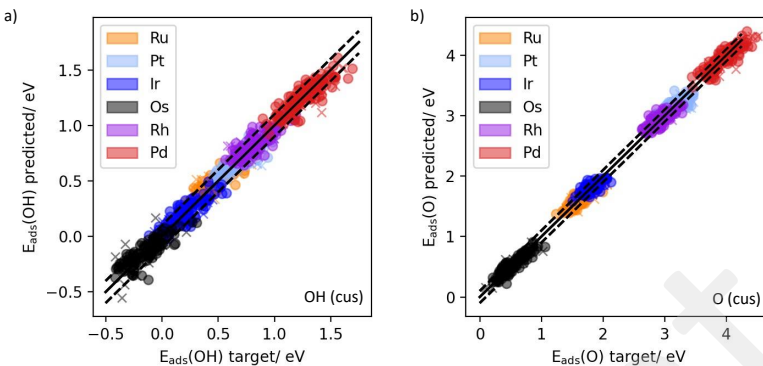


Figure S16: Predicted vs target values for adsorption of a) \*OH and b) \*O on the cus site. Circles represent structures that are used to fit the model and crosses represent structures that are not included in the fit. Dashed black lines indicate a deviation of 0.1 eV from the target value.

With the generated fits we can predict the \*OH and \*O adsorption energies for all the different sites within our model, and multiply by their statistical weight to get the distribution of adsorption energies for all possible sites. These are shown in Figure S17, where they are compared with histograms of the DFT calculated energies.

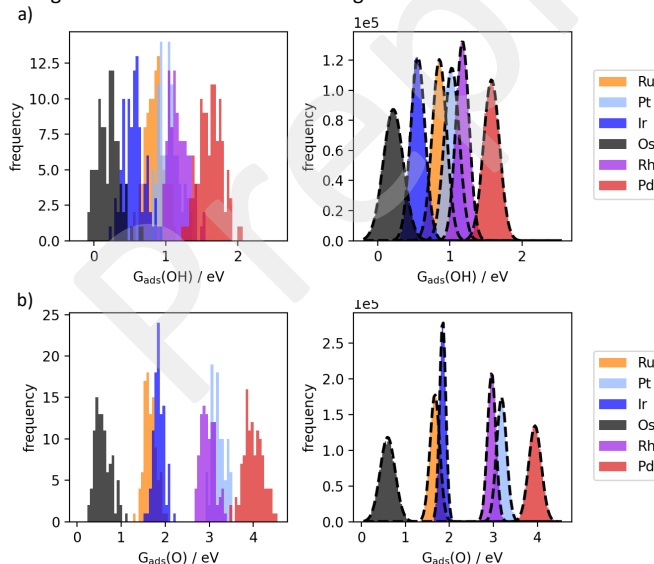
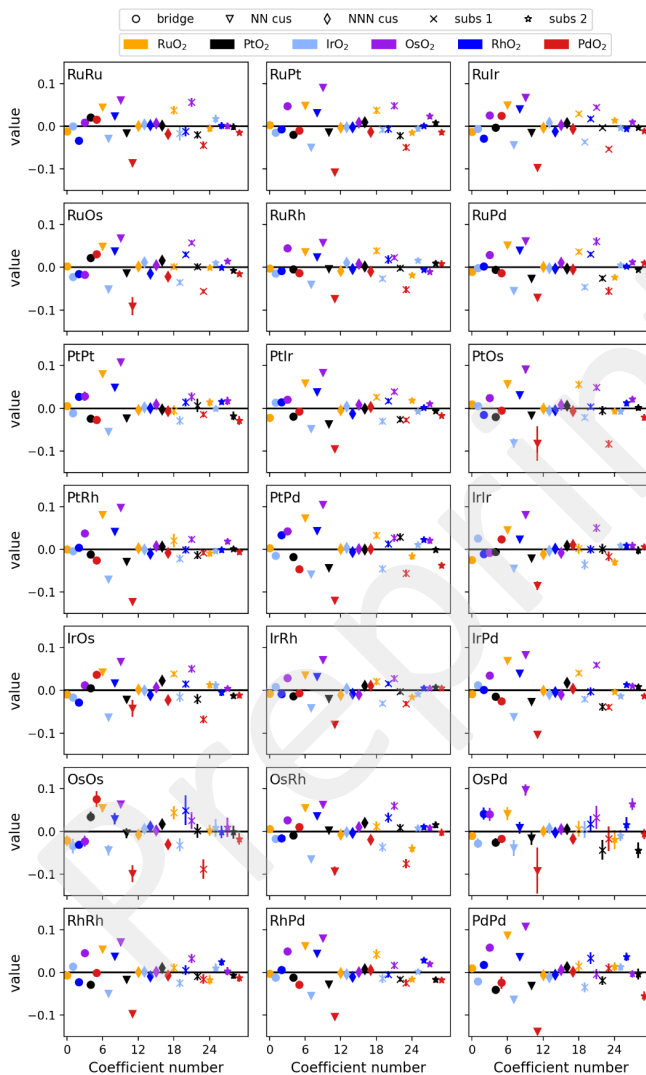


Figure S17: Distributions of adsorption energies on the cus sites as calculated by DFT (left) and with the fitted model for all possible sites (right) for a) \*OH and b) \*O.

*Fitting procedure and results on bridge sites*

To fit the energies on the bridge site, we use the adsorption energies of H<sub>b</sub> when \*O is present on the neighbouring cus site, corresponding to -ΔG<sub>2</sub>. In this way the fingerprint of the adsorption site remains that of the bridge site as shown in Figure S14b.

To fit the energies for adsorption on the bridge sites 637 slabs are considered, resulting in 1678 adsorption energies (since some are excluded, see below). The probability of creating a bridge site with two identical atoms is only half of the probability of creating a site with two different atoms. Thus, while all slabs are randomly generated, only 600 are randomly selected for calculation while 37 are chosen specifically because they contain IrIr or OsOs bridge sites, which are underrepresented in the first 600 slabs. This ensures that the 31 coefficients can be determined for all fits, with a minimum of 42 valid structures in the case of OsOs. The fitting coefficients and error bars are shown in Figure S18. The relatively large error bars on the OsPd fit arises because of the large difference in O binding strength which means that the bridging O will sometimes move to reside primarily on Os. If there are large differences between a structure and its corresponding reference structure, the structure is excluded from the fit as mentioned above, however even minor changes may lead to uncertainties in the fits. The predicted vs. target values are shown in Figure S19 showing that the model predicts most structures well. Finally, the distribution of energies are shown in Figure S20, demonstrating that the bridge sites span a large energy range.



**Figure S18:** Fitting coefficients for each of the 21 bridge site fits, with the elements on the bridge site given in the top left corner. The color of each point indicates the element and the shape indicates which of the NN positions the coefficient relates to, i.e. coefficient 1–6 represent the influence of NN bridge sites, coefficient 7–12 represent the influence of NN cus sites (cus1 in Figure S13b), coefficient 13–18 represent the influence of NNN cus sites (cus2), coefficient 19–24 represent the influence of the shared subsurface atom (sub1) and coefficient 25–30 represents the influence of the two other NN subsurface atoms (sub2). Error bars on each coefficient indicate the standard deviation from the 100 fits with different splitting of training and test data.

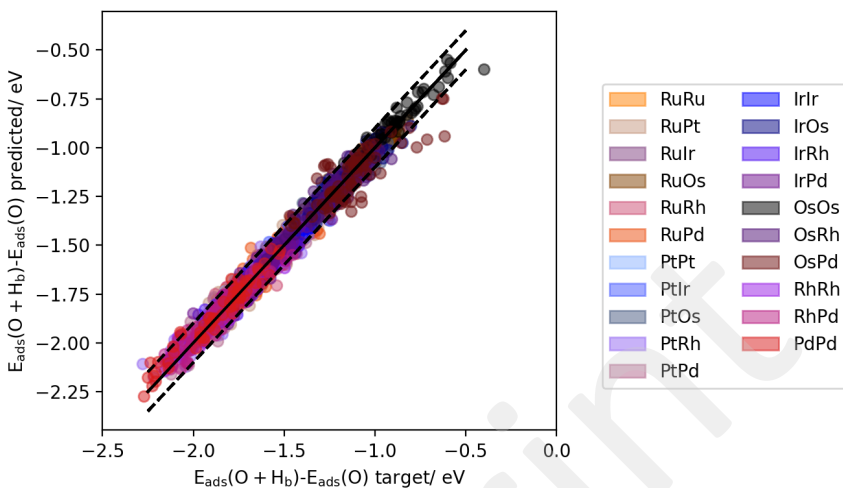


Figure S19: Predicted vs target values for  $E_{\text{ads}}(O + H_b) - E_{\text{ads}}(O)$ . Dashed black lines indicate a deviation of 0.1 eV from the target value.

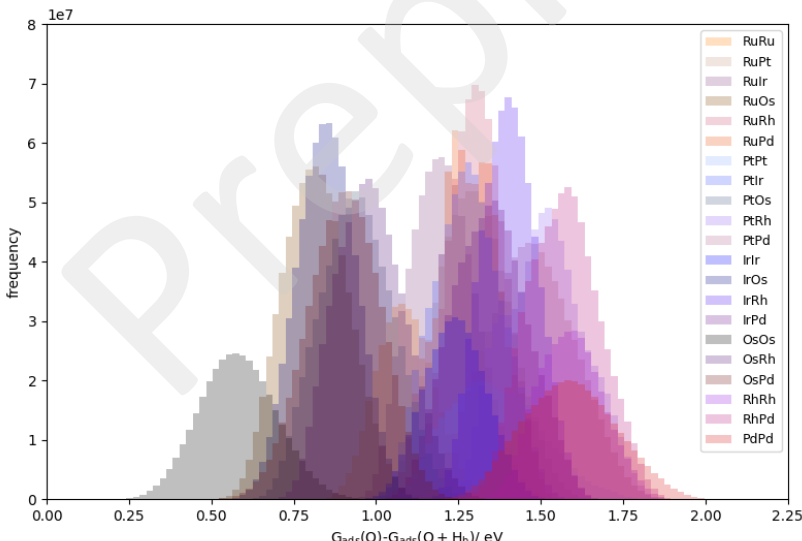


Figure S20: Distribution of  $G_{\text{ads}}(O) - G_{\text{ads}}(O + H_b)$  for all possible bridge sites calculated using our fitted model.

### Section S8: Explicit model for the current

The different surface sites are interdependent, because each bridge site has two cus sites neighbours but it can only accept one proton. To determine the HEO composition that results in the highest current it is therefore necessary to create an explicit model of the surface that takes this into account. The current from individual sites ( $j_i$ ) on 100x100 surfaces with different compositions are calculated as:

$$\frac{1}{j_i} = \frac{1}{j_{k,i}} + \frac{1}{j_d}$$

Where  $j_d$  is the diffusion current, here set to 100 (see note on this below), and  $j_{k,i}$  is the kinetic current from site  $i$ , which depends on the potential ( $U$ ) and the largest free energy step for that site ( $\Delta G_{\max,i}$ ), which can be determined using the fitted linear models:

$$j_{k,i} = \exp\left(\frac{-(|\Delta G_{\max,i} - \Delta G_{opt}| + \Delta G_{opt} - eU)}{k_b T}\right)$$

Here  $k_b$  is the Boltzmann constant,  $T$  is the temperature and  $\Delta G_{opt}$  is the optimum value for  $\Delta G_{\max}$ , here set to 1.3 eV which is the best possible value that can be achieved for the Ir site, assuming the bridge site scaling relation. The total current is taken as the sum of the currents from all  $N$  sites on the surface ( $j = \sum_i^N j_i$ ) and used as a measure of the catalytic activity of the given surface composition.

The code used to calculate the current from an explicit surface is an updated version of the code described in ref <sup>8</sup>, adjusted to handle a system with 6 different elements. A 100x100 surface is created for different compositions in 10% intervals throughout composition space. Fingerprints are generated for each surface site and used to calculate the adsorption energies of \*OH, \*O and \*O+H<sub>b</sub> using the corresponding fits, and the energies of \*OOH and \*O<sub>2</sub>+H<sub>b</sub> are calculated using the scaling relations determined in Section S7. Based on these energies the preferred pathway for each site can be determined, however each bridge site has two neighbouring cus sites, but it can only accept a proton from one of them. To generate the results in the paper it is assumed that the bridge site is used by the neighbouring cus site with the lowest adsorption energy for \*OH and \*OOH, if it lowers the energy on that site. A different version of the code, in which the cus site with the lowest energy of \*O+H<sub>b</sub> and \*O<sub>2</sub>+H<sub>b</sub> can use the bridge site has also been created. The optimum compositions identified with the two different versions of the code are very similar for this system, as shown in Figure S21. The figure also shows that the results are only marginally affected if the scaling constant for the conventional pathway is set to 3.0 eV as obtained from the fit in section S7 instead of 3.2 eV as obtained in previous studies.

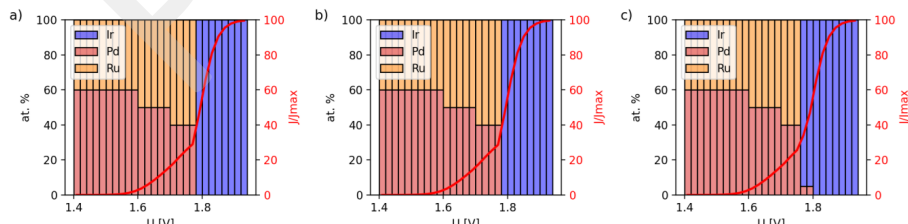


Figure S21: Optimum composition as a function of potential a) using the same code as for the results presented in the main text, b) as obtained with version 2 of the code, which assigns the bridge sites slightly differently and c) as obtained if the scaling relation on the cus site is set to 3.0 eV.

*Note on the alignment of experimental and theoretical voltages*

The diffusion current ( $j_d$ ) used to calculate the current for each site is set to 100. The choice of  $j_d$  affects the value of the maximum current, which is  $j_{max}=j_d \cdot N_{sites}$ , thus when plotting  $j/j_{max}$  the shape of the curves become independent of  $j_d$ , but they are shifted along the x-axis. An example of this is shown in Figure S22 for an arbitrary composition with three different values of  $j_d$ . The choice of  $j_d$  therefore does not affect the observed trends, only the potential values at which they are observed.

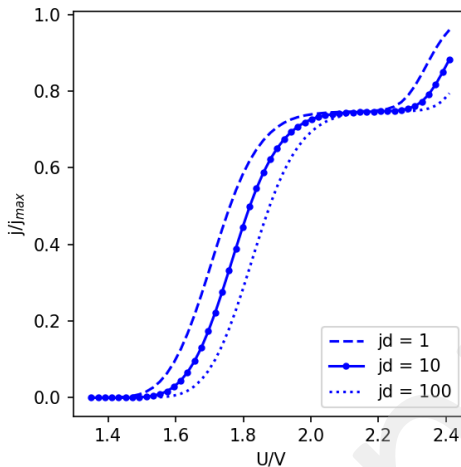


Figure S22: Activity ( $j/j_{max}$ ) as a function of potential for  $Ru_{0.4}Ir_{0.4}Pd_{0.2}$  for different choices of  $j_d$ .

### Section S9: RuIrOs subspace

The activity and optimum composition within the RuIrOs subspace, calculated with the DFT based model, is summarized in Figure S23. The figure shows that the most active composition is found close to the RuIr edge of the ternary diagram. 5 % of Os is found in the optimum composition at low potentials when very few sites on the surface are active, but at higher potentials no Os is found in the optimum.

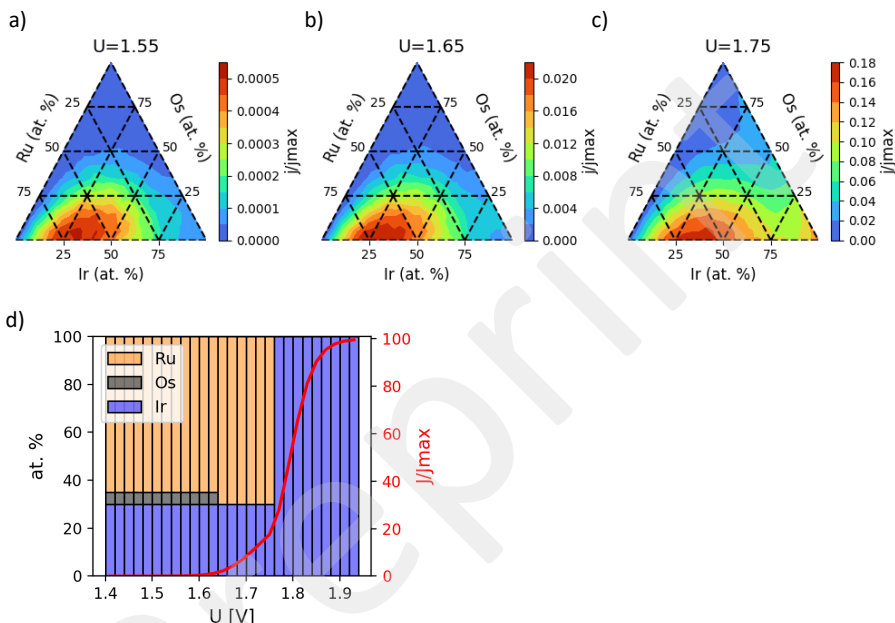


Figure S23: Catalytic activity of the RuIrOs subspace as calculated using the DFT based model at a) 1.55V, b) 1.65V and c) 1.75V. The activity is calculated as the total current relative to the maximum current that can be reached within the diffusion limit ( $j/j_{\max}$ ). d) Optimum composition within the RuIrOs subspace as a function of potential. The red line indicates ( $j/j_{\max}$ ) for the most active composition as a function of potential.

**Section S10: Comparison of DFT model and explicit calculations for pure oxides**

It should be noted that neither the computational nor the experimental model was constructed with data obtained near the edges and corners of the composition space. However, the results of the DFT based can be easily compared with data for the pure oxides. The value of  $\Delta G_{\max}$  for the pure metal oxides calculated directly with DFT and with the fitted linear model are listed in Table S2. The results show a reasonable level of agreement (less than 0.25 eV error for all elements) and a correct ordering of the activities except for the two most active elements, Rh and Ir, where Rh has a slightly lower  $\Delta G_{\max}$  within DFT, while Ir is predicted to be the most active material within the fitted model. This reversed order is expected to give rise to errors in the predicted optimum composition at high potentials, when nearly all sites on the surface are active. However, we note from the DFT calculated points in Figure S13a, that the alloying with other elements tends to decrease the activity of Rh sites while both increased and decreased activity is obtained for Ir sites. Thus, Ir sites would indeed be expected to be more active than Rh sites at lower potentials.

*Table S2: Overpotentials calculated by DFT and obtained from the fitted linear model.*

	Rh	Ir	Ru	Pt	Pd	Os
$\Delta G_{\max}$ (DFT)	1.71	1.73	1.84	2.56	2.61	2.80
$\Delta G_{\max}$ (fit)	1.77	1.68	1.91	2.31	2.49	2.91

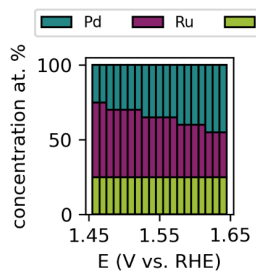
**Section S11: IrPdRu Subspace evaluated by the Gaussian Process models**

Figure S24: Optimum compositions as a function of potential from the GP models confined to the IrPdRu space.

**References**

1. Lundberg, S. M. & Lee, S. I. A unified approach to interpreting model predictions. *Adv Neural Inf Process Syst* **2017-Decem**, 4766–4775 (2017).
2. Rogers, D. B., Shannon, R. D., Sleight, A. W. & Gillson, J. L. Crystal chemistry of metal dioxides with rutile-related structures. *Inorg Chem* **8**, 841–849 (1969).
3. Matar, S. F., Demazeau, G., Möller, M. H. & Pöttgen, R. Electronic structure and equation of state of  $\text{PdO}_2$  from ab initio. *Chem Phys Lett* **508**, 215–218 (2011).
4. Man, I. C., Su, H. Y., Calle-Vallejo, F., Hansen, H. A., Martinez, J. I., Inoglu, N. G., Kitchin, J., Jaramillo, T. F., Nørskov, J. K. & Rossmeisl, J. Universality in Oxygen Evolution Electrocatalysis on Oxide Surfaces. *ChemCatChem* **3**, 1159–1165 (2011).
5. Halck, N. B., Petrykin, V., Krtík, P. & Rossmeisl, J. Beyond the volcano limitations in electrocatalysis-oxygen evolution reaction. *Physical Chemistry Chemical Physics* **16**, 13682–13688 (2014).
6. Rao, R. R., Kolb, M. J., Halck, N. B., Pedersen, A. F., Mehta, A., You, H., Stoerzinger, K. A., Feng, Z., Hansen, H. A., Zhou, H., Giordano, L., Rossmeisl, J., Vegge, T., Chorkendorff, I., Stephens, I. E. L. & Shao-Horn, Y. Towards identifying the active sites on  $\text{RuO}_2(110)$  in catalyzing oxygen evolution. *Energy Environ Sci* **10**, 2626–2637 (2017).
7. Divanis, S., Frandsen, A. M., Kutlusoy, T. & Rossmeisl, J. Lifting the discrepancy between experimental results and the theoretical predictions for the catalytic activity of  $\text{RuO}_2(110)$  towards oxygen evolution reaction. *PHYSICAL CHEMISTRY CHEMICAL PHYSICS* **23**, 19141–19145 (2021).
8. Svane, K. L. & Rossmeisl, J. Theoretical Optimization of Compositions of High-Entropy Oxides for the Oxygen Evolution Reaction\*\*. *Angewandte Chemie International Edition* **61**, (2022).

## Bibliography

1. Cantor, B., Chang, I. T. H., Knight, P. & Vincent, A. J. B. Microstructural development in equiatomic multicomponent alloys. *Materials Science and Engineering: A* **375–377**, 213–218 (2004).
2. Yeh, J. W., Chen, S. K., Lin, S. J., Gan, J. Y., Chin, T. S., Shun, T. T., Tsau, C. H. & Chang, S. Y. Nanostructured high-entropy alloys with multiple principal elements: Novel alloy design concepts and outcomes. *Adv Eng Mater* **6**, 299–303 (2004).
3. Yeh, J.-W. Alloy Design Strategies and Future Trends in High-Entropy Alloys. *JOM* **65**, 1759–1771 (2013).
4. Tsai, K. Y., Tsai, M. H. & Yeh, J. W. Sluggish diffusion in Co-Cr-Fe-Mn-Ni high-entropy alloys. *Acta Mater* **61**, 4887–4897 (2013).
5. Miracle, D. B. & Senkov, O. N. A critical review of high entropy alloys and related concepts. *Acta Mater* **122**, 448–511 (2017).
6. Batchelor, T. A. A., Pedersen, J. K., Winther, S. H., Castelli, I. E., Jacobsen, K. W. & Rossmeisl, J. High-Entropy Alloys as a Discovery Platform for Electrocatalysis. *Joule* **3**, 834–845 (2019).
7. Cantor, B. Multicomponent and high entropy alloys. *Entropy* **16**, 4749–4768 (2014).
8. Nugraha, A. S., Lambard, G., Na, J., Hossain, M. S. A., Asahi, T., Chaikittisilp, W. & Yamauchi, Y. Mesoporous trimetallic PtPdAu alloy films toward enhanced electrocatalytic activity in methanol oxidation: unexpected chemical compositions discovered by Bayesian optimization. *J Mater Chem A Mater* **8**, 13532–13540 (2020).
9. Clausen, C. M., Nielsen, M. L. S., Pedersen, J. K. & Rossmeisl, J. Ab Initio to Activity: Machine Learning-Assisted Optimization of High-Entropy Alloy Catalytic Activity. *High Entropy Alloys & Materials* (2022). doi:10.1007/s44210-022-00006-4
10. Danilovic, N., Subbaraman, R., Chang, K.-C., Chang, S. H., Kang, Y. J., Snyder, J., Paulikas, A. P., Strmcnik, D., Kim, Y.-T., Myers, D., Stamenkovic, V. R. & Markovic, N. M. Activity-Stability Trends for the Oxygen Evolution Reaction on Monometallic Oxides in Acidic Environments. *J Phys Chem Lett* **5**, 2474–8 (2014).
11. Huang, X., Yang, G., Li, S., Wang, H., Cao, Y., Peng, F. & Yu, H. Noble-metal-based high-entropy-alloy nanoparticles for electrocatalysis. *Journal of Energy Chemistry* **68**, 721–751 (2022).
12. Modupeola, D. & Popoola, P. High entropy nanomaterials for energy storage and catalysis applications. *Front Energy Res* **11**, (2023).

13. Chen, L.-W. & Wang, L. Reasonably constructed nano-alloyed materials as highly efficient electrocatalysts for the hydrogen evolution reaction. *Catal Sci Technol* **13**, 4590–4614 (2023).
14. Ashraf, S., Liu, Y., Wei, H., Shen, R., Zhang, H., Wu, X., Mehdi, S., Liu, T. & Li, B. Bimetallic Nanoalloy Catalysts for Green Energy Production: Advances in Synthesis Routes and Characterization Techniques. *Small* (2023). doi:10.1002/smll.202303031
15. Löffler, T., Ludwig, A., Rossmeisl, J. & Schuhmann, W. What Makes High-Entropy Alloys Exceptional Electrocatalysts? *Angewandte Chemie International Edition* **60**, 26894–26903 (2021).
16. Kusada, K., Mukoyoshi, M., Wu, D. & Kitagawa, H. Chemical Synthesis, Characterization, and Properties of Multi-Element Nanoparticles. *Angewandte Chemie International Edition* **61**, (2022).
17. Liu, Y., Tian, X., Han, Y.-C., Chen, Y. & Hu, W. High-temperature shock synthesis of high-entropy-alloy nanoparticles for catalysis. *Chinese Journal of Catalysis* **48**, 66–89 (2023).
18. Tomboc, G. M., Kwon, T., Joo, J. & Lee, K. High entropy alloy electrocatalysts: a critical assessment of fabrication and performance. *J Mater Chem A Mater* **8**, 14844–14862 (2020).
19. Shen, J., Hu, Z., Chen, K., Chen, C., Zhu, Y. & Li, C. Platinum based high entropy alloy oxygen reduction electrocatalysts for proton exchange membrane fuel cells. *Mater Today Nano* **21**, 100282 (2023).
20. Tao, L., Huang, B. & Zhao, Y. Low-Dimensional High-Entropy Alloys for Advanced Electrocatalytic Reactions. *The Chemical Record* **23**, (2023).
21. Al Zoubi, W., Putri, R. A. K., Abukhadra, M. R. & Ko, Y. G. Recent experimental and theoretical advances in the design and science of high-entropy alloy nanoparticles. *Nano Energy* **110**, 108362 (2023).
22. Yu, L., Zeng, K., Li, C., Lin, X., Liu, H., Shi, W., Qiu, H., Yuan, Y. & Yao, Y. High-entropy alloy catalysts: From bulk to nano toward highly efficient carbon and nitrogen catalysis. *Carbon Energy* **4**, 731–761 (2022).
23. Han, X., Wu, G., Zhao, S., Guo, J., Yan, M., Hong, X. & Wang, D. Nanoscale high-entropy alloy for electrocatalysis. *Matter* **6**, 1717–1751 (2023).
24. Wang, Y. & Wang, Y. High-entropy alloys in catalyses and supercapacitors: Progress, prospects. *Nano Energy* **104**, 107958 (2022).
25. Ma, Y., Ma, Y., Wang, Q., Schweidler, S., Botros, M., Fu, T., Hahn, H., Brezesinski, T. & Breitung, B. High-entropy energy materials: Challenges and new opportunities. *Energy Environ Sci* **14**, 2883–2905 Preprint at <https://doi.org/10.1039/d1ee00505g> (2021)

26. Bornet, A., Pittkowski, R., Nielsen, T. M., Berner, E., Maletzko, A., Schröder, J., Quinson, J., Melke, J., Jensen, K. M. Ø. & Arenz, M. Influence of Temperature on the Performance of Carbon- and ATO-supported Oxygen Evolution Reaction Catalysts in a Gas Diffusion Electrode Setup. *ACS Catal.* **13**, 7568–7577 (2023).
27. Cepitis, R., Kongi, N., Rossmeisl, J. & Ivaniščev, V. Surface Curvature Effect on Dual-Atom Site Oxygen Electrocatalysis. *ACS Energy Lett.* **8**, 1330–1335 (2023).
28. Ers, H., Voroshylova, I. V., Pikma, P. & Ivaniščev, V. B. Double layer in ionic liquids: Temperature effect and bilayer model. *J Mol Liq.* **363**, 119747 (2022).
29. Liu, H., Zhang, L., Wang, K., Wang, L., Zhang, L., Yu, B. & Yang, F. Composition-Dependent Near-Surface Structure of High-Entropy Alloy Catalysts for the Semihydrogenation of Alkynes. *The Journal of Physical Chemistry C* **127**, 7211–7219 (2023).
30. Zhan, C., Bu, L., Sun, H., Huang, X., Zhu, Z., Yang, T., Ma, H., Li, L., Wang, Y., Geng, H., Wang, W., Zhu, H., Pao, C., Shao, Q., Yang, Z., Liu, W., Xie, Z. & Huang, X. Medium/High-Entropy Amalgamated Core/Shell Nanoplate Achieves Efficient Formic Acid Catalysis for Direct Formic Acid Fuel Cell. *Angewandte Chemie International Edition* **62**, (2023).
31. Márquez, V., Santos, J. S., Buijnsters, J. G., Praserthdam, S. & Praserthdam, P. Simple, controllable and environmentally friendly synthesis of FeCoNiCuZn-based high-entropy alloy (HEA) catalysts, and their surface dynamics during nitrobenzene hydrogenation. *Electrochim Acta* **410**, 139972 (2022).
32. Zhang, N., Chen, X., Liu, S., Meng, J., Armbrüster, M. & Liang, C. PtFeCoNiCu High-Entropy Alloy Catalyst for Aqueous-Phase Hydrogenation of Maleic Anhydride. *ACS Appl Mater Interfaces* **15**, 23276–23285 (2023).
33. Cai, C., Xin, Z., Zhang, X., Cui, J., Lv, H., Ren, W., Gao, C. & Cai, B. Facile Synthesis of FeCoNiCuI<sub>r</sub> High Entropy Alloy Nanoparticles for Efficient Oxygen Evolution Electrocatalysis. *Catalysts* **12**, 1050 (2022).
34. Cao, X., Gao, Y., Wang, Z., Zeng, H., Song, Y., Tang, S., Luo, L. & Gong, S. FeNiCrCoMn High-Entropy Alloy Nanoparticles Loaded on Carbon Nanotubes as Bifunctional Oxygen Catalysts for Rechargeable Zinc-Air Batteries. *ACS Appl Mater Interfaces* **15**, 32365–32375 (2023).
35. Yu, Y., Xia, F., Wang, C., Wu, J., Fu, X., Ma, D., Lin, B., Wang, J., Yue, Q. & Kang, Y. High-entropy alloy nanoparticles as a promising electrocatalyst to enhance activity and durability for oxygen reduction. *Nano Res.* **15**, 7868–7876 (2022).
36. Wu, D., Kusada, K., Yamamoto, T., Toriyama, T., Matsumura, S., Kawaguchi, S., Kubota, Y. & Kitagawa, H. Platinum-Group-Metal High-Entropy-Alloy Nanoparticles. *J Am Chem Soc* **142**, 13833–13838 (2020).

37. Li, H., Han, Y., Zhao, H., Qi, W., Zhang, D., Yu, Y., Cai, W., Li, S., Lai, J., Huang, B. & Wang, L. Fast site-to-site electron transfer of high-entropy alloy nanocatalyst driving redox electrocatalysis. *Nat Commun* **11**, 5437 (2020).
38. Feng, G., Ning, F., Song, J., Shang, H., Zhang, K., Ding, Z., Gao, P., Chu, W. & Xia, D. Sub-2 nm Ultrasmall High-Entropy Alloy Nanoparticles for Extremely Superior Electrocatalytic Hydrogen Evolution. *J Am Chem Soc* **143**, 17117–17127 (2021).
39. Chang, J., Wang, G., Li, C., He, Y., Zhu, Y., Zhang, W., Sajid, M., Kara, A., Gu, M. & Yang, Y. Rational design of septenary high-entropy alloy for direct ethanol fuel cells. *Joule* **7**, 587–602 (2023).
40. Okejiri, F., Yang, Z., Chen, H., Do-Thanh, C.-L., Wang, T., Yang, S. & Dai, S. Ultrasound-driven fabrication of high-entropy alloy nanocatalysts promoted by alcoholic ionic liquids. *Nano Res* **15**, 4792–4798 (2022).
41. Liu, Y.-H., Hsieh, C.-J., Hsu, L.-C., Lin, K.-H., Hsiao, Y.-C., Chi, C.-C., Lin, J.-T., Chang, C.-W., Lin, S.-C., Wu, C.-Y., Gao, J.-Q., Pao, C.-W., Chang, Y.-M., Lu, M.-Y., Zhou, S. & Yang, T.-H. Toward controllable and predictable synthesis of high-entropy alloy nanocrystals. *Sci Adv* **9**, (2023).
42. Bueno, S. L. A., Leonardi, A., Kar, N., Chatterjee, K., Zhan, X., Chen, C., Wang, Z., Engel, M., Fung, V. & Skrabalak, S. E. Quinary, Senary, and Septenary High Entropy Alloy Nanoparticle Catalysts from Core@Shell Nanoparticles and the Significance of Intraparticle Heterogeneity. *ACS Nano* **16**, 18873–18885 (2022).
43. Broge, N. L. N., Bertelsen, A. D., Søndergaard-Pedersen, F. & Iversen, B. B. Facile Solvothermal Synthesis of Pt–Ir–Pd–Rh–Ru–Cu–Ni–Co High-Entropy Alloy Nanoparticles. *Chemistry of Materials* **35**, 144–153 (2023).
44. Broge, N. L. N., Bondesgaard, M., Søndergaard-Pedersen, F., Roelsgaard, M. & Iversen, B. B. Autocatalytic Formation of High-Entropy Alloy Nanoparticles. *Angewandte Chemie International Edition* **59**, 21920–21924 (2020).
45. Yang, Y., He, B., Ma, H., Yang, S., Ren, Z., Qin, T., Lu, F., Ren, L., Zhang, Y., Wang, T., Liu, X. & Chen, L. PtRuAgCoNi High-Entropy Alloy Nanoparticles for High-Efficiency Electrocatalytic Oxidation of 5-Hydroxymethylfurfural. *Acta Physico Chimica Sinica* **0**, 2201050–0 (2022).
46. Huang, K., Zhang, B., Wu, J., Zhang, T., Peng, D., Cao, X., Zhang, Z., Li, Z. & Huang, Y. Exploring the impact of atomic lattice deformation on oxygen evolution reactions based on a sub-5 nm pure face-centred cubic high-entropy alloy electrocatalyst. *J Mater Chem A Mater* **8**, 11938–11947 (2020).
47. Mei, Y., Feng, Y., Zhang, C., Zhang, Y., Qi, Q. & Hu, J. High-Entropy Alloy with Mo-Coordination as Efficient Electrocatalyst for Oxygen Evolution Reaction. *ACS Catal* **12**, 10808–10817 (2022).

48. Bertelsen, A. D., Hansen, A. R., Broge, N. L. N., Mamakhet, A., Bondesgaard, M. & Iversen, B. B. Composition space of PtIrPdRhRu high entropy alloy nanoparticles synthesized by solvothermal reactions. *Chemical Communications* **58**, 12672–12675 (2022).
49. Cheng, Y., Sun, Y., Deng, X., Zhang, M., Zhang, L. & Wang, W. High-performance high-entropy quinary-alloys as anode catalysts for direct ethylene glycol fuel cells. *Int J Hydrogen Energy* **48**, 8156–8164 (2023).
50. Abdelhafiz, A., Wang, B., Harutyunyan, A. R. & Li, J. Carbothermal Shock Synthesis of High Entropy Oxide Catalysts: Dynamic Structural and Chemical Reconstruction Boosting the Catalytic Activity and Stability toward Oxygen Evolution Reaction. *Adv Energy Mater* **12**, (2022).
51. Yao, Y., Huang, Z., Xie, P., Lacey, S. D., Jacob, R. J., Xie, H., Chen, F., Nie, A., Pu, T., Rehwoldt, M., Yu, D., Zachariah, M. R., Wang, C., Shahbazian-Yassar, R., Li, J. & Hu, L. Carbothermal shock synthesis of high-entropy-alloy nanoparticles. *Science (1979)* **359**, 1489–1494 (2018).
52. Gao, S., Hao, S., Huang, Z., Yuan, Y., Han, S., Lei, L., Zhang, X., Shahbazian-Yassar, R. & Lu, J. Synthesis of high-entropy alloy nanoparticles on supports by the fast moving bed pyrolysis. *Nat Commun* **11**, 2016 (2020).
53. Zhao, P., Cao, Q., Yi, W., Hao, X., Li, J., Zhang, B., Huang, L., Huang, Y., Jiang, Y., Xu, B., Shan, Z. & Chen, J. Facile and General Method to Synthesize Pt-Based High-Entropy-Alloy Nanoparticles. *ACS Nano* **16**, 14017–14028 (2022).
54. Mori, K., Hashimoto, N., Kamiuchi, N., Yoshida, H., Kobayashi, H. & Yamashita, H. Hydrogen spillover-driven synthesis of high-entropy alloy nanoparticles as a robust catalyst for CO<sub>2</sub> hydrogenation. *Nat Commun* **12**, 3884 (2021).
55. Qiao, H., Saray, M. T., Wang, X., Xu, S., Chen, G., Huang, Z., Chen, C., Zhong, G., Dong, Q., Hong, M., Xie, H., Shahbazian-Yassar, R. & Hu, L. Scalable Synthesis of High Entropy Alloy Nanoparticles by Microwave Heating. *ACS Nano* **15**, 14928–14937 (2021).
56. Shi, W., Liu, H., Li, Z., Li, C., Zhou, J., Yuan, Y., Jiang, F., Fu, (Kelvin) Kun & Yao, Y. High-entropy alloy stabilized and activated Pt clusters for highly efficient electrocatalysis. *SusMat* **2**, 186–196 (2022).
57. Chang, S.-Q., Cheng, C.-C., Cheng, P.-Y., Huang, C.-L. & Lu, S.-Y. Pulse electrodeposited FeCoNiMnW high entropy alloys as efficient and stable bifunctional electrocatalysts for acidic water splitting. *Chemical Engineering Journal* **446**, 137452 (2022).
58. Wang, Y., Yang, H., Zhang, Z., Meng, X., Cheng, T., Qin, G. & Li, S. Far-from-equilibrium electrosynthesis ramifies high-entropy alloy for alkaline hydrogen evolution. *J Mater Sci Technol* **166**, 234–240 (2023).

59. Yao, C.-Z., Zhang, P., Liu, M., Li, G.-R., Ye, J.-Q., Liu, P. & Tong, Y.-X. Electrochemical preparation and magnetic study of Bi–Fe–Co–Ni–Mn high entropy alloy. *Electrochim Acta* **53**, 8359–8365 (2008).
60. Liu, H., Qin, H., Kang, J., Ma, L., Chen, G., Huang, Q., Zhang, Z., Liu, E., Lu, H., Li, J. & Zhao, N. A freestanding nanoporous NiCoFeMoMn high-entropy alloy as an efficient electrocatalyst for rapid water splitting. *Chemical Engineering Journal* **435**, 134898 (2022).
61. Xie, P., Yao, Y., Huang, Z., Liu, Z., Zhang, J., Li, T., Wang, G., Shahbazian-Yassar, R., Hu, L. & Wang, C. Highly efficient decomposition of ammonia using high-entropy alloy catalysts. *Nat Commun* **10**, 4011 (2019).
62. Li, H., Sun, M., Pan, Y., Xiong, J., Du, H., Yu, Y., Feng, S., Li, Z., Lai, J., Huang, B. & Wang, L. The self-complementary effect through strong orbital coupling in ultrathin high-entropy alloy nanowires boosting pH-universal multifunctional electrocatalysis. *Appl Catal B* **312**, 121431 (2022).
63. Peng, H., Xie, Y., Xie, Z., Wu, Y., Zhu, W., Liang, S. & Wang, L. Large-scale and facile synthesis of a porous high-entropy alloy CrMnFeCoNi as an efficient catalyst. *J Mater Chem A Mater* **8**, 18318–18326 (2020).
64. Chida, Y., Tomimori, T., Ebata, T., Taguchi, N., Ioroi, T., Hayashi, K., Todoroki, N. & Wadayama, T. Experimental study platform for electrocatalysis of atomic-level controlled high-entropy alloy surfaces. *Nat Commun* **14**, 4492 (2023).
65. Waag, F., Li, Y., Ziefuß, A. R., Bertin, E., Kamp, M., Duppel, V., Marzun, G., Kienle, L., Barcikowski, S. & Gökce, B. Kinetically-controlled laser-synthesis of colloidal high-entropy alloy nanoparticles. *RSC Adv* **9**, 18547–18558 (2019).
66. Katiyar, N. K., Nellaiappan, S., Kumar, R., Malviya, K. D., Pradeep, K. G., Singh, A. K., Sharma, S., Tiwary, C. S. & Biswas, K. Formic acid and methanol electro-oxidation and counter hydrogen production using nano high entropy catalyst. *Mater Today Energy* **16**, 100393 (2020).
67. Yeh, J.-W. Recent progress in high-entropy alloys. *Annales de Chimie Science des Matériaux* **31**, 633–648 (2006).
68. Sharma, L., Katiyar, N. K., Parui, A., Das, R., Kumar, R., Tiwary, C. S., Singh, A. K., Halder, A. & Biswas, K. Low-cost high entropy alloy (HEA) for high-efficiency oxygen evolution reaction (OER). *Nano Res* **15**, 4799–4806 (2022).
69. Yi, L., Xiao, S., Wei, Y., Li, D., Wang, R., Guo, S. & Hu, W. Free-standing high-entropy alloy plate for efficient water oxidation catalysis: structure/composition evolution and implication of high-valence metals. *Chemical Engineering Journal* **469**, 144015 (2023).

70. Dai, W., Lu, T. & Pan, Y. Novel and promising electrocatalyst for oxygen evolution reaction based on MnFeCoNi high entropy alloy. *J Power Sources* **430**, 104–111 (2019).
71. Tang, J., Xu, J. L., Ye, Z. G., Ma, Y. C., Li, X. B., Luo, J. M. & Huang, Y. Z. Synthesis of flower-like cobalt, nickel phosphates grown on the surface of porous high entropy alloy for efficient oxygen evolution. *J Alloys Compd* **885**, 160995 (2021).
72. Chen, J., Ling, Y., Yu, X., Wang, G., Huang, L., He, A., Fan, Q., Qin, S., Xiang, S., Xu, M., Han, Z., Du, J. & Xu, Q. Water oxidation on CrMnFeCoNi high entropy alloy: Improvement through rejuvenation and spin polarization. *J Alloys Compd* **929**, 167344 (2022).
73. Kittel, C. in *Introduction to Solid States Physics* 427–452 (John Wiley & Sons Inc., 2005).
74. He, Y., Zhu, X., Zhang, C., Liu, Z., Cao, B., Sheng, L., Yang, Y., Feng, Q., Wang, N., Ou, J. Z. & Xu, Y. Self-Circulating Adsorption–Desorption Structure of Non-Noble High-Entropy Alloy Electrocatalyst Facilitates Efficient Water Splitting. *ACS Sustain Chem Eng* **11**, 5055–5064 (2023).
75. Liu, C., Zhu, H., Lu, S., Duan, F. & Du, M. High entropy alloy nitrides with integrated nanowire/nanosheet architecture for efficient alkaline hydrogen evolution reactions. *NEW JOURNAL OF CHEMISTRY* **45**, 22255–22260 (2021).
76. Wu, D., Kusada, K., Yamamoto, T., Toriyama, T., Matsumura, S., Gueye, I., Seo, O., Kim, J., Hiroi, S., Sakata, O., Kawaguchi, S., Kubota, Y. & Kitagawa, H. On the electronic structure and hydrogen evolution reaction activity of platinum group metal-based high-entropy-alloy nanoparticles. *Chem Sci* **11**, 12731–12736 (2020).
77. Fu, X., Zhang, J., Zhan, S., Xia, F., Wang, C., Ma, D., Yue, Q., Wu, J. & Kang, Y. High-Entropy Alloy Nanosheets for Fine-Tuning Hydrogen Evolution. *ACS Catal* **12**, 11955–11959 (2022).
78. Wang, J., Zhang, J., Hu, Y., Jiang, H. & Li, C. Activating multisite high-entropy alloy nanocrystals via enriching M–pyridinic N–C bonds for superior electrocatalytic hydrogen evolution. *Sci Bull (Beijing)* **67**, 1890–1897 (2022).
79. Wei, M., Sun, Y., Ai, F., Xi, S., Zhang, J. & Wang, J. Stretchable high-entropy alloy nanoflowers enable enhanced alkaline hydrogen evolution catalysis. *Appl Catal B* **334**, 122814 (2023).
80. Wei, M., Sun, Y., Zhang, J., Ai, F., Xi, S. & Wang, J. High-entropy alloy nanocrystal assembled by nanosheets with d–d electron interaction for hydrogen evolution reaction. *Energy Environ Sci* **16**, 4009–4019 (2023).

81. Jing, L., Zou, Y., Goei, R., Wang, L., Ong, J. A., Kurkin, A., Li, Y., Tan, K. W. & Tok, A. I. Y. Conformal Noble Metal High-Entropy Alloy Nanofilms by Atomic Layer Deposition for an Enhanced Hydrogen Evolution Reaction. *Langmuir* **39**, 3142–3150 (2023).
82. Löffler, T., Meyer, H., Savan, A., Wilde, P., Garzón Manjón, A., Chen, Y.-T., Ventosa, E., Scheu, C., Ludwig, A. & Schuhmann, W. Discovery of a Multinary Noble Metal-Free Oxygen Reduction Catalyst. *Adv Energy Mater* **8**, 1802269 (2018).
83. Chen, T., Ning, F., Qi, J., Feng, G., Wang, Y., Song, J., Yang, T., Liu, X., Chen, L. & Xia, D. PtFeCoNiCu high-entropy solid solution alloy as highly efficient electrocatalyst for the oxygen reduction reaction. *iScience* **26**, 105890 (2023).
84. Chen, Y., Zhan, X., Bueno, S. L. A., Shafei, I. H., Ashberry, H. M., Chatterjee, K., Xu, L., Tang, Y. & Skrabalak, S. E. Synthesis of monodisperse high entropy alloy nanocatalysts from core@shell nanoparticles. *Nanoscale Horiz* **6**, 231–237 (2021).
85. Yao, Y., Li, Z., Dou, Y., Jiang, T., Zou, J., Lim, S. Y., Norby, P., Stamate, E., Jensen, J. O. & Zhang, W. High entropy alloy nanoparticles encapsulated in graphitised hollow carbon tubes for oxygen reduction electrocatalysis. *Dalton Transactions* **52**, 4142–4151 (2023).
86. Tang, J., Xu, J. L., Ye, Z. G., Li, X. B. & Luo, J. M. Microwave sintered porous CoCrFeNiMo high entropy alloy as an efficient electrocatalyst for alkaline oxygen evolution reaction. *J Mater Sci Technol* **79**, 171–177 (2021).
87. Cechanaviciute, I. A., Antony, R. P., Krysiak, O. A., Quast, T., Dieckhöfer, S., Saddeler, S., Telaar, P., Chen, Y., Muhler, M. & Schuhmann, W. Scalable Synthesis of Multi-Metal Electrocatalyst Powders and Electrodes and their Application for Oxygen Evolution and Water Splitting. *Angewandte Chemie International Edition* **62**, (2023).
88. Wang, S., Huo, W., Fang, F., Xie, Z., Shang, J. K. & Jiang, J. High entropy alloy/C nanoparticles derived from polymetallic MOF as promising electrocatalysts for alkaline oxygen evolution reaction. *Chemical Engineering Journal* **429**, 132410 (2022).
89. Li, S., Nguyen, T. X., Su, Y., Lin, C., Huang, Y., Shen, Y., Liu, C., Ruan, J., Chang, K. & Ting, J. Sputter-Deposited High Entropy Alloy Thin Film Electrocatalyst for Enhanced Oxygen Evolution Reaction Performance. *Small* **18**, (2022).
90. Ma, P., Zhang, S., Zhang, M., Gu, J., Zhang, L., Sun, Y., Ji, W. & Fu, Z. Hydroxylated high-entropy alloy as highly efficient catalyst for electrochemical oxygen evolution reaction. *SCIENCE CHINA-MATERIALS* **63**, 2613–2619 (2020).
91. Wang, H., Wei, R., Li, X., Ma, X., Hao, X. & Guan, G. Nanostructured amorphous Fe<sub>29</sub>Co<sub>27</sub>Ni<sub>23</sub>Si<sub>9</sub>B<sub>12</sub> high-entropy-alloy: an efficient electrocatalyst for oxygen evolution reaction. *J Mater Sci Technol* **68**, 191–198 (2021).

92. Li, P., Wan, X., Su, J., Liu, W., Guo, Y., Yin, H. & Wang, D. A Single-Phase FeCoNiMnMo High-Entropy Alloy Oxygen Evolution Anode Working in Alkaline Solution for over 1000 h. *ACS Catal.* **12**, 11667–11674 (2022).
93. Johny, J., Li, Y., Kamp, M., Prymak, O., Liang, S.-X., Krekeler, T., Ritter, M., Kienle, L., Rehbock, C., Barcikowski, S. & Reichenberger, S. Laser-generated high entropy metallic glass nanoparticles as bifunctional electrocatalysts. *Nano Res.* **15**, 4807–4819 (2022).
94. He, R., Yang, L., Zhang, Y., Wang, X., Lee, S., Zhang, T., Li, L., Liang, Z., Chen, J., Li, J., Ostovari Moghaddam, A., Llorca, J., Ibáñez, M., Arbiol, J., Xu, Y. & Cabot, A. A CrMnFeCoNi high entropy alloy boosting oxygen evolution/reduction reactions and zinc-air battery performance. *Energy Storage Mater.* **58**, 287–298 (2023).
95. Zhang, P., Hui, X., Nie, Y., Wang, R., Wang, C., Zhang, Z. & Yin, L. New Conceptual Catalyst on Spatial High-Entropy Alloy Heterostructures for High-Performance Li-O<sub>2</sub> Batteries. *Small* **19**, (2023).
96. Jin, Z., Lyu, J., Zhao, Y.-L., Li, H., Lin, X., Xie, G., Liu, X., Kai, J.-J. & Qiu, H.-J. Rugged High-Entropy Alloy Nanowires with in Situ Formed Surface Spinel Oxide As Highly Stable Electrocatalyst in Zn–Air Batteries. *ACS Mater Lett.* **2**, 1698–1706 (2020).
97. Jin, Z., Zhou, X., Hu, Y., Tang, X., Hu, K., Reddy, K. M., Lin, X. & Qiu, H.-J. A fourteen-component high-entropy alloy@oxide bifunctional electrocatalyst with a record-low  $\Delta E$  of 0.61 V for highly reversible Zn–air batteries. *Chem Sci.* **13**, 12056–12064 (2022).
98. Luo, W., Wang, Y., Luo, L., Gong, S., Li, Y. & Gan, X. Constructing a bifunctional catalyst with both high entropy alloy nanoparticles and Janus multi-principal alloy nanoparticles for high-performance overall water splitting. *Appl Surf Sci.* **606**, 154808 (2022).
99. Huang, K., Xia, J., Lu, Y., Zhang, B., Shi, W., Cao, X., Zhang, X., Woods, L. M., Han, C., Chen, C., Wang, T., Wu, J. & Huang, Y. Self-Reconstructed Spinel Surface Structure Enabling the Long-Term Stable Hydrogen Evolution Reaction/Oxygen Evolution Reaction Efficiency of FeCoNiRu High-Entropy Alloyed Electrocatalyst. *Advanced Science* **10**, (2023).
100. Huang, C.-L., Lin, Y.-G., Chiang, C.-L., Peng, C.-K., Senthil Raja, D., Hsieh, C.-T., Chen, Y.-A., Chang, S.-Q., Yeh, Y.-X. & Lu, S.-Y. Atomic scale synergistic interactions lead to breakthrough catalysts for electrocatalytic water splitting. *Appl Catal B* **320**, 122016 (2023).
101. Zhou, P., Wong, P. K., Niu, P., Chen, M., Kwok, C. T., Tang, Y., Li, R., Wang, S. & Pan, H. Anodized AlCoCrFeNi high-entropy alloy for alkaline water electrolysis with ultra-high performance. *Sci China Mater.* **66**, 1033–1041 (2023).

102. Wang, B., Liu, W., Leng, Y., Yu, X., Wang, C., Hu, L., Zhu, X., Wu, C., Yao, Y. & Zou, Z. Strain engineering of high-entropy alloy catalysts for electrocatalytic water splitting. *iScience* **26**, 106326 (2023).
103. Sivanantham, A., Lee, H., Hwang, S. W., Ahn, B. & Cho, I. S. Preparation, electrical and electrochemical characterizations of CuCoNiFeMn high-entropy-alloy for overall water splitting at neutral-pH. *J Mater Chem A Mater* **9**, 16841–16851 (2021).
104. Wang, S., Xu, B., Huo, W., Feng, H., Zhou, X., Fang, F., Xie, Z., Shang, J. K. & Jiang, J. Efficient FeCoNiCuPd thin-film electrocatalyst for alkaline oxygen and hydrogen evolution reactions. *Appl Catal B* **313**, 121472 (2022).
105. Huo, X., Zuo, X., Wang, X., Xing, B. & Zhang, N. High Entropy Alloy CoCrFeNiMo Reinforced Electrocatalytic Performance for High-Efficient Electrocatalytic Water Splitting. *Chem Asian J* **18**, (2023).
106. Zhang, D., Shi, Y., Chen, X., Lai, J., Huang, B. & Wang, L. High-entropy alloy metallene for highly efficient overall water splitting in acidic media. *Chinese Journal of Catalysis* **45**, 174–183 (2023).
107. Hao, J., Zhuang, Z., Cao, K., Gao, G., Wang, C., Lai, F., Lu, S., Ma, P., Dong, W., Liu, T., Du, M. & Zhu, H. Unraveling the electronegativity-dominated intermediate adsorption on high-entropy alloy electrocatalysts. *Nat Commun* **13**, 2662 (2022).
108. Zuo, X., Yan, R., Zhao, L., Long, Y., Shi, L., Cheng, Q., Liu, D. & Hu, C. A hollow PdCuMoNiCo high-entropy alloy as an efficient bi-functional electrocatalyst for oxygen reduction and formic acid oxidation. *J Mater Chem A Mater* **10**, 14857–14865 (2022).
109. Jin, Y., Li, R., Zhang, X., Cao, K., Liao, B., Luo, X., Li, Y. & Ma, W. Ultrafine high-entropy alloy nanoparticles for extremely superior electrocatalytic methanol oxidation. *Mater Lett* **344**, 134421 (2023).
110. Yusenko, K. V., Riva, S., Carvalho, P. A., Yusenko, M. V., Arnaboldi, S., Sukhikh, A. S., Hanfland, M. & Gromilov, S. A. First hexagonal close packed high-entropy alloy with outstanding stability under extreme conditions and electrocatalytic activity for methanol oxidation. *Scr Mater* **138**, 22–27 (2017).
111. Ju, Y., Zhang, A., Xu, Z., Liu, Y., Zhu, X., Zhu, P., Zhou, L. & Yuan, X. Formicary-like PtBi<sub>1.5</sub>Ni<sub>0.2</sub>Co<sub>0.2</sub>Cu<sub>0.2</sub> high-entropy alloy aerogels as an efficient and stable electrocatalyst for methanol oxidation reaction. *Chemical Engineering Journal* **473**, 145347 (2023).
112. Fan, D., Guo, K., Zhang, Y., Hao, Q., Han, M. & Xu, D. Engineering high-entropy alloy nanowires network for alcohol electrooxidation. *J Colloid Interface Sci* **625**, 1012–1021 (2022).

113. Wang, W., Li, X., Cheng, Y., Zhang, M., Zhao, K. & Liu, Y. An effective PtPdAuCuFe/C high-entropy-alloy applied to direct ethylene glycol fuel cells. *J Taiwan Inst Chem Eng* **143**, 104714 (2023).
114. Zhan, C., Xu, Y., Bu, L., Zhu, H., Feng, Y., Yang, T., Zhang, Y., Yang, Z., Huang, B., Shao, Q. & Huang, X. Subnanometer high-entropy alloy nanowires enable remarkable hydrogen oxidation catalysis. *Nat Commun* **12**, 6261 (2021).
115. Gao, G. J., Xu, J. L., Tang, J., Zhang, L. W., Ma, Y. C. & Luo, J. M. Plasma nitrided CoCrFeNiMn high entropy alloy coating as a self-supporting electrode for oxygen evolution reaction. *Journal of Materials Research and Technology* **23**, 5357–5367 (2023).
116. Cui, Y., Jiang, S., Fu, Q., Wang, R., Xu, P., Sui, Y., Wang, X., Ning, Z., Sun, J., Sun, X., Nikiforov, A. & Song, B. Cost-Effective High Entropy Core–Shell Fiber for Stable Oxygen Evolution Reaction at  $2 \text{ A cm}^{-2}$ . *Adv Funct Mater* (2023). doi:10.1002/adfm.202306889
117. Li, Y., Tang, J., Zhang, H., Wang, Y., Lin, B., Qiao, J., Zheng, H., Yu, Z., Liu, Y., Zhou, T. & Lei, X. In-situ construction and repair of high catalytic activity interface on corrosion-resistant high-entropy amorphous alloy electrode for hydrogen production in high-temperature dilute sulfuric acid electrolysis. *Chemical Engineering Journal* **453**, 139905 (2023).
118. Zhu, Y., Dai, W., Zhong, X., Lu, T. & Pan, Y. In-situ reconstruction of non-noble multi-metal core-shell oxyfluorides for water oxidation. *J Colloid Interface Sci* **602**, 55–63 (2021).
119. Jia, Z., Yang, T., Sun, L., Zhao, Y., Li, W., Luan, J., Lyu, F., Zhang, L., Kružic, J. J., Kai, J., Huang, J. C., Lu, J. & Liu, C. T. A Novel Multinary Intermetallic as an Active Electrocatalyst for Hydrogen Evolution. *Advanced Materials* **32**, (2020).
120. Batchelor, T. A. A., Löffler, T., Xiao, B., Krysiak, O. A., Strotkötter, V., Pedersen, J. K., Clausen, C. M., Savan, A., Li, Y., Schuhmann, W., Rossmeisl, J. & Ludwig, A. Complex-Solid-Solution Electrocatalyst Discovery by Computational Prediction and High-Throughput Experimentation\*\*. *Angewandte Chemie International Edition* **60**, 6932–6937 (2021).
121. Schumacher, S., Baha, S., Savan, A., Andronescu, C. & Ludwig, A. High-throughput discovery of hydrogen evolution electrocatalysts in the complex solid solution system Co–Cr–Fe–Mo–Ni. *J Mater Chem A Mater* **10**, 9981–9987 (2022).
122. Krysiak, O. A., Schumacher, S., Savan, A., Schuhmann, W., Ludwig, A. & Andronescu, C. Searching novel complex solid solution electrocatalysts in unconventional element combinations. *Nano Res* **15**, 4780–4784 (2022).

123. Banko, L., Krysiak, O. A., Pedersen, J. K., Xiao, B., Savan, A., Loeffler, T., Baha, S., Rossmeisl Jan and Schuhmann, W. & Ludwig, A. Unravelling Composition–Activity–Stability Trends in High Entropy Alloy Electrocatalysts by Using a Data-Guided Combinatorial Synthesis Strategy and Computational Modeling. *Adv Energy Mater* **12**, (2022).
124. Strotkötter, V., Krysiak, O. A., Zhang, J., Wang, X., Suhr, E., Schuhmann, W. & Ludwig, A. Discovery of High-Entropy Oxide Electrocatalysts: From Thin-Film Material Libraries to Particles. *Chemistry of Materials* **34**, 10291–10303 (2022).
125. Suhr, E., Krysiak, O. A., Strotkötter, V., Thelen, F., Schuhmann, W. & Ludwig, A. High-Throughput Exploration of Structural and Electrochemical Properties of the High-Entropy Nitride System (Ti–Co–Mo–Ta–W)N. *Adv Eng Mater* (2023). doi:10.1002/adem.202300550
126. Clausen, C. M., Krysiak, O. A., Banko, L., Pedersen, J. K., Schuhmann, W., Ludwig, A. & Rossmeisl, J. A Flexible Theory for Catalysis: Learning Alkaline Oxygen Reduction on Complex Solid Solutions within the Ag–Pd–Pt–Ru Composition Space\*\*. *Angewandte Chemie International Edition* (2023). doi:10.1002/anie.202307187
127. Wan, X., Zhang, Z., Yu, W., Niu, H., Wang, X. & Guo, Y. Machine-learning-assisted discovery of highly efficient high-entropy alloy catalysts for the oxygen reduction reaction. *Patterns* **3**, 100553 (2022).
128. Araujo, R. B., Bayrak Pehlivan, I. & Edvinsson, T. High-entropy alloy catalysts: Fundamental aspects, promises towards electrochemical NH<sub>3</sub> production, and lessons to learn from deep neural networks. *Nano Energy* **105**, 108027 (2023).
129. Rittiruam, M., Setasuban, S., Noppakhun, J., Saelee, T., Ektarawong, A., Aumnongpho, N., Boonchuay, S., Khajondetchairit, P., Praserthdam, S., Alling, B. & Praserthdam, P. First-Principles Density Functional Theory and Machine Learning Technique for the Prediction of Water Adsorption Site on PtPd-Based High-Entropy-Alloy Catalysts. *Adv Theory Simul* **6**, (2023).
130. Araujo, R. B. & Edvinsson, T. N<sub>2</sub> adsorption on high-entropy alloy surfaces: unveiling the role of local environments. *J Mater Chem A Mater* **11**, 12973–12983 (2023).
131. Rittiruam, M., Khamloet, P., Tantitumrongwut, P., Saelee, T., Khajondetchairit, P., Noppakhun, J., Ektarawong, A., Alling, B., Praserthdam, S. & Praserthdam, P. First-Principles Active-Site Model Design for High-Entropy-Alloy Catalyst Screening: The Impact of Host Element Selection on Catalytic Properties. *Adv Theory Simul* **6**, (2023).
132. Clausen, C. M., Batchelor, T. A. A., Pedersen, J. K. & Rossmeisl, J. What Atomic Positions Determines Reactivity of a Surface? Long-Range, Directional Ligand Effects in Metallic Alloys. *Advanced Science* **8**, (2021).

133. Clausen, C. M., Pedersen, J. K., Batchelor, T. A. A. & Rossmeisl, J. Lattice distortion releasing local surface strain on high-entropy alloys. *Nano Res* **15**, 4775–4779 (2022).
134. Men, Y., Wu, D., Hu, Y., Li, L., Li, P., Jia, S., Wang, J., Cheng, G., Chen, S. & Luo, W. Understanding Alkaline Hydrogen Oxidation Reaction on PdNiRuIrRh High-Entropy-Alloy by Machine Learning Potential. *Angewandte Chemie International Edition* **62**, (2023).
135. Yan, D., Kristoffersen, H. H., Pedersen, J. K. & Rossmeisl, J. Rationally Tailoring Catalysts for the CO Oxidation Reaction by Using DFT Calculations. *ACS Catal* **12**, 116–125 (2022).
136. Bagger, A., Jensen, K. D., Rashedi, M., Luo, R., Du, J., Zhang, D., Pereira, I. J., Escudero-Escribano, M., Arenz, M. & Rossmeisl, J. Correlations between experiments and simulations for formic acid oxidation. *Chem Sci* **13**, 13409–13417 (2022).
137. Yu, Y., Zhang, W., Sun, F., Fang, Q., Pan, J., Chen, W. & Zhuang, G. High electrocatalytical performance of FeCoNiCuPd high-entropy alloy for nitrogen reduction reaction. *Molecular Catalysis* **519**, 112141 (2022).
138. Saidi, W. A., Shadid, W. & Veser, G. Optimization of High-Entropy Alloy Catalyst for Ammonia Decomposition and Ammonia Synthesis. *J Phys Chem Lett* **12**, 5185–5192 (2021).
139. Yu, Y., Zhang, W., Fang, Q., Zhang, X., Zhao, S.-T., Chen, W. & Zhuang, G. Computational design of one FeCoNiCuZn high-entropy alloy for high-performance electrocatalytic nitrate reduction. *Appl Surf Sci* **626**, 157246 (2023).
140. Chen, Z. W., Gariepy, Z., Chen, L., Yao, X., Anand, A., Liu, S.-J., Tetsassi Feugmo, C. G., Tamblyn, I. & Singh, C. V. Machine-Learning-Driven High-Entropy Alloy Catalyst Discovery to Circumvent the Scaling Relation for CO<sub>2</sub> Reduction Reaction. *ACS Catal* **12**, 14864–14871 (2022).
141. Pedersen, J. K., Batchelor, T. A. A., Bagger, A. & Rossmeisl, J. High-Entropy Alloys as Catalysts for the CO<sub>2</sub> and CO Reduction Reactions. *ACS Catal* **10**, 2169–2176 (2020).
142. Wang, J., Zhao, C.-X., Liu, J.-N., Ren, D., Li, B.-Q., Huang, J.-Q. & Zhang, Q. Quantitative kinetic analysis on oxygen reduction reaction: A perspective. *Nano Materials Science* **3**, 313–318 (2021).
143. Gileadi, E. in *Electrode Kinetics for Chemists Engineers and Material Scientists* 443–454 (Wiley-VCH, Inc., 1993).
144. Bard, A. J. & Faulner, L. R. in *Electrochemical Methods Fundamentals and Applications* 339–339 (John Wiley & Sons, Inc., 2001).

145. Nørskov, J. K., Rossmeisl, J., Logadottir, A., Lindqvist, L., Kitchin, J. R., Bligaard, T. & Jónsson, H. Origin of the overpotential for oxygen reduction at a fuel-cell cathode. *Journal of Physical Chemistry B* **108**, 17886–17892 (2004).
146. Pedersen, J. K., Clausen, C. M., Krysiak, O. A., Xiao, B., Batchelor, T. A. A., Löffler, T., Mints, V. A., Banko, L., Arenz, M., Savan, A., Schuhmann, W., Ludwig, A. & Rossmeisl, J. Bayesian Optimization of High-Entropy Alloy Compositions for Electrocatalytic Oxygen Reduction\*\*. *Angewandte Chemie - International Edition* **60**, 24144–24152 (2021).
147. Kondo, S., Nakamura, M., Maki, N. & Hoshi, N. Active Sites for the Oxygen Reduction Reaction on the Low and High Index Planes of Palladium. *The Journal of Physical Chemistry C* **113**, 12625–12628 (2009).

## **Declaration of consent**

on the basis of Article 18 of the PromR Phil.-nat. 19

Name/First Name: Mints Vladislav

Registration Number: 19-136-332

Study program: Chemistry and Molecular Science

Bachelor

Master

Dissertation

Title of the thesis: Machine Learning in High Entropy Alloy Research

Supervisor: Prof Dr. Matthias Arenz

I declare herewith that this thesis is my own work and that I have not used any sources other than those stated. I have indicated the adoption of quotations as well as thoughts taken from other authors as such in the thesis. I am aware that the Senate pursuant to Article 36 paragraph 1 litera r of the University Act of September 5th, 1996 and Article 69 of the University Statute of June 7th, 2011 is authorized to revoke the doctoral degree awarded on the basis of this thesis.

For the purposes of evaluation and verification of compliance with the declaration of originality and the regulations governing plagiarism, I hereby grant the University of Bern the right to process my personal data and to perform the acts of use this requires, in particular, to reproduce the written thesis and to store it permanently in a database, and to use said database, or to make said database available, to enable comparison with theses submitted by others.

Bern, 13-12-2023

Place/Date

*Vladislav Mints*  
Signature